Proceedings of the 9th Small Systems Simulation Symposium 2022

28.02. - 02.03.2022

Faculty of Electronic Engineering
Niš, Serbia

The Science and Technology park
Niš, Serbia

Organized by

Faculty of Electronic Engineering Niš

SCIENCE
TECHNOLOGY
PARK
NIS

Proceedings of the 9th Small Systems Simulation Symposium 2022

Publisher:

University of Niš, Faculty of Electronic Engineering
Aleksandra Medvedeva 14,
18000 Niš
http://elfak.ni.ac.rs

Editor:

Miljana Milić

Printed by:

XCopy, Niš

Number of copies printed: 40
Year of publication: 2022

Preface

To the Proceedings of the 9th Small Systems Simulation Symposium

Dear colleagues,

International Scientific Symposium SSSS 2022 is organized by the Laboratory for Electronic Design Automation (LEDA), at the Faculty of Electronic Engineering for the 9th time. The aim is to gather scientists and experts in order to exchange the information and disseminate best practices, ideas and advancements in the state-of-the-art and technical improvements in domains of Electronic and Information Systems, System Design, Energy Efficiency, Artificial Intelligence and other engineering applications.

Having that in mind it is understandable that the research staff of LEDA started contemplating the necessity of deepening the international cooperation with several main goals among which the most important were acquiring new knowledge and promoting research results. One of the opportunities was to start regular meetings with the research centres with which the collaboration already lasted for more than ten years. So the idea of Small Systems Simulation Symposium (SSSS) was born in the autumn of the year 1999 in Southampton and one may claim that Prof. Robert Damper was the one who mainly contributed to the final spelling of the name.

Among the large group of authors we appreciate the contributions of some who made the symposium to start and pertain during many years. In the attempt not to exaggerate we will most surely miss some names but still we wouldn’t like to miss all of them. These are Prof. V. Litovski, Prof. M. Zwolinski, Prof. R. Damper, Dr I. Bushehri, Prof. S. Bojanić, Prof. O. Nieto, Prof. V. Zerbe, Prof. D. Trajanov, Prof. V. Melikyan, Prof. T. Kazmierski ….

The symposium persisted in spite of many turbulent periods due to the political changes and wars conducted around and against the country. Even today, in the time of global Covid-19 pandemic circumstances, we have done our best to find some efficient and health-safe, virtual ways to create and maintain the communications among our colleagues and friends, and respectful authors in order to continue this tradition.

This year, the symposium will welcome authors of more than 25 papers. All that was possible thanks to a strong support obtained from other universities and companies, as well as respected sponsors and partners.

This year, our partner in symposium organization is the Science-technology park – Niš. This partnership seemed to be the best way to connect practice and theory, students and professors, researchers and engineers, experienced and unexperienced, young and old generations involved in the field of science and technology. We really hope that the established tradition will last for long, especially having in mind the recognition (by the Serbian society) of the importance of the advanced technologies for the national wealth and progress. We believe that SSSS, by its actions, had so far, and will have a noticeable influence and that it will flourish in the future together with the Serbian IT sector as a whole.

SSSS 2022 Organizing Committee

The 9th Small Systems Simulation Symposium
is supported by:

TERI Engineering, Belgrade, Serbia

Ministry of Education, Science, and Technological Development of the
Republic of Serbia

STEERING COMMITTEE OF THE SSSS2022

M. Milić, University of Niš (Serbia)
M. Andrejević Stošović, University of Niš (Serbia)
M. Dimitrijević, University of Niš (Serbia)
B. Blanuša, University of Banja Luka (Bosnia and Herzegovina)
S. Bojanić, Universidad politécnica de Madrid (Spain)
I. Bushehri, Lime Microsystems, (United Kingdom)
N. Cvetković, University of Niš (Serbia)
B. Dokić, University of Banja Luka (Bosnia and Herzegovina)
N. Janković, University of Niš (Serbia)
T. Kazmierski, University od Southampton (United Kingdom)
LJ.Kocarev, FCSE (FINKI) Skopje (Macedonia)
V. Litovski, University of Niš (Serbia)
V. Melikyan, Synopsys (Armenia)
S. Milenković, Lime microsystems (United Kingdom)
D. Milovanović, University of Niš (Serbia)
O. Nieto, Universidad politécnica de Madrid (Spain)
D. Pantić, University Niš (Serbia)
P. Petković, University of Niš (Serbia)
B. Reljin, University of Belgrade (Serbia)
M. Simić, School of Aerospace, Mechanical and Manufacturing Engineering (Australia)
M. Savić, Lime Microsystems (Serbia)
D. Trajanov, FCSE (FINKI) Skopje (Macedonia)
V. Zerbe, Technical University of Erfurt (Germany)
M. Živanov, University of Novi Sad (Serbia)
M. Zwolinski, University of Southampton (United Kingdom)

ORGANIZING COMMITTEE OF THE SSSS2022

M. Andrejević Stošović, University of Niš (Serbia)
M. Milić,University of Niš (Serbia)
M. Dimitrijević, University of Niš (Serbia)
S. Djordjević, University of Niš (Serbia)
B. Jovanović, University of Niš (Serbia)
D. Mirković, University of Niš (Serbia)
D. Stevanović, University of Niš (Serbia)
J. Milojković, University of Niš (Serbia)
M. Stanojlović Mirković, University of Niš (Serbia)
N. Radivojević, University of Niš (Serbia)
V. Arsić, University of Niš (Serbia)

SYMPOSIUM SECRETARY

Srđan Đorđević, PhD, Faculty of Electronic Engineering, Aleksandra Medvedeva 14, Niš, Serbia

Proceedings of

The 9th Small Systems Simulation Symposium

Faculty of Electronic Engineering, Niš, Serbia, 28th February – 2nd March, 2022

Contents

Plenary Session

Session 1

Session 2

Session 3

Session 4: Poster Session

Proceedings of the 9th Small Systems Simulation Symposium 2022, Niš, Serbia, 28th February - 2nd March 2022

On Cascade Realization of Active Gm-C Filters

Vančo Litovski, Jelena Milojković, and Slobodan Bojanić

Abstract – To our best knowledge we are the first to address cascade realization of Gm-C filter. Among the reasons for absence of solutions based on this type of synthesis we see a subtle difference between cascade active RC and Gm-C filters. It will be revealed here, and examples will be given of cascade synthesis of single- and two-phase filters.

Keywords – Gm-C filters, Cascade synthesis, $\mathcal{RM}$ software for filter design, Polyphase filters

I. INTRODUCTION

Synthesis of integrated electronic filters based on active RC solutions faces the important problem of large tolerances, high temperature dependence, and large consumed silicon area by the resistors [1]. The first step to overcome these problems was the introduction of the switched capacitor (SC) technology [2]. Here, however, new problems were introduced related to the need for high frequency sampling and for use of an active RC antialiasing filter to reduce the switching noise inherent to the technology. Of course, due to the nature of the technologies these two were limited to low frequency applications, mainly (but not only) in audio.

As an alternative to these solutions the GM-C (or OTA-C) technology emerged allowing integration with relatively small silicon area occupation and no resistors and switches [3]. Namely, by excluding the resistor, no time constant is possible to produce and, accordingly, no frequency dependence. The transconductance operational amplifier (OTA), however, offers its output voltage controlled current source, characterised by the transconductance (denoted Gm), as a substitution by forming a proper time constant with a capacitor. The resulting circuits are known as Gm-C or OTA-C filters.

Gm-C filters may be synthesized it three ways [4]: as parallel and cascade connections of biquads and as passive LC circuits in which the inductance is simulated by impedance converters built of OTAs. A study was reported in [4] aiming to compare these three alternatives from several points of view and it was found that every single one has its own advantages the cascaded one having them most. That was the reason much attention was devoted to that solution

In these proceedings we will first introduce the problem of cascaded filter synthesis as such. Then we will deliver a short review of biquads necessary to synthesize any type of realisable transfer function. That will be followed with a short description of the capabilities of the $\mathcal{RM}$ software for filter design in both system physical synthesis and transfer function synthesis. A glimpse on the two-phase filter will be given, too. The paper finishes with two representative examples.

Having developed a complete set of Gm-C cells capable to realize any physically realizable transfer function two examples are given representing a band-pass and a poly-phase filter.

II. THE CIRCUIT SYNTHESIS

A. On the cascade synthesis of electronic filters

Cascaded Gm-C filters in general does not differ from the active RC solutions. Namely, all rules related to the pole-zero pairing and order of extraction remain the same. The difference is in the structure of the cells.

In this paragraph we will go through a description of a set of Gm-C cells which are used in the $\mathcal{GM\_C\_}cascade$ program of the $\mathcal{RM}$ software for filter design. These are based on the theory described in literature [5].

As will be seen, the main difference between the active RC and the Gm-C cell is in the fact that the output impedance of the trans-conductor is large so that when the succeeding cell has finite input impedance it loads the output of the preceding cell so consequently changing the overall transfer function. To avoid that within the program $\mathcal{GM\_C\_}cascade$ all the Gm-C cells having finite input impedance are extended by a unity gain amplifier which is added to isolate them from the preceding cell. The unity gain amplifier has to have high frequency domain performances to comply with the application in Gm-C technology.

B. The Gm-C cells

A specific property of cascade synthesis is that it needs a proper first and second order cell for any type of transmission zero. That makes the software for circuit synthesis rather complex. Nevertheless, the $\mathcal{RM}$ software for filter design creates a complete set of first and second order Gm-C cells so allowing synthesis of any physically realizable transfer function.

The first order cells are depicted in Figs. 1-3. As can be

Vančo B. Litovski is retired prof. of Faculty of Electronic Engineering at the University of Niš, E-mail: petarznikolic@gmail.com,

Jelena Milojković is with the Faculty of Electronic Engineering at the University of Niš, E-mail: jelena.milojković@icnt.rs.

Slobodan Bojanić is with Universidad Politecnica de Madrid, E-mail: slobodan.bojanic@upm.es.

seen a generic cell [5] is used to create variants for different positions of the transmission zeros.

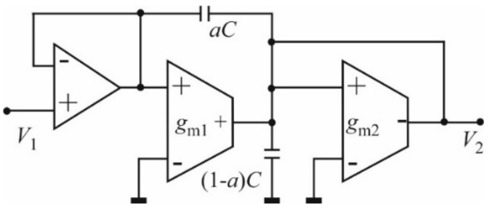

Fig. 1. Generic first order cell [5]

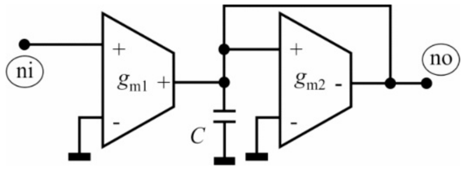

2. First order Gm-C flow-pass cell

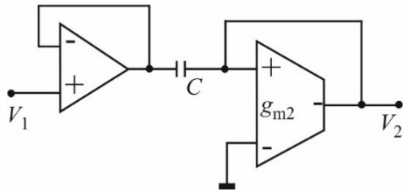

Fig. 3. First order high-pass cell

Note the isolating unity gain amplifier was necessary only for the high-pass cell. Here, again we start with a generic cell given in Fig. 4 [5].

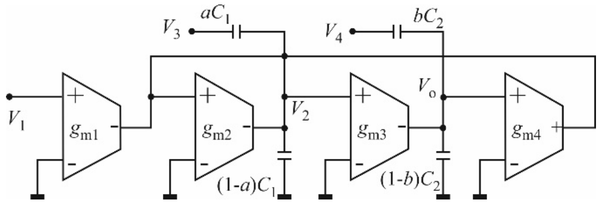

Fig. 4. A generic Gm-C biquad [5]

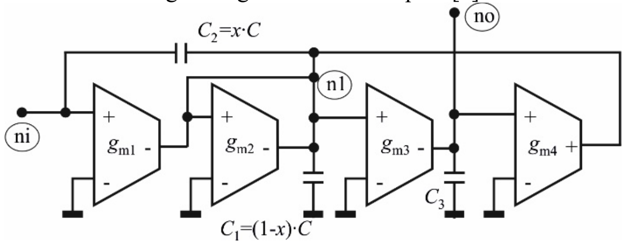

Fig. 5. The second order Gm-C cell used within the $\mathcal{RM}$ software. Note: $0 \leq x \leq 1$. "ni" stands for "input node" while "no" for the "output node"

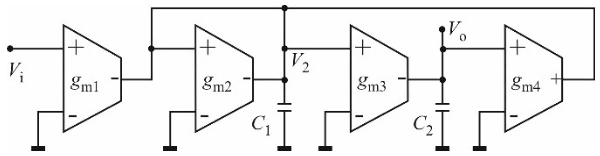

Fig. 6. Second order low-pass cell

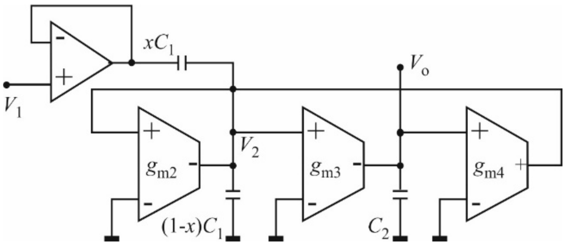

Fig. 7. A band-pass biquad

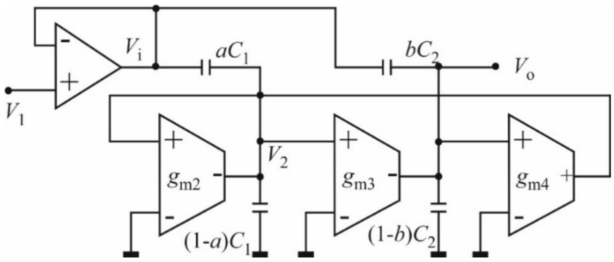

Fig. 8. A high pass biquad

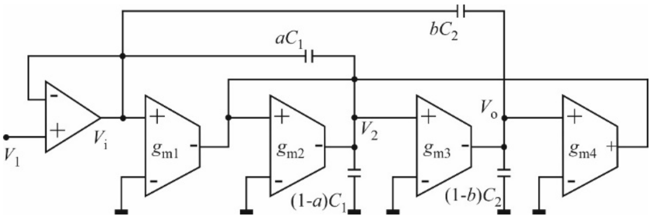

Fig. 9. A band-stop (notch) biquad and complex zeros including all-pass

The set of Figs. 4-9 represents the second order cells (biquads). $a=b=x=0.5$ was used in all cases.

C. Polyphase filters

There is one transformation of the filter's transfer function which is possible to be done only if the input signal has additional variant shifted in phase for π/2 rad. We call these signals are in quadrature. If so, it is possible to linearly translate the frequency response on both directions. In that way it is possible to eliminate the image of the amplitude characteristic existing at negative frequencies and disturbing the process of RF demodulation. The transformation is given by

$$I_{\mathrm{lp}}(\mathrm{j}\omega) = \mathrm{j}\omega C \cdot V_{\mathrm{lp}} \Rightarrow I_{\mathrm{bp}}(\mathrm{j}\omega) = j(\omega\text{-}\omega_0)C \cdot V_{\mathrm{bp}}. \quad (1)$$

Here indices lp and bp denote prototype and transformed variables, respectively.

The last expression may be decomposed so that

$$I_{\mathrm{bp}}(\mathrm{j}\omega) = \mathrm{j}\omega C \cdot V_{\mathrm{bp}} - \mathrm{j}\omega_0 C \cdot V_{\mathrm{bp}} = \mathrm{j}\omega C \cdot V_{\mathrm{bp}} - j g_m \cdot V_{\mathrm{bp}} (2)$$

hence $g_{\mathrm{m}}=\omega_0 C$.

Implementation of these expressions leads to creation of a specific two-phase cell for any of the ones depicted above.

To make it shorter, here we will show the first and second order low pass two-phase cells as depicted in Figs. 10-11.

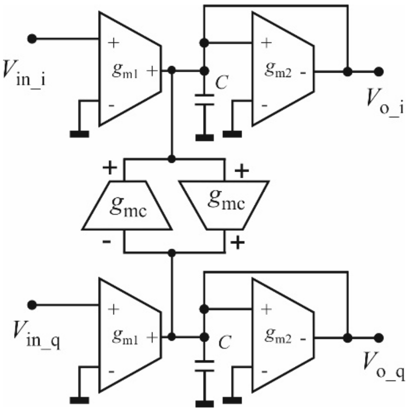

Fig 10. First order two-phase Gm-C cell

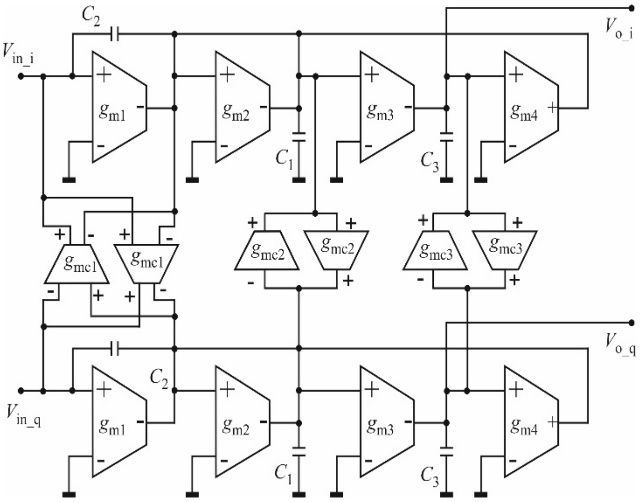

Fig. 11. Second order two-phase Gm-C cell

D. The system synthesis part of the RM software for filter design

For both transfer function synthesis and circuit synthesis we use the RM software for filter design [1].

As for the circuit synthesis the following technologies are available:

- Passive LC
- Active RC
- Active SC
- Active GM-C
- Active two-phase Gm-C
- Digital IIR

The program produces complete information for further studying of the circuits obtained including tolerance and noise analysis since it produces SPICE net lists wherever is appropriate.

III. TRANSFER FUNCTION SYNTHESIS USING THE RM SOFTWARE

The transfer function synthesis part covers a very wide variety of transfer function solutions in the low-pass domain being selective or linear phase. That includes polynomial and filters with rational transfer functions having transmission zeros on the imaginary axis. Using transformations band-pass, band-stop, and high-pass filters may be produced. Phase correctors may be synthesized in both low- and band-pass cases. Band-pass approximation of linearly changing group delay (including Hilbert transform filters) is possible, too. Finally, simultaneous amplitude and group delay approximation is offered for band-pass filter.

IV. EXAMPLES

In this paragraph examples will be given of implementation of the RM software for filter design in active Gm-C synthesis.

A. Example no. 1

In this example a bandpass filter with corrected group delay characteristic will be synthesized. The following are the primary requirements: Central frequency f_c=100 kHz, Passband attenuation a_{max}=3 dB, Passband width BW= 5 kHz, Stopband attenuation a_{min}= 40 dB and maximum group delay variation in the passband δ= 5%.

Table I depicts the synthesis flow using the RM software for filter design.

TABLE I. DESIGN FLOW

Step no.	Action	RM program
1	Low-pass polynomial synthesis	CMAC
2	Low-pass rational synthesis	Chang_1
3	Low pass to band-pass transformation	transformations
4	Group delay correction synthesis	Corrector_bp
5	Transfer function verification	TF_analysis
6	Cascade synthesis	GM_C_Cascade
7	Circuit verification	LTSpice

For the passband amplitude characteristic, the LSM [6] response was chosen. The order of the low-pass prototype was chosen to be n_{LP}=9, the number of transmission zeros on the ω-axis was chosen to be m_{LP}=4. After low pass to band-pass transformation the order of the selective part of the filter was n=18 with m=8. Then, a second order corrector was synthesized. Table 2 contains the poles and zeros of the final normalized transfer function.

TABLE II POLES AND ZEROS OF EXAMPLE 1

Zeros	
Real part	Imaginary part
1.469681430e-002	±1.001078808e+000
0.000000000e+000	±1.030475132e+000
0.000000000e+000	±9.704261351e-001
0.000000000e+000	±1.035971066e+000
0.000000000e+000	±9.652779240e-001
0.000000000e+000	0.000000000e+000
0.000000000e+000	0.000000000e+000
0.000000000e+000	0.000000000e+000
0.000000000e+000	0.000000000e+000
0.000000000e+000	0.000000000e+000
	Poles
-1.951484418e-003	±1.025616441e+000
-1.855212095e-003	±9.750198410e-001
-6.877653628e-003	±9.756635046e-001
-7.224679730e-003	±1.024892605e+000
-3.137394414e-002	±9.995077166e-001
-2.685377064e-002	±1.011501172e+000
-2.622808025e-002	±9.879332870e-001
-1.624784559e-002	±1.020928981e+000
-1.558456678e-002	±9.792520367e-001
-1.469681430e-002	±1.001078808e+000

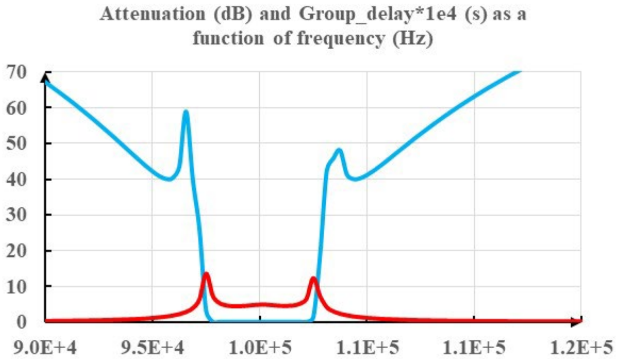

Fig. 12. Attenuation (blue) and Group delay (red) response of the Example 1 obtained by transfer function analysis

TABLE III STRUCTURE AND ELEMENT VALUES OF EXAMPLE 1

Cell	Element values
No. 1 Second order band-stop	C1=C2=C3= C4=2.038895899e-008 gm1=3.522695375e+000 gm2=1.e-004 gm3=1.e-004 gm4=6.905280960e+000
No. 2 Second order band-stop	C1=C2=C3= C4=5.507335586e-009 gm1=2.543008696e-001 gm2=1.e-004 gm3=1. e-004 gm4=5.031310372e-001
No. 3 Second Order all-pass	gm1=2.900438985e-002 gm2=1.e-004 gm3=1.e-004 gm4=5.800877971e-002 C1=C2=2.707303431e-009 C3==C4=1.353651716e-009
No. 4 Second order band-stop	C1=C2=C3= C4=1.481681523e-009 gm1=1.632391899e-002 gm2=1.e-004 gm3=1.e-004 gm4=3.549508574e-002
No. 5 Second order band-stop	C1=C2=C3= C4=2.448862253e-009 gm1=4.411874951e-002 gm2=1.e-004 gm3=1.e-004 gm4=9.873008050e-002
No. 6 Second order low-pass	gm1=gm2=gm3= gm4=1.e-004 C1=2.536419113e-009 C2=9.986636587e-012
No. 7 Second order low-pass	gm1=gm2=gm3= gm4=1.e-004 c1=3.034056278e-009 c2=8.547820677e-012
No. 8 Second order high pass	gm2=1.e-004 gm3=1.e-004 gm4=9.873008049e-002 C1=C2=C3= C4=2.553085776e-009
No. 9 Second order high pass	gm2=1.e-004 gm3=1.e-004 gm4=5.031310372e-001 C1=C2=C3= C4=5.785219484e-009
No. 9 Second order band-pass	gm2=gm3=gm4=1.e-004 C1=C2=2.144700106e-008 C3=6.211767830e-013

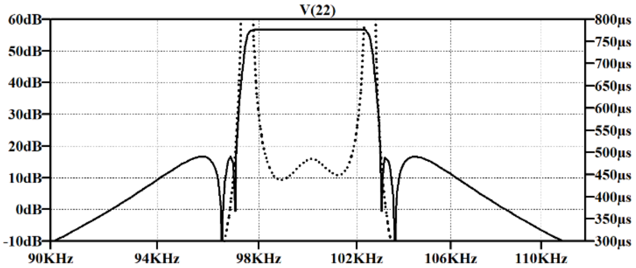

Fig. 13. Responses for Example 1 obtained by SPICE simulation of the circuit

B. Example no. 2

The second example will be given in short. The task was to synthesize a low-pass filter with bandwidth of 2 MHz which has no image at negative frequencies. Here a fifth order Chebyshev filter was used as prototype with f_c= 1 MHz and a_{max}= 0.5 dB. It was shifted towards the positive frequencies by 1.01 MHz. Table IV contains the structure of the filter and the element values while Fig.14

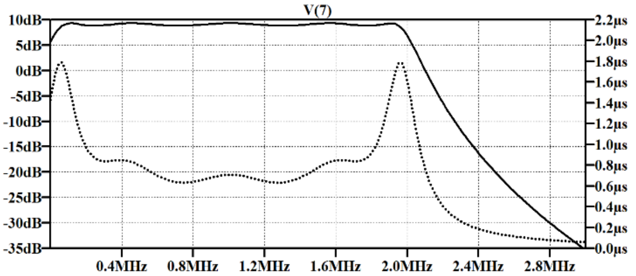

Fig. 14. Responses for Example 2 obtained by SPICE simulation of the circuit

depicts its frequency response obtained by SPICE simulation of the circuit. Note, the transfer function of the filter prior synthesis was renormalized to exhibit 3 dB at the band edge (f_c).

TABLE IV STRUCTURE AND ELEMENT VALUES OF EXAMPLE 2

Cell	Element values
No. 1 Second order TWO-PHASE low pass	gm1=gm2=gm3= gm4=1.e-4 C1=7.527409006e-011 C2=3.644053524e-012 gmc1=-4.776906673e-004 gmc2=-2.312522619e-005
No. 2 Second order TWO-PHASE low pass	gm1=gm2=gm3= gm4=1.e-4 C1=2.875214393e-011 C2=2.072635963e-011 gmc1=-1.824615988e-004 gmc2=-1.315298339e-004
No. 3 First order TWO-PHASE low pass	C=4.652194613e-011 gm1=2.923060084e-004 gm2=1.000000000e-004 gmc=-2.952290685e-004

V. CONCLUSION

A short study of the cascaded synthesis of single- and two-phase active Gm-C filters is given. The synthesis process, its results, and the capabilities of the *RM* software for filter design were demonstrated by two examples.

ACKNOWLEDGEMENT

This work has been supported by The Ministry of Education, Science and Technological Development of the Republic of Serbia.

REFERENCES

[1] Litovski, V., “Electronic filters, theory, numerical receipts and design practice using the RM software for filter design”, *Springer*, New Delhi, 2019.

[2] Fleisch, P.E., and Laker, K.R., “A family of active switched capacitor biquad building blocks”, *The Bell System Technical Journal*, Vol. 58, No. 10, 1979, pp. 2235-2269.

[3] Mahun, P.V.A., “VLSI analog filters: active RC, OTA-C, and SC, modeling and simulation in science engineering and technology”, *Springer*, New York, 2013.

[4] Litovski, V., “Gm-C filter synthesis for modern RF systems”, *Springer*, New Delhi, 2022.

[5] Schaumann R., and Van Valkenboug E., “Design of Analog Filters”. *Oxford University Press*, 2001, New York.

[6] Raković, B.D., and Litovski, V.B., “Least-squares monotonic low-pass filters with sharp cutoff”, *Electronic Letters*, Vol. 9, No. 4, pp.75-76, 1973

Non-linear Loads Identification Using Voltage Source with Second Harmonic Injection

Marko Dimitrijević, Vančo Litovski

Abstract - The existence of the higher harmonics in the current spectrum are well known and studied phenomena. Their negative effects on power grid and connected devices are of particular importance and subject of an extensive research. Nevertheless, higher harmonics in current spectrum can be utilized for identifying nonlinear loads connected to the power grid. The method of identification can be based on some type of machine learning or deep learning algorithm, where current harmonics are used as input parameters.

At most nonlinear loads, the harmonic amplitude decreases monotonically as the harmonic order increases, and current spectrum consists of odd harmonic only. This can reduce the number of input parameters and impair performance of an algorithm.

In this paper, we are proposing the method of voltage source second harmonic injection that can overcame identified problems.

Keywords – current harmonics, nonlinear loads identification.

I. INTRODUCTION

In the last 30 years, the way electricity has been used has changed significantly [1]. Increase in the number of consumer electronic devices had enormous influence on world economy and to our lifestyle. In addition, raising awareness of climate changing forces automotive industry to switch from internal combustion engines to electric ones. As a consequence, electronic devices immensely change the structure of total power consumption. With the increase in electric power consumption, load identification and monitoring became important.

Today, electronic systems are synonym for nonlinear load. They represent a circuit consisting of semiconductor devices, which require direct current for operation. However, electric energy is supplied in the form of alternating current, which cannot be directly used for electronic device operation. Hence, all electronic devices must have some kind of power converter.

The power converter can be modelled as two-port network with nonlinear input impedance connected to power grid. Hence, the characterization of the electronic device can be performed by characterization of the power converter. This characterization can be done by determining the current spectrum or other quantities that can be used as unique fingerprint of that device. The higher harmonic components in the current spectrum cause losses and disturbance in the power grid. Favourably, they can be regarded as specific signature of a nonlinear load, therefore providing the means for classifying nonlinear loads connected to the power grid [2].

The identification and classification methods of nonlinear loads can be direct – using harmonic components of current spectrum, or indirect – using some of the parameters that depend on harmonics. In our previous research, an indirect method for classification of nonlinear loads using artificial neural networks (ANNs), based on active, reactive and distortion power was investigated [3, 4].

The direct method, using current spectrum is elaborated in [2]. In this research, amplitudes of current harmonics as inputs for classification of nonlinear loads were used. The presented method fits into NILM category – one measuring device for various combinations of devices were used. The method consists of three phases: signal acquisition, current harmonic extraction and device identification and classification using ANNs. The acquisition and harmonic extraction are performed using system for nonlinear load analysis [5]. The extracted parameters, i.e., amplitudes of current harmonics are used for ANN training. Finally, the trained ANN was employed for identification of similar nonlinear loads and unknown combinations of loads connected to the power grid.

For most nonlinear loads, the harmonic amplitude decreases monotonically as the harmonic order increases, and current spectrum consists of odd harmonic only. This reduces number of input parameters and impairs performance of an algorithm. In this paper, the issues of identification and classification based on current harmonics are discussed and the method of voltage second harmonic injection is proposed, that can overcome identified problems.

The paper is organized as follows: in the second section the classification of nonlinear loads using current spectrum is discussed. In third section, the method of second voltage injection is proposed and discussed. The measured results with nonlinear loads are presented. Forth section concludes the paper.

II. CLASSIFICATION OF NONLINEAR LOADS USING CURRENT SPECTRUM

A. Harmonic analysis

The first step in recognizing and classifying nonlinear consumers is harmonic analysis. It will provide parameters

Marko Dimitrijević and Vančo litovski are with Faculty of Electronic Engineering, University of Niš, A. Medvedeva 14, 18000 Niš, Serbia. (email: marko.dimitrijevic@elfak.ni.ac.rs, vanco.litovski@elfak.ni.ac.rs.

for ANN training. Harmonic analysis is performed using system for nonlinear load analysis, in order to measure current and to determine the current spectrum, i.e., higher harmonics using Fourier analysis. The system is based on acquisition modules for A/D conversion, computer interface and software component for harmonic analysis, described in great detail in [5].

Having in mind that power grid impedance is low, the voltage waveform can be regarded as constant and independent on current at the point of common connection (PCC). The mains can be approximated with ideal voltage generator (Fig 1).

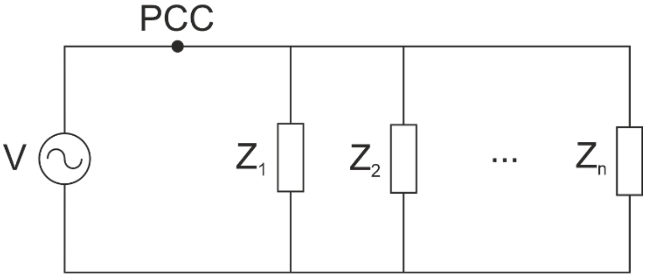

Fig. 1. The mains is approximated with ideal voltage generator V, suppling various loads Z1, ..., Zn.

The total current flowing through PCC is equal to the sum of all currents flowing through loads Zn.

The current can be represented using Fourier series:

$$\begin{aligned} i(t) &= A_0 + \sum_{k=1}^{\infty}\left(A_k \cdot \cos(k\omega t) + B_k \cdot \sin(k\omega t)\right) \\ i(t) &= I_0 + \sum_{k=1}^{\infty} I_k \cdot \cos(k\omega t + \varphi_k) \end{aligned} \tag{1}$$

where $I_0 = A_0$ represents DC current, $I_k = \sqrt{A_k^2 + B_k^2}$ amplitude and $\varphi_k = \arctan\frac{A_k}{B_k}$ phase of the k^{th} harmonic.

$\omega = \frac{2\pi}{\mathrm{T}}$ represents fundamental frequency.

The orthogonal coefficients A_k, B_k are calculated as:

$$A_0 = \frac{1}{\mathrm{T}}\int_{-\mathrm{T}/2}^{+\mathrm{T}/2} i(t)dt, \quad A_k = \frac{2}{\mathrm{T}}\int_{-\mathrm{T}/2}^{+\mathrm{T}/2} i(t)\cdot\cos\left(\frac{2k\pi t}{\mathrm{T}}\right)dt \tag{2}$$

and

$$B_k = \frac{2}{T}\int_{-\mathrm{T}/2}^{+\mathrm{T}/2} i(t)\cdot\sin\left(\frac{2k\pi t}{\mathrm{T}}\right)dt. \tag{3}$$

For the further analysis, it is convenient to represent current as complex vector, which k-th component $A_k + jB_k$ correspond to k-th harmonic:

$$\tilde{I} = \left[A_0 \quad A_1 + jB_1 \quad \dots \quad A_m + jB_m\right]^{\mathrm{T}} \tag{4}$$

The total current, measured at the PCC, is equal to the vector sum of all loads' currents:

$$\tilde{I}_{\mathrm{PCC}} = \tilde{I}_1 + \tilde{I}_2 + \dots + \tilde{I}_{\mathrm{n}}. \tag{5}$$

Equation (5) provides means for efficient calculation of total currents corresponding to various combinations of different loads. One does not need to measure currents for all combination of loads, it is sufficient to measure currents for separate loads, and the total current for a combination is vector sum of separate currents.

B. Input parameters

In previous research [4],], only amplitudes I_k of current harmonics as inputs for classification of nonlinear loads were used. The parameter space of phase is S^1, which is not simply connected topological space with fundamental (first homotopy) group $\pi_1\left(S^1\right) = \mathbb{Z}$. The two infinitesimally close points can differ for 2π, which makes phase unsuitable as input parameter. However, the phase carries an information which should not be disregarded.

The solution is to represent components of current vector by real and imaginary parts $A_k + jB_k$ in Cartesian complex plane, which is simply connected topological space $\mathbb{R}^2$. This approach effectively doubles number of input parameters.

C. Training and identification

Artificial neural network is trained using input parameters: the set of measured harmonic amplitudes I_k, or calculated orthogonal components A_k, B_k for different combination of loads represents input parameters. Having in mind that harmonic amplitudes decrease with harmonic order, the highest harmonic order used is forty. Since even harmonics are not present in the spectrum of most electronic devices only odd harmonics are considered. Hence, one has only twenty input parameters in case of harmonic amplitudes used as input parameters, or forty in case of orthogonal components.

The process of identification is straightforward: once ANN is trained and look-up table is formed, the measured value of current in point of common coupling is transformed using (1) – (3), and corresponding amplitudes or orthogonal components used for identification.

III. SUPPLY VOLTAGE SECOND HARMONIC INJECTION – MEASURED VALUES

The number of input parameters is limited due to the absence of even harmonics in the current spectrum and the choice of the highest harmonic order used in training/identification. First limitation is intrinsic to the structure of nonlinear loads. The order of highest harmonic in the current spectrum taken into consideration is arbitrary but having in mind that harmonic amplitudes decrease (near) monotonically as harmonic order increases, the resolution of measuring equipment determines the highest order. Those limitations are illustrated in Fig. 2.

Fig. 2 presents current spectrum of nonlinear load (LED lamp, 6W) connected to 230VRMS, 50Hz sinusoidal voltage source:

$$v_1(t) = 230\sqrt{2} \cdot \sin(2\pi \cdot 50\text{Hz} \cdot t) \quad [\text{V}] \tag{6}$$

The highest measured harmonic is of order twenty. As voltage source, Omicron CMC365 instrument was used [5]. Measurements are performed using system for nonlinear load analysis [4].

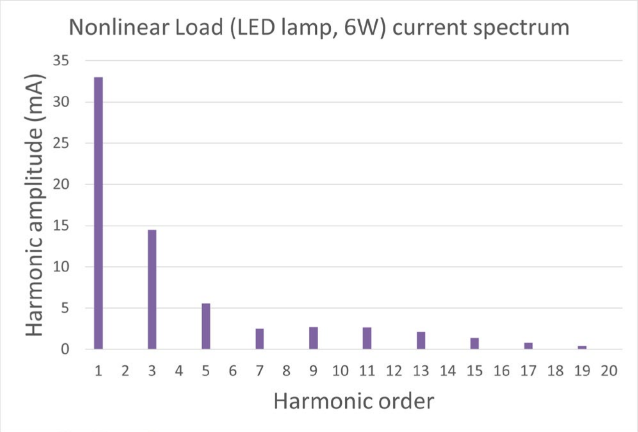

Fig. 2. The current spectrum of LED lamp, up to 20th harmonic. The limitations due absence of even harmonics and decrease of amplitudes are evident.

The current spectrum represented using orthogonal components A_k, B_k, for same load and conditions, are shown in Fig. 3. Each harmonic is represented with two real parameters.

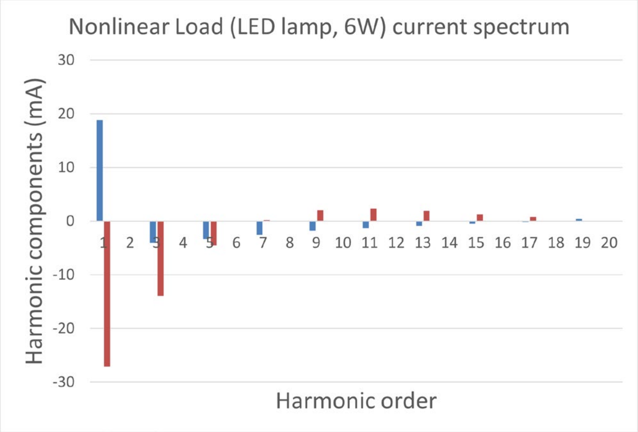

Fig. 3. The current spectrum of LED lamp, up to 20th harmonic, represented with orthogonal components, i.e., real (blue) and imaginary (red) part. The number of parameters is effectively doubled.

The spectra of most nonlinear loads do not have even harmonics. In order to instigate even harmonics, the supply voltage should be non-sinusoidal, i.e., in addition to the fundamental harmonic, it should also contain a second harmonic:

$$\begin{aligned} v_2(t) = {} & 230\sqrt{2} \cdot \sin(2\pi \cdot 50\text{Hz} \cdot t) + \\ & +20\sqrt{2} \cdot \sin(2\pi \cdot 100\text{Hz} \cdot t) \quad [\text{V}]. \end{aligned} \tag{7}$$

The current spectrum of nonlinear load, measured with using voltage supply with second harmonic injection (7) is shown in Fig 4.

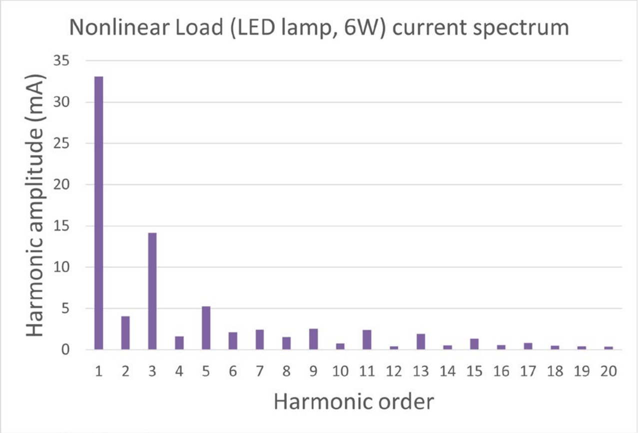

Fig. 4. The current spectrum of LED lamp, measured using supply voltage second harmonic injection.

By careful examination of measured spectrum (Fig 4.), one can conclude that even harmonics in current spectrum are not simple scaled and translated odd harmonics. This is due to nonlinear nature of load, and superposition theorem does not apply. The easiest way to see that is to notice new 4th, 8th and subsequent harmonics (of order divisible by four) emerging in the spectrum, and which would not exist if the voltage excitation consisted only of the second harmonic.

TABLE I
Current harmonic amplitudes

Harmonic order	Harmonic amplitude [mA]	
	Sinusoidal	2nd harmonic injection
1	32,98	33,11
2	0,02	4,07
3	14,5	14,16
4	0	1,65
5	5,57	5,25
6	0	2,1
7	2,52	2,45
8	0	1,54
9	2,72	2,56
10	0,01	0,74
11	2,66	2,41
12	0,01	0,4
13	2,1	1,91
14	0	0,54
15	1,39	1,32
16	0	0,57
17	0,79	0,82
18	0	0,5
19	0,41	0,43
20	0	0,39

The measured harmonic amplitudes for same load, obtained by sinusoidal and second harmonic injection voltage supply are compared in Table I.

Finally, modified spectrum obtained using (7) can be represented with orthogonal components instead amplitude, as shown in Fig 5.

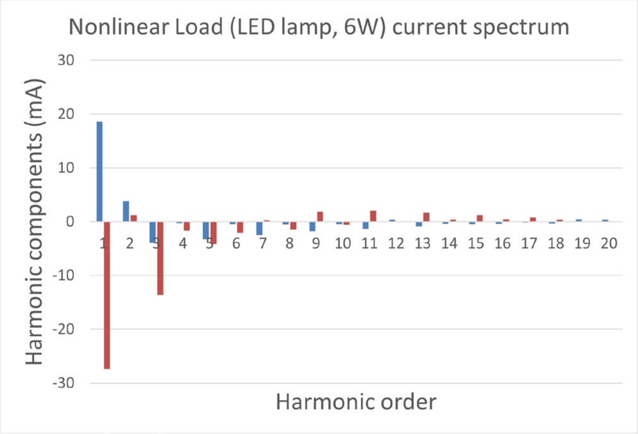

Fig. 5. The current spectrum of LED lamp, measured using supply voltage second harmonic injection, represented with orthogonal components, i.e., real (blue) and imaginary (red) part. The number of parameters is effectively multiplied by four.

IV. CONCLUSION

In this paper, three new improvements for improving nonlinear loads identification are proposed.

First, representing current harmonics as complex numbers in Cartesian coordinates rather than polar and using KCL enables establishing a west base of signatures related to various combinations of nonlinear loads, by measuring current spectrum of single loads individually. This approach significantly reduces number of measurements.

The Cartesian complex representation uses complete information that current harmonics have, by transforming harmonic phase which is unsuitable as input parameter and amplitude into orthogonal components. This method, in comparison with previously used harmonic-amplitude-only method for identification effectively doubles the number of input parameters for equal highest harmonic order.

The third improvement is addition of second harmonic into the voltage supply. In case of pure sinusoidal voltage supply, current spectrum contains only odd harmonics. By introducing second voltage harmonic, even harmonics emerge into current spectrum and can be used in same manner as input parameters. By combining second and third improvement, the number of parameters is effectively multiplied by four.

ACKNOWLEDGEMENT

This work has been supported by the Ministry of Education, Science and Technological Development of the Republic of Serbia.

REFERENCES

[1] M. E. Olsen, M. N. Marger, V. Fonseca, “*Power in Modern Societies*”, May 31, 2021, Routledge.

[2] M. Dimitrijević, M. Andrejević-Stošović, and D. Stevanović, "*Classification of Nonlinear Loads using Current Spectrum,*" presented at the Proceedings of the 6th IcETRAN Conference, Srebrno Jezero, 03.06.-06.06., 2019.

[3] M. Andrejević-Stošović, D. Stevanović, and M. Dimitrijević, "*Monitoring and Classification of Nonlinear Loads Based on Artificial Neural Networks*," presented at the 13th Int. Conference on Advanced Technologies, Systems and Services in Telecommunications (TELSIKS), Niš, Serbia, 18.10.-20.10., 2017. 10.1109/TELSKS.2017.8246320.

[4] M. Andrejević-Stošović, D. Stevanović, and M. Dimitrijević, "*Classification of Nonlinear Loads Based on Artificial Neural Networks*," presented at the IEEE 30th International Conference on Microelectronics (MIEL), Niš, Serbia, 9.10.-11.10., 2017. 10.1109/MIEL.2017.8190107.

[5] M. Dimitrijević, "*Elektronski sistem za analizu polifaznih opterećenja baziran na FPGA*," PhD, Faculty of Electronic Engineering, University of Niš, Niš, 2012.

[6] Omicron CMC 365 Universal relay test set and commissioning tool, https://www.omicronenergy.com/en/products/cmc-356/#.

PA Linearization in SDR-based Base Stations

Borisav Jovanović, Srđan Milenković

Abstract – Modern modulation schemes produce signals with high Peak to Average Power Ratio (PAPR). Power amplifier linearization, realized by utilization of digital predistortion (DPD) techniques, makes better PA energy efficiency and decreases wireless infrastructure running costs. However, in the presence of high PAPR signals, the DPD operation is degraded. In order to achieve the compliance of wireless infrastructure with strict telecommunication specifications, it is highly required to reduce the PAPR of transmitted signals. In this paper the solution is presented which implements the Peak Windowing for PAPR Reduction and DPD. The results for Long-Term Evolution (LTE) waveforms are presented.

Keywords - Crest factor reduction, Peak to Average Power Ratio, Peak Windowing method.

I. INTRODUCTION

Telecommunication infrastructure must meet strict standard specifications regarding signal distortions [1]. At the same time, it has to provide energy efficient operation. To cancel signal distortion of radio frequency (RF) base station (BS) power amplifiers (PA), the power is simply backed-off. However, the power reduction worsens PA energy efficiency and shortens the BS range. Digital predistortion (DPD), based on complex valued memory polynomials (MP), represents an efficient method for RF PA linearization [2, 3]. However, modern modulation schemes generate signals with high Peak to Average Power Ratio (PAPR), which results in intercarrier interference, high out-of-band emission and bit error rate performance degradation [2]. To ensure that signals at PA input reside within linear region of the PA transfer function, the solution is to deal with signals which have reduced PAPR [4]. The Crest Factor Reduction (CFR) techniques are used for PAPR reduction [4, 5]. We have selected the CFR method which is based on Peak Windowing (PW) [6]. We have implemented the PW and DPD in our solution; the results of implementation are provided in the paper.

Standard specifications [1] quantify the transmitted signal quality by Error Vector Magnitude (EVM) and Adjacent Channel Power Ratio (ACPR), as key metrics. The EVM measures in-band signal distortion and it is defined as dislocation of the received symbols in in-phase and quadrature (I/Q) plane compared to the ideal symbol positions. A standard figure of merit representing out-of-band signal distortions is the ACPR, defined as the ratio of signal power leaked to the adjacent spectrum channels and the main channel power. Following the specifications, we provide the results in terms of ACPR and EVM.

II. METHODS FOR PA LINEARIZATION

A. Peak Windowing Method

The Hard Clipping (HC) is a CFR approach which limits signal peaks which exceed selected threshold. The operation of HC is described by clipping function *c(n)*:

$$c(n) = \begin{cases} 1, |x(n)| \le Th \\ \dfrac{Th}{|x(n)|}, |x(n)| > Th \end{cases}, \tag{1}$$

In the Eq. (1) the parameter *Th* is the threshold and the *x(n)* is input signal. The HC limits the peaks in the envelope signal |*x(n)*| to stay below the *Th*. As a consequence of clipping operation, HC produces sharp edges in output signal at the clipping points, which increases out-of-band signal distortion.

The HC is replaced by Peak Windowing method in which the sharp edges are smoothened. The input signal, in the narrow regions around the clipping points, is multiplied with the windowing function.

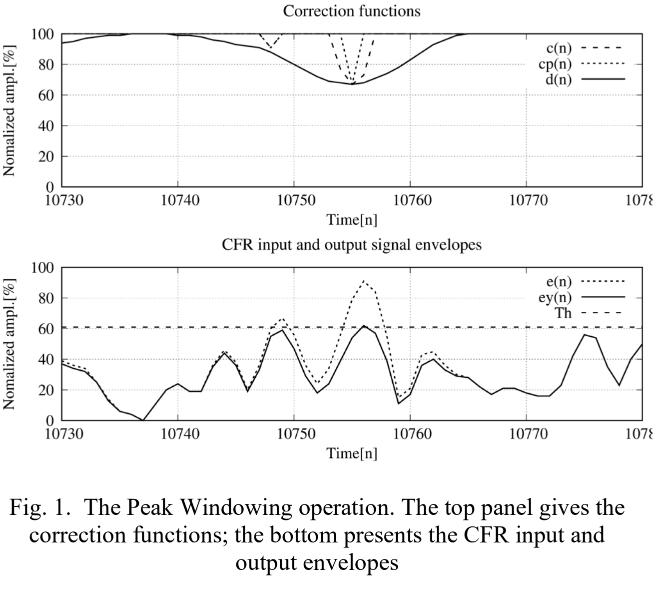

Fig. 1. The Peak Windowing operation. The top panel gives the correction functions; the bottom presents the CFR input and output envelopes

Borisav Jovanović is with the Faculty of Electronic Engineering Niš, University of Niš, Aleksandra Medvedeva Street 14, E-mail: borisav.jovanovic @elfak.ni.ac.rs

Srđan Milenković is with Lime Microsystems, Surrey Technology Centre, Occam Road, Guildford GU2 7YG, United Kingdom, E-mail: s.milenkovic@limemicro.com.

The Hann, Kaiser or Hamming windowing functions can be used [4, 5]. Multiplication of original signal with windowing function not only forces the peaks in $|x(n)|$ to stay under the selected *Th* but also reduces the amount of generated out-of-band distortions (Fig. 1).

In PW, the clipping coefficients *c(n)* are replaced with *b(n):*

$$b(n) = 1 - \sum_{k=-\infty}^{k=\infty}(1 - c(k))q(n-k)\,, \tag{2}$$

where *q(n)* is a common symmetric window function.

The implementation of PW method consists of several blocks: the pre-processing stage, PWFIR filtering and post-CFR low-pass filtering stages.

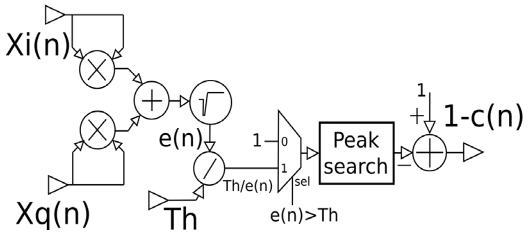

Fig. 2. CFR pre-processing operations

The pre-processing stage takes I/Q components of input signal and calculates the clipping function *c(n)*. The sequence of operations is given in Fig. 2. More details can be found in [6].

The calculation of clipping coefficients *b(n)* is performed by PWFIR filter. The PWFIR takes input signal 1-*c(n)* and generates *1-b(n)*. Before filtering operations, negative values of *1-c(n)* are replaced by zeros.

The simplified architecture of PWFIR is given in Fig. 3. It is designed to be programmable and to save FPGA resources. The PWFIR circuit has provision to change the window filter length and filter coefficients [6]. In order to minimize in-band signal distortion the narrow PWFIR window lengths should be used [4]. If clipping rate is too large or wide window length is chosen, the adjacent windows in *b(n)* overlap more often, reducing *b(n)*, yielding to more attenuation in the output signal.

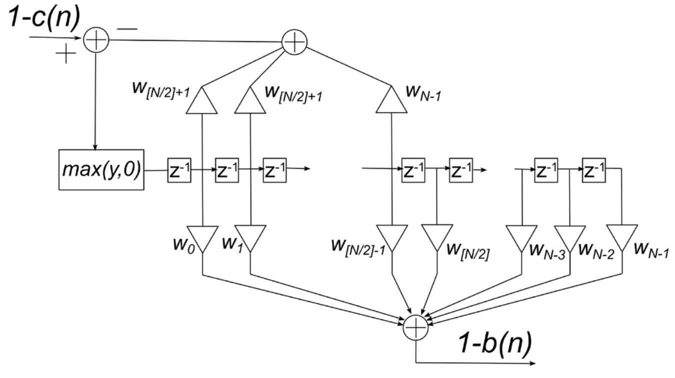

Fig. 3. PWFIR operations

B. PA linearization by DPD

The DPD computes the inverse function of the PA transfer characteristic. Utilization of DPD provides both PA linearity and high energy efficiency [2].

We have implemented the DPD using complex-valued memory polynomials (MP). The MP model takes into account both PA nonlinearity and memory effects and represents the simplified structure of the Volterra series [3].

The predistorter is positioned in the base-band (BB), before the digital-to-analogue (DA) conversion and BB to RF frequency up-conversion are performed.

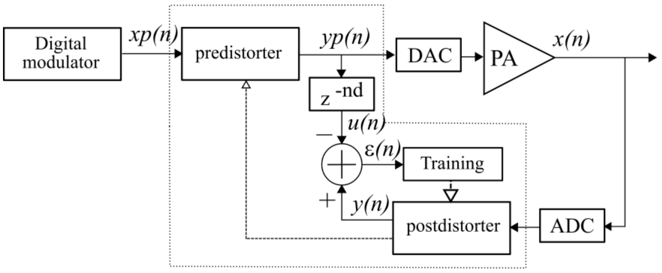

Fig. 4. Indirect learning architecture

The signal *x(n)*, which is obtained at PA output, is processed by post-distorter block which produces the *y(n)*:

$$y(n) = \sum_{i=0}^{N}\sum_{j=0}^{M} w_{ij} \cdot x(n-i) \cdot e(n-i)^{j} \tag{3}$$

where w_{ij} are complex valued model coefficients:

$$w_{ij} = a_{ij} + \mathbf{j}b_{ij} \tag{4}$$

$$e(n) = x_I(n)^2 + x_Q(n)^2 \tag{5}$$

The parameters *N* and *M*, used in Eq. (3), represent the DPD memory length and nonlinearity order respectively. The signal *e(n)* is the envelop function.

The predistorter output *yp(n)* is described by similar Eqs. (6) and (7):

$$yp(n) = \sum_{i=0}^{N}\sum_{j=0}^{M} w_{ij} \cdot xp(n-i) \cdot ep(n-i)^{j} \tag{6}$$

$$ep(n) = xp_I(n)^2 + xp_Q(n)^2 \tag{7}$$

The DPD coefficients are calculated in an iterative training process which uses Recursive Least Squares (RLS) method and indirect learning architecture (Fig. 4). The signal *u(n)* in Fig.4 is delayed version of *yp(n)*. According to indirect learning architecture, in the training process, the difference between signals *u(n)* and *yp(n)* is minimized.

For training algorithm, the RLS algorithm [3] is used. The weighted cost function *E(n)* is minimized.

$$E(n) = \frac{1}{2}\sum_{m=0}^{n} \lambda^{n-m} \varepsilon(m)^2 ,\ \lambda < 1 \tag{8}$$

The detailed description of DPD method and its implementation is described in detail in [7].

III. IMPLEMENTATION RESULTS

A. Hardware implementation

The DPD and CFR algorithms have been implemented using Software Defined Radio (SDR) board, a high level block diagram of which is shown in Fig. 5 [8]. For clarity, figure shows the minimum hardware options required to illustrate the implementation. The SDR board includes a transceiver IC for frequency conversion between base band (BB) and RF, covering the frequency range up to 3.8GHz. [9] Additional on-board Altera Cyclone V FPGA IC is used for DPD and CFR block realization [8]. Regarding data converters, transceiver chip incorporates 12-bit DACs and ADCs. The data rate at interface between FPGA and transceiver chip is limited to 61.44 MS/s. The board is connected to CPU core through high-speed PCIe interface. For the development or demo, test waveform is uploaded and played from WFM RAM Block, implemented using Altera Cyclone V FPGA resources. In real applications, the CPU Core performs BB digital modem functions. In this case, through PCIe interface, the real waveform is fed directly to the CFR block input.

One spare receive chain is used as DPD monitoring path. In transmit channel, beside DPD and CFR blocks, a low-pass FIR filter is used. The CFR output is filtered by low- pass FIR filter, reducing residual out-of-band spectrum regrowth.

PC/GUI implements graphical display for debugging purposes. GUI shows important signals at CFR and DPD block input and outputs in FFT (frequency), time and constellation (I vs. Q) domains.

CFR digital blocks implemented in FPGA operate at 122.88 MHz system clock. The waveform sample rate, produced by WFM RAM block in Fig. 5, is 30.72 MS/s and it is defined by standards [1]. The interpolation block is used to double sample rate of 30.72 MS/s before driving DPD block. The DPD operates at sample rate of 61.44 MS/s. In DPD implementation, the memory length *N*=4 and nonlinearity order *M*=2 are chosen.

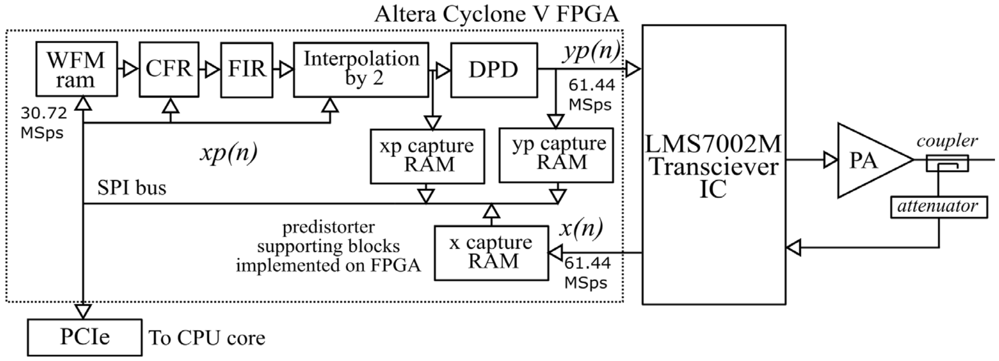

Fig. 5. The CFR and DPD implementation based on SDR transceiver board

B. Measurement Results

In the test case, the 10MHz Long Term Evaluation (LTE) Test Model 3.1 (E-TM 3.1) was used. The E-TM 3.1 test specification applies to most LTE modulation schemes such as 64 Quadrature Amplitude Modulation (QAM) at maximum power, and this specification is regarded as one of the most important specifications of all LTE test specifications. To accommodate design to selected waveform, the post-CFR low-pass FIR filter cut-off frequency is set to 10MHz.

The PAPR value of unmodified E-TM 3.1 waveform when DPD and CFR are bypassed is 10.2 dBm. The following CFR parameters are changed: the PWFIR order – represented by parameter *L* and the threshold value *Th.* The threshold is changed in the range from 1.0 down to 0.5. The filter order is changed from *L*=5 to *L*=40. The goal was to find *L* and *Th* which give the best ACPR and EVM values.

The target PAPR value is determined by ability of DPD circuits to efficiently linearize PA. We used energy efficient PA with 10W modulated output power operating at RF centre frequency of 761MHz. The PAs have following characteristics: the bandwidth is 700-850 MHz; average output power at 1 dB compression point is 40 dBm at the frequency of 761 MHz.

When using CFR block, there is always trade-off between selected threshold level and amount introduced in-band signal distortions. For utilized PA, we have found that DPD efficiently removes distortion without any power back-off if PAPR of input signal is less than 8.2dB. Therefore, by setting the parameter *Th* equal to 0.75 we achieved the goal of reducing the PAPR by 2.0dB.

However, we intentionally introduced in-band distortion.

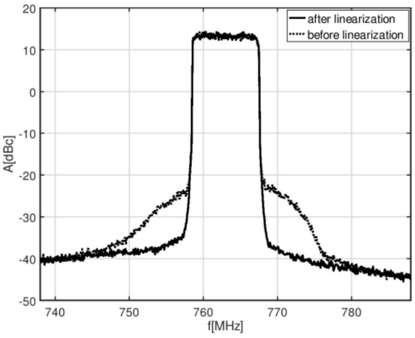

Fig. 6. The comparison of spectra of the signal obtained at PA output, in cases when PA is not compensated and when linearization is done

The results which are given in the paper are obtained by measuring the signal at PA output after input waveform is processed by CFR and low-pass FIR filter blocks. The amount of out-of-band and in-band distortion is calculated in terms of ACPR and EVM respectively.

After the threshold level has been determined *Th*=0.75 we have evaluated different values for PWFIR filter order in order to find the optimal one. The EVM increases with *L*. For example, the combination of *L*=9 and *Th*=0.6 yields to EVM=5.8%. In the case of *L*=39 and *Th*=0.6, the EVM=7.7%.For selected waveform 10MHz E-TM 3.1 we have chosen the PWFIR filter order *L*=17. The obtained EVM value is equal to 2.23%. It is slightly greater that the EVM value of the signal obtained at transmitter output (without PA) when unmodified 10MHz E-TM 3.1 test waveform is used. In this case the EVM is equal to 1.2%. However, the lower PWFIR order values produce worse ACPR results. In order to compensate out-of-band distortion, the CFR output is additionally filtered by 10MHz low-pass FIR filter; therefore, residual out-of band distortion is removed by this additional FIR filter. The obtained ACPR result of the signal obtained at transmitter output (without PA) is -54dBc.

At starting point, when neither CFR nor DPD are utilized, at PA output, the ACPR= -37.5 dBc and EVM=3.32%. The measured PA output power is *P_out*=39.7 dBm. The distortion is removed when DPD and CFR are employed. The ACPR is decreased to the value equal to -50.8 dBc. The PA output power is maintained at the same level as in the starting point, before any CFR and DPD data processing is done. The obtained EVM value is equal to 2.23%; it is determined by EVM of the signal at CFR output. Therefore, the ACPR is improved by 13.3 dBc and EVM by 1%.

IV. CONCLUSION

CFR and DPD algorithms have been implemented on SDR board and verified by measured results. When DPD is used without CFR, the modulated signal power at PA output needs to be backed-off for approximately 2 dB to enable DPD to remove distortions down to the system noise floor. When CFR is utilized, DPD is capable of cancelling any out-of-band distortion above system noise floor, without any PA power back-off.

The main characteristics of our solution are low implementation complexity and good performance measured in terms of EVM and ACPR as key parameters.

ACKNOWLEDGMENT

This research was partially funded by The Ministry of Education, Science and Technological Development of Republic of Serbia under contract No. TR32004.

Special thanks to PhD Ebrahim Bushehri and Lime Microsystems.

REFERENCES

[1] Evolved Universal Terrestrial Radio Access (E-UTRA); Base Station (BS) radio transmission and reception 2012, www.3gpp.org

[1] Eun, C. and Powers, E. J., “*A New Volterra Predistorter Based on the Indirect Learning Architecture*”, IEEE Trans. Signal Process., Vol. 45, 1997, pp. 223–227

[2] Cavers, J. K. “*Amplifier Linearization Using a Digital Predistorter with Fast Adaptation and Low Memory Requirements*”, IEEE Trans. Veh. Technol., Vol. 39, No. 4, 1990, pp. 374–382

[3] Lim, D.W., Heo, S.J., No J.S., “*An Overview of Peak-to-Average Power Ratio Reduction Schemes for OFDM Signals*”, Journal of Communications and Networks, Vol. 11, No. 3, June 2009, pp. 229-239.

[4]Jiang, T., Wu, Y., “*An Overview: Peak-to-Average Power Ratio Reduction Techniques for OFDM signals*”, IEEE Trans. Broadcasting, Vol. 54, No. 2, June 2008, pp. 257-268.

[5] Mistry, H., “*Implementation of a Peak Windowing algorithm for Crest Factor Reduction in WCDMA*”, Master of Engineering Thesis, Simon Fraser University, Canada, 2006

[6] Jovanović, B. Milenković, S, “*PA Linearization by Digital Predistortion and Peak to Average Power Ratio Reduction in Software Defined Radios*“, Journal of Circuits Systems and Computers, World Scientific Publishing Co. Pte. Ltd., Singapore, 2019

[7]Jovanović, B. Milenković, S, “*The Peak Windowing For PAPR Reduction In Software Defined Radio Base Stations*“, FACTA UNIVERSITATIS, Series: Electronic and Energetics, University of Niš, 2019

[8] Limemicrosystems LimeSDR QPCIe (2019), https://wiki.myriadrf.org/LimeSDR-QPCIe

[9] Limemicrosystems LMS7002M (2019), https://limemicro.com/

GPU-Supported simulation for ABEP and QoS analysis of SC receiver with L-branch in k-μ fading and η-μ interference environment

Dejan Milić, Suad Suljović, Nenad Petrović, Dejan Rančić

Abstract - In this paper we consider Selection combining (SC) diversity receiver with L branches operating over correlated k-μ fading channel with η-μ co-channel interference (CCI). Moment generating function (MGF) approach is applied to calculate the average bit error probability (ABEP) of the SC diversity system using BDPSK and BPSK modulations. Results are graphically presented and the effects of different system parameters on performance discussed. The obtained analytical expressions are used for the GPU-enabled mobile network planning and simulation environment to determine the value of Quality of Service (QoS) parameter. Finally, linear optimization is proposed as an approach to improve the QoS parameter of the fading-affected system observed in this paper.

Keywords - Camera ready papers, Proceedings of papers. Moment generating function (MGF), Selection combining (SC), k-μ fading, η-μ co-channel interference (CCI), GPGPU, linear optimization.

I. INTRODUCTION

On its path from transmitter to the receiver a wireless signal undergoes various effects such as multipath attenuation, interference and other effects that significantly reduce the quality of signal. Since the transmitter and receiver could be fixed or mobile, the transmission channel can also be time varying or steady. In either case, Quality of Service (QoS) at the receiver side could be significantly reduced due to impediments such as fast fading and co-channel interference. The result of fast fading is a spread of the signal in multiple directions (multipath propagation). Due to reflection, refraction or diffraction of the useful wave on the objects on its way, at the receiver input there are multiple copies of the original signal. Due to a fast fading, the signal envelope varies and therefore its power which affects the system performance.

Statistical nature of the signal in such environment can be modelled by various statistical distributions: Rayleigh, Rician, Nakagami-*m*, Weibull or κ-μ [2]. In linear environments, where there is a dominant component of the signal, κ-μ distribution is a proper model to describe the envelope variations. κ-μ distribution has two factors: κ – the Rician factor equal to the quotient of the power of dominant component and the power of scattered components. Parameter μ is related to the number of clusters in propagation environment [3]. Co-channel interference (CCI) is an interfering signal with the same carrier. Two or more signals from different locations operating at the same frequency, interfere and cause significant degradation of the quality of transmission. In η-μ interference environment, parameter η is related to the scattered wave power ratio between in-phase and quadrature components of each cluster of multipath. To mitigate the impact of fast fading and co-channel interference on the system performance, various diversity techniques are implemented, where multiple replicas of the same useful signal are combined. The signal processing in SC receiver is simple for realization as the it proceeds the signal from the branch with the highest signal-to-noise ratio [4,5]. We have calculated the expression for the moment-generating function (MGF) of the signals at the output of the SC receiver. The obtained expression for MGF can be used for further evaluating the ABEP of non-coherent BFSK and BDPSK modulated signals [6].

II. AVERAGE BIT ERROR PROBABILITZ OVER MOMENT GENERATING FUNCTION

Initially, we consider the first-order statistics of the 5G wireless communication system with *L*-branch SC receiver. The signal is affected by *k-μ* fading and *η-μ* co-channel interference. The model is shown in Fig. 1:

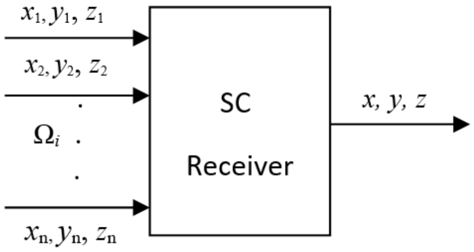

Figure 1. The model of the SC receiver with *L* branches

The multiple signal envelopes at the receiver inputs are denoted by the components $x_1, x_2, \ldots, x_n$. The SC receiver

Dejan Milić, Nenad Petrović and Dejan Rančić are with University of Niš, Faculty of Electronic Engineering, Niš, Serbia, E-mails: dejan.milic@elfak.ni.ac.rs, nenad.petrovic@elfak.ni.ac.rs, dejan.rancic@elfak.ni.ac.rs
Suad Suljović is with Academy of Technical Vocational Studies Belgrade, Serbia, E-mail: suadsara@gmail.com

with L branches accepts the signal from the antenna that has the highest SIR. The output signal from the SC receiver will be labelled with an x. Also, the cochannel interference components appear as $y_1, y_2, \ldots, y_n$, at each of the L inputs of the SC receiver, providing the corresponding output signal y. The probability density function (PDF) of signal envelopes is modelled by the κ-μ distribution given by [7;23]:

$$p_{x_i}\left(x_i\right)=2e^{-\frac{\mu(1+k)x_i^2}{\Omega_i}-\mu K_i}\sum_{i=0}^{+\infty}\frac{\mu^{2i_1+\mu}K_i^{i_1}x_i^{2i_1+2\mu-1}}{\Gamma\left(i_1+\mu\right)i_1!}\left(\frac{1+K_i}{\Omega_i}\right)^{i_1+\mu} \quad (1)$$

where parameter K is Rice factor, parameter μ represents number of clusters in propagation environment, Ω_i is the mean value of the signals power and $\Gamma(\cdot)$ is a Gamma function.

The co-channel interference follows the η-μ distribution [7; 2.52]:

$$p_{y_i}(y_i)=\frac{4\sqrt{\pi}\,h^{\mu}}{\Gamma(\mu)}e^{-\frac{2\mu h}{g_i}y_i^2}\sum_{i=0}^{+\infty}\frac{H^{2i}y_i^{4i+4\mu-1}}{\Gamma\left(i+\mu+1/2\right)i!}\left(\frac{\mu}{g_i}\right)^{2i+2\mu} \quad (2)$$

where the expressions of h and H are given by:

$$h=\frac{2+\eta^{-1}+\eta}{4},H=\frac{\eta^{-1}-\eta}{4} \quad (3)$$

The fading parameter η is the ratio of the powers in-phase and in quadrature of scattered waves in each multipath cluster, and $0< \eta < \infty$ [8]. In the above expression H-parameter of the in-phase component and h-fading parameter related to in-phase powers and g stands for the average power of the interferer's envelopes y, $y_i \geq 0$. The ratio of the desired signal and the co-channel interference at the i^{th} input branch of the SC receiver is:

$$z_i = x_i / y_i, x_i = z_i y_i \quad (4)$$

At the output of the SC receiver, the signal to interference ratio for i=2,3,…n will be:

$$z=\max(z_1, z_2 \ldots z_i) \quad (5)$$

The PDF of the signal z_i is given by [9]:

$$p_{z_i}\left(z_i\right)=\int_0^{\infty}\mathrm{d}y_i y_i p_{x_i}\left(z_i y_i\right)p_{y_i}\left(y_i\right)=\frac{4\sqrt{\pi}\,h^{\mu}}{\Gamma\left(\mu\right)e^{\mu K_i}}\sum_{i_1=0}^{+\infty}\sum_{i_2=0}^{+\infty}\frac{K_i^{i_1}H^{2i_2}}{i_1!i_2!}\cdot$$

$$\cdot\frac{K_i^{i_1}\mu^{2i_1+2i_2+3\mu}\Omega_i^{2i_2+2\mu}\left(g_i\left(1+K_i\right)\right)^{i_1+\mu}\Gamma\left(i_1+2i_2+3\mu\right)z_i^{2i_1+2\mu-1}}{\Gamma\left(i_1+\mu\right)\Gamma\left(i_2+\mu+1/2\right)\left(2\mu h\Omega_i+\mu g_i(1+K_i)z_i^2\right)^{i_1+2i_2+3\mu}} \quad (6)$$

Cumulative distribution function (CDF) of z_i is [9]:

$$F_{z_i}\left(z_i\right)=\int_0^{z_i}\mathrm{d}t p_{z_i}\left(t\right)=\frac{2\sqrt{\pi}}{\Gamma\left(\mu\right)e^{\mu K_i}}\sum_{i_1=0}^{+\infty}\sum_{i_2=0}^{+\infty}\frac{\left(\mu K_i\right)^{i_1}}{i_1!i_2!2^{2i_2+2\mu}h^{2i_2+\mu}}\cdot$$

$$\cdot\frac{H^{2i_2}\Gamma\left(i_1+2i_2+3\mu\right)}{\Gamma\left(i_1+\mu\right)\Gamma\left(i_2+\mu+1/2\right)}B_{\frac{\mu g_i(1+K_i)z_i^2}{2\mu h\Omega_i+\mu g_i(1+K_i)z_i^2}}\left(i_1+\mu, 2i_2+2\mu\right) \quad (7)$$

Incomplete Beta function in the previous equation may be presented in the following form [10, eq.8.39]:

$$B_x\left(p,\mathrm{q}\right)=\int_0^x t^{p-1}\left(1-t\right)^{q-1}dt=\frac{x^p}{p}\,{}_2F_1\left(p,1-q;p+1;x\right)=$$

$$=\frac{x^p}{p}\,{}_2F_1\left(\mathrm{a},\mathrm{b};\mathrm{c};\mathrm{z}\right)=\sum_{j=0}^{\infty}\frac{a_j b_j}{c_j}\frac{z^j}{j!} \quad (8)$$

where function ${}_2F_1$ is the hyper geometric function of the second order and $(a)_n$ denoting the Pochhammer symbol. By combining expression (8), we can write CDF from expression (7) in the following form:

$$F_{z_i}\left(z_i\right)=\frac{2\sqrt{\pi}}{\Gamma\left(\mu\right)e^{\mu K_i}}\sum_{i_1=0}^{+\infty}\sum_{i_2=0}^{+\infty}\sum_{i_3=0}^{\infty}\frac{\left(1-2i_2-2\mu\right)_{i_3}}{i_1!i_2!i_3!h^{2i_2+\mu}}\cdot$$

$$\cdot\frac{\left(i_1+\mu\right)_{i_3}\Gamma\left(i_1+2i_2+3\mu\right)}{2^{2i_2+2\mu}\left(i_1+\mu+1\right)_{i_3}\Gamma\left(i_2+\mu+1/2\right)\left(i_1+\mu\right)}\cdot$$

$$\cdot\frac{\left(\mu K_i\right)^{i_1}H^{2i_2}}{\Gamma\left(i_1+\mu\right)}\left(\frac{\mu g_i(1+K_i)z_i^2}{2\mu h\Omega_i+\mu g_i(1+K_i)z_i^2}\right)^{i_1+i_3+\mu} \quad (9)$$

PDF of the SIR at the output of the L-branch SC receiver can be calculated [11]:

$$p_z\left(z\right)=Lp_{z_i}\left(z_i\right)\left(F_{z_i}\left(z_i\right)\right)^{L-1}=\frac{2^{L+1}L\sqrt{\pi}^{L}h^{\mu}}{\Gamma^{L}\left(\mu\right)e^{\mu K_i L}}\sum_{i_1=0}^{+\infty}\sum_{i_2=0}^{+\infty}\frac{K_i^{i_1}H^{2i_2}}{i_1!i_2!}\cdot$$

$$\cdot\frac{\mu^{2i_1+2i_2+2\mu+\mu L}\Omega_i^{2i_2+2\mu}\left(g_i\left(1+K_i\right)\right)^{i_1+\mu}\Gamma\left(i_1+2i_2+3\mu\right)z_i^{2i_1+2\mu-1}}{\Gamma\left(i_1+\mu\right)\Gamma\left(i_2+\mu+1/2\right)\left(2\mu h\Omega_i+\mu g_i(1+K_i)z_i^2\right)^{i_1+2i_2+3\mu}}\cdot$$

$$\cdot\left(\sum_{i_3=0}^{+\infty}\sum_{i_4=0}^{+\infty}\sum_{i_5=0}^{\infty}\frac{\left(i_3+\mu\right)_{i_5}\left(1-2i_4-2\mu\right)_{i_5}H^{2i_4}\mu^{i_3L+i_5L-i_5}}{i_3!i_4!i_5!\left(i_3+\mu+1\right)_{i_5}2^{2i_4+2\mu}\left(i_3+\mu\right)\Gamma\left(i_3+\mu\right)}\cdot\right.$$

$$\left.\cdot\frac{K_i^{i_3}\Gamma\left(i_3+2i_4+3\mu\right)}{h^{2i_4+\mu}\Gamma\left(i_4+\mu+1/2\right)}\left(\frac{g_i(1+K_i)z_i^2}{2\mu h\Omega_i+\mu g_i(1+K_i)z_i^2}\right)^{i_3+i_5+\mu}\right)^{L-1} \quad (10)$$

Using the expression for the joint PDF, we can calculate the MGF of a random variable z at the output of the SC system shown in Fig 1. [12]:

$$M_z\left(s\right)=\overline{e^{zs}}=\int_0^{\infty}\mathrm{d}z\mathrm{e}^{-zs}p_z\left(z\right)=\frac{2^{L+1}L\sqrt{\pi}^{L}}{\Gamma^{L}\left(\mu\right)e^{\mu K_i L}}\sum_{i_1=0}^{+\infty}\sum_{i_2=0}^{+\infty}\frac{\left(\mu K_i\right)^{i_1}}{\Gamma\left(i_1+\mu\right)i_1!}\cdot$$

$$\cdot\frac{H^{2i_2}\Omega_i^{2i_2+2\mu}\Gamma\left(i_1+2i_2+3\mu\right)}{i_2!\Gamma\left(i_2+\mu+1/2\right)\left(g_i(1+K_i)\right)^{2i_2+2\mu}}\left(\sum_{i_3=0}^{+\infty}\sum_{i_4=0}^{+\infty}\sum_{i_5=0}^{\infty}\frac{1}{i_3!i_4!i_5!}\left(\frac{H}{h}\right)^{2i_4}\cdot\right.$$

$$\left.\cdot\frac{\left(1-2i_4-2\mu\right)_{i_5}\left(i_3+\mu\right)_{i_5}\left(\mu K_i\right)^{i_3}\Gamma\left(i_3+2i_4+3\mu\right)}{\left(i_3+\mu+1\right)_{i_5}2^{2i_4+2\mu}\left(i_3+\mu\right)\Gamma\left(i_3+\mu\right)\Gamma\left(i_4+\mu+1/2\right)}\right)^{L-1}\cdot$$

$$\int_0^{\infty}\frac{z_i^{2i_1+2(i_3+i_5)(L-1)+2\mu L-1}}{\left(\frac{2\mu h\Omega_i}{\mu g_i(1+K_i)}+z_i^2\right)^{1-(1-i_1-2i_2-(i_3+i_5)(L-1)-\mu(2+L))}}\mathrm{d}z\mathrm{e}^{-zs} \quad (11)$$

Using form [10; 3.389]:

$$\int_0^\infty \frac{x^{2v-1}e^{-\mu x}}{\left(u^2+x^2\right)^{1-q}}dx=\frac{u^{2v+2q-2}}{2\sqrt{\pi}\,\Gamma(1-q)}G_{13}^{31}\left(\frac{\mu^2u^2}{4}\middle|\begin{matrix}1-v\\1-q-v,0,\frac{1}{2}\end{matrix}\right)\quad(12)$$

where G[·]is Meijer's G-function [10; 9.301], expression (11) becomes:

$$M_z(s)=\frac{2^{L-4\mu}L\left(\sqrt{\pi}\right)^{L-1}}{\Gamma^L(\mu)e^{\mu K_iL}}\sum_{i_1=0}^{+\infty}\sum_{i_2=0}^{+\infty}\frac{(\mu K_i)^{i_1}\Gamma(i_1+2i_2+3\mu)}{i_1!i_2!h^{2i_2+2\mu}2^{2i_2}\Gamma(i_2+\mu+1/2)}\cdot$$
$$\cdot\frac{H^{2i_2}}{\Gamma(i_1+\mu)}\left(\sum_{i_3=0}^{+\infty}\sum_{i_4=0}^{+\infty}\sum_{i_5=0}^{\infty}\frac{(1-2i_4-2\mu)_{i_5}(\mu K_i)^{i_3}(i_3+\mu)_{i_5}(H/h)^{2i_4}}{i_3!i_4!i_5!(i_3+\mu+1)_{i_5}(i_3+\mu)\Gamma(i_3+\mu)}\cdot\right.$$
$$\left.\cdot\frac{\Gamma(i_3+2i_4+3\mu)}{2^{2i_4}\Gamma(i_4+\mu+1/2)}\right)^{L-1}\frac{1}{\Gamma(i_1+2i_2+(i_3+i_5)(L-1)+\mu(2+L))}\cdot$$
$$\cdot G_{13}^{31}\left(\frac{s^2\mu h\Omega_i}{2\mu g_i(1+K_i)}\middle|\begin{matrix}1-(i_1+(i_3+i_5)(L-1)+\mu L)\\2i_2+2\mu,0,\frac{1}{2}\end{matrix}\right)\quad(13)$$

One of the performance measures of the wireless communication system is the average symbol error probability (ASEP). If there are two bits per symbol, this property is equivalent to the average bit error probability (ABEP) [13]. Using the obtained expression for MGF, the ABEP of non-coherent BFSK and BDPSK modulation signals can be directly calculated as [14]:

$$\begin{aligned}&\mathrm{P_{be}}(\Omega_0)=0.5\mathrm{M_z}(0.5),\ \text{ for BFSK;}\\&\mathrm{P_{be}}(\Omega_0)=0.5\mathrm{M_z}(1),\ \text{ for BDPSK.}\end{aligned}\quad(14)$$

Graphical representation of the ABEP for the range of different values of parameters from expression (14) for BFSK and BDPSK modulation is given in Figures 2 and 3.

III. NUMERICAL AND GRAPHICAL RESULTS

By illustrating the numerically obtained results we will discuss the influence of fast fading and co-channel interference on ABEP.

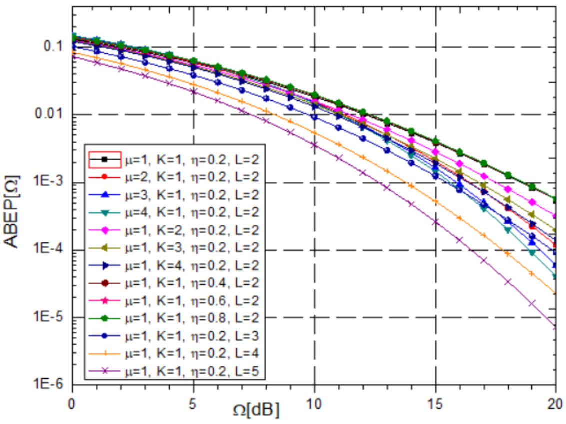

Fig. 2. Average BEP versus Ω for BDPSK

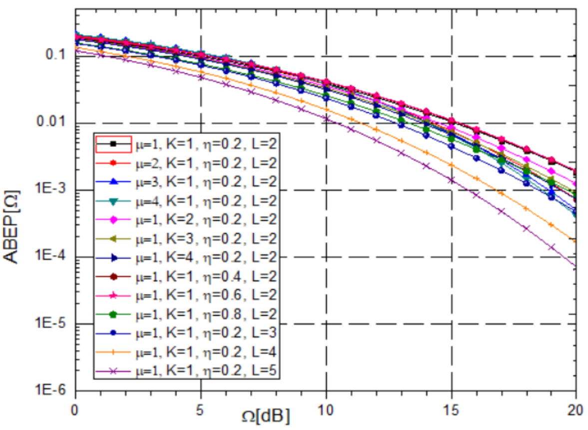

Fig. 3. Average BEP versus Ω for BFSK

Figures 2 and 3 show ABEP of the SC receiver output presented in expression (14) in terms of the parameter **Ω** for several different values of k-μ fast fading severity parameter, η-μ co-channel interference, fading parameter *η*, and number of branches at the input of SC receiver for BFSK and BDPSK modulation.

The figures 2, and 3 for BFSK and BDPSK modulations show that, as the parameters *μ, k* and *L* are increasing ABEP function decreases and the system has better performance and stability. The increase in fading parameter *η* affects the increase in ABEP and the system becomes unstable. It can be observed that the higher values of **Ω** lead to a lower error and better performance. By comparing the graphical results, we can conclude that the better stability of the system and a smaller ABEP are achieved for the BDPSK than the BFSK modulation.

IV. GPU-ENABLED PLANNING AND SIMULATION SOFTWARE ENVIRONMENT

This section introduces software environment whose goal is to enable efficient, proactive planning and simulation regarding state-of-art network deployments within smart cities. The proposed approach relies on synergy of deep learning and multi-objective linear optimization building upon our previous works [12, 15]. Furthermore, it leverages Graphics Processing Unit (GPU) hardware in order to accelerate the calculations, when it comes to both ABEP determination and deep learning predictions, by adopting NVIDIA CUDA [16]. Fig. 4 depicts the workflow behind this software environment.

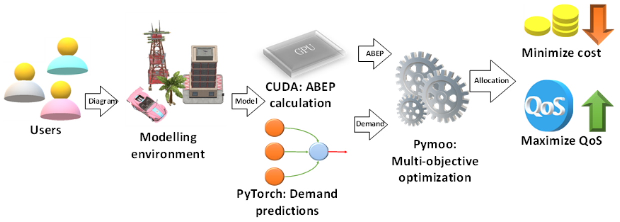

Fig. 4. Planning and simulation software workflow.

In this context, network planning is considered as component allocation problem. The goal is to assign the most suitable base stations (denoted as *b*) that will be placed on the considered locations within smart city (denoted as *l*). As first step, user has to create a network model within GUI-enabled web-based tool [15] by setting both the communication channel properties and base station characteristics with additional information about the number of users for past periods. After that, ABEP values are calculated for given model by leveraging NVIDIA CUDA kernel whose structure is based on our work described in [15]. Due to loop-level parallelization provided by this technology, considering the fact that ABEP expression involves infinite sums approximated by limited number of terms calculated within loop (up to 50 in this case), the achieved speed up compared to CPU-only Mathematica program is obvious, reaching up to 68 times.

On the other side, GPU is also leveraged for user number prediction. For this purpose, PyTorch [17] framework for deep learning in Python was used. The problem is treated as regression, while the target, output variable is the predicted number of users for location *l*, denoted as *u[l]*. The input variables are day number, location identifier, season number, number of new COVID-19 cases for the considered day.

Once the values for both LCR and predicted number of users are calculated, the last step is multi-objective linear optimization process which aims optimal base station allocation for selected smart city locations. For this purpose, we make use of pymoo framework [18] in Python, while the optimization model itself is built upon our previous works from [19]. The first objective function has goal to minimize the total network deployment and maintenance costs, considering two factors: *e[b, l]* - energy consumption of base station b at location l and *c[b, l]* – installation, configuration and maintenance of base station.

$$minimize \sum_{b\in B, l\in L} (e[b,l]+c[b,l])assign[s,p] \tag{16}$$

On the other side, Quality of Service (QoS) aims to be maximized by keeping ABEP as low as possible, due to its negative impact on performance in case of higher values:

$$minimize \sum_{b\in B, l\in L} ABEP[b,l]assign[s,p] \tag{17}$$

Furthermore, a constraint for the maximum number of users relying on base station *b* on location *l* *max[b,l]* should be greater or equal to *users[l]*, which is the predicted number of potential users for the location of interest *l*.

$$\sum_{b\in B} max[b,l]assign[b,l] \geq users[l], l\in L \tag{18}$$

In the previous three equations, *assign [b, l]* represents the decision variable which takes value 1 in case when base station *b* is selected to be deployed on location *l*, but it is 0 otherwise.

IV. CONCLUSION

In this paper, the combined SC system with L branches with *k-μ* fast fading channel and co-channel interference η-μ has been studied. In a cellular mobile radio system, SC combines signal envelopes with multiple *L* antennas at base stations resulting in a reduction in multiple effects of *k-m* fading and η-μ co-channel interference. Closed form expression for MGF at the SC receiver output is derived for a correlated composite inhomogeneous fading channel for two modulation schemes: BFSK and BDPSK. It is observed that the ABEP significantly improves with increasing number of antennas *L*, while increasing fading parameters η weakens system performance. The ABEP function is smaller and the system performance is better when the number of branches at SC is greater than *L=2*.

In the final section of the work, we have proposed the implementation of GPU-powered calculations that significantly speed up the determination of QoS parameters based on ABEP function. This is of the utmost importance for the QoS performances in real-time wireless systems dealing with data transmission such as real-time video. Within the analysis for the improvement in QoS parameter of the fading-affected system observed in this paper the linear optimization is proposed.

ACKNOWLEDGEMENT

This work has been supported by the Ministry of Education, Science and Technological Development of the Republic of Serbia.

REFERENCES

[1] G. L. Stüber, Principles of mobile communication, 2nd ed. New York: Kluwer Academic Publishers, 2002.
[2] S. Panic, M. Stefanovic, J. Anastasov, and P. Spalevic, Fading and Interference Mitigation in Wireless Communications, 1st ed. Boca Raton, FL, USA: CRC Press, Inc., 2013.
[3] M. M. Smilić, B. S. Jakšić, D. N. Milić, S. R. Panić, P. Ć. Spalević, "Channel Capacity of the Microdiversity SC system in the presence of kappa-mu fading and correlated

slow gamma fading", Facta Universitas, Series: Electronics and Energetics, vol.31, no.3, pp. 447-460, 2018.

[4] N. Yadav, N. Kumar, N. Rathi, "Performance Analysis of Selective Combining Diversity over Rayleigh Fading Channel in Wireless Communication", International Journal of Engineering and Innovative Technology (IJEIT) Volume 3, Issue 12, June 2014.

[5] J. Iong-Zong Chen, Y. Chuan-Chen, Shan-Jiau, Da-Tsuen, Chang-Hua, "SC Diversity with Equal and Un-equal Gain Branches in Correlated-Weibull Fading Environments", Proceedings of the 11th WSEAS International Conference on Communications, Agios Nikolaos, Crete Island, Greece, July 26-28, 2007.

[6] G. Femenias, "MGF-based performance analysis of selection diversity with switching constraints in nakagami fading", in *IEEE Transactions on Wireless Communications*, vol. 5, no. 9, pp. 2328-2333, September 2006, doi: 10.1109/TWC.2006.1687752.

[7] S. N. Suljović, "Analysis of performance improvement in relay communication systems from the aspect of diversity combining techniques", Ph.D. dissertation, University of Niš, Faculty of Electronic Engineering, 2019.

[8] N. Y. Ermolova and O. Tirkkonen, "Outage probability analysis in generalized fading channels with co-channel interference and background noise: η-μ/η-μ, η-μ/κ-μ, and κ-μ/η-μ scenarios", IEEE Transactions on Wireless Communications, vol. 13, no. 1, pp. 291–297, 2014. doi:10.1109/twc.2013.110813.130624

[9] S. Suljović, D. Krstić, D. Bandjur, S. Veljković, and M. Stefanović, "Level crossing rate of macro-diversity system in the presence of fading and co-channel interference", Revue Roumaine des Sciences Techniques, Publisher: Romanian Academy, vol. 64, pp. 63–68, 2019.

[10] I. S. Gradshteyn and I. M. Ryzhik, Tables of Integrals, Series and Products Academic. New York: 1980.

[11] M. Savic, M. Smilic, and B. Jaksic, "Analysis of Shannon capacity for SC and MRC diversity system in α-k-μ fading channel", University Thought, Publication in Natural Sciences, Vol.8, No.2, pp. 61-66, 2018.

[12] N. Petrović, S. Vasić, D. Milić, S. Suljović, S. Koničanin, "GPU-Supported simulation for ABEP and QoS in Gama-Shadowed k-μ fading channel", Facta universitatis, Series: Electronic and Energetics, vol. 34, pp. 89-104, 2021.

[13] A. S Lioumpas, A. P Doukeli, G. K Karagiannidis, "Another look at multibranch switched diversity systems", IEEE Commun Lett. April2007;11(4):325–327. G. L. Stüber, Principles of mobile communication: 2nd ed., Technology & Engineering, Kluwer Academic Publisher, 2000.

[14] M K Simon, and M S Alouni, *Digital Communication Over Fading Channels*, 2nd ed., New Jersey: Wiley-Interscience; 2005.

[15] N. Petrović, S. Koničanin, D. Milić, S. Suljović, and S. Panić, "GPU-enabled framework for modelling, simulation and planning of mobile networks in smart sities", ZINC 2020, pp. 1-6, 2020,

[16] J. Sanders, E. Kandort, CUDA By Example: An Introduction to General-Purpose GPU Programming, Addison-Wesley, 2011.

[17] E. Stevens, L. Antiga, T. Viehmann, *Deep Learning with PyTorch*, Manning Publications, 2020.

[18] J. Blank and K. Deb, "Pymoo: Multi-objective optimization in python", IEEE Access, 8:89497–89509, 2020.

[19] N. Petrović, I. Al-Azzoni, J. Blank, "Model-driven multi-objective optimization approach to 6G network planning", TELSIKS 2021, pp. 223-226, 2021.

Model-Driven Approach to COVID-19 Vaccination Planning Leveraging Multi-Objective Optimization and Deep Learning

Nenad Petrović and Issam Al-Azzoni

Abstract – Vaccination is recognized as one of crucial measures in battle against COVID-19, contributing to both the reduction of its negative impact on infected person and overall spread reduction. In this paper, we focus on adoption of model-driven approach to proactive and cost-effective vaccine distribution, relying on deep-learning (for vaccine-demand predictions) and multi-objective optimization (for solving the allocation problem). As outcome, software simulation tool for efficient vaccination planning, relying on the proposed approach is presented, showing promising results. Furthermore, the adoption of model-driven approach reduces both the learning curve and time necessary for experimentation.

Keywords – coronavirus, deep learning, Ecore, model-driven engineering, optimization, PyTorch.

I. INTRODUCTION

Since the beginning of 2020, the still ongoing COVID-19 pandemic has changed our life in all dimensions – from work, everyday habbits and activities to travel and entertainment. At first, the lack of applicable vaccine and medication resulted with many restrictive measures worldwide, such as lockdown and long quarantine periods as outcome of interaction with potentially infected persons. However, such strict government responses have shown many negative side-effects, such as economic losses and country development stagnation in many sectors.

Therefore, one of the possible solutions was the development of vaccine. Despite the huge efforts by many health-oriented research organizations worldwide, it took almost one year to reach the approved products for this purpose. Since early 2021, multilple vaccines have been approved (Sinopharm BBIBP, Pfizer BioNTech, Moderna, AstraZeneca, Sputnik V and others), resulting in almost 60% (mid-January 2022) of world population receiving at least one vaccine dose [1].

However, despite the high percentage of vaccinated citizens, many countries still suffer from huge number of new daily coronavirus cases and high death rate [2]. In this context, it is identified that timely, organized, well-planned and cost-efficient vaccination combined with endangered population priortization and mild restriction measures is one of the key solutions to this issue [3].

In this paper, we explore the adoption of deep learning-based predictions in synergy with multi-objective optimization procedure with aim to enable proactive, but efficient vaccination process planning within the software simulation environment. It builds upon our previous works on single objective pandemic-related resource planning [4] and model-driven approach to component allocation problem, which has been approved in telecommunications domain for network planning [5]. Additionally, we leverage our model-driven component allocation framework [6] on of the solution in order to reduce the learning curve of complex underlying mechanisms and speed-up the overall experimentations process making use of automated code generation. In our case, model-driven software engineering approach relies on leveraging metamodels which describe vaccination and general component allocation problem-related aspects. The main contributions of this paper are: 1) vaccination problem metamodel 2) deep learning-based model for vaccine demand prediction 3) generalized prediction problem metamodel 4) optimization model for efficient vaccine distribution.

II. BACKGROUND AND RELATED WORK

A. Multi-Objective Optimization with MD-CAP: Pymoo and PyEcore

Multi-objective optimization problems include more than one objective functions that should be either maximized or minimized. Generalized form of a multi-objective optimization problem [7] is given as follows:

$$\begin{aligned} &\textit{minimize}\ f_m(\mathrm{x}),\ \forall\ \mathrm{m} \in 1...\mathrm{M} \\ &\textit{subject}\ \mathrm{g}_j(\mathrm{x}) \le 0,\ \forall\ \mathrm{j} \in 1...\mathrm{J} \\ &\qquad \mathrm{h}_k(\mathrm{x})=0,\ \forall\ \mathrm{k} \in 1...\mathrm{K} \\ &\qquad \mathrm{x}_i^{(L)} \le \mathrm{x}_i \le \mathrm{x}_i^{(U)},\ \forall i \in 1...\mathrm{N} \end{aligned} \tag{1}$$

The variables have the following meaning: 1) $x \in \Omega$ - represents a vector in the search of length N; 2) $f_m(x)$ – the m^{th} objective function; 3) $g_j(x)$ - the j^{th} inequality constraint;

Nenad Petrović is with the Department of Computer Science, University of Niš, Faculty of Electronic Engineering, Niš, Serbia, E-mail: nenad.petrovic@elfak.ni.ac.rs

Issam Al-Alzzoni is with Department of Software Engineering and Computer Science, Al Ain University, Al Ain, UAE, E-Mail: issam.alazzoni@aau.ac.ae

4) $h_k(x)$ – the kth equality constraint; 5) $i \in (1 \dots N)$ - for each dimension i of the variable vector x, each xi stands for the i^{th} variable that will be optimized, while there are box constraints for each of them, which are epressed as $x_i^L \leq x_i \leq x_i^U$. Here, x_i^L is lower, while x_i^U represents the upper bound of the variable x_i. However, minimizing the desired objective functions f_m, all the constraints have to be satisfied. If we want to maximize one of the objective functions (should change with *maximize* f_i in the first line of (1) instead), it would be necessary to redefine problem as minimization of its negative value (which is denoted as *minimize* $-f_i$). Multi-objective optimization has goal to find a set of non-dominated solutions which are as close as possible to the Pareto front. Commonly, convergence and diversity of the obtained solution set are quantified for measurement of performance.

We rely on pymoo [8, 9] for implementation, which is a well-known framework that tackles the multi-objective optimization directly. It provides implementations of state-of-the-art algorithms for optimization with multi-objective support in Python. The framework itself is modular, so the distinct tasks, such as decision making, visualization, or post-processing procedures can be easily accessed.

On the other side, we also leverage PyEcore [10], whose purpose is to handle EMF/Ecore metamodels and models in Python. It offers an API compatible with the original Java implementation. Relying on pyecore, the vaccine distribution planning problems can be represented as Ecore model instances. Moreover, model instance can be imported and verified as set of Python objects, which makes it suitable for automated solving and further code generation based on these models. In pymoo, apart from vaccination planning model and pymoo-specific optimization model specificiations, the output of optimization procedure is defined using a model as well.

Both pymoo and pyecore, provide the necessary tools to develop vaccine distribution pipeline within the so-called pyallocation framework [6] for model-driven optimal solution of Component Allocation Problem (CAP). While pyecore ensures correct definition of both input and output, on the other side, pymoo offers the necessary mechanisms which enable solving the optimization problem itself. In this paper, the vaccination plan model is first transformed to a form with respect to auxiliary metamodel representing component allocation problems in general. Finally, the corresponding component allocation problem instance is further used for execution of optimization process relying on pymoo optimization framework in Python. We decide

B. Deep Learning and PyTorch

An artificial intelligence approach to prediction leveraging neural networks which contain several hidden perceptron layers between their input and output is kown as *deep learning* [11]. The goal of these layers is extraction of prediction-relevant features from huge amount of raw input data, which are as suitable as possible for determination of target variable value. In this paper, we make use of PyTorch framework [12] in Python programming language for purpose of vaccination demand prediction within cities of interest, which gives the ability to timely acquire the required number of vaccine doses. The functionality provided by PyTorch covers the following aspects that enable convenient implementation of deep learning-based predictive models [12, 13]: 1) high-level modelling and architecture design for various types of purpose-specific neural networks 2) tensor-based arithmetic and logical manipulations 3) management of datasets. The framework itself is object-oriented and in what follows we give a brief overview of crucial modules [12, 13] relevant to scope of this paper.

Class named *Module* represents the abstraction of highest-level used for neural network representation in PyTorch, so any custom predictor should be inherited from it. Additionally, it is required to provide the implementation for the following methods: 1) *__init__*: Class constructor where we define the architecture of a neural network, considering number of layers, number of nodes per layer and their type (such as linear and convolutional); 2) *forward*: A function where we establish connections between the layer and define how input data passes through neural network towards the output layer. Depending on purpose, layer type and role, various activation functions provided by PyTorch's package *torch.nn.functional* can be adopted, such as *linear* (for input), *ReLU* (common for hidden layers), *sigmoid* (output for binary classifier) and *softmax* (multiclass classifier output). Additionally, PyTorch also covers a set of loss functions inside its *torch.nn* package. Their task is to perfrom distance estimation between the expected and predicted outcome. Typical loss function for regression is Mean Squared Error Loss (*torch.nn.MSELoss*), while different variants of Binary Cross Entropy (*torch.nn.BCELoss*) are used for classification problems. When it comes to neural network training, PyTorch includes several widely used optimizers inside *torch.optim* package, such as Stochastic Gradient Descent (SGD) and Adam, commonly used for supervised learning. In each training iteration, the invocation of *optimizer.step()* updates the weights of neural network, considering the value of learning rate (α) which specifies how much the model will be adjusted as a response to the estimated loss function value.

III. IMPLEMENTATION

A. Framework Overview

Initially, user has to design a model providing the information necessary for vaccination planning, relying on modelling environment which executes on of Eclipse Modelling Framework (EMF) [14]. Several aspects relevant to planning are considered, such as budget limitations, vaccine prices, demand and their availability.

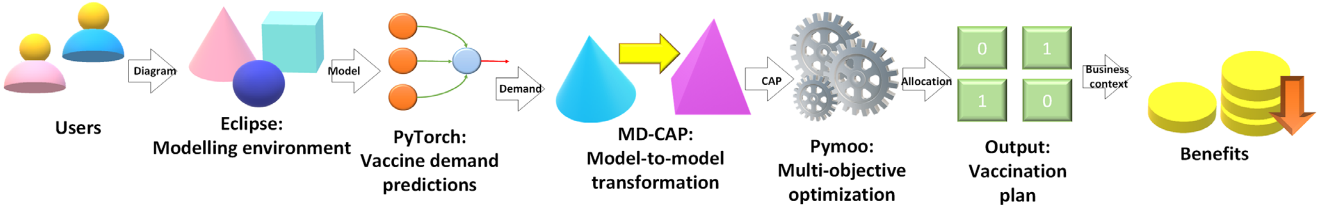

Fig. 1. Vaccination planning simulation environemnt workflow

After that, the user-provided vaccination plan model is augmented with the predicted values, so the optimal vaccine distribution among the cities of interest can be done. In order to achieve this, the model is first transformed to a suitable form with respect to CAP metamodel [5, 6], making use of model-to-model transformation. For this task, we rely on our previous work - Model-Driven Component Allocation Problem Framework (denoted as MD-CAP) [6]. Finally, optimization procedure can be executed on the CAP-alike model. For this purpose, we leverage pymoo framework for multi-objective optimization in Python. The output of framework represents the vaccine transfers between the involved cities.

Fig. 1 illustrates the workflow of the described simulation and planning framework.

B. Vaccination Plan Metamodel

In Fig. 2, the underlying metamodel is depicted in UML class diagram representation from.

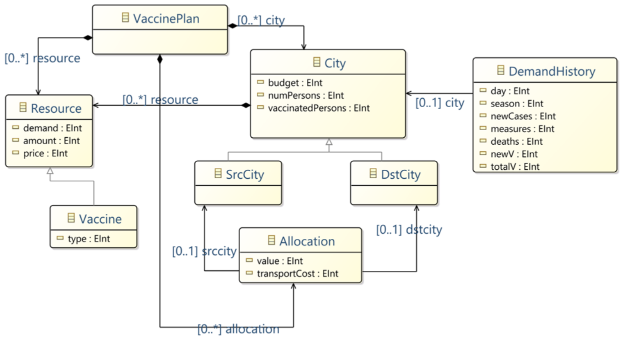

Fig. 2. Vaccination Plan Metamodel as UML class diagram

In this metamodel, the highest-level entity is entitled *VaccinePlan*. It summarizes the component allocation problem of vaccine distribution between the cities of interest and each instance includes the following elements: 1) *City* – an abstraction of administrative unit which is involved into vaccination planning with certain amount of people and limited budget; 2) *Resource* – an object of interest which should be distributed between the cities; 3) *Vaccine* – specific category of *Resource* which is considered for allocation in this paper, can be further split according to their type; 4) *Allocation[i,j]* – value assigned to each pair of cities – source city (denoted as *SrcCity* and later $city_j$) and destination city (*DstCity*, later $city_i$), which becomes 1 in case that the desired amount of vaccine units will be sent from source to destination, but takes 0 otherwise. Its value is assigned as outcome of the multi-objective optimization process; 5) *DemandHistory* - element which encapsulated vaccination-related data history for specific city, relevant to vaccination demand prediction.

C.Vaccine Demand Predictive Model

In order to enable proactive vaccine acquirance for each city, we rely demand estimation leveraging deep learning neural network. For this purpose, the problem is treated as regression, while the layout of the dataset is depicted as Table I. The following attributes are considered as input (independent) variables: 1) *day* [0-366] – number of day within the year for which the vaccine demand is predicted 2) *season* [0-4] – ordinal number of year's season, as demand might be affected by season-related activities and travelling 3) *measure level* [0-3] – restrictions and/or limitations for non-vaccinated persons, such as forbidden entry at hospitality objects and institutions, greater number means more strict measures 4) *new cases* [int] – number of new COVID-19 cases identified within the city that day 5) *deaths* [int] – daily count of persons who died as a consequence of coronavirus disease 5) *total vaccinated* [0-100] – the total percentage of vaccinated persons for city of interest. On the other side, the predicted value (dependent varible) is *new vaccinated*, which represents the integer number of people who decided to take the vaccine that day.

TABLE I
VACCINE DEMAND PREDICTION DATASET LAYOUT

day	*season*	*measure level*	*new cases*	*deaths*	*total Vac*	*new Vac*

The predictive model itself performs regression and it is implemented in Python, relying on PyTorch framework for deep learning. The aim of regression is to predict real-valued outcome based on provided input variables. The neural network in this case consists of two hidden layers, with 45 nodes each, performing ReLU activation. The first input layer has number of nodes which is equal to the count of input variables, while the last, output layer has just a single node with linear activation. Furthermore, during training, Adam optimizer and Mean Squared Error loss function were used with learning rate α=0.01. Fig. 3 shows an excerpt of code written in Python that is used for creation of the proposed neural network.

```
class VaccinePredictionModel(torch.nn.Module):
    def __init__(self, input_length):
        super(MyNeuralNetwork, self).__init__()
        self.input_size = input_length

        self.l_1 = torch.nn.Linear(input_length, 45)
        self.l_2 = torch.nn.Linear(45, 45)
        self.l_3 = torch.nn.Linear(45, 1)

    def forward(self, x):
        out_1 = F.relu(self.l_1(x))
        out_2 = F.relu(self.l_2(out_1))
        demand = self.l_3(out_2)
        return demand

vaccine_demand_predictor=VaccinePredictionModel(6)
```

Fig. 3. PyTorch code for vaccine demand prediction treated as regression

D. Generalized Prediction Problem Metamodel

Additionally, we leverage the model-driven approach for automatizing one more aspect - deep learning code generation. For that purpose, we introduce a metamodel depicted in Fig. 4.

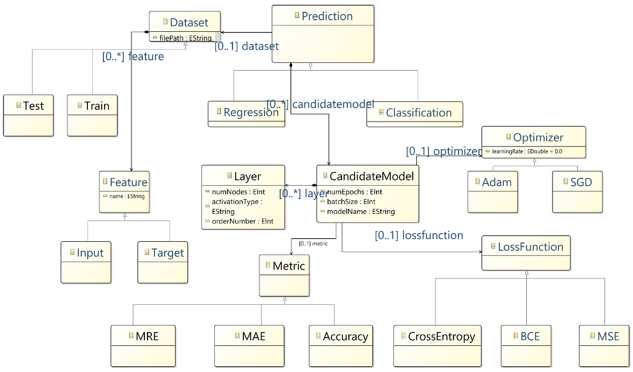

Fig. 4. Generalized Prediction Problem Metamodel

It describes the general structure of prediction problems and enables creation of framework-independent descriptions. Furthermore, code generation algorithms are leveraged in order to generate neural networks that aim different programming languages and target platforms. In this paper, the output of code generation process is PyTorch code for Python programming language. We cover two types of most common prediction problems within the metamodel: regression and classification. *Prediction* is performed against some *Dataset* that can be used in *Test* or *Training* phase and its main properties are file path and columns, denoted as *Feature*. Additionally, each Feature is treated either as Input or Target variable. Furthermore, in case of Prediction there could be one or more CandidateModels with different configurations, covering parameters, such as learning rate, batch size, optimizer type and loss function. Finally, once the code for all candidate models is generated, each of them is evaluated using the appropriate *LossFunction* metric (Mean Relative Error - MRE and *Mean Absolute Error* - MAE for regression, *Accuracy* in case of classification). After that, the one which has the highest performance metric value is returned as output.

E. Vaccine Distribution Optimization Model

The goal of the underlying optimization model for optimal vaccine distribution is to allocate some of the available vaccine doses from given set of *Cities*, where surplus units taken from current vaccine amount VA_j are sent by source $city_j$ in order to fulfil the vaccine demand VD_i of destination $city_i$. The goal of the first objective function is to minimize the overall acquirance costs, taking into account both the vaccine price VP_j offered by $city_j$ and transport cost $TC_{i,j}$ between the cities:

$$minimize \sum_{i,j \in Cities} (TC[i,j] + VP[j]) Allocation[i,j] \tag{2}$$

On the other side, another objective function aims to maximize vaccination coverage, so each city gets as much as possible vaccine units from the cities that have surplus amount available:

$$minimize \sum_{i,j \in Cities} \frac{VA[i] + (VA[j] - VD[j])}{VD[i]} Allocation[i,j] \tag{3}$$

In these equations, $Allocation_{i,j}$ is a decision variable which takes value 1 if vaccine transfer between the cities with indices *j* and *i* is performed.

However, several allocation constraints have to be satisfied while performing vaccine distribution among cities. First, the overall transfer cost should not exceed the budget limit B_i of destination $city_i$:

$$B[i] \geq \sum_{j \in Cities} (TC[i,j] + VP[j]) Allocation[i,j] \tag{4}$$

Moreover, after the transfer, vaccine demand should be satisfied in all the destination cities *cityi* where it was initially greater than the available amount:

$$VD[i] - VA[i] \leq \sum_{j \in Cities} (VA[j] - VD[j]) Allocation[i,j] \tag{5}$$

While in source cities, the remaining amount of vaccines after the transfer should still be at least 10% greater than the minimal vaccine demand for that city, given as:

$$1.1(VA[j] - VD[j]) \leq \sum_{j \in Cities} (VA[i] - VD[i]) Allocation[i,j] \tag{6}$$

IV. EVALUATION AND RESULTS

In this section, we evaluate the proposed model-driven framework for cost-efficient vaccination planning, considering several aspects: 1) processing time for various steps 2) benefits - cost reduction and coverage increage 3) reduction of time needed for execution in single-objective mode 4) prediction accuracy 5) reduction of time necessary for experimentation. The results are compared to our previous works relying on AMPL and CPLEX performing single-objective linear optimization [4]. We perform the experiments for varying sizes of model instances (number of cities involved). For evaluation purposes, the following laptop configuration was used: i5 10300 quad-core CPU, 8 GB of DDR4 RAM, 512GB M2 SSD and NVIDIA GTX 1650 GPU with 4 GB of VRAM. All the execution times are expressed in seconds, as average value of 100 consecutive runs with same parameters.

In Table II, the results obtained as outcome of the experiments are summarized. The first column denotes how many cities were involved into vaccine distribution. Moreover, the next three columns show the processing time necessary for distinct steps: vaccine demand prediction, model-to-model transformation and optimization-based allocation. Furthermore, the next two columns represent the achieved benefits compared to single-objective approach, expressed as percentage of cost reduction, coverage increase. Finally, the last column shows the processing time speed-up in single-objective mode. With respect to results from Table II, it is noticeable that processing time increases with model size.

TABLE II

PAGE LAYOUT DESCRIPTION

Num. cities	Processing time [s]			Benefits [%]		Speed -up
	Pred.	M2M	Optim.	Cost red.	Cover inc.	
3	0.97	0.01	0.041	87	41	1.83
5	1.09	0.02	0.063	137	98	2.14
10	1.76	0.05	0.084	10	72	2.57

On the other side, the prediction accuracy of the vaccine demand model was evaluated on publicly available data from [15]. In our experiments, it reaches the relative error up to 12% based on records for 10 countries. The order of magnitude for predictive model code generation was 10 ms. Finally, the adoption of model-driven approach and automated code generation reduces the time necessary for manual optimization model creation, modification and data import, requiring up to 10 times less than averagely in the carried out experiments.

V. CONCLUSION

In this paper, we present a model-driven approach to vaccination planning, tackled as multi-objective resource allocation problem, implemented relying on pymoo and model-driven approach for network model representation. Furthermore, deep learning-based predictions are leveraged to enable proactiveness. According to the achieved results, it can be concluded that the proposed approach is quite faster than AMPL in single-objective mode (up to around 2.5 times). Furthermore, the adoption of multi-objective optimization enables to perform both the cost minimization and coverage maximization at the same time, which is not possible for single-objective linear optimization. Finally, the adoption of model-driven approach reduces the time necessary for experimentation, relying on automated code generation and model-to-model transformations.

VI. ADDITIONAL REMARKS

Metamodel and AMPL optimization model used for comparison are available on GitHub: https://github.com/penenadpi/covid19-vaccination-plan

ACKNOWLEDGEMENT

This work has been supported by the Ministry of Education, Science and Technological Development of the Republic of Serbia.

REFERENCES

[1] Coronavirus (COVID-19) Vaccinations [online], available on: https://ourworldindata.org/covid-vaccinations , last accessed: 17/01/2022.

[2] COVID Live [online], available on: https://www.worldometers.info/coronavirus/, last accessed: 17/01/2022.

[3] Younus, M. & Al-Jumaili, A. A., “Overview of the COVID-19 vaccine effectiveness”, *Al-Rafidain Journal of Medical Sciences*, Vol. 1 (2021): July-December, pp. 94-96, 2021. https://doi.org/10.54133/ajms.v1i.38

[4] Petrović, N., “Simulation Environment for Optimal Resource Planning During COVID-19 Crisis”, 2020 55th International Scientific Conference on Information, Communication and Energy Systems and Technologies (ICEST), 2020, pp. 23-26, 2020. https://doi.org/10.1109/ICEST49890.2020.9232908

[5] Petrović, N., Al-Azzoni, I. and Blank, J., “Model-driven Multi-objective Optimization Approach to 6G Network Planning”, 2021 15th International Conference on Advanced Technologies, Systems and Services in Telecommunications (TELSIKS), 2021, pp. 223-226, 2021. https://doi.org/10.1109/TELSIKS52058.2021.9606345

[6] Al-Azzoni, I., Blank, J., Petrović, N., “A Model-Driven Approach for Solving the Software Component Allocation Problem”, *Algorithms 2021*, 14(12), 354, pp. 1-19, 2021. https://doi.org/10.3390/a14120354

[7] Sawaragi, Y., Nakayama, H., Tanino, T., “Theory of Multiobjective Optimization”, 1st edition, *Elsevier Science*, 1985.

[8] Pymoo: Multi-objective Optimization in Python [online], available on: https://pymoo.org/getting_started/preface.html, last accessed: 17/01/2022.

[9] Blank, J. and Deb, K., “Pymoo: Multi-objective optimization in python”, IEEE Access, 8:89497–89509, 2020. https://doi.org/10.1109/ACCESS.2020.2990567

[10] PyEcore: A Pythonic Implementation of the Eclipse Modeling Framework [online], available on: https://github.com/pyecore/pyecore, last accessed: 17/01/2022.
https://doi.org/10.1109/TELSIKS52058.2021.9606345
[11] Bengio, Y., "Learning Deep Architectures for AI", *Foundations and Trends in Machine Learning*, Vol. 2, No. 1, pp. 1-127, 2009.
[12] PyTorch [online], available on: https://pytorch.org/, last accessed: 16/01/2022.
[13] Stevens, E., Antiga, L., Viehmann, T., "Deep Learning with PyTorch", *Manning Publications*, 2020.
[14]Eclipse Modelling Framework (EMF) [online], available on: https://www.eclipse.org/modeling/emf/ , last accessed: 17/01/2022.
[15] Immunization Data [online], available on: https://data.unicef.org/resources/dataset/immunization/ , last accessed: 17/01/2022.

Supervised Non-intrusive Load Monitoring for Non-linear Appliances

Srdjan Djordjevic

Abstract - The aim of the paper is to develop a computationally efficient load disaggregation method that performs well in recognizing small non-linear loads. The paper considers non-intrusive load monitoring based on the use of two appliance specific features: active power and harmonic current. Several machine learning algorithms including k-nearest neighbours, support vector machine, decision tree, Naive Bayes were developed for the appliance load monitoring. The performance of these classification algorithms was compared according to prediction accuracy and prediction time. The experimental results show that the k-nearest neighbours and decision tree are the most appropriate classification algorithms for load disaggregation with the specified load signature.

Keywords - Non-intrusive load monitoring, Load signature, Nonlinear devices, Machine learning.

I. INTRODUCTION

In recent years, there has been a growing interest in the improvement of energy efficiency due to increasing energy demands and environmental issues. Many research teams have been focused on the energy efficiency of the residential sector. The most important technological solution toward this goal is the use of home energy management system. The existing home energy management systems control the electricity usage based on the measurement of the household consumption in real time. A further enhancement in the functionality can be achieved by feeding appliance specific information into the HEMS.

Information on the electricity usage of individual appliances is valuable not only for demand side management but also for the residential consumers. Namely, the significant electricity savings can be achieved by providing residential consumers with the appliance energy consumption data [1, 2].

There are two approaches for collecting the appliance specific electricity consumption data, intrusive load monitoring and Non-Intrusive Load Monitoring (NILM). The first is a direct measurement of individual appliance consumption. The second approach is disaggregation of the total electricity consumption into the appliance level data. Direct measurement provides more accurate data but it is not practical because it is expensive and difficulty to maintain. On the other hand, NILM has attracted much attention in the recent years due to increase in computational power and developments in machine learning algorithms [3].

This paper is an extension of our earlier study on the non-intrusive load disaggregation of small nonlinear loads [4], which was motivated by the increasing number of nonlinear-loads in residential settings [5]. Our previous research has arrived at the conclusion that small appliances have clear separation of features in the feature space of the total harmonic current and active power. However, the classification capabilities of this method were not tested. The goal of this paper is to explore which of the machine learning algorithms is the most appropriate for the classification of the appliances.

The process of NILM consists of three stages: acquisition of the aggregated load, feature extraction and classification. The role of the acquisition is to collect the row data of the current and voltage at an adequate sampling rate. Feature extraction derives the appliance signature, or a unique feature that characterize that appliance, from the aggregated measurements. The performance of a NILM method is determined by the load signature and the applied machine learning algorithm. In the present research, we tested a set of machine learning algorithms on a validation dataset to select the most appropriate one. The algorithms were compared according to prediction accuracy and prediction time. In the proposed method the number of features and examples are not limiting factors for the algorithm.

The paper is divided into five parts. The next section gives an overview of the machine learning algorithms used in the non-intrusive load monitoring. The third section is devoted to the method of NILM based on the usage of total harmonic current and active power. The experimental results and evaluation are given in the fourth section. Finally, the fifth section summarizes the results of this work.

II. MACHINE LEARNING ALGORITHMS IN THE NON-INTRUSIVE LOAD MONITORING

Classification algorithms are more or less suitable for the task of load disaggregation depending on the feature set and the type of target appliances. The selection of the appropriate machine learning algorithm should take into account the complexity of the algorithm, prediction time, capability of the model to handle given number of features, interpretability of the model etc [6]. The classification models need to be of appropriate complexity with respect to the observed data set. The use of an unnecessarily complex model leads to overfitting of data, or very good predictions

Faculty of Electronic Engineering, University of Nis,
Address: Aleksandra Medvedeva 14, Nis, Serbia.
E-mail: srdjan.djordjevic@elfak.ni.ac.rs

of the training data including noisy examples and poor predictions on unseen data. On the other hand, too simple prediction model is not able to describe training data and does not predict well on seen and unseen data.

There are two approaches in machine learning: unsupervised and supervised. In the unsupervised machine learning, the classes of the objects are not defined and the task of the algorithm is to identify them. The most important problem in unsupervised machine learning is clustering, or grouping of the examples according to the similarity between them. Clustering can be performed by different cluster models and cluster algorithms. One of the drawbacks of clustering is computational complexity in the case of a large number of data points and high dimensionality of the feature vector. In addition, the performance of the algorithm depends on the distance metrics.

The decision tree learning algorithm constructs a directional graph which enable us to predict the class of an example. During the building of the decision tree each node is associated with a set of training examples. At the beginning, the hole training set is divided into two subsets according to the value of a specific feature. The training example whose feature value is larger than a given threshold is assigned to the first child node, otherwise it is assigned to the second child node. The process is iteratively repeated on the child nodes until it results in a set of examples which all belong to the same class.

A very simple and popular non-parametric machine learning algorithm, called k-nearest neighbours, predicts the class of an example according to its distances to the k nearest training examples. A specificity of this machine learning algorithm is that the model for prediction is training data set. Hyperparameters of the k-nearest neighbours classifier are distance metric and the number of nearest neighbours, k. The most frequently used distance metric for continues features is Euclidean distance.

The classification performance of the k-nearest neighbours algorithm significantly depends on the number of voting neighbours, k. The greater value of k makes classifier more resistant to noisy nearest neighbours but too high value of k give rise to misleading examples among the voting neighbours. The main problems of the k-nearest neighbours algorithm are related to irrelevant features, sparse data and disproportion between the values of different features.

Multilayer Perceptron is an artificial neural network composed of neurons arranged in multiple layers. In this architecture, the outputs of neurons in one layer are connected by the links to the inputs of the neurons in the next layer. The model of the multilayer perceptron is parametrized by the weights associated to the links. Therefore, the goal of the training procedure is to minimize the cost function by adjusting the link weights. The best-known technique for the training of the multilayer perceptron is backpropagation of error, which uses gradient descent of the mean square error.

The classification model that makes prediction according to the probabilities of class labels is known as Bayes learning algorithm. It is based on the Bayes theorem which assumes the statistical independence of the features. The model of Bayesian classifier are probability distribution functions of each particular feature given that example belong to a specific class. The algorithm estimates probability distribution functions exclusively from the training examples of one class under assumption that they follow normal distribution. Bayesian classifier may attain the best classification accuracy if it is provided with adequate training data.

Support vector machine learning model creates an optimal decision boundary called hyperplane in order to separate examples of different classes. The algorithm minimize distance between hyperplane and closest examples of each class. SVM algorithm is a binary classifier, but it can be applied to multi-class domains after converting training data set into binary training sets. In the case when classes are not linearly separable it is necessary to use kernel functions which transform training data set in such a way that non-linear decision surface become linear. These transformations should be carefully applied, because they increase computational cost and may cause overfitting. The main limitation of SVM classifier is that it can not handle a large number of features and examples. SVM algorithm performs high prediction speed.

III. NON-INTRUSIVE LOAD MONITORING BY USING HARMONIC CURRENT AND ACTIVE POWER

The accuracy of the NILM system strongly depends on the electrical parameters used as the load signature. The appliances can be efficiently discerned and recognized only if they are well separated in the feature space. The initial load disaggregation procedure, proposed by Hart [7], detects loads by analysing changes in the active and reactive power. This method has been broadly used, because it performs well in recognizing large linear loads. However, the presence and number of certain types of electrical appliances in households has changed significantly in the last few decades. An increasing number of nonlinear loads has motivated many researchers to incorporate current harmonic content into the NILM methods. There is a variety of NILM methods based on the different steady-state or transient harmonic signatures [8-15].

In the literature there are several different solutions for the current harmonic based load disaggregation. These methods differ by the current spectral components used in the load signature. The use of the greater number of current harmonics as classification features will enhance the accuracy of the method. On the other hand, larger number of features will result in higher computational cost. The computational efficiency of the harmonic based NILM methods is critical since the number of classes is very large and exponentially grows with the number of target appliances. There is an open question which of the current harmonics are optimal for the load disaggregation.

In our previous study, we propose a load signature composed of total harmonic current and active power. The advantage of the proposed approach is computational efficiency since higher harmonic components of the current are characterized by only one parameter instead of individual harmonics. Another benefit of using the total current harmonic instead of other electrical parameters is that it is not related to the fundamental current harmonic, which is dominantly determined by the high-power linear loads.

Current signal is composed of two components: fundamental current and harmonic component which are related by the following equation:

$$I_{RMS}{}^2 = I_1^2 + \sum_{\mathrm{h}=2}^{\infty} I_{\mathrm{h}}^2 = I_1^2 + I_{TH}^2 \tag{1}$$

where: I_{RMS} is the RMS value of the current, I_h is the RMS value of the h-th harmonic component, I_{TH} is the total harmonic current.

Total harmonic current is equal to the square root of the squared sum of higher current harmonics. However, it can be simply calculated in terms of the effective current and fundamental current harmonic as follows:

$$I_{TH} = \sqrt{I_{RMS}^2 - I_1^2} \tag{2}$$

The effective value of the current is usually calculated from the samples as:

$$I_{RMS} = \sqrt{\frac{1}{N}\sum_{n=1}^{N} i[n]^2} \tag{3}$$

where: n is the sample index, i[n] is the current value measured at sampling point n and N is the number of samples taken during a full-wave of the current.

IV. EXPERIMENTAL RESULTS AND EVALUATION

Data acquisition and feature extraction was conducted by Fluke 434 II energy analyser. It samples current and voltage signals at a sampling rate of 200 KHz and quantize the samples to 16-bits. The analyser detects and measures a broad set of power distribution system parameters. Current signal was measured by a current clamp put around the conductor of one phase. For single phase measurements, the energy analyser needs to be connected to the one phase wire, neutral wire and ground wire. The experimental setup of the NILM prototype system used in the research is shown in Fig. 1.

The proposed method is tested on a group of small household non-linear loads listed in Table I. Appliances of each combination need to be connected in parallel in order to measure current and voltage waveforms.

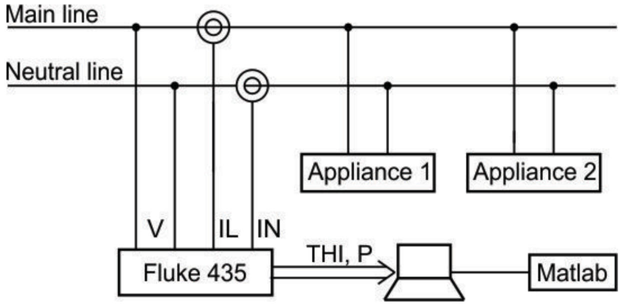

Fig. 1. The experimental setup

The average values of two load signatures used in the experiment, active power and harmonic current, were recorded each second for 2 minutes. Training data set is composed of 1000 examples per class, where each class corresponds to a device combination. In the experiment, we compared several machine learning algorithms to recognize operating state of small nonlinear appliances. All classifications were conducted using MATLAB 2017a (MathWorks, Natick, MA, USA). The models of supervised machine learning algorithms were trained on the same training data set.

Table I shows several important electrical parameters of the appliances used in the experiment. Each parameter in the table is represented by its mean value and its standard deviation.

TABLE I

ELECTRICAL PARAMETERS OF THE TARGET APPLIANCES

	P(W)	Q(Var)	IRMS(A)	THDI(%)
Refrigerator	40±0.74	226.1±4.8	0.99±0.05	12.3±0.14
Fluo. Lamp	40.3±2.06	172.9±4.5	0.79±0.06	10.4±0.18
Laptop	43.56±5.2	55.5±8.0	0.42±0.14	29.1±2.57
PC	111.8±3.9	121±4.16	1.02±0.08	87.6±1.12
TV	89.3±3.5	103.9±4.9	0.66±0.1	23.1±0.55
Air Condit.	359.8±5.7	1060±7.3	4.9±0.04	23.5±0.09

The proposed method requires a unique load signature with respect to all possible appliance combinations. In the experiment we have considered each pair of the target appliances.

The distribution of the aggregate loads in P-THI feature space is shown in the Fig. 2. This figure is divided into two parts for clarity. Each signature is represented by a point in the feature space. Aggregate loads are denoted by two letters, each of which represent the first letter of the appliance type name: refrigerator-R, fluorescent lamp-F, laptop-L, PC-P, TV-T, Air Conditioner-A.

Some combinations of appliances exhibit overlapping in the P-THI feature space. A significant overlapping occurs between the following aggregate loads: AR-AL, AR-AP, LP-RP. As a consequence, the operation of these aggregate loads is identified with lower accuracy.

Table II contains the classification accuracies of the classifiers with respect to the considered aggregate loads. The experimental results show that overlapping between some classes have different effects on different classifiers. It is observed that the Naive Bayes and SVM have not good performance over several combinations of appliances. For example, aggregate loads of air-conditioner-fridge, laptop-TV and laptop-PC were classified with low accuracy. On the other hand, KNN and decision tree algorithms are more robust against overlapping between classes.

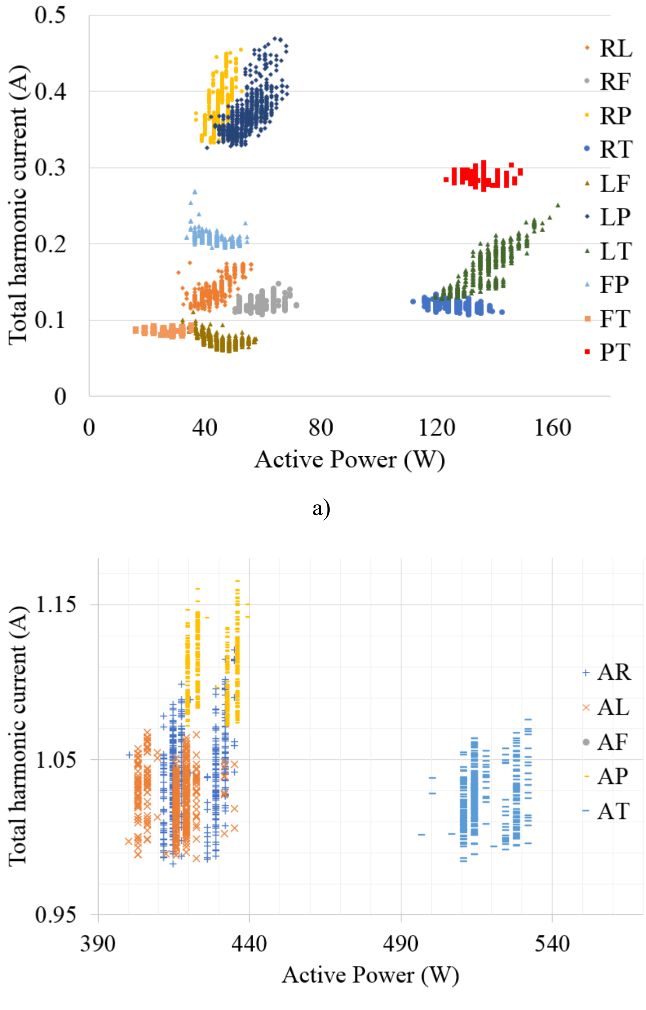

a)

b)

Fig. 2. Distribution of the aggregate loads in P-THI feature space

Table III shows the total classification accuracy of the inspected machine learning algorithms over testing data set. According to the experimental results k-nearest neighbours classifier achieves the highest accuracy. The decision diagram algorithm has slightly lower accuracy than KNN algorithm due to poor detection of the simultaneous operation of laptop-PC, laptop-TV and air conditioner-PC.

TABLE II

CLASSIFICATION ACCURACIES OF THE CLASSIFIERS WITH RESPECT TO THE CONSIDERED AGGREGATE LOADS

	Naive Bayes	KNN	Decision tree	SVM
Air Condit. Fluo. Lamp	100%	100%	100%	96,5%
Air Condit. Laptop	60,5%	95,5%	91,5%	59,5%
Air Condit. PC	99,25%	100%	73,5%	75,75%
Air Condit. Refrigerator	54%	98%	92,5%	57,5%
Air Condit. TV	100%	100%	98,5%	100%
Fluo. Lamp. Laptop	100%	100%	100%	100%
Fluo. Lamp. PC	89,5%	93,5%	99,25%	99,75%
Fluo. Lamp. Refrigerator	100%	100%	100%	96,5%
Fluo. Lamp. TV	99,75%	99,75%	99,75%	99,5%
Laptop PC	59%	77%	59%	72,75%
Laptop Refrigerator	99,75%	98,75%	99,75%	99,5%
Laptop TV	51%	98,25%	70,75%	52%
PC Refrigerator	99,25%	92,25%	92,5%	98,5%
PC TV	100%	76,2%	100%	100%
Refrigerator TV	99,5%	99,5%	98,25%	100%

TABLE III

TOTAL CLASSIFICATION ACCURACY OF THE INSPECTED MACHINE LEARNING ALGORITHMS

	Naive Bayes	KNN	Decision tree	SVM
the total classification accuracy	87,43%	95,25%	93,25%	84,2%

Table IV shows the average computation times used for the training stage and testing stage of the different classification algorithms. Both training speed and testing speed are represented in the form of the calculation time per classification. It is apparent from the data in table IV that the algorithms of decision tree and KNN have significantly lower testing and training computation times compared to the other two classifiers. The experimental results also indicate that the most computationally expensive machine learning algorithm is Support vector machine.

TABLE IV
ELECTRICAL PARAMETERS OF THE TARGET APPLIANCES

	Naive Bayes	KNN	Decision tree	SVM
Training time per samples [μs]	25,5	3,7	4,8	4823
Testing time per classifications [μs]	30,67	4,95	9,31	165,8

V. CONCLUSION

Among the tested classifiers, KNN algorithm exhibits the highest classification accuracy. The decision tree algorithm also performs well for the task of load disaggregation. These two algorithms also have high computational efficiency.

The experimental results show that the SVM with the linear kernel does not performs well on predicting the nonlinear loads. This implies that features used in the method are not linearly separable and can be accurately modelled only by the SVM with non-linear kernel.

The classification accuracy of the Bayesian classifier on load disaggregation was below that of the other machine learning algorithms used in the study. This is an unusual result since Bayesian classifier is known for its high accuracy. The reason for this low accuracy is that classifier is not provided with sufficiently precise information about probabilities. The problem arises from the fact that voltage and current of the power network are not stationary stochastic variables and that they vary due to conditions outside of the household.

The experimental results of this paper give an initial insight into the applicability of different machine learning algorithms into the proposed load monitoring procedure. Before obtaining a definitive answer which of the classifiers is the most adequate it is necessary to take into consideration the adjustment of the hyperparameters of the classifiers.

REFERENCES

[1] Darby, S., "The effectiveness of feedback on energy consumption", Literature Review for the Energy Demand Research Project, University of Oxford, UK, 2006.

[2] Neenan, B., Robinson, J., Boisvert, R.N., "Residential Electricity Use Feedback: A Research Synthesis and Economic Framework", Electric Power Research Institute, Palo Alto, CA, USA, 2009.

[3] Zoha, A., Gluhak, A., Imran, M., Rajasegarar, S., "Non-intrusive load monitoring approaches for disaggregated energy sensing: a survey", *Sensors*, Vol. 12, No. 12, pp. 16838-16866, Dec. 2012.

[4] Djordjevic, S., Dimitrijevic, M., Litovski, V., "A Non-Intrusive Identification of Home Appliances Using Active Power and Harmonic Current", Facta Universitatis, Series: Electronics and Energetics, Vol. 30, No 2, pp. 159-175, 2017.

[5] Muscas C. "Power quality monitoring in modern electric distribution systems", *IEEE Instrumentation & Measurement Magazine*, Vol. 13, No. 5, pp. 19-27, Oct. 2010.

[6] Kahl, M., "Machine Learning for Non-Intrusive Load Monitoring", PhD dissertation, der Technische Universität München, Germany, 2019.

[7] Hart, G., "Nonintrusive appliance load monitoring", *Proceedings of the IEEE*, Vol. 80, No. 12, pp. 1870–1891, 1992.

[8] Laughman, C., Lee, D., Cox, R., Shaw, S., Leeb, S., Norford, L., Armstrong, P., "Power signature analysis", *IEEE Power and Energy Magazine*, Vol. 1, No. 2, pp. 56-63, 2003.

[9] Srinivasan, D., Liew, A., "Neural-network-based signature recognition for harmonic source identification", *IEEE Transactions on Power Delivery*, Vol 21, No.1, pp. 398–405, 2006.

[10] Huang, S., Hsieh, C., Kuo, L.C., Lin, C.W., Chang, C.W., Fang, S.A, "Classification of Home Appliance Electricity Consumption Using Power Signature and Harmonic Features", In *IEEE Ninth International Conference on Power Electronics and Drive Systems-PEDS*, pp. 596-599, Dec. 2011.

[11] Lee, K.D., Leeb, S.B., Norford, L.K., Armstrong, P.R., Holloway, J., Shaw, S.R., "Estimation of variable-speed-drive power consumption from harmonic content", *IEEE Transactions on Energy Conversion*, Vol. 20, No. 3, pp. 566–574, 2005.

[12] Meehan, P., McArdle, C., Daniels, S., "An Efficient, Scalable Time-Frequency Method for Tracking Energy Usage of Domestic Appliances Using a Two-Step Classification Algorithm", *Energies* , Vol.7, No. 11, pp. 7041-7066, 2014.

[13] Lee, K.D., Leeb, S.B., Norford, L.K., Armstrong, P.R., Holloway, J., Shaw, S.R., "Estimation of Variable-Speed-Drive Power Consumption from Harmonic Content", *IEEE Transactions on Energy Conversion*, Vol. 20, No. 3, pp. 566-574, Sept. 2005.

[14] Wichakool, W., Avestruz A.T., Cox, R.W., Leeb, S.B., "Modeling and Estimating Current Harmonics of Variable Electronic Loads", *IEEE Transactions on Power Electronics*, Vol. 24, No. 12, pp. 2803-2811. Dec. 2009.

[15] Djordjevic, S., Simic, M., "Nonintrusive identification of residential appliances using harmonic analysis", *Turkish Journal of Electrical Engineering & Computer Sciences*", Vol. 26, No. 2, pp. 780-791, 2018.

Implementation and Evaluation of Network Intrusion Detection System on Raspberry Pi Device

Dimitrije Krstic, Nadja Gavrilovic, and Vladimir Ciric

Abstract – In recent years, with the growing development of IoT, devices with limited resources are increasingly present. Having a simple architecture and short time-to-market makes cyber security defence of these devices challenging. One possible approach in securing a system is to place a dedicated Intrusion Detection System (IDS) as a common network gateway of all devices, while the other is to embed the IDS into the device itself. Until recently, the first approach was dominant in IoT because of the limited device resources. The goal of this paper is to explore possibilities of robust mainstream IDS implementation on an IoT device itself. The implementation of the Snort IDS on Raspberry Pi 4 is given, and the performances are analysed under the simulated attack. It is shown that the device can process up to 30% of malicious packets from incoming traffic, which is sufficient not only to protect itself, but others as well.

Keywords – Intrusion Detection Systems, Raspberry Pi, Snort IDS.

I. INTRODUCTION

Technology is constantly evolving, which makes it easier for people to function on a daily basis. New technology wave in recent years introduced a whole new set of small devices and systems embedded in common appliances, bringing new qualities and expanding its applications. Nowadays it is not uncommon to have a dishwasher connected to the Internet [1].

As a consequence, the number of devices connected to the Internet exceeded the number of people using it [1]. Those systems are developed to make tasks easier for everyone. However, their simple architecture and insufficiently tested software because of short time-to-market make the task of an intruder easier too [2].

An analysis of common attack techniques led to the following conclusion. Attacks that have the greatest consequences use common packets but with content modified by the attacker. Therefore, protection systems are implemented to analyze the content of the packet against the known malicious signatures in order to determine whether the packet was sent by the attacker [3]. As the database that holds malicious signatures can have a large number of entries, analysis can be a resource-demanding task. This task was hard to reach until recently for almost all IoT devices. Because of that, the security was usually implemented as a common and centralized IDS system on the network gateway.

The goal of this paper is to explore the possibilities of robust mainstream IDS implementation on an IoT device itself. The implementation of the Snort IDS on Raspberry Pi 4 will be given, and the performances will be analysed under simulated attack. In the simulation, we will use different quantities of malicious packets and evaluate the utilization of system resources. It will be shown that the device can process up to 30% of malicious packets from incoming traffic, which is sufficient not only to protect itself, but others as well in most cases.

The paper is organized as follows. Section 2 gives a brief introduction to Raspberry Pi device. Section 3 gives a quick overview of IDS. Section 4 explains how Snort is implemented on a Raspberry Pi, and where device is set in topology, as a basis for the proposed implementation. Also, a detail view of malicious traffic that is used in simulation is given. Section 5 is the main section and presents evaluation results of proposed system, while concluding remarks are given in Section 6.

II Raspberry Pi

In 2006, Eben Upton have seen that students and entry level engineers are not familiar enough with practical use of personal computers. He then realized that the main issue is the market price of computers. So, he came up with an idea to invent one affordable computing platform for wide area of application [4].

In 2012, Eben presented the first two models of new Raspberry Pi device (model A and model B) that represented the beginning of a low price personal computers era [4].

In further years this device was enhanced even more. This produced several versions of Raspberry Pi: Raspberry Pi 2 (February, 2015); Raspberry Pi 0 (November, 2015); Raspberry Pi 0W (February, 2017); Raspberry Pi 3B (February, 2016); Raspberry Pi 3B+ (2018); Raspberry Pi 4B (2019) [4].

In Fig. 1 Raspberry Pi 4B which is used for the implementation proposed in this paper is shown [4].

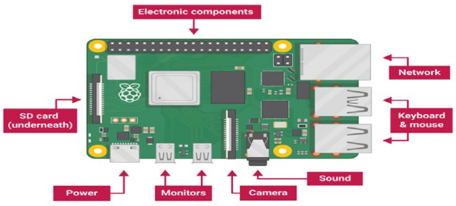

Figure 1. Raspberry Pi device [5]

Dimitrije Krstic, Nadja Gavrilovic, and Vladimir Ciric are with the University of Nis, Faculty of Electronic Engineering, Aleksandra Medvedeva 14, E-mail: dimitrije.krstic@elfak.rs, nadja.gavrilovic@elfak.ni.ac.rs and vladimir.ciric@elfak.ni.ac.rs.

Regardless the fact that Raspberry Pi is labeled as low performance device, this small device has very powerful hardware, which is given in the Table I bellow.

TABLE I
Raspberry Pi device specification [6]

Procesor	Broadcom BCM2711, Quad core Cortex-A72 (ARM v8) 64-bit SoC @ 1.5GHz
RAM	4GB LPDDR4-3200 SDRAM
Wi-Fi adapter	2.4 GHz and 5.0 GHz IEEE 802.11ac wireless
Bluetooth adapter	Bluetooth 5.0, BLE
Ethernet adapter	Gigabit Ethernet
USB ports	2 USB 3.0 ports; 2 USB 2.0 ports.
Display ports	2 × micro-HDMI ports (do 4kp60) 2-lane MIPI DSI display port 2-lane MIPI CSI camera port
GPU	OpenGL ES 3.0 graphics
SD slot	Micro-SD slot
Power	5V DC via USB-C connector
Work temperature	0 – 50 degrees C ambient

This hardware can not only perform common IoT tasks, but it is also suitable for more demanding computations.

III Overview of IDS

IDSs are divided in two large groups based on the technique used to determine whether network packet is regular or malicious. There are pattern (signature) matching and anomaly-based IDSs [7].

Anomaly-based IDSs monitor network traffic and compare packets and events occurred on network against the definitions of the activity that is assumed to be normal, to identify significant deviation. These systems are capable of detecting zero-day attacks, because the detection does not depend on previously detected attacks. Unfortunately, sometimes they can generate high amount of false positive alerts. In newer IDS systems, artificial intelligence is often used in order to further improve system detection [7].

IDSs that use detected properties of previous attacks for conclusion are called Signature based systems. Pattern of previous attacks and threats which are identified during attack are stored in a database of signatures. Pattern matching IDSs recognize possible intrusions by comparing network traffic to malicious attempt patterns. However, it can't detect threats that haven't been seen before [7].

One of the most used signature based IDSs is Snort. This open-source IDS is portable and very customisable. Great advantage is that the operation of Snort does not take much memory and processor time to be efficient. Snort can be deployed on various network hosts and platforms. For detection of attacks and malicious activities, Snort uses a set of patterns. Those patterns define what kind of network traffic is labeled as a threat. Snort's pattern sets are called Snort rules. Formal definition of a rule, and a typical example of a Snort rule, are given bellow, respectively [8]:

<rule action><protocol><source ip><source port><direction><dest ip><dest port><rule options>

alert tcp any any -> any any 21 (content:"user root";)

In the given example, *alert* option is set as rule action, which defines that the alert data is stored for later gathering and further analysis. The rest of the fields, except the rule options field, describe packet attributes (source and destination ip address, source and destination port, protocol). In the example, ip addresses are defined as *any*. The last part of the rule gives key-value pairs with further rule description. In the given example, the *content* is the name of the field that should be matched against the value of *user root* [8].

The main components of Snort architecture are given in Fig. 2. Sniffer component monitors network traffic and sends data to the preprocessor, which checks packets against available plug-ins for a certain type of behaviour from the packets. Detection of the intrusion is done in detection engine component. This component verifies data against set of rules. As soon as the first rule matches the data, the action specified by the rule is triggered. Examples of an action can be sending the alert to the log file through network connection, storing the alerts in an SQL database, sending the event via e-mail to notify system administrator, etc. [9].

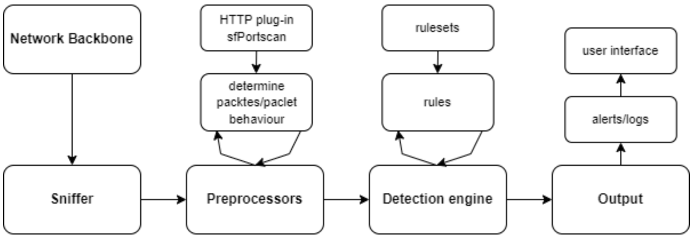

Figure 2. Snort architecture

The Snort implementation used in this paper utilizes the Boyer-Moore string matching algorithm, which is widely regarded to provide the best average-case performance of any known algorithm [10].

IV. IMPLEMENTATION OF IDS SYSTEM ON RASPBERRY PI DEVICE

One possible approach in IoT security is to place a dedicated IDS system as a common network gateway of all

IoT devices [11]. This approach is cost-effective if the number of devices is large. In case there is a single or a small number of IoT devices, the better solution is to embed the security mechanisms into it. The goal of the system implemented in this paper is to mix those two approaches.

A. Network topology

The Raspberry Pi with Snort IDS system is implemented as a common gateway for the local network, as shown in Fig. 3. In this setting, the Snort IDS protects at the same time both Raspberry Pi on which it is installed and the other devices on the local network. It is assumed that the attacker is positioned outside the network.

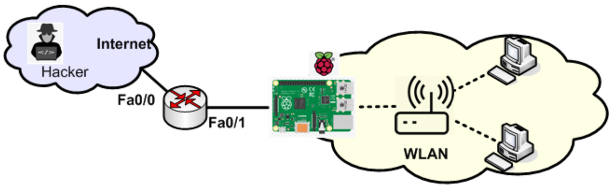

Figure 3. Network topology used for simulation

As shown in Fig. 3, the inbound and outbound traffic for the local network passes through the proposed system. In order to detect malicious traffic, we used the Snort IDS 2.9. This software comes with the rules within the malicious signatures database for packet analysis, which consists of 58219 signatures.

B. Preparation of malicious traffic

For the malicious attack simulation, we used previously prepared .pcap files that contain regular as well as malicious packets. The .pcap is the common file format for storing network traffic packets [9].

The test files are prepared by merging files that recorded normal traffic with files that recorded malicious traffic. The malicious traffic includes packets that are commonly found in known attacks. The prepared files contain the network packets which include following attacks:

DDoS (distributed denial-of-service) is a malicious attempt to disrupt the normal traffic of a targeted server, service or network by overwhelming the target or its surrounding infrastructure with a flood of Internet traffic. Flood of traffic is generated when large number of packets is sent to target IP address in order to flood the network and disrupt regular traffic [12].

DNS spoofing is a term that describes an attack where a DNS server accepts and responds to incorrect information from a host that is not authorized to get that information. DNS spoofing is malicious cache poisoning where fabricated information is stored in the name servers cache memory. On the internet 33% of all DNS servers are not immune to these types of attacks. Spoofing attacks can be root of significant security issues for devices susceptible to DNS attacks, for example users can be directed to wrong IP address of internet page, or an e-mail could be routed through mail servers which are not reliable [13].

The ZeroAccess botnet is an incredibly huge set of attacked machines, which are joined by a custom peer-to-peer protocol. They can be instructed to carry out click fraud and Bitcoin mining by the creator of botnet. Also, consequences of this type of an attack can be even more malicious activities. It can be made up of approximately 1 million attacked devices that have the potential to generate large monthly income for their creators [14].

For this simulation, files containing 10%, 20%, and 30% of malicious traffic were used. In order to highlight the difference in resource requirements, the malicious traffic is concentrated in the middle of the file (Table II). This distribution relates to the time sequence of the packets as well. File names, sizes, and malicious traffic percentages are shown in Table II.

TABLE II
Files used for the simulation

File name	File size[Gb]	Malicious packets [%]
test10.pcap	2.38	10
test20.pcap	2.33	20
test30.pcap	2.41	30

V. EVALUATION RESULTS

The proposed system is evaluated using Raspberry Pi 4 with 4GB LPDDR4-3200 SDRAM RAM, Quad core Cortex-A72 (ARM v8) 64-bit SoC @ 1.5GHz processor, Gigabit Ethernet adapter and 2.4 GHz and 5.0 GHz IEEE 802.11ac wireless Wi-Fi adapter.

During the simulation of attacks, we monitored RAM and CPU to determine resources utilization of the device to perform intrusion detection for the scenario that we prepared.

Fig. 4 displays RAM usage for the test files test10.pcap, test20.pcap, and test30.pcap, with solid, dashed, and dotted lines, respectively.

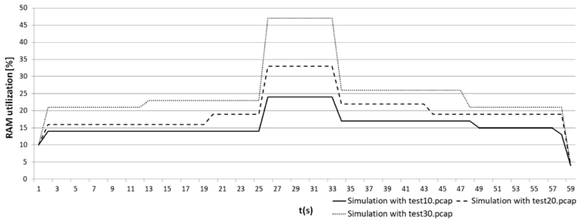

Figure 4. Utilization of RAM during simulated attack

In Fig. 4 vertical axis shows RAM utilization in percents, and the horizontal axis represents time in seconds since the beginning of the simulation. As we can see in Fig.

4, RAM utilization is the greatest around the middle of the simulation. During the simulation, the memory consumption didn't exceed 50% even in the case of 30% of malicious packets.

Utilization of CPU for test files test10.pcap, test20.pcap, and test30.pcap from Table II is given in Fig. 5.

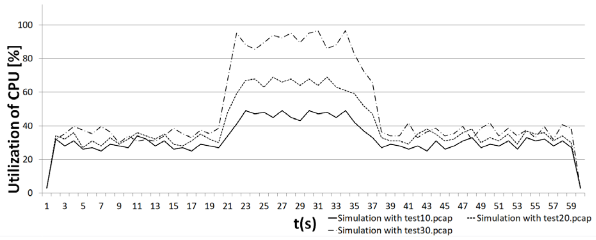

Figure 5. Utilization of CPU during simulated attack

In Fig. 5 y-axis represents CPU utilization in percent, while the x-axis represents time in seconds since the beginning of the simulation. As shown in Fig. 5, CPU utilization is the greatest in the middle of the simulation where the majority of the malicious packets are located, as was the case with the memory utilization. While varying the percentage of malicious packets we determined that the analysed device can handle up to 30% of malicious packets before reaching its CPU limits (Fig. 5).

VI. CONCLUSION

In this paper, the possibilities of the robust mainstream IDS implementation on an IoT device were explored. The implementation of the Snort IDS on Raspberry Pi 4 was given, and the performances were analysed under the simulated attack. In the simulation, malicious packets were used to evaluate the utilization of system resources. It is shown that the device can process up to 30% of malicious packets from incoming traffic, which is sufficient not only to protect itself, but others as well in most cases.

REFERENCES

[1] Van Der Spek, P. and Verhoef, C. "Balancing Time-to-Market and Quality in Embedded Systems", Systems Engineering, 17, pp. 166-192, 2014.

[2] Breitenbacher, Dominik & Homoliak, Ivan & Aung, Yan & Tippenhauer, Nils Ole & Elovici, Yuval, "HADES-IoT: A practical host-based anomaly detection system for IoT devices", Proceedings of the 2019 ACM Asia Conference on Computer and Communications Security, pp. 479-484, 2019.

[3] Dhanabal, L., and S. P. Shantharajah, "A study on NSL-KDD dataset for intrusion detection system based on classification algorithms", International journal of advanced research in computer and communication engineering, pp. 446-452, 2015.

[4] Richardson, Matt and Shawn P. Wallace, Getting Started With Raspberry Pi. Sebastopol, CA: O'Reilly Media, 2012.

[5] Raspberry Pi 4 Computer Model B, Product Details https://www.seeedstudio.com/Raspberry-Pi-4-Computer-Model-B-2GB-p-4079.html, visited 28.11.2021.

[6] Raspberry Pi 4, Specifications https://www.raspberrypi.com/products/raspberry-pi-4-model-b/specifications/, visited 28.11.2021.

[7] H. J. Liao, C. R. Lin, Y. C. Lin, K. Y. Tung, "Intrusion detection system: A comprehensive review", Journal of Network and Computer Applications, Vol. 36, Issue 1, pp. 16-24, 2013.

[8] U. Aickelin, J. Twycross, T. Hesketh-Roberts, "Rule Generalisation in Intrusion Detection Systems using Snort", International Journal of Electronic Security and Digital Forensics, Vol. 1, 2008.

[9] Vladimir Ciric, Dušan Cvetkovic, Nadja Gavrilovic, Natalija Stojanovic, Ivan Milentijevic, "Input Splits Design Techniques for Network Intrusion Detection on Hadoop Cluster", Facta Universitatis, Series: Electronics and Energetics, Vol 34, No 2, pp. 239-257, 2021.

[10] S. O. Al-Mamory, A. Hamid, A. Abdul-Razak and Z. Falah, "String matching enhancement for snort IDS", 5th International Conference on Computer Sciences and Convergence Information Technology, pp. 1020-1023, 2010.

[11] Wanjohi, Rose Wambui, and Michael Gitau Mbuguah, "Open Source IDS for a Resoure Constrained Set-Up", 2016.

[12] Douligeris, Christos & Mitrokotsa, Aikaterini, "DDoS attacks and defense mechanisms: classification and state-of-the-art", Computer networks, Volume 44, Issue 5, pp. 643-666, 2004.

[13] Singh, Simar Preet & Maini, A. Raman, "Spoofing attacks of domain name system internet", National Workshop-Cum-Conference on Recent Trends in Mathematics and Computing (RTMC), 2011.

[14] Wyke, James, "The zeroaccess botnet-mining and fraud for massive financial gain" Sophos Technical Paper, 2012.

Integrated Circuits: Evolution, Market, Challenges and Solutions

Vazgen Melikyan

Abstract - In this paper developments, occurring in integrated circuit area are observed, what challenges they lead to. Their advanced solutions are described.

Keywords – integrated circuits, IC evolution, IC market, IC challenges, IC solutions.

I. INTEGRATED CIRCUITS: EVOLUTION

It is known that the first integrated circuits (ICs) have been developed in 1958 by Robert Noice and in 1959 by Jack Kilby and contained 3-5 transistors. At present, i.e. only after 64 years, there are such ICs as Google TPUv4, Qualcomm snapdragon 865, Huawei Kirin 9000e and ARM Cortex-A78 (Fig. 1) the number of components of which is extremely large.

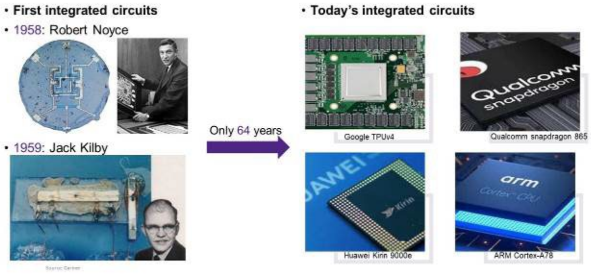

Fig. 1. Evolution of integrated circuit applications

The development of ICs, i.e. IC evolution, has been according to Moore's Law (Fig. 2) [1] who did exact prediction for IC scaling in 1965.

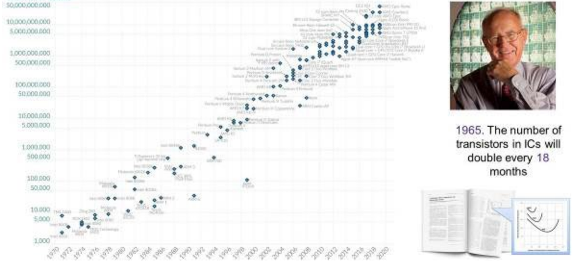

Fig. 2. Moore's Law

Due to IC scaling, the dimensions of transistors have been reduced for about 7000 times (from 20 um to 3 nm) and 4 changes in transistor type (bipolar, MOS, FinFET, GAA) (Fig. 3).

Vazgen Melikyan, Educational department, Synopsys Armenia, 41, Arshakunyats Ave., Yerevan 0026, Republic of Armenia
Email: vazgenm@synopsys.com

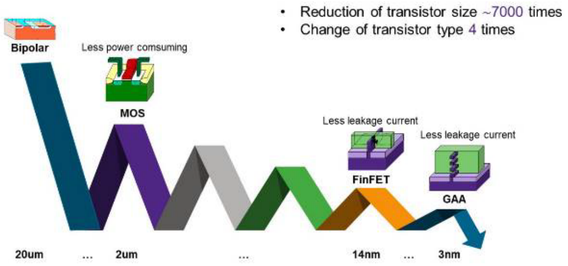

Fig. 3. IC scaling

The number of transistors have increased 18 billion times – from 3 transistors of the first IC up to 54 billion transistors for Google TPUv4 (Fig. 4).

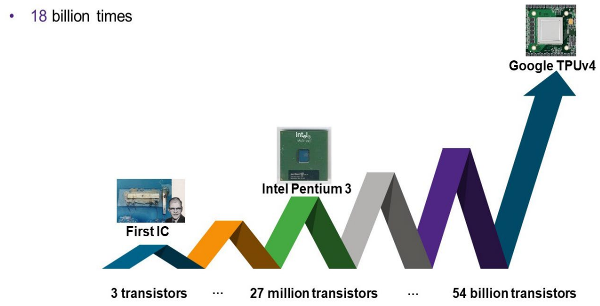

Fig. 4. Increase of Component Number

The absolute power consumption has increased 1000 times – from 2 W in the first IC to 2 kW in Huawei Kirin 9000e (Fig. 5). It is equal to the power consumption of two electrical panels.

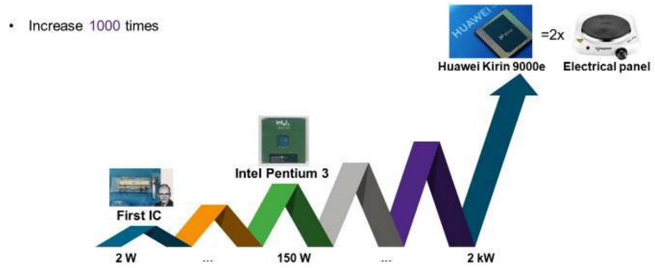

Fig. 5. Increase of Absolute Power Consumption

The specific power consumption has increased 300 times – from ~1W/cm^2 to ~300W/cm^2 (Fig. 6). It is equal to the value of neculear weapon.

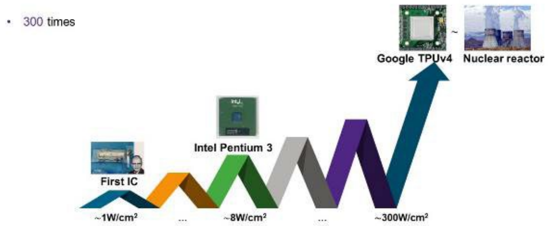

Fig. 6. Increase of Specific Power Consumption

Performance has increased for about 33 million times - from 10 KHz to 8x8x5,2 GHz.

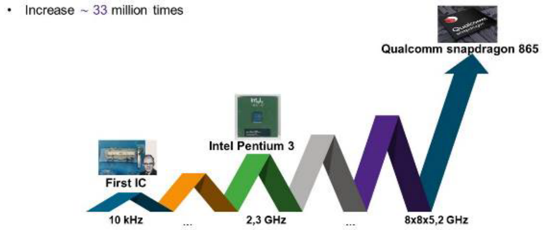

Fig. 7. Increase of Performance

IC applications have expanded. If they were used only on old computers in the past, now they are used everywhere. The most important applications are automotive and IoT (Fig. 8).

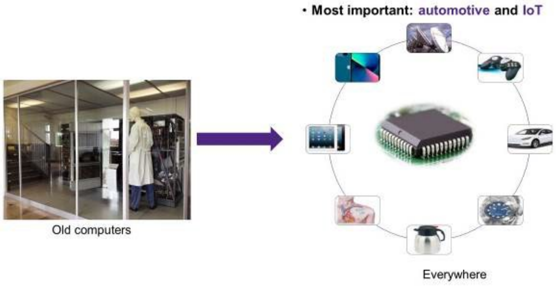

`

Fig. 8. Evolution of Integrated Circuit Applications

At present various ICs are used in automotice. Figure 9 shows only factory installed electronics. It is predicted that in 2030 50% of automotive cost will be only ICs in it.

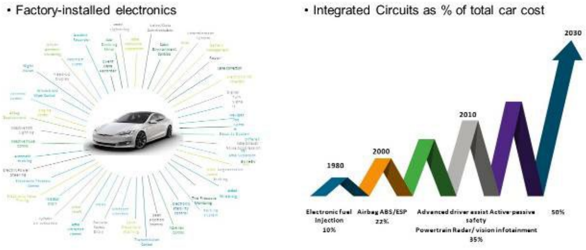

Fig. 9.Automotive Integrated Circuits

ICs are also widely applied in IoT (Fig. 10). The device number there already surpasses 50 billion.

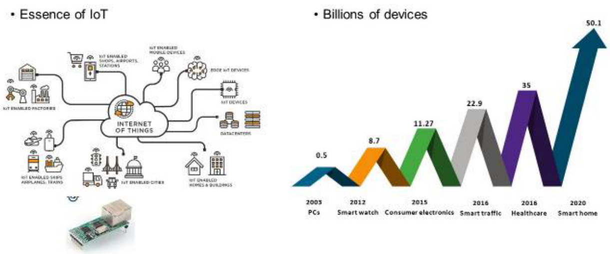

Fig. 10. IoT Integrated Circuits

So, ICs are getting more complex, power consuming, larger, faster…and this is not all.

II. INTEGRATED CIRCUITS: MARKET

IC sales revenue drastically increases and already surpassed 543 billion USD (Fig. 11).

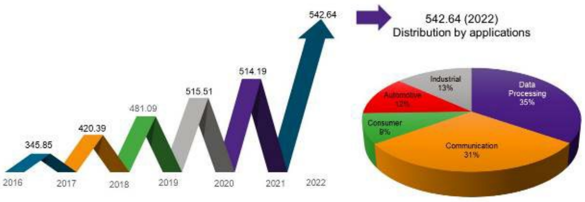

Fig. 11. Integrated circuit sales revenue (billion USD)

It is distributed by region as per Fig. 12. The largest portion is Asia Pacific.

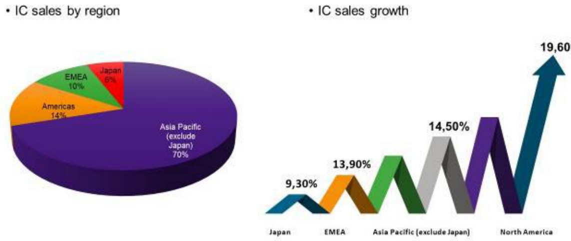

Fig. 12. Integrated Circuit Sales (2022)

IC sales distribution by sales areas is shown in Fig. 13 according to which IC Design market is 444,6 billion USD.

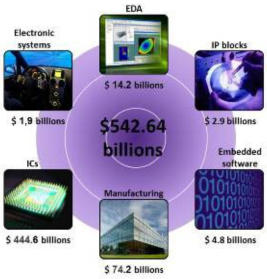

Fig. 13. Integrated Circuit Sales by Areas

IC role is becoming dominant (Fig. 14). For example, in China import IC started to surpass the crude oil.

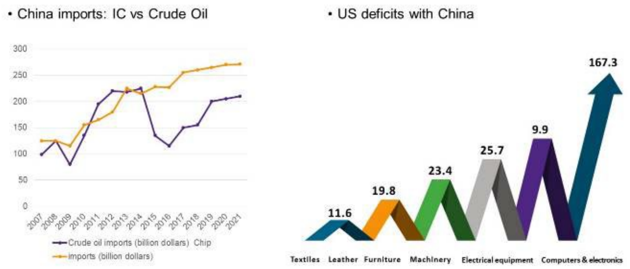

Fig. 14. Integrated Circuits Role Becoming Dominant (billion USD)

In global AI market, AI Chip Market has also become dominant (Fig. 15).

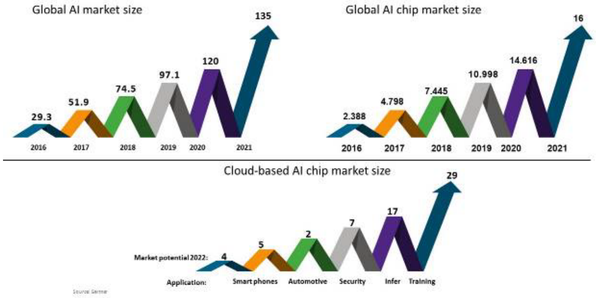

Fig. 15. Global AI and AI Chip Market (billion USD, 2022)

III. INTEGRATED CIRCUITS: CHALLENGES

All this gives rise to many challenges that can be classified by IC creation phases: fabrication, design and its automation, verification. Currently technological variations, lithography and others are dominant in IC fabrication challenges (Fig. 16).

`

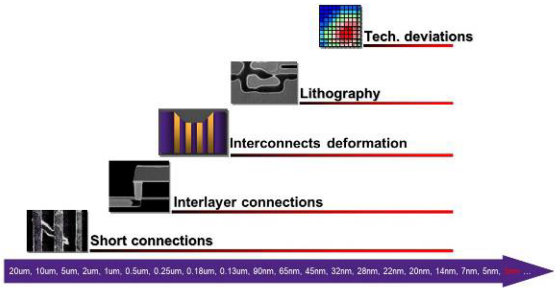

Fig. 16. Challenges in IC Fabrication

For example, lithographic challenges occur due to small sizes of IC components, starting with 90 nm technologies (Fig. 17).

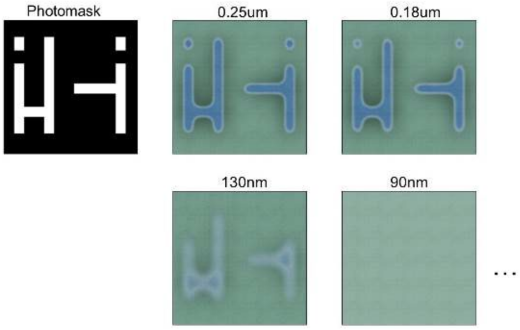

Fig. 17. An Example of IC Fabrication Challenge

Another IC fabrication challenge is connected to pitching between interconnects. For example, 64nm pitch is required on 1 metal layer but 193nm lithography can achieve only 80nm pitch (Fig. 18).

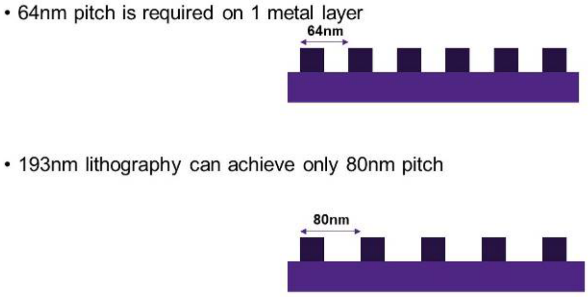

Fig. 18. An Example of IC Fabrication Challenge

Increase in the number of design rules, power consumption, etc. are important from IC design challenges (Fig. 19).

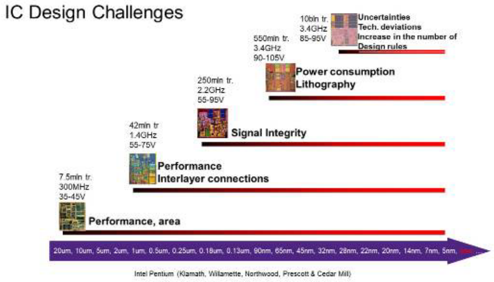

Fig. 19. IC Design Challenges

For example, in case of transition from 7 nm into 5nm technology node, design rules increase more than 10 times (Fig. 20).

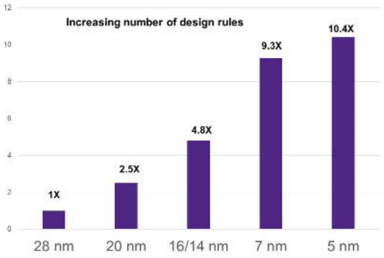

Fig. 20. An Example of IC Design Challenge

The most important challenges in IC verification are complexity, predictability, etc. (Fig. 21).

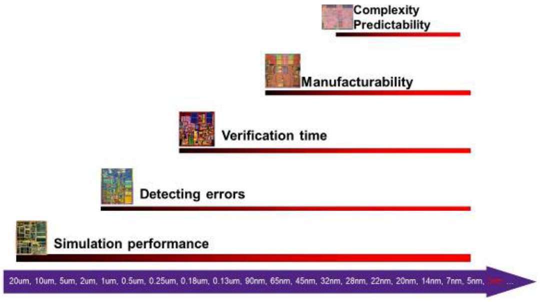

Fig. 21. Chellenges in IC Design Verification

IC scaling challenges can also be classified by type.
First, deterioration of traditional challenges occur (Fig. 22). For example, the role of signal integrity increases and the signal change in any interconnect can harm the signal of any adjacent parallel interconnect.

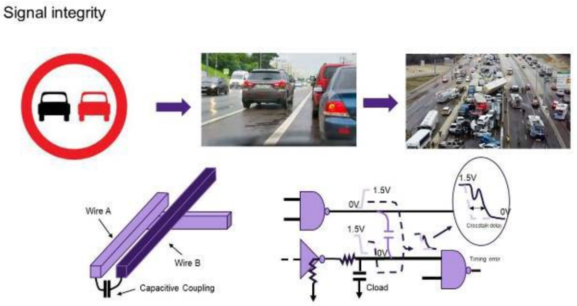

Fig. 22. Deterioration of Traditional Challenges

Another such example is the increase of the role of IR voltage drop (Fig. 23). Due to it, logic gates, connected to the same power bus from different points, get different power supply voltage (Fig. 23).

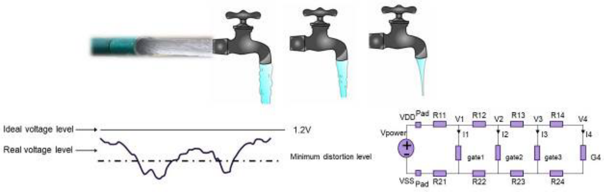

Fig. 23. Deterioation of Traditional Challenges

On the other hand, changes of ratio of traditional challenges occur (Fig. 24). For example, if in the past gate delay significantly exceeded interconnect delay, now it is the opposite. Or, for example, if static power consumption in the past was a slight part in the whole power consumption, now it has become significant.

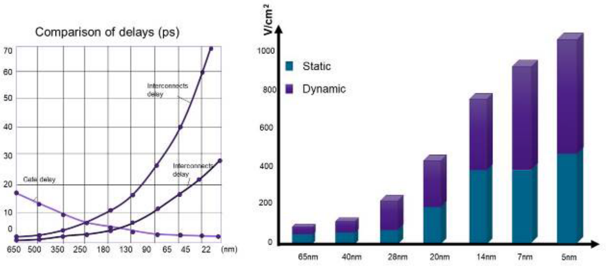

Fig. 24. Changes of Ratio of Traditional Challenges

Besides, new challenges occur of which is self heating (Fig. 25) and due to the heating of a transistor, all parameters of transistors and interconnects change.

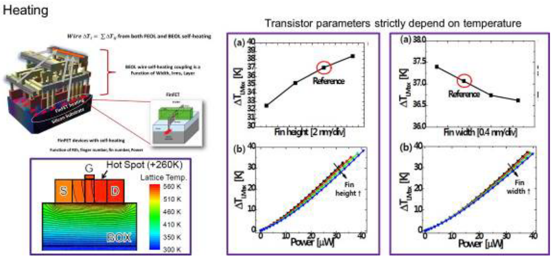

Fig. 25. Occurrence of New Chellenges

Aging is also an example of a new challenge (Fig. 26). It is when the transistor changes its parameters and properties while being used.

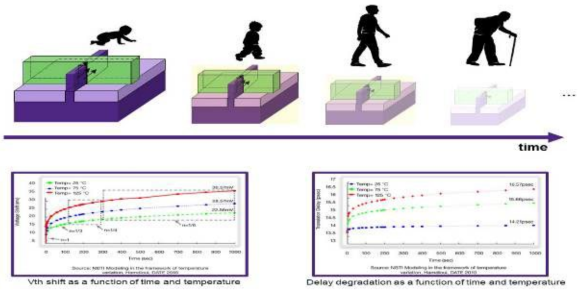

Fig. 26. Occurrence of New Chellenges

Electromigration is another example of a new challenge (Fig. 27). Due to it, breaks and short connections can occur in interconnects with time.

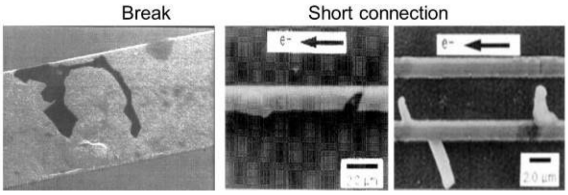

Fig. 27. Occurrence of New Chellenges

Thus, key IC challenges are: aging, power consumptions, technological variations…and this is not all.

IV. INTEGRATED CIRCUITS: SOLUTIONS

To overcome the mentioned challenges, the following advanced solutions are currently applied: usage of new transistors, double patterning, application of Artificial Intelligence (AI), low power design and 3D IC design (Fig. 28).

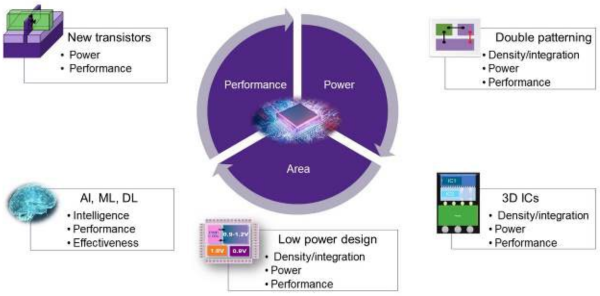

Fig. 28. Advanced Solutions

Due to disproportionate scaling, in case of even 28nm technology, transistor characteristics have deteriorated so much that necessity to develop a new transistor has risen (Fig. 29).

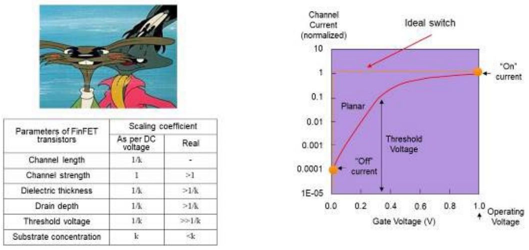

Parameters of FinFET transistors	Scaling coefficient	
	As per DC voltage	Real
Channel length	1/k	-
Channel strength	1	>1
Dielectric thickness	1/k	>1/k
Drain depth	1/k	>1/k
Threshold voltage	1/k	>>1/k
Substrate concentration	k	<k

Fig. 29. Disproportionate Scaling

In the result, planar MOS was replaced with FinFET in which the gate controls a thin body (fin) from more than one side (Fig. 30).

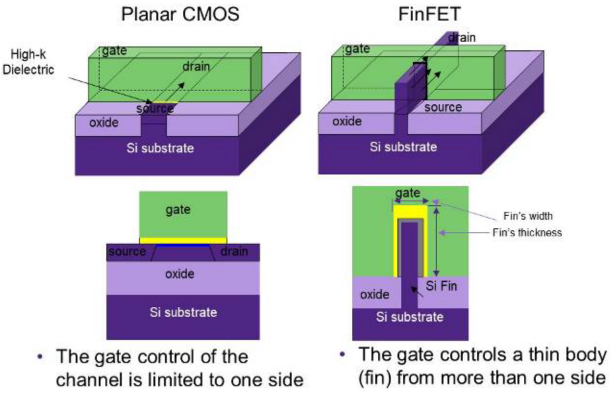

- The gate control of the channel is limited to one side
- The gate controls a thin body (fin) from more than one side

Fig. 30. Planar MOS vs. FinFET

In the result, all characteristics of FinFET are better than the ones of a MOS transistor (Fig. 31).

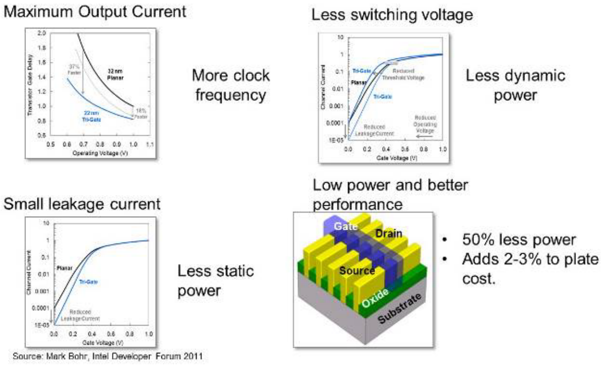

- 50% less power
- Adds 2-3% to plate cost.

Source: Mark Bohr, Intel Developer Forum 2011

Fig. 31. FinFET advantages

However, after 7nm technology node, further FinFET scaling became impossible as the width and height ratio became impermissible (Fig. 32).

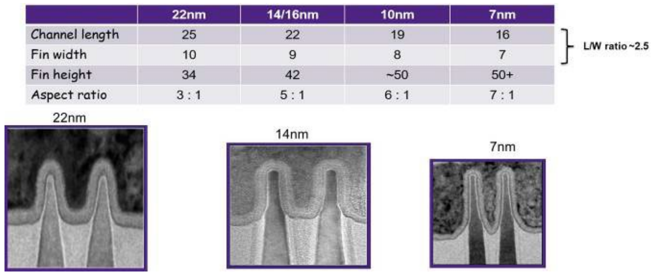

	22nm	14/16nm	10nm	7nm
Channel length	25	22	19	16
Fin width	10	9	8	7
Fin height	34	42	~50	50+
Aspect ratio	3 : 1	5 : 1	6 : 1	7 : 1

Fig. 32. Impossibility of Further FinFET Scaling

That's why Gate All Around (GAA) transistors started to be used starting with 3 nm technology (Fig. 33).

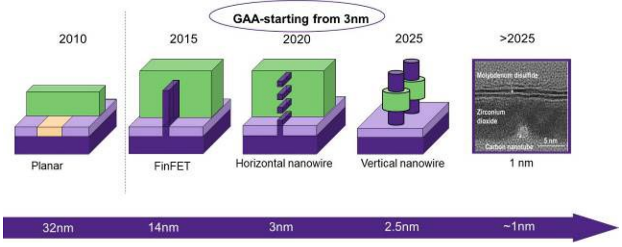

Fig. 33. Further Scaling

Another advanced solution is double/multiple patterning. It is when the interconnects that are close to one another, are fabricated in several steps (Fig. 34), using several masks.

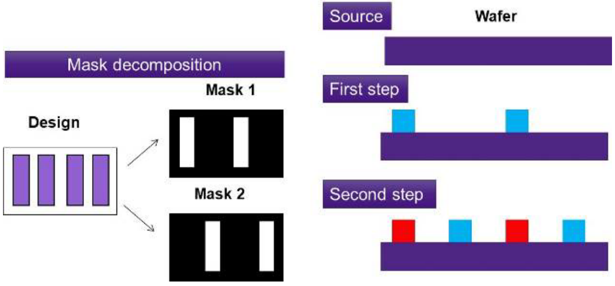

Fig. 34. Double (Multiple) Patterning

Another advanced solution is AI, Machine Learning (ML) and Deep Learning (DL) application in IC Design (Fig. 35).

Fig. 35. AI, ML and DL

AI in ICs is used in two viewpoints – in IC design and ICs are being developed that implement AI (Fig. 36).

Fig. 36. AI and Integrated Circuits

Using ML for IC design leads to more efficient results (Fig. 37).

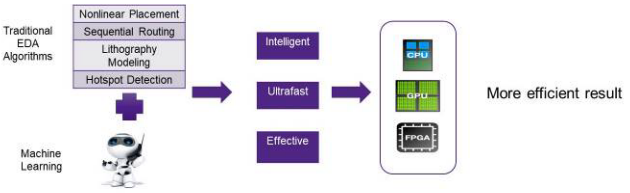

Fig. 37. Using ML for IC Design

AI IC examples are NvIdia Xavier, HSilicon Kirin, etc. (Fig. 38).

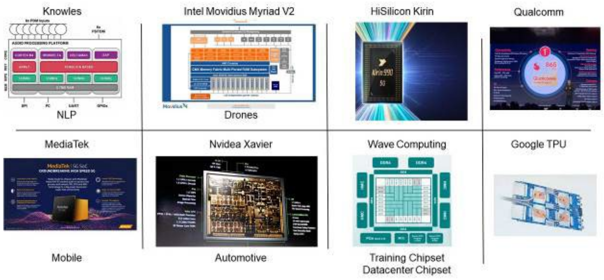

Fig. 38. AI ICs

Another advanced solution is application of 3D ICs. It is when several dies are vertically installed in one package (Fig. 39). 3D integration can save space. Memory can be separately manufactured. Short paths increase frequency.

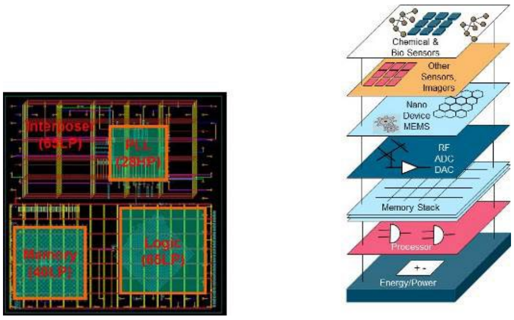

Fig. 39. 3D IC

Another advanced solution is usage low power design techniques (Fig. 40). For example, in case of multi voltage technique, IC is divided into several voltage areas that have different power supply values – the ones with high speed more, the ones with low performance – less. Usage of these techniques can significantly reduce IC power consumption.

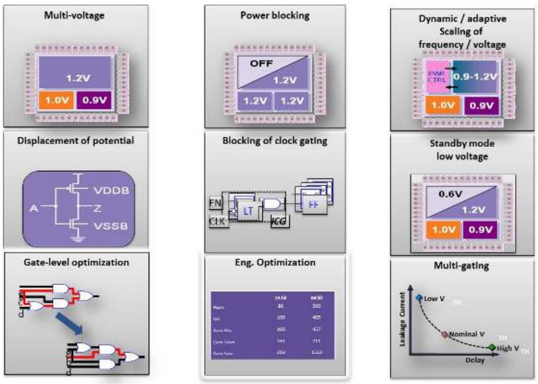

Fig. 40. Low Power IC Design

V. CONCLUSION

Changes in IC design area are carried out at rapid pace. It gives rise to many difficulties in IC design, verification and application. They constantly require advanced solutions that can overcome those challenges.

ACKNOWLEDGEMENT

My acknowledgement to my parents Shavarsh Melikyan and Siranush Hakobyan, all my tutors Archangelsky Alexei Yakovlevich, Agakhanyan Tatevos Mamikonovich, Norenkov Igor Petrovich, Rusakov Sergey Grigorievich, Petrosyants Konstantin Orestovich, famous professors who cooperated with me Vanco Litovski and Predrag Petkovic and my company Synopsys.

REFERENCES

[1] Gordon Moore., “Cramming more components onto integrated circuits”, *1065*.

Complex Autoregressive Modelling of RR Intervals

Miljan Petrović

Abstract - Estimation of power spectrum density (PSD) based on autoregressive modeling is a widely accepted approach in frequency domain analysis of RR (beat-to-beat) interval sequences. Proper model order selection is crucial for yielding an interpretable PSD. This article explores the effect of Hilbert transform of RRs on their PSD estimation. It was shown that the PSD estimate of the RR's analytic representation exhibits traits that are expected in an estimate for the actual RRs due to underlying physiological mechanisms. Therefore, it was deemed promising as a complementary source for heart rate variability measurements. Information theoretic inspection of model quality confirmed its appropriateness, whereas the complex domain exhibited more consistency across examined sequences, between the estimated PSD and the model order, reveiling a reliable framework.

Keywords - Autoregressive model, Heart rate variability, Hilbert transform, Power spectrum estimation, RR intervals.

I. INTRODUCTION

A. Motivation

Recent development of mathematical tools in signal processing has attributed to the ongoing exploration of human body regulatory mechanisms and physiological signals. Heart rate variability (HRV) analysis appears to be a promising tool for the contemporary diagnostics and assessment of risk [1]-[2]. However, the stochastic nature of biomedical signals renders the results of the analysis hard to interpret on a larger scale. Problems emerge such as validity of assumptions of stationarity, and discrepancies both in records of different subjects and records of the same subject at different times. This is why new and more reliable measures and algorithms for their analysis are still being developed [3]-[4].

One of the key approaches in the study of HRV is the analysis in the frequency domain. Since RR interval sequences (intervals between consequtive R peaks of an electrocardiogram) are considered to be stochastic signals, a common approach is to assume their stationarity and perform autoregressive (AR) modelling. Consequently, the power spectrum density (PSD) estimate is found through the model coefficients and variance of the residuals. Choosing the optimal order of the model is a task that cannot be straightforwardly automated, due to the aforementioned discrepancies between records, and often low signal quality. Though the estimated optimal order could vary a lot across different sequences, it is commonly found via minimum of the applied information criterion [5]. In most of cases, this produces satisfactory results, but still there is no assurance of appropriateness of the model, as different information criteria might suggest different choices.

In this article, we examine how transforming an RR sequence into a complex analytic signal prior to AR modelling affect the consequent PSD estimates. It was shown that certain peaks of the PSD expected by the nature of the signal are indeed only accessed with the complex transform. Furthermore, by moving into the complex domain, the framework gains some consistency due to lower variability of the optimal model order across different subjects' RR sequences.

B. Related work

Hilbert transform has been examined for the purpose of HRV analysis, but as a part of Hilbert-Huang transform [6]-[8]. Within the scope of that research, Hilbert transform is applied through an empirical mode decomposition of the signal into components that are analytic signals. On the other hand, this article is concerned on applying the discrete Hilbert transform to the original signal and afterwards, calculating the AR based PSD.

II. AR MODEL AND HILBERT TRANSFORM

An autoregressive modelling of a discrete signal $x[n]$ consists of estimating the coefficients $\alpha_{i}{}_{i}$, $i = 0,1,\dots,p$ such that

$$x[n] = \alpha_0 + \sum_{i=1}^{p} \alpha_i \, x[n-i] + \varepsilon \qquad (1)$$

for all samples of the signal. Eq. (1) reflects that a signal's value at a given moment depends linearly on its previous values in the presence of white noise ε. The model order p gives how many of the previous signal values are involved.

Along with the estimation of coefficients, the value of p is chosen to be the one which minimizes a criterion such as Akaike information criterion (AIC). If the minimum doesn't exist, a value is taken above which the criterion reaches a (low) plato. AIC is calculated as:

$$AIC = \log(\sigma_r^2) + \frac{2p}{N} \qquad (2)$$

where σ_r^2 is the variance of the model's residuals, and N is the number of samples in the signal. The residuals present the error of fitness for the model, and can be seen as the sequence which produces x after filtering through a filter with 1 in the numerator and coefficients α_i in the

Miljan Petrović is with the École Polytechnique Fédérale de Lausanne, Institute of Bioengineering, and University of Geneva, Department of Radiology and Medical Informatics, Campus Biotech, Chemin des Mines 9, Geneva, Switzerland, E-mail: miljan.petrovic@epfl.ch.

denominator of its transfer function.

The Hilbert transform $H\{x[n]\}$ of a signal $x[n]$ is a real signal $y[n]$ such that

$$y[n] = DTFT^{-1}\{\mathrm{X}(\omega)(-j{\cdot}\mathrm{sign}(\omega))\} \tag{3}$$

where $DTFT^{-1}$ denotes the inverse discrete-time Fourier transform, $\mathrm{X}(\omega)$ is the discrete-time Fourier transform of $x[n]$, ω is the angular frequency, and j is the imaginary unit. The Hilber transform adds a phase of $\pm\frac{\pi}{2}$ into every spectral component of $x[n]$ with the sign depending on the sign of that component's frequency. Then, the complex signal $u[n]$ known as the analytic representation of $x[n]$:

$$u[n] = x[n] + j{\cdot}y[n] \tag{4}$$

has Fourier spectrum equal to zero at negative frequencies. In fact, if $\mathrm{U}(\omega)$ is the Fourier transform of $u[n]$, then it holds:

$$\mathrm{U}(\omega) = \begin{cases} 2\,\mathrm{X}(\omega), & \omega > 0 \\ \mathrm{X}(\omega), & \omega = 0 \\ 0, & \omega < 0 \end{cases} \tag{5}$$

Therefore, one can easily find the analytic representation $u[n]$ by properly scaling the Fourier transform of a signal $x[n]$, removing its components at negative frequencies, and reverting back to time domain.

This article aims to compare the differences between AR modelling of signal $x[n]$ and of its corresponding analytic representation $u[n]$, in the case when $x[n]$ is an RR interval sequence. More specifically, power spectrum density (PSD) estimate of $x[n]$ and the PSD estimate of $u[n]$ are compared. The AR model is used to find PSD estimate $\mathrm{P}(\omega)$ as:

$$\mathrm{P}(\omega) = \frac{2\sigma_r^2}{f_s}|TF(\omega)|^2 \tag{6}$$

where f_s is the sampling frequency of the signal, and $TF(\omega)$ is the transfer function of the discrete AR filter $1/(\alpha_0 + \sum_{i=1}^{p} \alpha_i z^{-i})$, with $z = e^{j\omega}$.

III. ANALYSIS OF RR INTERVALS

A. Data and Preprocessing

Recordings used for analysis presented in this article are obtained from PhysioNet [9], specifically the Normal Sinus Rhythm RR Interval Database. RR interval annotations were extracted from the corresponding long-term ECG recordings (approximately 24 hours long). The presented analysis was performed on 27 recordings, 12 of which were taken from male subjects, and 15 from females. The sampling frequency of ECG recordings was 128Hz.

The first step in preprocessing the RR intervals was to remove ectopic beats by detecting outliers of the derivative of RR sequence. They are replaced with values given by spline interpolation of neighborhood samples. Consequently, interpolation was performed on the full signal length in order to derive uniformly sampled RR sequences. The sampling frequency was chosen at 2Hz so as to encompass all physiologically meaningful components of the sequences, commonly upper bounded to 1 Hz. In order to be able to assume stationarity of signals, which is necessary for AR modelling, only sections with duration of 1 minute were extracted from each interpolated record.

B. Power Spectrum Density Estimation

Power spectrum density estimates of RR sequences were based on autoregressive modeling via covariance method. Model order selection was performed by calculating the function of AIC w.r.t p. The knee point of the function was found by fitting a two-line function with the break point at the position which minimizes the error of the fit. The order of the model corresponding to the knee point is considered optimal, since increasing it above that point leads to no significant decrease of AIC.

Further, analytic representations of RR sequences were derived using Hilbert transform and Eq. (4). AR models and PSD estimates of these were also found for all provided sequences. The knee point method on AIC suggested optimal orders in the range from 24 to 31. These values tend to overfit data when it comes to RR intervals, which usually tend to be optimally modelled by orders up to 15. For this reason, and to counterbalance the double complexity as compared to real sequences, the orders were fixed to half the size of the ones optimal for the actual RRs. A useful phenomenon was then observed (Fig. 1). It is expected that a higher model order yields more peaks in the shape of PSD. However, a certain variance of the number of peaks is still present across subjects with the same model order. It turned

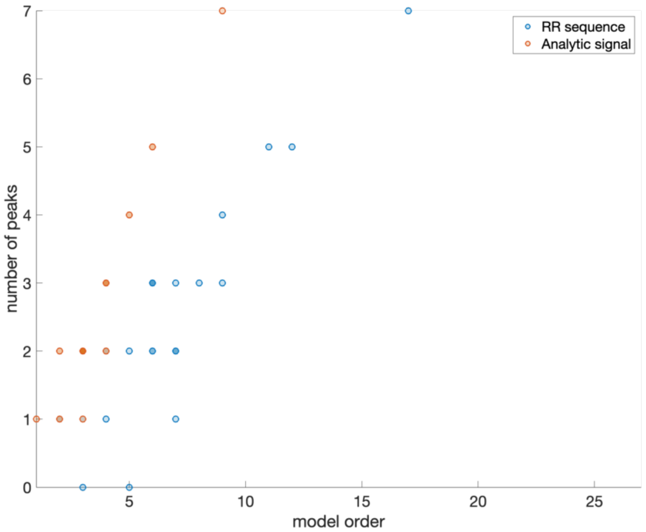

Fig. 1. The number of peaks of PSD and order of AR models of all 27 subjects for the real RR sequence (blue) and their analytic representations (red). Higher opacity of the color indicates there are more subjects with the same pair of the two parameter values

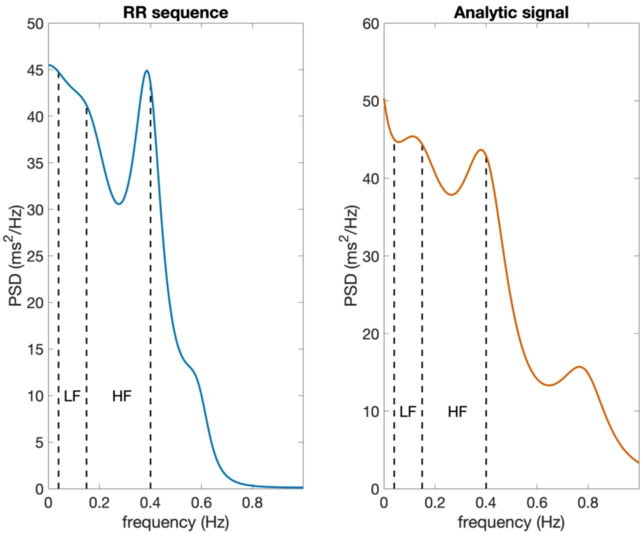

Fig. 2. The PSD estimates of RR sequence (blue, $p = 7$) and its analytic signal (red, $p = 4$) for subject no. 9

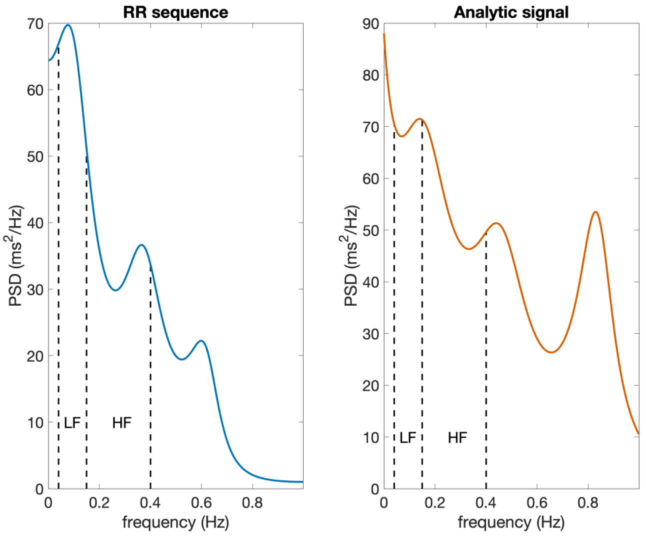

Fig. 4. The PSD estimates of RR sequence (blue, $p = 6$) and its analytic signal (red, $p = 4$) for subject no. 18

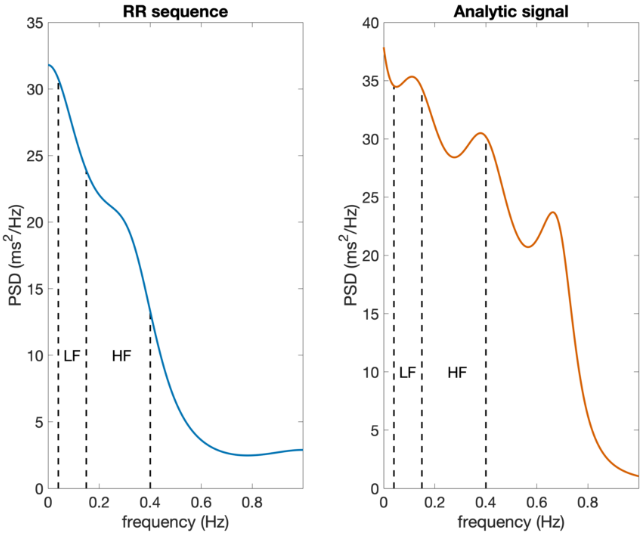

Fig. 3. The PSD estimates of RR sequence (blue, $p = 3$) and its analytic signal (red, $p = 4$) for subject no. 27

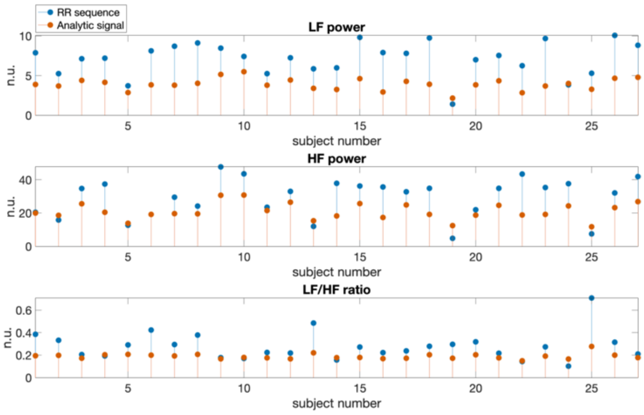

Fig. 5. LF and HF power and LF/HF ratio from PSD of RRs (blue) and their analytic signals (red), for all subjects

out this variance is lower for PSDs of analytic signals as compared to real, and a stronger linear trend emerges between the number of peaks and the order, for $p \geq 3$. In fact, the number of peaks is either equal to $p - 1$ or $p - 2$.

This relation is beneficial since a priori knowledge of signals is present. Indeed, one might expect three peaks in PSD of RR intervals, one in LF (low frequency) range (sympathetic modulations), one in HF (high frequency) range (parasympathetic activity) and one reflecting respiration [10]. In order to consistently model these, the final p of the AR models of all complex RRs was fixed to 4.

Power spectrum density estimates are shown in Figs. 2, 3 and 4, for three different subjects. In Fig. 2, PSD of real sequence shows one prominent peak in HF area, but not in LF. However, the PSD based on the analytic representation has three highly distinct peaks, which makes it easier to pinpoint the dominant frequency in the LF area. The same observation can be made in Fig. 3, where even in the HF area there is only a lump instead of a peak for the real sequence. However, if there is already a meaningful PSD produced by the real RRs, the analytic representation might be detrimental to the estimate. In the case of Fig. 4, the estimate clearly shows one peak in LF and one in HF region, plus one smaller just below 0.6 Hz (which might be a result of fast respiration). The corresponding PSD estimate of the analytic representation pushes both peaks to higher frequencies, with the one that was in HF area now located above the standard limit of the range (0.4 Hz). Morover, there is a big peak around 0.8 Hz, and the power of other spectral components in this area (above 0.4 Hz) is boosted. Certain explanations for the power in this range exist, such as the one noting that HF peak can be shifted to frequencies up to 1.04 Hz in case of exercise [11]. However, the data here is representing normal sinus rhythm, and one should expect low power and no peaks in this range [10]. This emphasizes the importance of examining both real and complex sequences, and in relation to the nature of the recording.

HRV measurements were extracted from these PSDs: the power in LF band (0.04 Hz to 0.15 Hz), power in HF band (0.15 Hz to 0.4 Hz), and LF/HF ratio of the powers. These measurements indicate levels of sympathetic and vagal modulations, and also sympatho-vagal balance or more complex mechanisms [12]. Even though the ratio is calculated with values of power in ms^2, those are afterwards converted into normalized units, and represent the percentage of the power in the relevant range within the power over all frequencies above 0.04 Hz. Normalization allows for a proper comparison between the two PSD estimates for the same subject.

The values obtained for both cases of AR modelling are different but exhibit mid-to-high correlation across the subjects (Fig. 5). Those are 0.61, 0.77, and 0.89 for LF power, HF power and LF/HF ratio, respectively. This means that even though the values of HRV measurements differ, the analytic signal still provides useful information on human body regulatory systems as RR sequences do. Due to observed correlation, one might resort to the already affirmed power measurements made on the real sequences. However, note that the markers such as PSD peak height or location might be accessed by one of the two approaches – analysis of real sequence, and analysis of analytic signal – but not necessarily by both.

Finally, quality of derived AR models was assessed. Note that AIC is calculated using the absolute value of the residual variance in the case of complex sequences. For all but 3 subjects, AIC is lower when analytic representation is used. The difference between criteria has the mean 1.28 and variance 0.75. It is confirmed that this result is not reached solely due to lower model order, since variances of residuals are also lower for complex sequences in most subjects. Though this might suggest that AR model of an analytic representation is a better fit than that of an actual sequence, one still needs to consider the specific traits of both PSDs for a proper analysis, as shown in Figs. 2, 3 and 4.

IV. CONCLUSION

Frequency domain analysis of RR sequences and their analytic representations derived by the discrete Hilbert transform showed the alternative way of accessing HRV measurements. Indeed, the physiological meaning of those is not disturbed by moving into the complex domain, whereas additional traits of PSDs can be explored. One of the main advantages of analytic signals is that they seem to provide more control over the shape of PSD by means of model order, at least in the case of RR sequences.

Beyond the scope of this article, theoretical work should be done regarding the link between AR models of a signal and its analytic representation. This might shed light onto the observed lower variability of the optimal order of the complex model. Furthermore, the presented analysis is limited to frequency domain HRV measurements, and normal sinus rhythm RR intervals. The time-domain measurements need to be properly adjusted for the complex nature of the analytic signal, whereas a larger dataset, including recordings of an abnormal heart rate, is needed to confirm the diagnostic use of the described approach.

REFERENCES

[1] Wang, Y., et al., “HRV complexity as a diagnostic tool for late onset sepsis in sick premature infants,” *8th IEEE Conf. on BioInformatics and BioEngineering*, Athens, pp. 1-6, Oct. 2008.

[2] Melillo, P., De Luca, N., Bracale, M., Pecchia, L., “Classification tree for risk assessment in patients suffering from congestive heart failure via long-term heart rate variability,” *IEEE J. Biomed. Health Inform.*, vol. 17, no. 3, pp. 727-733, May 2013.

[3] Thong, T., et al., “Accuracy of ultra-short heart rate variability measures,” *Proceed. Of the 25th Annual Int. Conf. of the IEEE*, vol. 3, pp. 2424-2427, Sep. 2003.

[4] Vollmer, M., “A robust, simple and reliable measure of heart rate variability using relative RR intervals,” *Computing in Cardiology Conference*, Nice, pp. 609-612, Sep. 2015.

[5] Giurcaneanu, C.D., Razavi, S.A., “Ar order selection with information theoretic criteria based on localized estimators,” 16th European Signal Processing Conference, Lausanne, pp. 1-5, August 2008.

[6] Li, H., Yang, L., Huang, D., “Application of Hilbert-Huang transform to heart rate variability analysis,” *2nd Int. Conf. on BioInformatics and Biomedical Engineering*, Shanghai, pp. 648-651, May 2008.

[7] Li, H., Kwong, S., Yang, L., Huang, D., Xiao, D., “Hilbert-Huang transform for analysis of heart rate variability in cardiac death,” *IEEE/ACM Trans. Comput. Biol. Bioinf.*, vol. 8, no. 6, pp. 1557-1567, Nov. 2011.

[8] Hsu, C.M., et al., “Heart rate variability signal processing for safety driving using Hilbert-Huang transform,” *Int. Symp. on Computer, Consumer and Control*, Taichung, pp. 434-437, June 2014.

[9] Goldberger, A.L., et al., “PhysioBank, PhysioToolkit, and PhysioNet: Componentsof a new research resource for complex physiologic signals,” *Circulation*, vol. 101, no. 23, pp. 215-220, June 2013.

[10] Task Force of The European Society of Cardiology, The North American Society of Pacing and Electrophysiology, “Heart rate variability: Standards of measurements, physiological interpretation, and clinical use,” *European Heart Journal*, vol. 17, pp. 354-381, Mar. 1996.

[11] Berntson, G.G., et al., “Heart rate variability: origins, methods, and interpretive caveats,” *Psychophysiology*, vol. 34, no. 6, pp. 623-648, Nov. 1997.

[12] Billman, G.E., “The LF/HF ratio does not accurately measure cardiac sympatho-vagal balance,” *Front. Physio.*, vol. 4, pp. 1-5, Feb. 2013.

Design of IIR bandstop filters with approximately linear phase

Goran Stančić, Ivana Kostić and Petar Stančić

Abstract – In this paper three different bandstop filters with approximately linear phase configurations are analyzed. The first proposed configuration has parallel nature with pure delay in one path and corresponding allpass filter in the another. The second examined filter has two IIR allpass filters in parallel with same transfer function order as first solution. The design algorithms are explained in details. Elliptic filter with phase corrector is compared with first two solutions. Hardware complexity of all desribed filters is also inspected.

Keywords **–** Bandstop filter**,** allpass filter, parallel connection, approximately linear phase, elliptic filter, phase corrector, hardware complexity.

I. INTRODUCTION

Bandstop filter rejects the particular range of frequencies of input signal. The bandstop filter are used in telephone technology to reduce noise and provide DSL internet services, in communication systems to reduce signal distortion, in audio and radio applications, in biomedical devices... They can be obtained as FIR or IIR structures [1-4]. Design of bandstop and bandpass filters remains actuel till nowadays [5]. Multilevel and multiphase systems require filters that have flat phase delay i.e. the linear phase in the passband to preserve pulse integrity in the time domain, giving less intersymbolic interference than other kinds of filters [6].

Special case of bandstop filter is a notch filter with narrow rejection band [7]. Proposed algorithm could be modified and applied to notch filter design. In many practical applications linear phase of filter is preferable characteristic [8-10].

The rest of the paper is structured as follows. In the Section II, the basic relations are derived between allpass filter phase and stopband filter magnitude and a method for determination of filter coefficients is described. Obtained results are presented in Section III. The result of alternative allpass solution is given in Section IV and equalized elliptic filter in Section V. Complexity of all considered filters is analyzed in Section VI.

The authors are with the Dep. of Electronics, University of Niš, Faculty of Electronic Engineering, Aleksandra Medvedeva 14, 18000 Niš, Serbia, E-mail: ivana.kostic@elfak.ni.ac.rs.

II. PROBLEM DEFINITION

In this section filters design procedure will be discussed. Selective filters could be obtained by structure given in Fig.1.

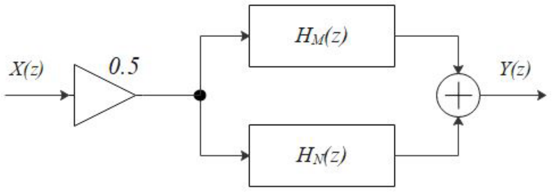

It is well known that selective filters could be realized using parallel connection of two unselective allpass filters. The transfer function of the proposed bandpass filter can be written in the next form

$$H(\mathrm{z})=\frac{1}{2}\left[H_M(\mathrm{z})+H_N(\mathrm{z})\right] \tag{1}$$

where M and N represent allpass filters order. Allpass filter has magnitude equal to one at all frequencies and phase

$$\begin{aligned}&\varphi_M(\omega)=-M\omega+\\&2\,\mathrm{atan}\,\frac{a_1\sin\omega+\cdots+a_M\sin M\omega}{1+a_1\cos\omega+\cdots+a_M\cos M\omega}\end{aligned} \tag{2}$$

The magnitude of resulting filters is given with

$$\left|H(\mathrm{e}^{j\omega})\right|=\left|\cos\frac{\varphi_M(\omega)-\varphi_N(\omega)}{2}\right| \tag{3}$$

while resulting phase has value

$$\varphi_H(\omega)=\frac{\varphi_M(\omega)+\varphi_N(\omega)}{2} \tag{4}$$

It is obvious from eq. (3) that design of desired magnitude will be replaced with a design of adequate allpass phase. If the passband filter linear phase is a final goal, from eq. (4) we conclude that simplest way to achieve that is to use the allpass filters with linear phase. Minimal complexity will be achieved choosing one allpass filter to be pure delay i.e.

$$H_N(z) = z^{(-N)}, \quad \varphi_N(\omega) = -N\omega \tag{5}$$

The phase of real coefficients allpass filter of order M starts at $\omega = 0$ with value $\varphi_M(0) = 0$ and ends at $\omega = \pi$ with $\varphi_M(\pi) = -M\pi$. The phase is monotonically decreasing function of frequency. The bandstop filter has passband region at low frequencies. According to eq. (3) to achieve unity magnitude, phase $\varphi_M(\omega)$ need to has the same value as $\varphi_N(\omega)$ in ideal case. To realize stopband at middle frequencies, the phase jump of π radians is necessary to provides and another π radians jump for second passband at high frequencies. It means that stable IIR allpass filters could provide such a phase if its order is $M=N+2$. For narrow transition zones one need sharp phase jumps of π radians, so the second allpass filters phase approximates the ideal linear phase of slope $-N$ in all bands, to reach value $\varphi_M(\pi) = -M\pi$. According to the eq. (4) obatined filter would have linear phase in both passbands and stopband. Of course the value of phase in stopband is not of interest but given structure offers to realize the complementary filter

$$G(z) = \frac{1}{2}\left[H_M(z) - H_N(z)\right] \tag{6}$$

at cost of only one additional adder (subtractor). This filter has magnitude and phase given with

$$\left|G\left(e^{j\omega}\right)\right| = \left|sin\frac{\varphi_M(\omega) - \varphi_N(\omega)}{2}\right| \tag{7}$$

$$\varphi_G(\omega) = \frac{\varphi_M(\omega) + \varphi_N(\omega) + \pi}{2}. \tag{8}$$

Hence the both complementary filters have linear phase in all bands and don't demand the phase correctors.

To obtain bandstop filter one need to determine allpass filters coefficients that in ideal case holds

$$\varphi_M(\omega) = \begin{cases} -N\omega, & 0 \le \omega \le \omega_{b1} \\ -N\omega - \pi, & \omega_{b1} < \omega \le \omega_{b2} \\ -N\omega - 2\pi, & \omega_{b2} < \omega \le \pi \end{cases} \tag{9}$$

where ω_{b1} and ω_{b2} represent boundary frequencies between adjacent bands. The real filters have finite tranzition zones defined with two boundary frequencies (ω_{pi} – passband edge and ω_{si}– stopband edge) instead of one ω_{bi}. For given minimal attenuation a in dB, from eq. (3) maximum allowed phase approximation error could be determined

$$\varepsilon = 2\arcsin(10^{-a/20}) \tag{10}$$

for every band independently. Hence pure delay do not contribute to total error, equiripple phase error function will lead to equiripple magnitude of bandstop filter.

The allpass filters coefficients will be obtained by solving

$$\varphi_M(a_k, \omega_i) - \varphi_N(\omega_i) = (-1)^{p+i}\varepsilon \quad i = 1, \ldots, M \tag{11}$$

where parameter p has value 1 or 0 and determine first extremum to be maximum or minimum, respectively. For allpass filter with pure complex poles system of equations (11) becomes

$$\begin{aligned} \varphi_M(a_k, \omega_i) + K\omega_i &= (-1)^{1+i}\varepsilon_1 \quad & i = 1, \ldots, m_1 \\ \varphi_M(a_k, \omega_i) + K\omega_i + j_1 &= (-1)^{i}\varepsilon_2 \quad & i = 1, \ldots, m_2 \\ \varphi_M(a_k, \omega_i) + K\omega_i + j_2 &= (-1)^{i}\varepsilon_3 \quad & i = 1, \ldots, m_3 \end{aligned} \tag{12}$$

where m_1 and m_3 are odd while m_2 is even number, and $m_1 + m_2 + m_3 = M$. Frequencies ω_i corresponds to locations of phase error extrema and j_1 and j_2 are phase jumps with value π and 2π radians in last iteration, respectively. First m_1 and last m_3 extrema are from the passbands while m_2 extrema belong to the stopband. In order to solve (12) function $\varphi_M(a_k, \omega_i)$ will be replaced with truncated Taylor series expansion

$$\varphi_M(a_k, \omega_i) = \varphi_M(a_k^*, \omega_i) + \sum_{k=1}^{M} \frac{d\varphi_M}{da_k}\Delta a_k \tag{13}$$

where a_k^* are coefficients values from previous iteration. Coefficients correction stops when maximum increment is small enough (we chose $max|\,\Delta a_k\,| < 10^{-10}$). For first iteration, starting a_k^* values are obtained by placing allpass filters poles at circle inside unit circle (for all filters order convenient value for poles module is $\rho_k = 0.95$) regularly distributed ($\theta_k = \pm\frac{(2k-1)\pi}{M}, k = 1, \ldots, M/2$). Such poles make phase to approximate ideal linear phase of slope $-M$ (at all frequencies i.e. $[0,\pi]$) with equiripple nature and an error which depends only on poles distance from the unit circle. To reach final slope $-N$ in L steps ($l = 1, 2, \ldots, L.$, in all examples we chose L=5) in l^{th} step ideal linear phase in eq. (12) has slope

$$K = M - \frac{l}{L}(M - N). \tag{14}$$

with appropriate phase jumps

$$j_1 = \frac{l}{L}\pi, \qquad j_2 = \frac{2l}{L}\pi. \tag{15}$$

The phase errors are also controled and converge linearly to final values

$$\varepsilon_i = \varepsilon_{starti} - \frac{l}{L}\left(\varepsilon_{starti} - \varepsilon_{finali}\right), \; i = 1, 2, 3. \tag{16}$$

The approximation error depends on bandwidth and number of poles dedicated to that band.

Even a low order filter can approximate wide band if desired error is big enough. The bandstop filter has two passbands and one stopband. If the given final values for the phase error are too big, approximation bands will overlap making the algorithm to diverge. To avoid such a problem small final values for the phase error are preferable. The smaller errors lead to wider tranzition zones but guarantee convergence. Respecting the given final errors, obtained stopband filter has predefined attenuations in all bands and tranzition zones width depends on filters order and poles distribution. Desribed method can be given in matrix form

$$\mathbf{A}\boldsymbol{\Delta} = \boldsymbol{\beta} \tag{17}$$

where a_{ij} elements of matrix $\boldsymbol{A}$ are

$$\begin{aligned} a_{ij} &= 2\frac{P}{Q} \\ P &= \sin j\omega_i\left(1 + a_1\cos\omega_i + \ldots + a_M\cos M\omega_i\right) - \\ &\quad \cos j\omega_i\left(a_1\sin\omega_i + \ldots + a_M\sin M\omega_i\right) \\ Q &= \left(1 + a_1\cos\omega_i + \ldots + a_M\cos M\omega_i\right)^2 + \\ &\quad \left(a_1\sin\omega_i + \ldots + a_M\sin M\omega_i\right)^2 \end{aligned} \tag{18}$$

elements b_i of column vector $\boldsymbol{\beta}$ are

$$b_i = -\varphi_M\left(a_k^*, \omega_i\right) - K\omega_i + \left(-1\right)^{1+i}\varepsilon_1, \quad i = 1,\ldots,M \tag{19}$$

$$\boldsymbol{\Delta} = [\Delta a_1, \Delta a_2, \Delta a_3, \ldots, \Delta a_M]^T \tag{20}$$

III. EXAMPLES

The efficiency of prorposed method will be demonstrated on design of bandstop filter with attenuation of $a = 40$ dB ($\varepsilon_2 = 0.02$ rad, according to eq. (10)) for $N = 8$ and $M = 10$ with $m_1 = 5, m_2 = 2$ and $m_3 = 3$. The passband of one is the stopband of the complementary filter. If one needs the both filters it is convenient to define phase error in passband using information about minimal attenuation in stopband of complementary filter. Value $a = 55$ dB is chosen ($\varepsilon_1 = \varepsilon_3 = 0.0036$ rad what corresponds to $a = 1.37 \cdot 10^{-5}\ dB$ in passband of complementary filter). Attenuation of obtained stopband filter is shown in Fig.2. in blue color. Equiripple nature of attenuation in passbands is evident from red color characteristic with scale shown at right part of Fig. 2.

In case the both complementary filters are designed, as in this example, the passband attenuation is extremely small. The small phase errors require poles with small magnitude as shown in Fig. 3. Only poles which provide phase jump of π radians between two bands are closer to the unit circle. Bandpass edge frequencies are $\omega_{p1} = 0.401\pi$ and $\omega_{p2} = 0.813\pi$ while stopband boundaries are $\omega_{s1} = 0.564\pi$ and $\omega_{s2} = 0.653\pi$.

Phase of both allpass filters are displayed in Fig. 4. Corresponding passband filter attenuation is shown in Fig. 5. Maximum attenuation in passband has value $4.34 \cdot 10^{-4}$ dB as displayed in black color in Fig. 5.

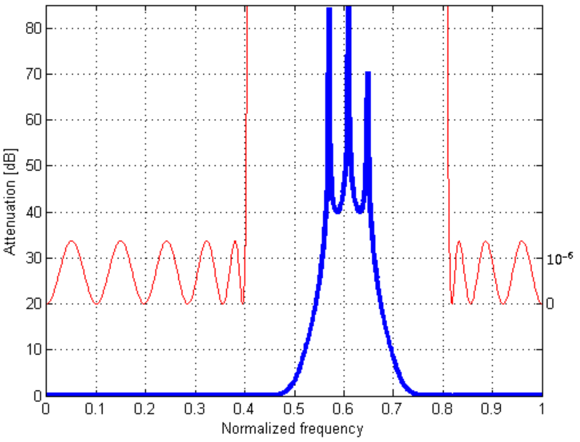

$N = 8$ and $M = 10$.

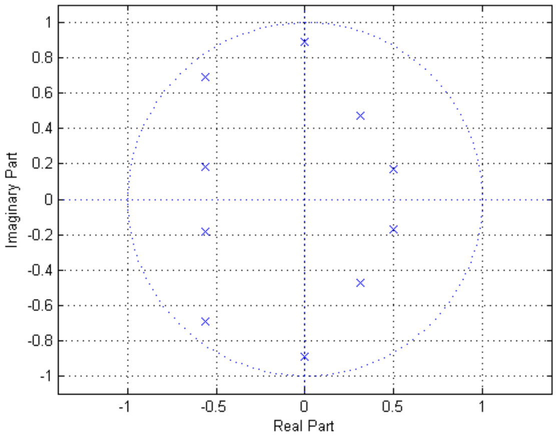

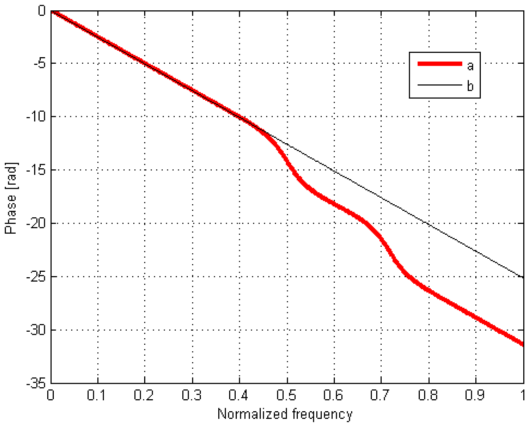

of allpass filter $H_M(z)$ a) and $H_N(z)$ b).

To achieve approximately the same phase errors in all bands it is necessary to fulfill

$$\frac{\omega_{p1}}{m_1} = \frac{\omega_{s1} - \omega_{s1}}{m_2} = \frac{\pi - \omega_{p2}}{m_3} \qquad (17)$$

Equation (21) is good starting point to determine number of poles in each band for given bands edges.

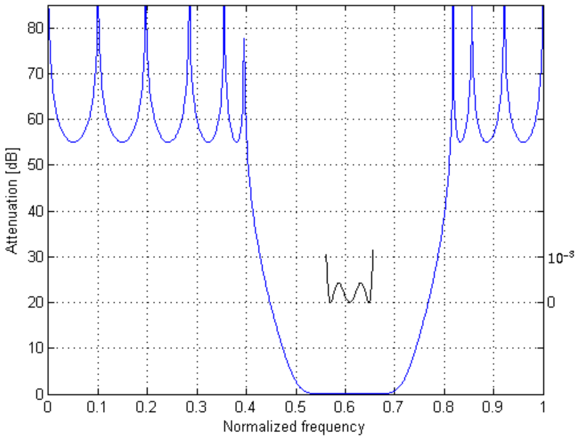

of passband filter for $N = 8$ and $M = 10$.

IV. ALTERNATIVE SOLUTION

The stopband filter can be also obtained with parallel allpass structure where filters are of same order K. To achieve transfer function of same order as in already explained example, $K = 9$ is chosen with $m_1 = 4, m_2 = 5$ for one, and $m_1 = 7, m_2 = 2$ for another allpass filter. Now both filters contribute to the final error. To obtain filter with same attenuations in worst case, described method will be applied with halved errors $\left(\frac{\varepsilon_1}{2} \text{ and } \frac{\varepsilon_3}{2}\right)$. Attenuation of obtained filter is displayed in Fig. 6. alongside with previous example.

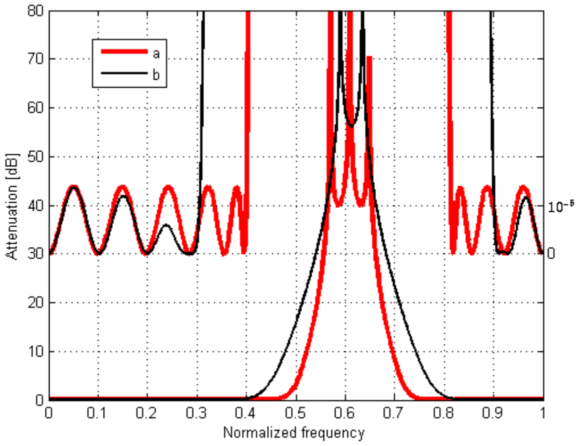

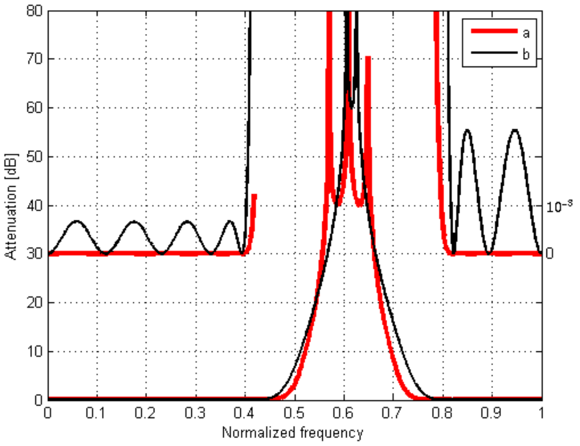

Unlike first example which always give eliptic-like magnitude this solution has minima and maxima with different values. To compare two solutions we will recalculate last filter in order to get the same passband edges. For that purpose system of equations (12) is modified incorporating passband edge frequencies in vector of extrema. Widening of approximation bands cause the errors to increase as shown in Fig. 7. Now attenuation in passbands have values $6.6 \cdot 10^{-4}$ dB and 0.0025 dB. This values are not critical for stopband filter but if one needs passband filter also to realize, this values unambiguously determine minimal attenuation in stopband which value will be 38.16 dB and 32.32 dB, respectively. Phase of allpass filters are shown in Fig. 8.

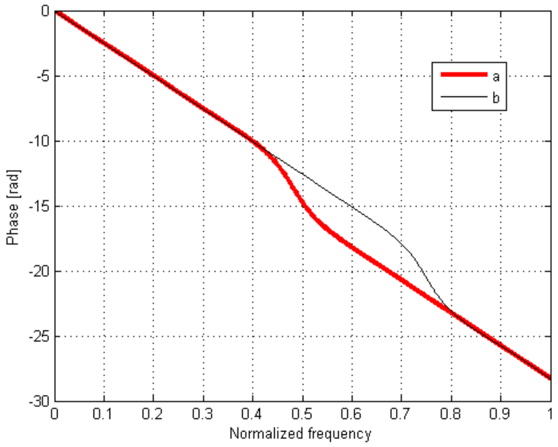

Design of allpass filters now control two erros but resulting filter has three bands. To guarantee 55 dB attenuation in stopband ε_1 and ε_3 are adequately determined. This two errors define stopband attenuation of complementary filter and it is the reason that in Fig. 6 value has to be at least 55 dB (it is not feasible to obtain 40 dB).

To get desired band edges one allpass filter is corrected in first and another in second band. Spreading of approximation band cause error significantly to increase. The error of another allpass filter in the same band remain small and it is the reason why in Fig. 7 characteristic b) looks like equiripple. Resulting filter again is of order 18 but both allpass filters are of IIR type and demand double number of multipliers affecting the total consumption.

V. EQUALIZED ELLIPTIC FILTER

The given magnitude specifications are fulfilled with eliptic filter of order N=10. The parallel allpass configurations have approximately linear phase and constant group delay $\tau = 8$ with passband error less than 0.03 samples, except near edge frequencies. Group delay error in stopband is 0.2 samples as shown in Fig. 9. Eliptic filter has nonlinear phase and need phase (group delay) corrector to be compared with given allpass solutions. It is known that phase corrector could be more complex than filter itself. In Fig. 10 is diplayed group delay of eliptic filter itself in red color, and group delay after equalization. The bandpass filter has narrow band that corrector of order 10 was enough to provide better result compared to bandstop filter with corrector of order 30. Maximum group delay approximation error has value 2.77 with average value 31.74, at low frequencies and 2.8 error with average value 37.13 samples at high frequencies for bandstop filter.

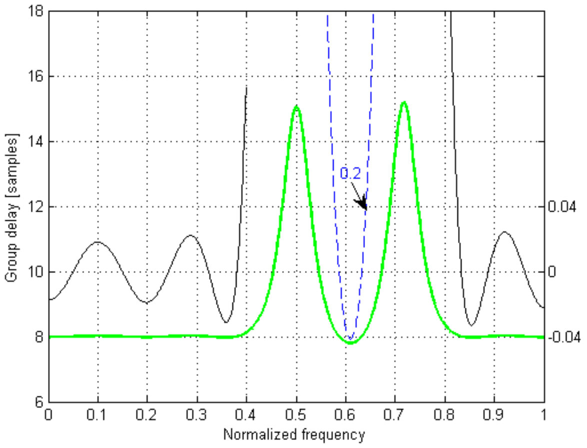

Fig. 9. Group delay of allpass based stopband filter

The bandpass filter has average group delay 54.91 with approximation error less than 1.66 samples. Elliptic filter provide narrow tranzition zones but including the phase (group delay) correctors complexity of such a solution is significantly higher if the same phase (group delay) error is the goal.

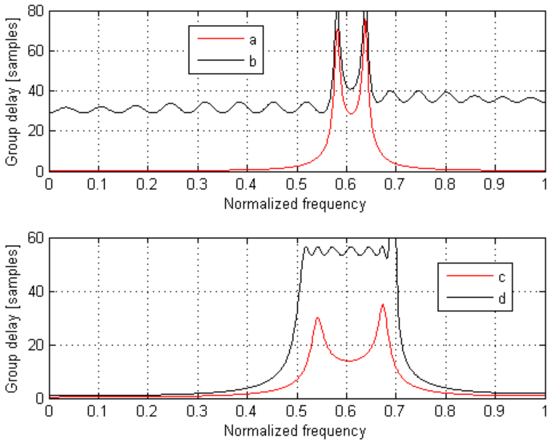

Fig. 10. Group delay of: a) eliptic bandstop filters of order 10; b) uqualized group delay with corrector of order 30; c) bandpass filters of order 10 and d) uqualized group delay with corrector of order 10.

VI. REALIZATION COMPLEXITY

It is important to emphasise that allpass solution simultaneously provide linear phase and deseired magnitude with option to realize complementary filter at the same cost. Hardware complexity of three considered configurations is given in Table I. Bandpass filter column gives information about number of additional adders, multipliers and delay elements required for realization besides already realized bandstop filter. The Table I indicates that elliptic filter with The Table I indicates that elliptic filter with corrector is noticeably more complex than allpass structure despite significantly higher group delay approximation error.

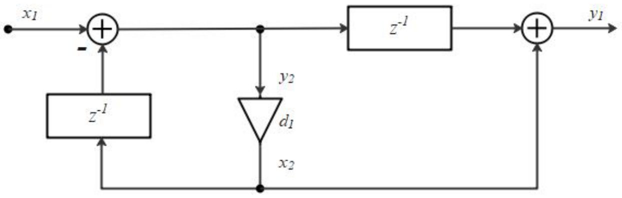

Fig. 11. First order section Type 1A

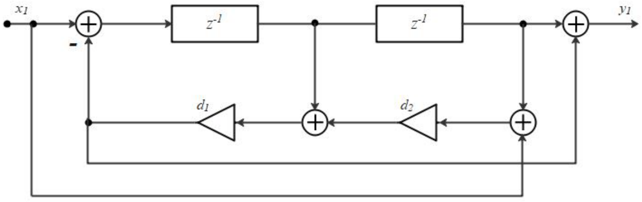

Fig. 12. Second order section Type 2A

All filters are realized by cascaded first and second order sections, displayed in Fig. 11 and Fig. 12.

Allpass filters are realized by structure which demand minimal number of multipliers (we chose the second order section Type 2A and the first order section Type 1A) [11].

This configurations have minimal possible number of multipliers at cost of increased number of adders or delay elements. The multipliers are the most energy hungry components and take up the most space in on cheap realization.

TABLE I

NUMBER OF ADDERS, MULTIPLIERS AND DELAY ELEMENTS FOR BANDSTOP FILTER AND NUMBER OF ADDITIONAL COMPONENTS FOR BANDSTOP FILTER REALIZATION

	Bandstop filter			Bandpass filter		
	N+M	K+K	Ellip.	N+M	K+K	Ellip.
Add.	21	37	40	+1	+1	+80
Mul.	11	19	31	0	0	+51
Delay	18	20	20	0	0	+40

Allpass based solutions are suitable in applications where total consumption is important due to noticeably less number of multipliers.

VII. CONCLUSION

Three diferent structures for realization of stopband and passband filter are presented in this paper. The parallel allpass configuration is obtained by solving the phase approximation problem. The resulting filter fulfills given magnitude specifications thanks to straighforward dependance between magnitude and allpass filters phase. If pure delay is applied in one of two parallel paths, equiripple phase approximation leads to elliptic magnitude. Besides desired magnitude this solution provide approximately linear phase and don't demand correctors. At the same time obtained constant group delay has minimal possible value. In given first example no poles are dedicated to the stopband but even in that case group delay error is less than 0.2 samples.

Two IIR allpass filters in parallel is second option with the same level of group delay. The resulting phase and magnitude are not equiripple no matter both allpass filters are designed in such a manner. The transfer function order is same as in first option but both allpass filters are IIR structures demanding more hardware elements.

Elliptic filter is convenient for comparison because it possess ripples in passband and stopband as allpass solutions. Elliptic filter which fullfil given magnitude specifications has the narrowest transition zones but phase is nonlinear. The corresponding phase corrector is usually of higher order than filter itself. In the given example complexity of that solution is significantly higher than allpass counterparts no matter the group delay approximation error is eight times larger.

ACKNOWLEDGEMENT

This work has been supported by the Ministry of Education, Science and Technological Development of the Republic of Serbia.

REFERENCES

[1] S.C. Dutta Roy,B. Kumar and S. B. Jain, “FIR notch filter design – a review”, *Facta Universitatis Series Electronics and Energetics*, vol. 14, No. 3, 2001, pp. 295-327.

[2] E. S. Kolawole, W. H. Ali, P. Cofie, J. Fuller, C. Tolliver and P. Obiomon, “Design and implementation of low-pass, high-pass and band-pass finite impulse response (FIR) Filters using FPGA”, *Circuits and systems*, vol. 6, 2015, pp. 30-48.

[3] T. Saramaki, “On the design of digital filters as a sum of two all-pass filters”, *IEEE Transactions on circuits and systems,* vol. CAS-32, No. 11, 1985, pp. 1191-1193.

[4] P. P. Vaidyanathan and S. K. Mitra “A new approach to the realization of low sensitivity IIR digital filters”, *IEEE Transactions on acoustic, speech and signal processing,* ASSP-34, 1986, pp. 350-361.

[5] M. R. Panicker, A. P. Vinod, “Low complexity flexible filter banks for uniform and non-uniform channelisation in software radios using coefficient decimation”, *IET Circuits, devices and systems*, vol. 5, No. 3, 2011, pp. 232-242.

[6] I. Aryanfar, A. Choudhary, S. Shahnia, M. Pagani, Y. Liu, D. Marpaung and B. J. Eggleton, “Signal interference RF photonic bandstop filter”, *Optics express*, vol. 24, No. 13, 2016, pp. 14 995–15 004.

[7] G. Stančić and S. Nikolić, “Design of narrow stopband recursive digital filter”, *Facta Universitatis*, vol. 24, no.1, pp. 121-132, 2011.

[8] G. Stančić and S. Nikolić, “Design of digital recursive notch filter with linear phase characteristic”, *11th International Conference on Telecommunications in Modern Satellite, Cable and Broadcasting Services*, pp. 69-72, 2013.

[9] G. Stančić and S. Nikolić, “Digital linear phase notch filter design based on IIR all-pass filter application”, *Digital Signal Processing*, vol. 23, no. 3, pp. 1065-1069, 2013.

[10] S. Nikolić, G. Stančić: "Design of IIR notch filter with approximately linear phase", *Circuits, Systems & Signal Processing*, vol. 31, Issue 6, pp. 2119-2131, 2012.

[11] S. K. Mitra, "Digital signal processing a computer - based approach", *McGraw-Hill*, New York, 2006.

Educational Open SPICE Models Neural Network-Based Generation Method

Suren Abazyan and Shavarsh Melikyan

***Abstract*—SPICE model creation method is represented for educational technologies. It is using neural network for data extraction from open source information. Method creates accurate SPICE models without any foundry information in them. Experiments show, that by using proposed method, in average about ~~86...93% accuracy can be reached because of neural network usage in model attribute prediction in comparison with benchmark foundry open access information.**

***Keywords*—SPICE models, educational purpose libraries, model generation**

I. INTRODUCTION

A SPICE model [1] parameters' set is a text-description of a device or circuit component, which is being used by the SPICE Simulator to mathematically predict the behavior of that part under varying conditions. SPICE models' parameters set can be very simple, for example for passive components like resistor, which is one or two lines, but it can also be extremely complex and include hundreds of lines, like the model of transistors or diodes. (Fig. 1) [2-3]

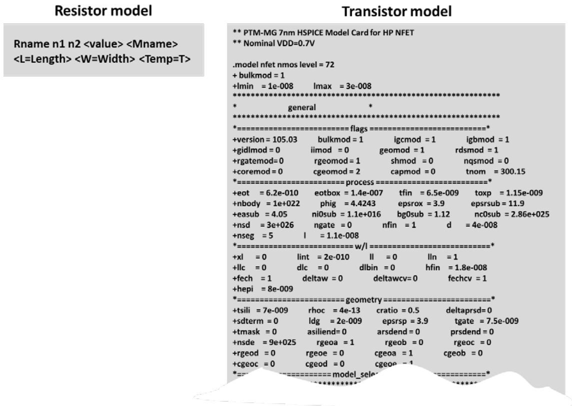

Resistor model

```
Rname n1 n2 <value> <Mname>
<L=Length> <W=Width> <Temp=T>
```

Transistor model

```
** PTM-MG 7nm HSPICE Model Card for HP NFET
** Nominal VDD=0.7V

.model nfet nmos level = 72
+ bulkmod = 1
+lmin   = 1e-008       lmax   = 3e-008
*****************************************************************
*                    general                     *
*****************************************************************
*========================= flags ==========================*
+version = 105.03       bulkmod = 1          igcmod  = 1          igbmod  = 1
+gidlmod = 0           iimod   = 0          geomod  = 1          rdsmod  = 1
+rgatemod= 0           rgeomod = 1          shmod   = 0          nqsmod  = 0
+coremod = 0           cgeomod = 2          capmod  = 0          tnom    = 300.15
*======================== process =========================*
+eot    = 6.2e-010     eotbox  = 1.4e-007     tfin   = 6.5e-009     toxp   = 1.15e-009
+nbody  = 1e+022       phig    = 4.4243       epsrox  = 3.9         epsrsub = 11.9
+easub  = 4.05         ni0sub  = 1.1e+016     bg0sub  = 1.12        nc0sub  = 2.86e+025
+nsd    = 3e+026       ngate   = 0            nfin    = 1           d       = 4e-008
+nseg   = 5            l       = 1.1e-008
*========================== w/l ===========================*
+xl     = 0            lint    = 2e-010       ll      = 0           lln     = 1
+llc    = 0            dlc     = 0            dlbin   = 0           hfin    = 1.8e-008
+fech   = 1            deltaw  = 0            deltawcv= 0           fechcv  = 1
+hepi   = 8e-009
*======================== geometry ========================*
+tsili  = 7e-009       rhoc    = 4e-13        cratio  = 0.5         deltaprsd= 0
+sdterm = 0            ldg     = 2e-009       epsrsp  = 3.9         tgate   = 7.5e-009
+tmask  = 0            asiliend= 0            arsdend = 0           prsdend = 0
+nsde   = 9e+025       rgeoa   = 1            rgeob   = 0           rgeoc   = 0
+rgeod  = 0            rgeoe   = 0            cgeoa   = 1           cgeob   = 0
+cgeoc  = 0            cgeod   = 0            cgeoe   = 1
*==              ========== model_sele
```

Fig. 1: Examples of resistor and transistor SPICE models

In general SPICE models are property information of the current technology/foundry and for making them, different tools and methods are used. For simplicity, companies are providing the datasheets of devices, on what later tools create SPICE models.

LTspice is one of the spice simulators [4], which is using SPICE models to simulate circuits. To create LTspice model, original datasheet of devices and pSPICE models are needed. For example, to define MOSFET device in LTspice, the parameter that need to be defined are:

- R_g - Gate ohmic resistance
- R_d - Drain ohmic resistance
- R_s - Source ohmic resistance.
- V_{to} - Zero-bias threshold voltage.
- K_p - Transconductance coefficient
- Lambda - Change in drain current with Vds
- C_{gdmax} - Maximum gate to drain capacitance.
- C_{gdmin} - Minimum gate to drain capacitance.
- C_{gs} Gate to source capacitance.
- C_{jo} Parasitic diode capacitance.
- I_s Parasitic diode saturation current
- R_b Body diode resistance.

After the parameters are known, the spice model can be constructed by *.model* statement. The final statement for a simple MOSFET device will be - *".model EXAMPLE_MOS MOSFET (Rg=1 Rd=10m Rs=3m Vto=1.9 Kp=57 Cgdmax=1n Cgdmin=3n Cgs=1.6n Cjo=1n Is=2.8p Rb=2m Vds=30 Ron=15m Qg=27n)"*

After the creation, SPICE models need to be tested by creating sub-circuits and instancing them in it.

Another method for SPICE model creation is "SPICE Model Wizard" (SMW) [5], which is semi-automated tool for model creation and linking for different devices, that are either built-in to SPICE or require linked model file (*.mdl). The device behavioral information needs to be inserted to the SMW by the user, and the type and amount of the information needed depends on what model need to be created. It can vary from simple models with small amount of data needed to more advanced devices, which data need to be taken from the manufacturer's data sheet.

The access ways to SWM tool depend on what type of model creation need to be done. The ways, that models can be created are:

- On newly created model
- To an already existing device from schematic library
- To a placed device in schematic library

The SMW can be used to create models for Diode, Semiconductor Capacitor, Semiconductor Resistor, Current-Controlled Switch, Voltage-Controlled Switch, Bipolar Junction Transistor (BJT), Lossy Transmission Line, Uniform Distributed RC Transmission Line.

While creating the model with SMW tool, one of the most important steps, is the name of it, and the process cannot be continued, until the name is defined. When the name is specified, it will appear in the Sim Model dialog.

After the name is specified, the model characteristics attribute insertion step is taking place. For these attributes, the tool supports two ways of parameter insertion: direct entry of them and entry of data, which has been captured from the physical devices of manufacturers. When all the required data is inserted, the SMW will display the generated model. This data later is being saved as MDL file and is the SPICE description of modeled device. The tool later provides functionality of checking the final model and saving it into a file. After model creation, linking it to a existing schematic or creating a new schematic for it is also supported. In this step, the tool is mapping pin/ports to their corresponding model names, verifies it and makes final attachments of model and schematic.

Predictive Technology Models (PTM) are another type of open purpose models. [6] This type of models are using already known information and predicting values for next technologies. One of this type model creation methods [6-8] is at first using previously published 25nm or higher gate length devices for fitting. After this step forms the initial parameters for a nominal model and derives parameters for starting to scale them. (Fig. 2)

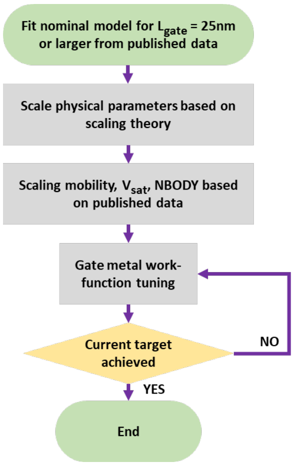

Fig. 2. The algorithm for PTM creation

Although the described methods are easy to use, user-friendly and fast, they have some disadvantaged, which makes their integration into the educational purpose SPICE model creation process harder to be established. In particular:

- Model creation SMW method is based-on user inserted data and required specific information about the devices, however, for educational purposes, it's not always possible to find technology specific data of devices and/or models
- SMW method is not extracting model data for some of devices, so they need to be created from scratch
- Open source predictive models do not include their generation algorithms, so model generation for new technologies would be impossible.
- Predictive models do not include all technologies, so it would be hard to see new technologies in practice
- Models may not be very accurate, because they are using either user inserted data or are predicted based on previous technologies.

II. NEURAL NETWORK BASED DEVICE SPICE MODEL CREATION METHOD FOR EDUCATIONAL OPEN PURPOSE TECHNOLOGIES

For addressing accuracy challenges for educational devices' SPICE models and adding ability to generate models for newer tech-nodes, while keeping them independent from any industrial technology and making them open, the proposed method is using neural network (NN) to generate device characterization attributes from open-source information, extract device specific data and returns the values for mentioned parameters. The overall principle of mentioned method consists of 4 main parts (Fig. 3):

- Model initialization
- Device parameter extraction from benchmark technology open source information
- Biasing
- Simulation and data extraction
- NN-based parameter updates

Model initialization is the initial step for proposed method execution. The process starts by the user selection of type of the device that is going to be created. Devices, that are being supported, are:

- nch_*vt - N-channel transistor (NMOS), with different threshold voltages. For example, nch_svt, which will be standard threshold voltage device for current technology
- pch_*vt - P-channel transistor (NMOS), with different threshold voltages. For example, pch_svt, which will be standard threshold voltage device for current technology
- nch_hc - N-channel high current device
- pch_hc - P-channel high current device
- pdiode - P+ and NW diode
- ndiode - N+ and PW diode
- resistor - standard poly resistance
- capacitor - gate capacitance
- pnp - PNP vertical bipolar junction transistor (BJT)

After the type selection, the method is creating corresponding files for the model. For simplicity, the

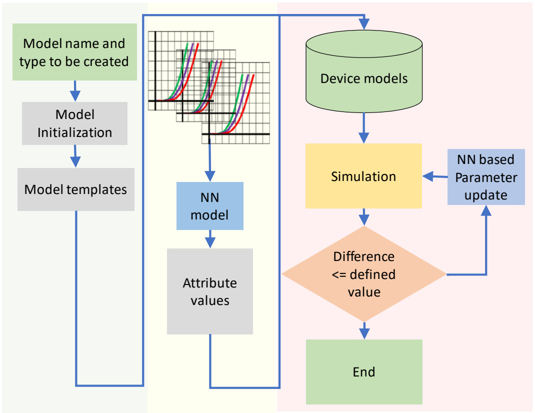

Fig. 3. The main flow for the proposed method

operating point variables, model parameters and sub-circuit parameters are kept in separate files.

While the initialization process, model variables are being set at first by random selection. As the created models will be open source and not include any foundry secret, the number of parameters, that are being considered are about 300-400. (Table 1)

Table 1. Example of Device parameters

Device Parameters					
ngate	pvag	xl	kt1	vsat	cigc
njd	qm0	jtsd	mexp	ute	cigd
njs	tcj	njtsd	psat	cdsc	cigs
nsd	tfin	aigc	ptwg	cdscd	cjd
ntox	tmexp	aigd	ptwgt	cfd	cjs
pbd	toxp	aigs	tss	cfs	dlbin
pbs	tpb	at	u0	cgbn	dlc
phig	uc1	cit	ua	cgbo	dsub
phin	ud	eta0	ua1	cgdl	dvt0
pqmacc	vsatcv	eu	uc	cgdo	dvt1
pvag	vtsd	k0	utl	cgeomod	drout

Device parameter extraction from benchmark technology open source information. At the second step for the proposed method is technology data extraction using NN. As for now, for most of industrial technologies, there is open-source information, which does not include any technological secret and/or data. This type of data is mostly in form of I-V characteristics, charts, graphics etc. Based on this, data extraction from this information, gives opportunity to get model parameters and optimize it.

The inputs for this step can be two types:

- I-V characteristics in graphical format
- Dependency chart of different simulation values, ex. Threshold voltage, total capacitance, saturation voltage, etc.

After taking the inputs, method is feeding them into NN, which consists of one input layer, 2 convolutional layers, two max pooling layers for down sampling and one output layer. [9] (Fig. 4) The output for this step is the I-V dependencies, which are later being feed into device parameter extractor, to generate biasing parameters. For the first step for device **parameter biasing** actual values for devices are not being considered. The main aim for this step is to get the approximate value for all parameters, i.e. the order of them.

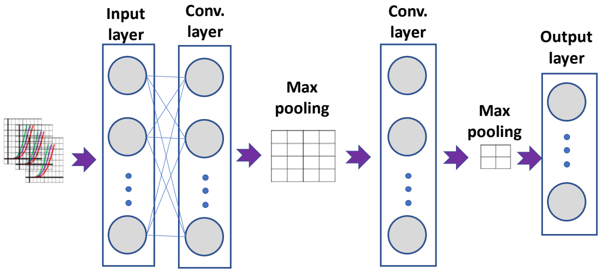

Fig. 4. The neural network for proposed method

After the value biasing, **simulation and data extraction** step is taking, where the previous values taken from biasing step are being set as devices parameters. For having different operating points (ex. FF, SS, TT), same parameters are at first being set for different cases.

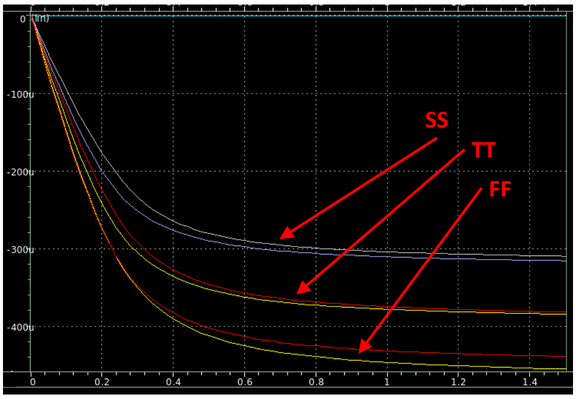

Fig. 5. Comparison results

The last step for the proposed method is **NN based parameter update.** At this step simple iterative algorithm is running SPICE simulation on created model, taking output I-V characteristics, compares it with reference technology values and updates model parameters (Fig. 5). The process finishes in two cases:

- Difference between I-V curves is less than preset threshold value (the default is 10%)
- Maximum iteration count is reached (the default is 30 iterations)

After the process successful finish (or termination), it is reporting the final model names and parameter list taken from SPICE simulations.

III. EXPERIMENTAL RESULTS

For demonstrating the proposed method in practice, two types of technologies have been considered – 14nm and 5nm [10-12] FinFET chemical mechanical polishing processes. The NN training data has been obtained from open access publications and foundry data. For each technology, data have been divided into two parts- training data and testing data with the ratio of 4 to 1. [13] After the processes are successfully finished, SPICE simulations on all types of models have been run and main attributes of devices were captured. (Table 2)

The final devices and technologies are summarized under OpA05 and OpA14 nm names, where 05 and 14 represent the gate lengths for each technology.

IV. CONCLUSION

SPICE model creation method is represented for educational purpose technologies, which creates accurate SPICE models without any foundry information in them. Network training data is obtained from foundry open access information, and values for device characterization parameters are being updates based on it. After the parameters are set, method is running spice simulations on newly created devices and in case the device parameters deviations are bigger than pre-defined values, another phase of their optimization is taking place. The final values are considered to be acceptable, when either the difference between required and obtained values are within the defined limits, or the maximum iteration count is reached.

Experiments show, that by using proposed method, in average about ~86...93% accuracy can be reached because of neural network usage in model attribute prediction in comparison with benchmark foundry open access information.

ACKNOWLEDGMENT

The work was supported by the Science Committee of RA, in the frames of the research project № 21T-2B002.

REFERENCES

[1] A. Vladimirescu, *The Spice Book*, John Wiley, New York, NY, USA, 1994.

[2] Bokalič, Matevž & Topic, Marko. (2015). SPICE Model and Simulations. 10.1007/978-3-319-14651-5_4.

[3] Canova, Aldo & Gruosso, Giambattista & Quercio, Michele. (2021). Characterization of Electromagnetic Device by Means of Spice Models. International Journal of Emerging Technology and Advanced Engineering. 11. 12-22. 10.46338/ijetae0921_02.

[4] May, Colin. (2020). LTspice Essentials. 10.1007/978-3-030-38304-6_1.

[5] Cao, Yu. (2009). What is Predictive Technology Model (PTM)?. ACM SIGDA Newsletter. 39. 1-1. 10.1145/1862891.1862892.

[6] Joca, Davi. (2016). Tutorial Altium Designer Software. 10.13140/RG.2.1.3128.5369.

[7] Jasani, Karan & Mehta, Sanket & Mehta, Jagrat. (2015). Altium: A Fast Schematic Designer. Indian Journal of Applied Research. 5. 60.

[8] David Money Harris, Nancy Wei, Zunyan Wang, Austin Fikes, Avi Thaker, Evaluation of predictive technology models, Microelectronics Journal, Volume 80, 2018, Pages 7-17, ISSN 0026-2692, https://doi.org/10.1016/j.mejo.2018.06.002. (https://www.sciencedirect.com/science/article/pii/S0026269218302064)

[9] Mariani, Maria & Tweneboah, Osei & Beccar‐Varela, Maria. (2021). Neural Networks. 10.1002/9781119674757.ch17.

[10] Koli, Dinesh. (2012). Technical challenges in 14nm FinFET CMP processes.

[11] Moroz, Victor. (2016). Transistor and Logic Design� for 5nm Technology Node.

[12] Tasdemir, Zuhal & Wang, Xiaolong & Mochi, Iacopo & Protasova, Lidia & Meeuwissen, Marieke & Custers, Rolf & Rispens, Gijsbert & Hoefnagels, Rik & Ekinci, Yasin. (2018). Evaluation of EUV resists for 5nm technology node and beyond. 10.1117/12.2502688.

[13] Li, Yang. (2021). Training data and test data.

Table 2. Results for comparisons

Device	nch_hc_FF	nch_hc_FF	nch_hc_SS	nch_hc_SS	nch_hc_TT	nch_hc_TT	nch_hc15_FF	nch_hc15_FF	nch_hc15_SS	nch_hc15_SS	nch_hc15_TT	nch_hc15_TT
Tech	ref	OpA05	ref	OpA05	ref	OpA05	OpA05	ref	ref	OpA05	ref	OpA05
vgs	0	0	0	0	0	0	0	0	0	0	0	0
vth	326.0525m	359.0640m	450.9144m	418.3308m	389.2782m	391.9213m	359.2082m	326.0525m	450.9144m	421.0776m	389.2782m	391.9112m
vdsat	99.9350m	104.7630m	109.5623m	104.7626m	104.7627m	104.7627m	104.6607m	99.9350m	109.5623m	104.6604m	104.7627m	104.6605m
vod	-326.0525m	-359.0640m	-450.9144m	-418.3308m	-389.2782m	-391.9213m	-359.2082m	-326.0525m	-450.9144m	-421.0776m	-389.2782m	-391.9112m
beta	6.3942m	5.9107m	3.9550m	5.0268m	5.1081m	5.1081m	5.6877m	6.3942m	3.9550m	4.3188m	5.1081m	5.1238m
gm	0	0	0	0	0	0	0	0	0	0	0	0
gds	1.3005n	349.1780p	8.2596p	35.0673p	102.6299p	92.3189p	338.1603p	1.3005n	8.2596p	27.6513p	102.6299p	93.7961p
gmb	0	0	0	0	0	0	0	0	0	0	0	0
cdtot	137.8049a	106.8940a	126.8603a	90.4395a	132.2005a	91.9541a	91.9541a	137.8049a	126.8603a	77.0478a	132.2005a	91.9932a
cgtot	216.7733a	230.3266a	184.6488a	197.4153a	200.4443a	200.4451a	221.4643a	216.7733a	184.6488a	170.6319a	200.4443a	200.5234a
cstot	137.8049a	106.8940a	126.8603a	90.4395a	132.2005a	91.9541a	102.4629a	137.8049a	126.8603a	77.0478a	132.2005a	91.9932a
cbtot	90.8748a	16.5360a	103.1839a	16.5360a	97.0294a	16.5360a	16.5360a	90.8748a	103.1839a	16.5360a	97.0294a	16.5360a
cgs	100.3787a	106.8953a	83.7964a	90.4397a	91.9541a	91.9545a	102.4642a	100.3787a	83.7964a	77.0479a	91.9541a	91.9937a
cgd	100.3787a	106.8953a	83.7964a	90.4397a	91.9541a	91.9545a	102.4642a	100.3787a	83.7964a	77.0479a	91.9541a	91.9937a

Design of Virtual Reference Standard for Calibration in University Education

Zivko Kokolanski and Petar Vidoevski

Abstract - The paper elaborates the design and implementation of a low-cost virtual reference standard for teaching calibration principles in metrology in higher education. Two major aspects have been analysed: the virtual instrument architecture, and metrological evaluation of the proposed solution consisting of a virtual instrument and power amplifier. It has been shown that the applied programming architecture allows implementation of most functionalities provided by the modern calibration instruments, which can be further exploited in the University education laboratory practice. The obtained experimental results suggest that the system offers good stability and low non-linearity, which can be used for calibration of low to medium-accuracy instruments, and for teaching metrology in higher education. Besides the virtual reference standard, the metrological performances of the power amplifier are also analysed.

Keywords - calibration; LabVIEW; power amplifier; virtual instrument.

I. INTRODUCTION

Metrology is the science of measurements and its application in all areas of industry and everyday life [1]. One can easily say that without the development of metrology, progress in science and modern life can be hardly imagined. However, despite its undoubted technological, economic, scientific and social significance, there is a lack of teaching content in metrology in the higher education [2]. This is especially important if we emphasize that metrology is a multidisciplinary science and it covers different educational profiles. One of the basic prerequisites that should be provided for proper implementation of metrology in higher education is laboratory instrumentation. On the other hand, the high-accuracy instrumentation commonly used in the metrological laboratories is quite expensive and often inaccessible to universities, especially considering that for good transfer of knowledge an individual laboratory approach to students must be applied. Therefore, the educational practices of metrology in the university education are often too theoretical or significantly differ from those in the industry.

One approach that can contribute to overcoming the above mentioned challenges is the application of virtual instrumentation. Namely, virtual instruments enable the development of software-defined instrumentation with easy-to-define functional and metrological performances. Instruments developed in this way are significantly cheaper than classical instruments and provide great flexibility, which is crucial for their application in the University education. The user interface and the operation of virtual instruments can be developed in accordance to the professional equipment used in the calibration laboratories. In this way, efficient and high-quality laboratory practice can be provided to higher education students. This paper aims to propose the design and implementation of a virtual reference standard for electrical quantities.

A lot of scientific papers on using virtual instrumentation in the field of metrology have being published. Authors in [3] propose a virtual instrument for automatic control and calibration of electrical reference standards. Similarly, [4] proposes a remote calibration system by using virtual instrumentation, whereas [5] elaborates an automated system for multimeter calibration in LabVIEW. There are also papers on using virtual instrumentation for calibration of Data Acquisition (DAQ) systems for rocket propulsion test facilities [6], and on-site calibration systems for electronic instrument transformers [7]. However such approaches doesn't eliminate the need of realistic reference standards and instruments to be exploited in the university education.

This paper proposes a complete hardware and software solution of a low-cost virtual reference standard for electrical quantities [8] with improved accuracy. Two aspects are covered in the paper: the instrument design and implementation, and metrological evaluation. In order to extend the output signal levels of the virtual instrument, an external power amplifier [9] is used. The broader scope of such virtual reference standard is its integration into remote virtual laboratory, which will be considered in future publication.

II. VIRTUAL REFERENCE STANDARD DESIGN

The virtual reference standard (calibrator) for electrical quantities consists of several functional modules: PC-based virtual instrument, data acquisition card, power amplifier and device under test (DUT). The simplified block-diagram of the system is given in Fig.1.

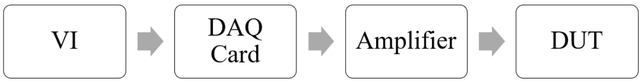

Fig. 1. Simplified diagram of virtual standard for electrical quantities

Zivko Kokolanski and Petar Vidoevski are with the Ss. Cyril and Methodius University in Skopje, Faculty of Electrical Engineering and Information Technologies, Rugjer Boskovikj 18, 1000 Skopje, E-mail: kokolanski@feit.ukim.edu.mk

The virtual instrument (VI) is a specialized software program running on a personal computer (PC) which provides all user and system functionalities. In general, the VI processes the user interactions with the graphical user interface and reproduces the appropriate electrical signals with a data acquisition card. In order to obtain a higher amplitude, the output signal generated by the DAQ card is amplified with a specialized power amplifier. Such a signal can be finally used to test a device (DUT) or calibrate an instrument used to measure given electrical quantity.

B. Virtual instrument implementation

The front panel of the virtual instrument given in Fig. 2 consists of several parts: two text indicators for specific user-related messages, connection terminals realized as a logical indicators glowing according to the defined electrical quantity, keyboard for setting all system and functional parameters, potentiometer for changing the signal amplitude, and a power button. In general, the calibrator operates in two modes: standby or operate. The transition between the standby and the operate mode is possible by pressing the corresponding keys on the VI's front panel. In the standby mode, the user actions are related to setting the signal parameters. The text indicator on the left side in Fig.2 is used to show the signal parameters, the mode of operation, and message whether the generated voltage is dangerous. The indicator on the right hand side shows the current value entered on the keyboard, a reminder to enter the measurement unit, and whether a decimal or integer part is entered. Additionally, by pressing the setup key in the standby mode, the user can modify additional signal parameters such as: wave shape, offset, phase shift, etc. On the other hand, the operate mode is used to generate the signal according to the predefined parameters. The user can use the potentiometer to modify the signal value in real-time when the calculated relative error will be displayed on the text indicator on the right hand side. It is important to note that the signal parameters cannot be modified in the operate mode. However, by pressing the save button, the user can record the calibration results into comma separated values or configuration file.

The block-diagram of the virtual instrument is given in Fig. 3. In order to have low dependence on other modules, and high cohesion, the program is organized into three iterative loops. The first is the producer loop in which events are generated, and based on those events data is fed into a specific buffer.

The second loop is responsible for the main operation of the virtual calibrator, i.e. initialization of default values, switching to operating mode, message display, and signal parametrization. The third loop is related to the data acquisition, i.e. it generates messages to start/stop the acquisition and generate a signal.

The virtual calibrator loop consists of five states. At the beginning, the program is in an initialization state where the controls, indicators, and global function variables are initialized. Afterwards, the program enters into idle state and waits for the power up button to be pressed, which initiates the standby state given in Fig. 4. The virtual instrument now reads the data from the functional global variables in which the signal values are stored, the values entered from the keyboard, as well as handles certain messages. The "operate" state reads the function global variable for the signal parameters, the function global variable for error calculation, as well as the voltage and current check. Next, the value of the signal is sent through a special buffer in the signal generation loop. When switching from operate to standby in the third loop, a message that the acquisition will stop is generated. In the "end" state, the variant buffer is read and the virtual calibrator shuts down. Two types of messages are possible, one stating that an error has occurred, or that the program has finished normally by pressing the power up button.

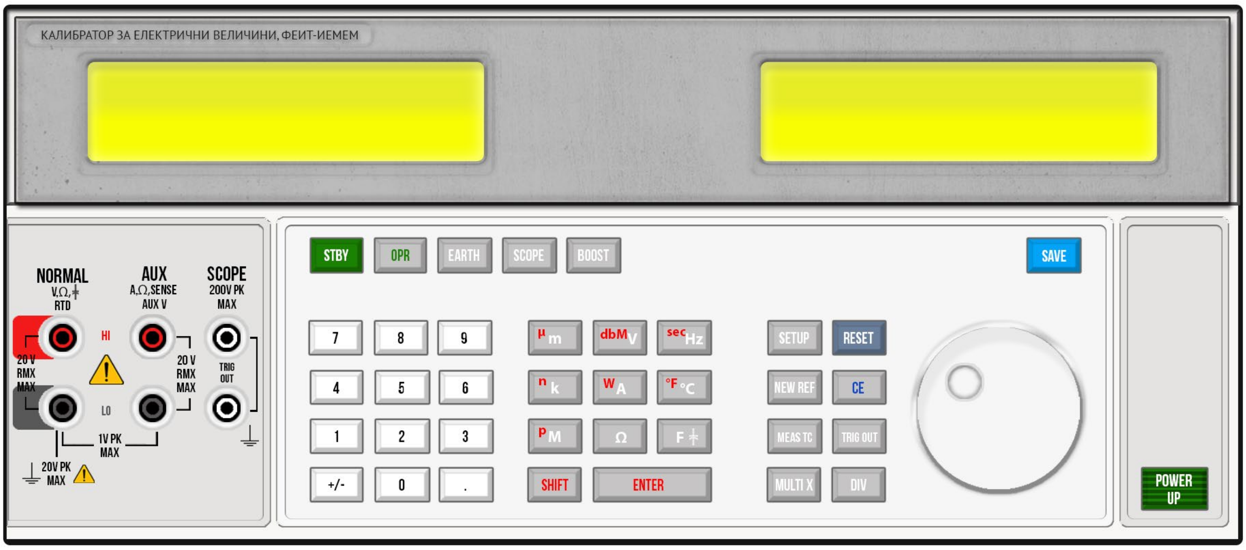

Fig. 2. Front panel of the virtual calibrator for electrical quantities

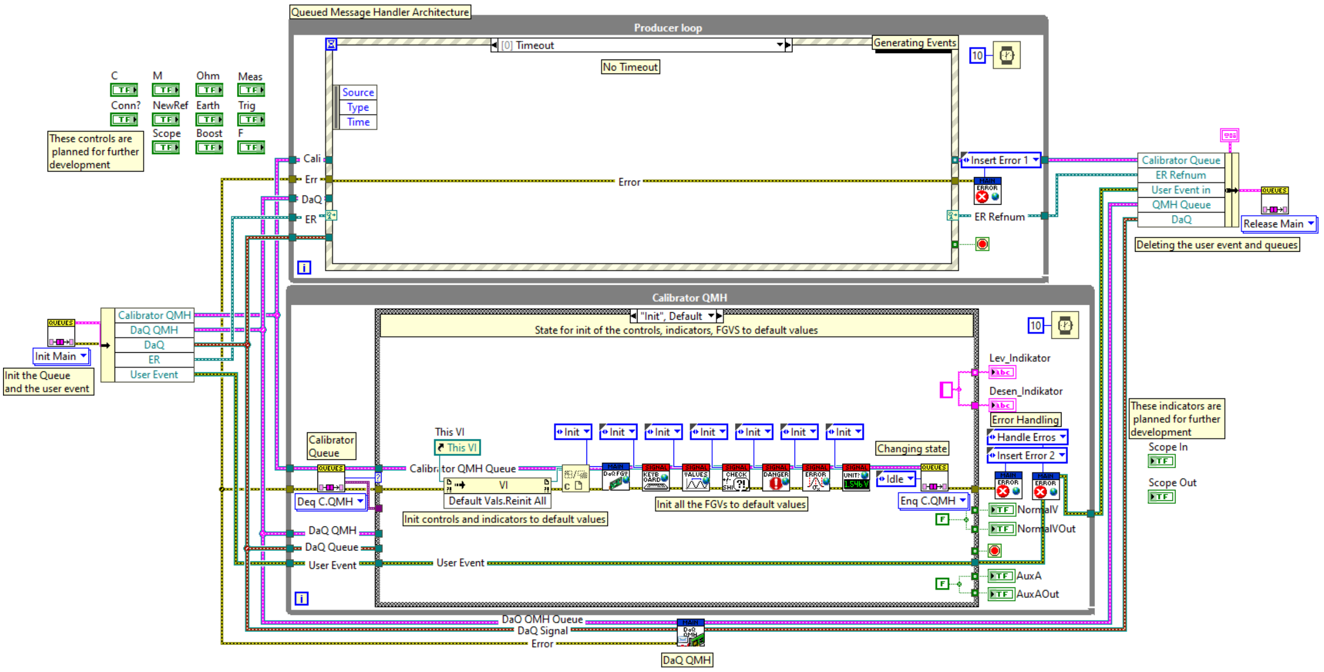

Fig. 3. Block diagram of the virtual calibrator. General view of the implemented programming architecture – queued message handler.

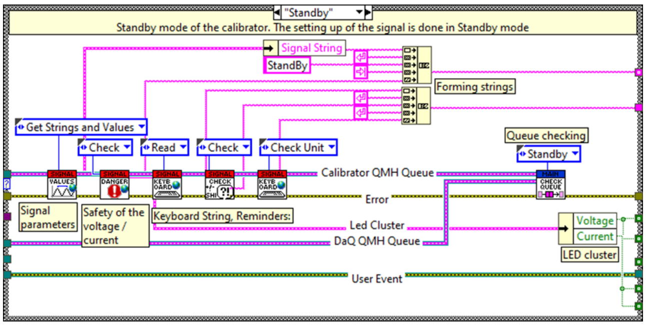

Fig. 4. Block diagram of the standby state in the calibrator loop

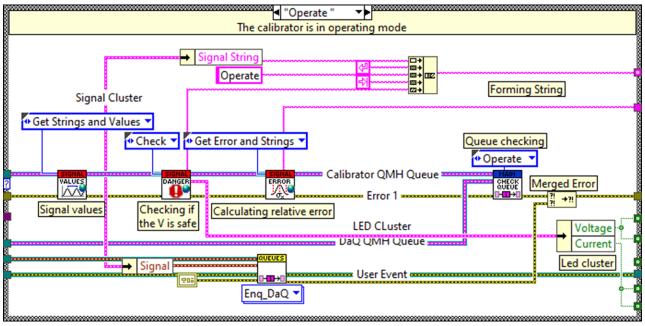

Fig. 5. Block diagram of the operate state in the calibrator loop

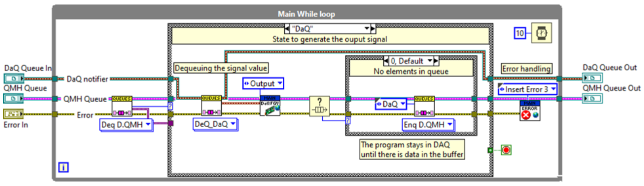

Fig. 6. Block diagram of the data acquisition loop

The third loop in Fig. 3 also consists of five different states: wait, message generation, start/stop acquisition, signal generation, and end. To perform the acquisition, a functional global variable is created which is called from one of the states. Regarding the signal generation, this variable is initiated when the measurement unit is selected because the type of task depends on whether the signal is voltage or current. The generated signal is a waveform data type containing the start time, time step, and array of double precision amplitude values. Two modes of signal acquisition are possible: finite and continuous. Considering applications related to real-time signal generation, the continuous acquisition mode is favourable. However, only some data acquisition cards support such acquisition mode. Therefore, considering the DAQ card used, the proposed virtual calibrator is realized by using the finite acquisition mode. It is also important to note that, when an external amplifier is used, the output signal from the DAQ card must be divided by the amplification coefficient.

B. Data acquisition card

The data acquisition card is used to reproduce the signals generated by the virtual instrument, thus having critical role regarding the metrological performances of the instrument. There are different types DAQ cards that can be used for realization of the proposed virtual calibrator. In general, the DAQ cards must contain an analog output channel for the signal generation. On the other hand, other technical specifications of the DAQ card are important considering the signal quality, such as: digital-to-analog (DA) converter resolution, sampling speed, acquisition mode, timing resolution, computer interface, etc. In order to have a wider impact, one of the mostly exploited low-cost DAQ card in the universities NI myDAQ was used within this paper. The most important technical parameters of NI myDAQ are summarized in table I.

TABLE I
IMPORTANT TECHNICAL PARAMETERS OF NIMYDAQ

Parameter	Quantity
DA converter resolution	16 bit
Sampling speed	200 kS/s
Analog output voltage	± 10 V
Output impedance	1 Ω
Maximal output current	2 mA
Timing resolution	2 ns

C. Power amplifier

The power amplifier is intended to amplify signals generated by a DAQ card with a "low voltage" output. The DA converter voltage of the DAQ card is usually standardized to a given voltage level, e.g. ±2.5 V, ±5 V or ±10 V. Such voltage levels are highly restrictive because they limit the calibration of instruments in a low measurement range. The aim of this section is to show one possibility to extend the output voltage range to the nominal power line voltage of 230V (or 110 V) prior connection with the instrument. The simplified block diagram of the power amplifier is given in Fig. 7.

The power amplifier is usually a digital system which reproduces the output signal by a DA converter. In such case, the DA converter must meet the metrological requirements regarding the desired output signal quality. Namely, it must have well-enough resolution (which is defined by the required output signal uncertainty), and support high-enough sampling frequency. Theoretically, the sampling frequency has to be at least twice higher than the frequency of the highest harmonic that needs to be generated. According the PQ standard EN50160 (takes up to 50th harmonic), the minimum sampling frequency is 5 kHz (for 50 Hz power grids). However, in practice the sampling frequency should be significantly higher to maintain the accuracy of the higher harmonics.

The generated signal with the DA converter is amplified by a PQ amplifier to the nominal power line voltage level of 230 V. To do so, several analog signal processing modules are used: low pass filter (restricts the input signal bandwidth and eliminate noise), preamplifier (amplifies the input signal to a given reference level and limits the input voltage level), power amplifier (amplifies the signal to nominal power line level and increase the load current capability). The detailed description of the power amplifier is given in [9], whereas its metrological performances are evaluated in [10].

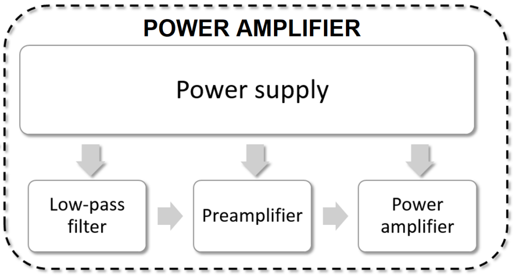

Fig. 7. Simplified block diagram of a power amplifier

The PQ amplifier was experimentally verified by using the PQ analyzer Fluke 435. The reference voltage waveforms, were generated by PC based virtual PQ signal generator [11]. The experimental system including PQ signal generator and reference instrument Fluke 435 is given in Fig. 8 and its practical implementation in Fig. 9.

The experiment was performed by using a data acquisition card NI PCIe 6343 containing analog output channel with maximal output voltage of ± 10 V. Signal with the first seven high-order odd harmonic was generated by using a virtual PQ generator with sampling frequency of 100 kS/s. The screenshots obtained from the FLUKE 435 front panel are given in Fig. 10 and Fig.11. The example given in Fig.10 represents signals with high-order harmonics, whereas the example given in Fig.11 shows occurrence of a burst transients.

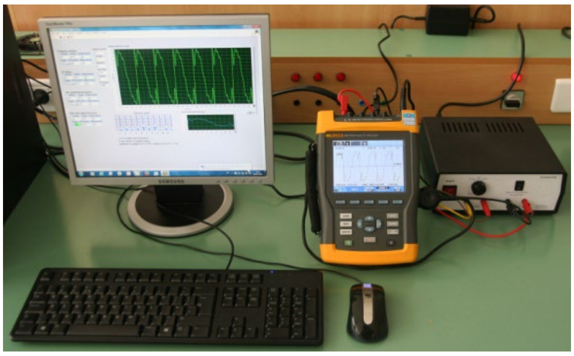

Fig. 8. Experimental system for verification of PC-based PQ signal generator

Fig. 9. Practical realization of the PQ amplifier

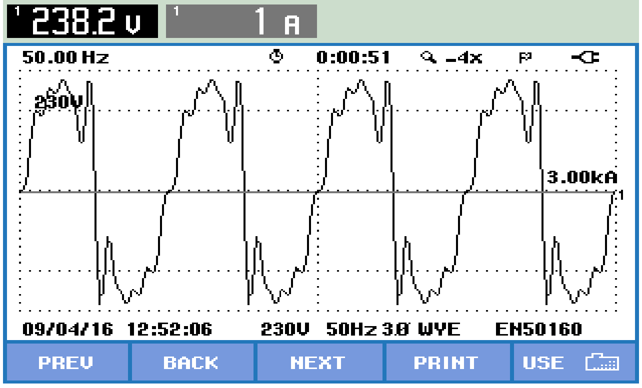

Fig. 10. Screenshot from the FLUKE 435 instrument. Signal with harmonics generated by PC and amplified with the PQ amplifier.

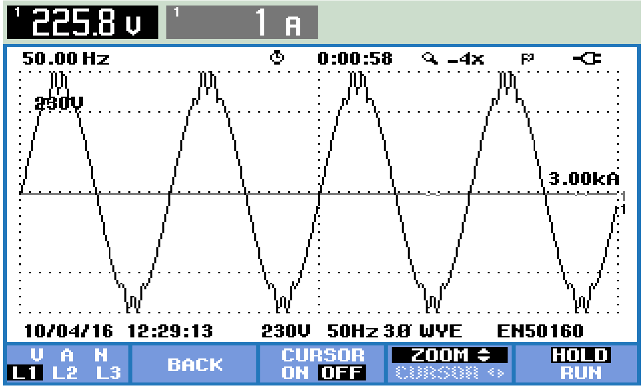

Fig. 11. Screenshot from the FLUKE 435 instrument. Burst transients generated by PC and amplified with the PQ amplifier.

III. VIRTUAL REFERENCE STANDARD METROLOGICAL EVALUATION

The metrological performances of the virtual reference standard were evaluated by using a high precision instrument FLUKE 8846A with resolution of 6.5 digits. The measurement of the transfer function were performed for the direct current (DC) voltages in the range from 10-250V with a step of 10V, and for alternating current (AC) sinusoidal voltage with a root mean square (RMS) values from 10-250V with a frequency of 50Hz. The sampling frequency of the analog output channel was set to 1000 S/s. The amplifier input range of ± 5V was used resulting in amplification constant of 84.28.

The measured transfer characteristic of the virtual calibrator for DC voltage is given in Fig. 12, whereas the transfer characteristic for AC voltage is given in Fig. 13. Both transfer characteristics were approximated by using the least square methods resulting in a very low gain and offset component mainly originating from the power amplifier. Considering the results reported in Fig. 12 and Fig. 13 it can be seen that both transfer characteristics for DC and AC voltage are highly linear. In fact, when approximated by the least squares method the maximal non-linearity of the instrument is around 0.32 %. The overall uncertainty of the virtual calibrator can be additionally reduced if a higher output voltage range of the DAQ card is used, thus resulting in a lower amplification constant of the amplifier. Having in mind the DAQ card DA converter resolution of 16 bit (given in Table I), the theoretical output voltage resolution of the virtual calibrator in the measurement range of 250 V is 3.8 mV in a frequency range up to 3 kHz. The virtual calibrator can be also used in the current output mode, but having in mind the low output current capability of NI myDAQ, and external current amplifier have to be used. We could say that such performances of the virtual calibrator can be used for calibration and testing of low to medium accuracy instruments and can be successfully exploited in the laboratory practice in the higher education in the field of metrology.

The broader scope of such virtual reference standard realization is its integration into a remote virtual laboratory framework considered in the ongoing Erasmus+ project “A ubiquitous virtual laboratory framework – UbiLAB” under number 2020-1-MK01-KA226-HE-094548. It is envisaged that the virtual reference standard will coexist with a full palate of virtual laboratory instruments with a possibility to control remotely over the internet.

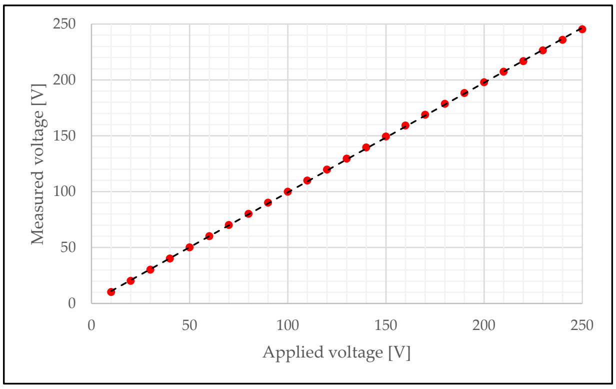

Fig. 12. Measured DC voltage transfer characteristics of the virtual calibrator in the range from 0 - 250 V

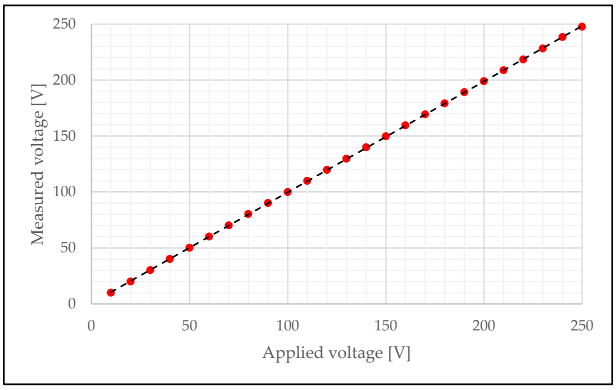

Fig. 13. Measured AC voltage transfer characteristics of the virtual calibrator in the range from 0 - 250 V

IV. CONCLUSION

The paper summarizes the design and implementation aspects of a virtual reference standard for electrical quantities aimed to be used in the higher education in the field of metrology. The paper is mainly focused on the implementation of the virtual instrument by using the queued message handler programming architecture. This programming architecture offers great modification flexibility which is crucial when used for education purposes. Besides the basic calibrator functionalities, the proposed realization offers possibility for data logging and automatic report generation. Moreover, the virtual instrument functional performances can be easily adjusted according the existing commercial instruments providing an additional value in the student's laboratory practice.

The metrological performances of the virtual calibrator were evaluated by using a high accuracy multimeter, power amplifier and a data acquisition card. The transfer characteristics of the virtual calibrator was measured in the measurement range of 250 V for DC and AC voltage with a frequency of 50 Hz. The experimental results suggested that the maximal nonlinearity error of the transfer characteristics are around 0.32%. The theoretical resolution of the virtual calibrator in this measurement range is 3.8 mV. We could say that such metrological performances can be considered satisfactory having in mind the simplicity of the solution. The virtual reference standard proposed herein is conceived as a part of ubiquitous remote laboratory framework which is to be published in future scientific publication.

ACKNOWLEDGEMENT

This paper was supported by the Erasmus+ project UbiLAB: A ubiquitous virtual laboratory framework, no. 2020-1-MK01-KA226-HE-094548.

REFERENCES

[1] S. V. Muravyov, V. Savolainen, “Teaching Measurement Theory in Metrology, Standardization and Certification,” XVII IMEKO World Congress Metrology Jun. 2003

[2] S. M. Ibrahim, P. Bills, J. Allport, “Metrology Education Impediment – What do we need to do?”, Proceedings of Academics World International Conference, Aug., 2017

[3] H. M. Abdel Mageed, A. M. El-Rifaie, “Electrical Metrology Applications of LabVIEW Software,” Journal of Software Engineering and Applications, vol. 6, pp. 113-120, 2013

[4] L. I. Khudonogova, “Remote Calibration Using LabVIEW Virtual Instrument Technology”, XIX International conference - Modern technique and technologies, pp.225-226, 2013

[5] V. Slavov, T. Tashev, V. Mladenov, “Automated System for DMM Calibration”, 6th WSEAS Int. Conference on Computational Intelligence, Man-Machine Systems and Cybernetics, pp.371-374, 2007

[6] P. W. Hebert, D. M. Davis, M. P. Turowski, W. T. Holladay “NASA Data Acquisition System Software Development for Rocket Propulsion Test Facilities”, 31st AIAA Aerodynamic Measurement Technology and Ground Testing Conference, DOI: 10.2514/6.2015-2561, 2015

[7] M. Zhang, K. Li , J. Wang, S. He “An On-site Calibration System for Electronic Instrument Transformers Based on LabVIEW”, Metrol. Meas. Syst., Vol. XXI, No. 2, pp. 257–270, 2014

[8] Z. Kokolanski, P. Vidoevski „Design of Virtual Calibrator for Teaching Metrology in Higher Education“, Proc. XI National Conference with International Participation "Electronica 2020", May 14 - 15, 2020, Sofia, Bulgaria

[9] Z. Kokolanski, C. Gavrovski, I. Mircevska, V. Dimcev, M. Simic “On the design of power quality signal amplifier”, XXV International Scientific Conference Electronics, DOI: 10.1109/ET.2016.7753491, 2016

[10] M. Simić, Z. Kokolanski, D. Denić, V. Dimcev, D. Živanović, D. Taskovski “Design and evaluation of computer-based electrical power quality signal generator”, Measurement, vol. 107, pp.77-88, 2017

[11] M. Simić, D. Denić, D. Živanović, D. Taskovski and V. Dimcev, "Development of a data acquisition system for the testing and verification of electrical power quality meters", JPE – Journal of Power Electronics, vol. 12, no. 5, pp. 813-820, September 2012.

A deep learning approach for hydrological time-series prediction with ELM model

M. Jeremić, M. Milić, M. Gocić, and J. Milojković

Abstract - Prediction is a significant task during resources planning and management. Several traditional and deep learning models have been applied to simulate the complex nature of different systems. The aim of this research is to apply a deep learning model to simulate the behaviour of the hydrological system. In this paper, the Extreme Learning Machine (ELM) methodology is investigated to perform one step ahead predictions for daily time horizons in the Danube River, Serbia. The performance analysis of the ELM model is also presented. The ELM model training has a faster training process in comparison to traditional/deep learning architectures. It gives a comparable performance with a fast execution rate. In numerical terms, the superiority of ELM over some alternative models is more expressive.

Keywords – Artificial Neural Network, Machine Learning, Extreme Learning Machine, Danube River.

I. INTRODUCTION TO EXTREME LEARNING MACHINE

The entire drainage region of 801.463 km^2 makes the Basin of the Danube River the second in Europe [1]. The river connects 19 countries and over 80 million people. The economic importance of the river is enormous. It has a vital influence on water and power supply, biodiversity, agriculture, industry, fishing, tourism, etc. [1].

Critical decision-making problems require reliable predictions for different forecast horizons. Some of the problems that depend on hydrological parameters of the Danube River are navigation, floods or droughts, power plants capacities, etc. Many studies deal with the hydrological forecasting problems of the Danube River, using different statistical or neural-networks based modelling techniques [2-5].

The study described in this paper investigates the Extreme Learning Machine (ELM) methodology to perform one step ahead predictions for daily-time horizons in the Danube River at the territory of the Republic of Serbia. The paper continues with a short explanation of the ELM modelling and mathematical problem formulation. The implementation required a thorough analysis of the initial data series. The forecasting methodology is implemented in Python programming language. Appropriate forecast performance measures are then assessed and discussed at the end, as well as the concluding remarks.

II. EXTREME LEARNING MACHINE MODELLING

Extreme Learning Machine (ELM) is a machine learning technique used for classification and regression tasks.

ELM represents a single-hidden layer feed-forward neural network (SLFN) capable of faster learning, compared to gradient-based learning techniques. It can be described as a typical neural network with one hidden layer that does not require the learning process. This type of neural network does not perform iterative tuning, which makes it faster and with better generalization performance than in networks trained by the backpropagation method.

ELM is one of the neural network algorithms that uses a single hidden layer to pass values forward. The ELM network topology has three layers: the input layer, the hidden layer, and the output layer as shown in Fig. 1.

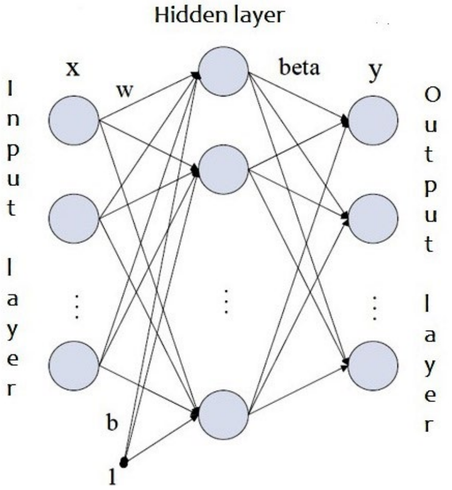

The extreme learning machine algorithm is one of the most efficient machine learning algorithms among all neural network topologies. Due to the non-iterative training, all parameters are set once. This results in high-speed training. Its application is easy to understand and can be used to solve complex problems.

Miljan Jeremić is with Knjaževac gymnasium, Karađorđeva 16, Knjaževac; Miljana Milić and Jelena Milojković are with the Faculty of Electronic Engineering, University of Niš, Aleksandra Medvedeva 14, Niš; Milan Gocić is with the Faculty of Civil Engineering, University of Niš, Aleksandra Medvedeva 14, Niš, Serbia
E-mail:miljan.jeremic@gmail.com, miljana.milic@elfak.ni.ac.rs, milan.gocic@gaf.ni.ac.rs, jelena.milojkovic@elfak.ni.ac.rs

II. Mathematical Formulation of the Problem and Models

A. *ELM model*

There are several computational methods that could be used for forecasting the Danube flow. The most common are hydrological, statistical or machine learning modelling. Here we will discuss the ability of the ELM model for predicting the behaviour of the particular hydrological system. Advantages of using the ELM model are its good generalization abilities, the convenience of modelling and faster learning rate than in the backpropagation algorithms. ELMs can solve classification and regression tasks with significant accuracy if it has sufficient hidden neurons and training data to learn for all hidden neurons. The input weights and node thresholds of the hidden layer neurons can be randomly generated.

In the given training set $(t_i, x_i)_{i=1}^{N}$, for $x_i \in R^n$, [6], N denotes the number of training samples. If $\boldsymbol{h}(\boldsymbol{x})$ represents the outputs of hidden layer neurons, the matrix form of the functions H(X) can be written as (1).

$$H(X) = \begin{bmatrix} g(w_1 \cdot x_1 + b_1) & \dots & g(w_L \cdot x_1 + b_L) \\ \vdots & \ddots & \vdots \\ g(w_1 \cdot x_N + b_1) & \dots & g(w_L \cdot x_N + b_1) \end{bmatrix}_{NxL} = \begin{bmatrix} h(x_1) \\ \vdots \\ h(x_N) \end{bmatrix} \qquad (1)$$

Here L denotes the number of hidden nodes, b_i is the bias of the i-th hidden neuron, w_i is the input weights associated with the i-th hidden layer neuron and g is the corresponding activation function. The output signal of the ELM network can be written in the following form (2):

$$y(p) = \sum_{j=1}^{L} \beta_j \cdot g\left(\sum_{i=1}^{N} w_{ij} \cdot x_i + b_j\right) \qquad (2)$$

where β_j represents the weights between the input layer and the hidden layer and b_j represents the weights between the output layer and the hidden layer. Input layer weights and biases are randomly generated and the activation function assigned at the beginning of the input and hidden-layer. The output of the entire network written in the matrix form can be given as (3).

$$\hat{Y} = H(X)\beta \qquad (3)$$

The optimization goal of the network is to minimize the error between the output generated by the network and the real values [7].

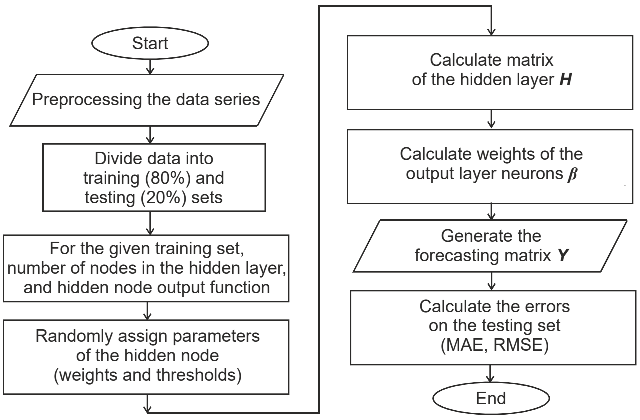

Fig. 2. Steps in implementation of ELM

In order to implement the procedure in the chosen programming language one has to follow few relatively simple steps:

1. Prepare the training set.
2. Randomly assign hidden node parameters (*w, b*).
3. Calculate the output matrix of the hidden layer H.
4. Calculate the output neurons weights $\boldsymbol{\beta}$; $\boldsymbol{\beta} = H^{+} \cdot \boldsymbol{Y}$, where H^{+} represents generalized Moore-Penrose inverse matrix H.

This algorithm is illustrated in Fig. 2.

III. STATISTICAL ANALYSIS OF THE OBSERVED TIME SERIES DATA

The available dataset is written in the files *Danube_Level.csv* and *Danube_Level012.csv*. The first file contains 2 columns, one represents the date of the river level measurement, and the second column represents the river level expressed in mm. The second file contains the same data i.e., three more discretized values of the river level marked as Value0, Value1, Value2 shifted in time. The values of the first five points in the dataset are shown in Table I, while the graphical representation of the entire dataset is shown in Fig. 3.

TABLE I
Data organization in the *Danube_Level.csv* file

Date	Value [mm]
11/18/2009	348.631413
11/19/2009	376.318908
11/20/2009	439.514743
11/21/2009	334.435802
11/22/2009	498.399002

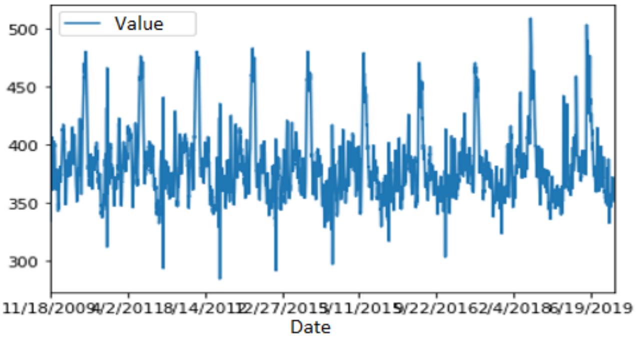

Fig. 3. Time series data

Descriptive statistics help describe specificities of the dataset and give summaries about different measures of the data. These descriptive statistics for the given data set are shown in the Table II.

TABLE II
Descriptive statistics for data

Name	Value
Count	2918
Mean	381.887597
Standard deviation	28.953503
Min..	334.435802
25%	284.555908
50%	377.238211
75%	392.688802
Max	498.399002

Results of Python statistical data analysis are given in Table III:

Descriptive statistics for dataset

Name	Min [mm]	Max [mm]	Median [mm]	Skew [mm]
value	284.55591	498.39900	377.23821	1.253833

It is sometimes important to calculate the correlation of the observed time series with the same observations shifted in time steps, called lags. This correlation is calculated for values of the same series at previous and current time steps, this is referred to as autocorrelation. A graphical representation of the time series autocorrelation by lag is called the **A**uto **C**orrelation **F**unction (ACF). Usually, the ACF plot also contains confidence intervals that are drawn as a cone. Also, the confidence interval is usually set to 95%. This indicates that values outside of this cone are very likely a correlation and not a statistical fluke.

The diagram of autocorrection (ACF) and partial autocorrelation function (PACF) of the Danube level data series are shown in Figs. 3 and 4, respectively.

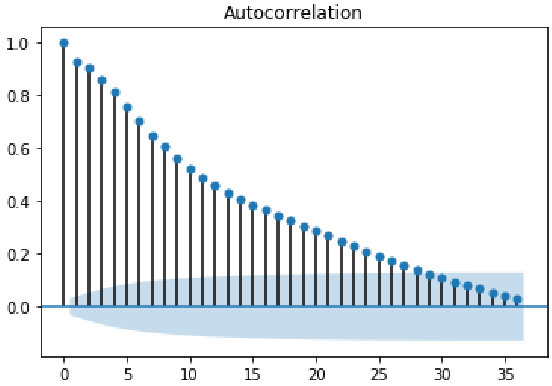

Fig. 3. Graphical representations of ACF

A partial autocorrelation is a summary of the relationship between an observation in a time series with observations at prior time steps after removing the relationships explained by the previous lags.

In general, the autocorrelation for observation and observation at the previous time step consists of both direct and indirect correlations. The indirect correlations are a linear function of the correlation of the observation, with observations at intervening time steps. Partial autocorrelation function aims to eliminate these indirect correlations.

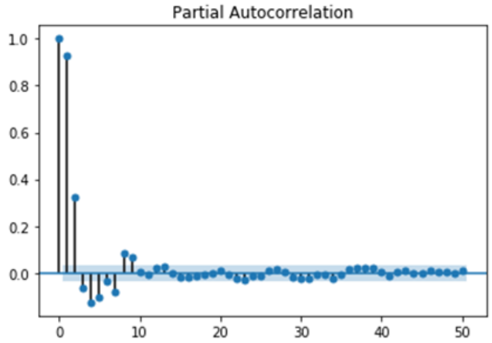

b)

Fig. 4. Graphical representations of PACF

IV. ACCURACY MEASURES FOR THE ELM MODEL

Measures related to the accuracy of some prediction models are usually assessed after its implementation and training [8]. The most important ELM model accuracy measures are defined below:

RMSE - Root Mean Square Error (RMSE) is a commonly used measure of the difference between the values predicted or estimated by a model and the observed values.

$$RMSE = \sqrt{\frac{\sum_{i=1}^{N} \|y(i) - \hat{y}(i)\|^2}{N}}, \tag{4}$$

The RMSE is calculated as the square root of the mean of the squares of all errors, as given in (4). The use of RMSE is very common, and it is considered as an excellent general-purpose error metric for numerical predictions. The deviations of predicted values from the original data are called residuals.

MAPE – The mean absolute percentage error is also a measure of the forecasting system accuracy. This accuracy is measured as a percentage, and can be calculated as the average absolute percent error for each time period reduced by the actual values, and then divided by actual values, as shown in (5). The mean or average of the absolute percentage errors of forecasts is also known as the mean absolute percentage deviation (MAPD). It is a measure of the accuracy of a method for constructing fitted time series values in statistics, specifically in trend estimation.

$$MAPE = \frac{100\%}{n}\sum_{i=1}^{n}\left|\frac{y_i-\hat{y}_i}{y_i}\right|, \qquad (5)$$

MPE is the mean percentage error and is computed as the average of percentage errors by which forecasted values of a model differ from actual values of the quantity that is being forecasted. This is shown in the following equation.

$$MPE = \frac{100\%}{n}\sum\left(\frac{y-\hat{y}}{y}\right), \qquad (6)$$

The mean percentage error (MPE) equation looks like the one for the calculation of MAPE. The only difference is that MPE does not consider the absolute values of the errors. This fact sometimes makes the MPE useful.

In the research performed in this paper the original data set consisted of 3650 daily level measurements performed in the time period between 18 November 2009, and 15 November 2019.

After the model development and implementation in Python, a topology of 100 neurons in the hidden layer showed to be sufficient to achieve a good accuracy forecasting model. The computation time required for the ELM model development was not so demanding, since it required less than a second.

The ELM was trained with 80% of the original data set with 2918 measurements. In order to assess its accuracy, the remaining 20% of data was used as the test set. The accuracy measures obtained by the Python program for the test set are given in the following Table V.

TABLE V
Accuracy measures of the ELM model on the test set

Error	Value
RMSE	10.124 [mm]
MAPE	1.324 [%]
MPE	-0.013 [%]

A graphical representation of the residual values is shown in the following Fig. 5.

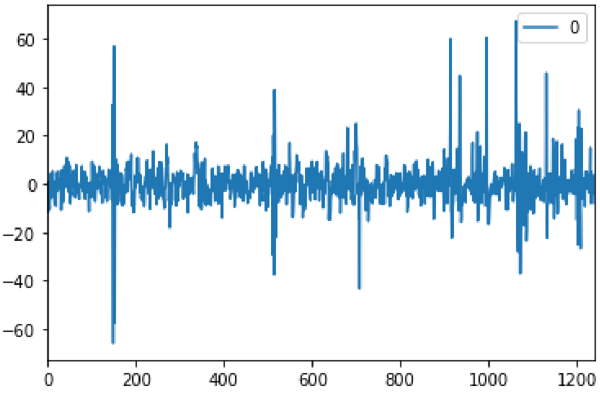

Fig 5. A graphical representation of the residual values

When performing a linear regression, one obtains a line of best fit. The data points usually do not fall exactly on the regression equation line. They are scattered around it. A residual is a vertical distance between a data point and a regression line. Since they represent the difference between the observed value and the predicted value, they can be sometimes considered as errors.

The descriptive statistics for the residual graph are given in in Table VI:

TABLE VI
Descriptive statistics for data

Name	Value
Count	1241
Mean	-0.068408
Standard deviation	8.557295
Min..	-65.977423
25%	-3.905593
50%	-0.333333
75%	3.343750
Max	67.354167

A graphical representation of the original and predicted level of the Danube River for time period between 02 October 2017, and 21 December 2017 is given in Fig. 6.

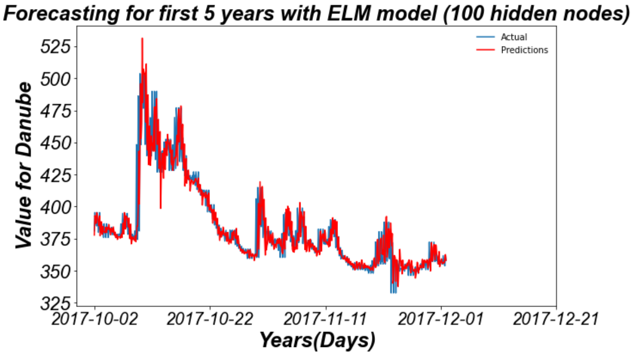

Fig. 6. Original data versus predicted data for a certain period

One can conclude that the ELM network quite accurately follows trend changes of the original data set over time.

V. CONCLUSION

Based on all the above, the ELM model of machine learning proved to be adequate for the observed problem in relation to other models (regression). ELM modelling using the Python programming language showed to be easy to develop.

In this paper, we have investigated the application of ELM for forecasting the daily level of the Danube River. The ELM technique showed good potential for prediction considering the complexity, accuracy and training time. Further research would be oriented to the application of alternative models and machine learning techniques that could perform the required prediction, as well as the implementation of some ensemble predictive models.

ACKNOWLEDGEMENT

This work has been supported by The Ministry of Education, Science and Technological Development of the Republic of Serbia.

REFERENCES

[1] River Basin | ICPDR - International Commission for the Protection of the Danube River

[2] Bezak, N., et al. "A catalogue of the flood forecasting practices in the Danube River Basin." *River Research and Applications,* Vol. 37, Issue 7, pp. 909-918, 2021.

[3] Zabolotnia, T., Liudmyla, G., Borys, K. "Estimation of the long-term cyclical fluctuations of snow-rain floods in the Danube basin within Ukraine." *Meteorology Hydrology and Water Management. Research and Operational Applications*, Vol.7, Issue. 2, pp. 3-7, 2019.

[4] Santos, I. M., et al. "Analysis of seasonal hindcasts for mean-term hydrological forecasting in the Upper Danube River Basin." *Geophysical Research Abstracts*. Vol. 21, EGU2019-15082-1, 2019.

[5] Liptay, Z. Á., and Balázs G. "Operational river ice and water temperature forecasting on the Hungarian Danube reach."*FLOODrisk 2020-4th European Conference on Flood Risk Management*. Budapest University of Technology and Economics, 2021.

[6] Zhao, Y. P., and Chen, Y. B. "Extreme learning machine based transfer learning for aero engine fault diagnosis", *Aerospace Science and Technology*, Vol. 121, 107311, 2022.

[7] Mohammadi, K., Shamshirband, S., Motamedi, S., Petković, D., Hashim, R., Gocic, M. "Extreme learning machine based prediction of daily dew point temperature." *Computers and Electronics in Agriculture*, Vol. 117, pp. 214-225, 2015.

[8] Milić, M., Milojković, J., Marković, I., and Nikolić, P. "Concurrent, performance-based methodology for increasing the accuracy and certainty of short-term neural prediction systems." *Computational intelligence and neuroscience*, Vol. 2019*,* Article ID 9323482.

Digital Twin in Control Cabinet Construction

Dr. Dusko Lukac

Abstract - The digital twin adds a great value to the interlinking of work steps in control cabinet construction. The model is created in electrical design and during assembly planning. The twin then accompanies the entire production process and provides the individual departments with their information. The unique feature: customer, switchgear manufacturers, and their suppliers work with the same model. The device manufacturers supply macros in which all the properties of their products are mapped. The electrical designers insert these devices into their schematic and thus generate a logical version of the model. The layout planner then puts the model into physical form by arranging the devices in the virtual switchgear cabinet. The finished model includes all dimensions and shows the individual devices inside the realistic 3D digital layout. Also included is the entire wiring with all wire paths, cable ducts, top-hat rails (position and length), and all drill holes and cutouts. The haptic representation simplifies many activities, as individual positions in the cabinet are more easily recognized. As a result, production is less time-consuming, and the susceptibility to errors is significantly reduced. Such a solution is presented using the EPLAN platform and the products Data Portal, Electric P8, Pro Panel, including the connection of the software to the actual machines, which have the task of creating a real construction out of the simulation of a digital twin.

Keywords – Digital Twin, Engineering Process, Optimisation, CAE, EPLAN

I. INTRODUCTION

One-third (30%) of the respondents to a survey made by Dassault Systems [1, p.5] consider a digital twin to be a fully defined model that can simulate the entire behavior of a final product.

The second most frequently cited view, at 17%, is that the digital twin is a model that resembles a real product and draws its data from sensors on the real product. 12% of respondents defined the digital twin simply as a 3D model, while another 10% did not know what a digital twin was. Most of those who do not know what a digital twin is are primarily in the oil and gas (19%), automotive (14%), manufacturing (14%), and construction (13%) industries. In other studies [2,3,4], most respondents hope to use digital twins to improve their products and processes. Data sources for Digital Twins according to Gartner study [4] are CAE software / 48%, ERP / 47%, MRO / 45%, Sensors (IoT) / 44%, System Engineering / 44% [2].

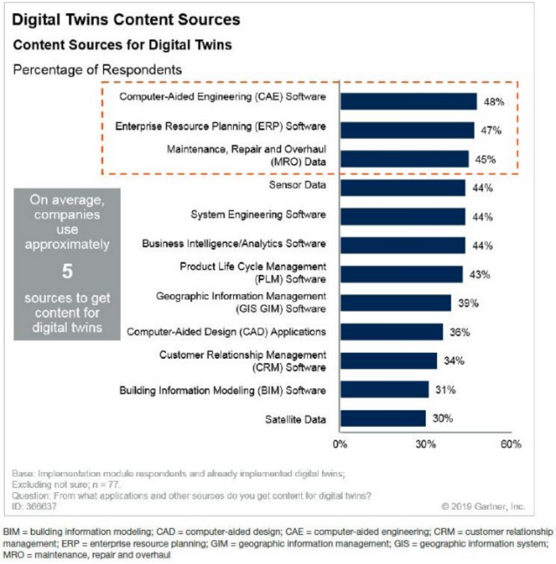

The following paper deals with implementing the digital twin in the CAE area using the example of EPLAN.

II. INDUSTRIAL POTENTIAL OF THE DIGITAL TWIN

The U.S. market researchers declared that digital twins would develop their full potential in five to ten years. In a mentioned study, Gartner now examined the status quo. According to the survey, 13% of the nearly 600 companies surveyed from six countries (including Germany) are currently using digital twins. A further 62% declare that they have already implemented them or intend to do so within a year. Gartner speaks of an early stage of adaptation. The provider market is correspondingly immature. The Internet of Things (IoT) is driving interest in digital twins. Users want, for example, to reduce downtime and repair costs or differentiate their products. More than two-thirds (69 %) use digital twins exclusively or primarily for just one interest group [3,4]. However, in different studies, it is emphasized that the technology offers further possibilities. For example, if we consider self-driving cars: here, four stakeholders - OEM, customer, service provider, and insurance company - can benefit from a digital twin. On the other side, the topic, of course, touches on data privacy issues. But if necessary, not every stakeholder group may be allowed to see all the data. This demands discipline by CIOs. The same applies to managing the digital twin: if something is changed in the haptic product, the digital one has to be upgraded. 87% of respondents say they do this. A large majority of 88% of companies use digital twins for simulation purposes. For example, they test products, plants, or, e.g., how the flight characteristics of an aircraft change when individual parts are designed differently. Similarly, the setup of a stationary store can be simulated [5,6,7]. To implement and to realize a digital twin in the field of CAE, it is necessary to achieve a continuity of the data starting from the initial development process, over device data provision and project planning of a circuit diagram, till to the construction of a 3D model and the data transfer to the physical manufacturing machines.

III. PROCESS OF CREATION OF A DIGITAL TWIN

The digital twin is a complete, application-independent digital description of products, devices, machines, plants, factories, and systems or processes. It connects people, physical assets, digital entities, and systems as a data hub. Data analysis and decision latency have the greatest efficiency potential in the design and development or production segments. The aim is to significantly reduce the time required and the costs incurred while at the same time increasing the quality of the measures taken. The comparison of analog and digital strategies outlines the considerable potential. The more unstructured and decentralized the asset data (concerning products, plants, etc.) is documented and available, the more time each individual work step takes. The digital design based on the digital twin consistently networks data and processes for strategic planning, development, documentation, and production. Suppose data on the digital twin is available in real-time through the coupling of information flow and industry-appropriate software. In that case, deficits such as escalating latency times can be overcome and defeated [8].

A. Parts database and Data Portal

The basis for the development of the digital twin is the parts database. An essential prerequisite for automated enclosure planning and assembly had to be created in advance. All components required for the design of the schematics and, in the second step, the creation of control cabinets for industrial use are stored in EPLAN with all necessary characteristic data and dimensions.

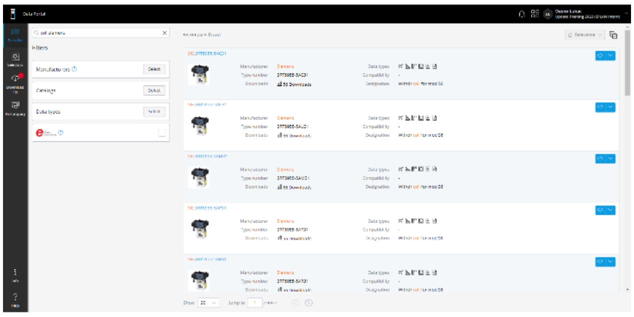

This data is available at EPLAN in the so-called EPLAN Data Portal, where over 1 million device data, such as coils, terminals, connectors, etc., including their dimensions, are available. These form the basis for the construction of the digital twin.

Fig. 3. Device example

For example, suppose a coil with the original Part number of the manufacturer SIE.3RT5935-5AN21 is intended for use the control cabinet. In that case, it must be integrated into a circuit diagram, and it must also include it mechanical dimensions in the parts description.

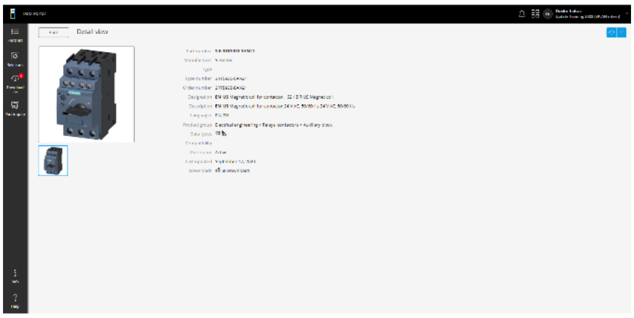

Fig. 4. SIE.3RT5935-5AN21in
EPLAN Data Portal

These data are transferred from the EPLAN Data Portal to the EPLAN Platform.

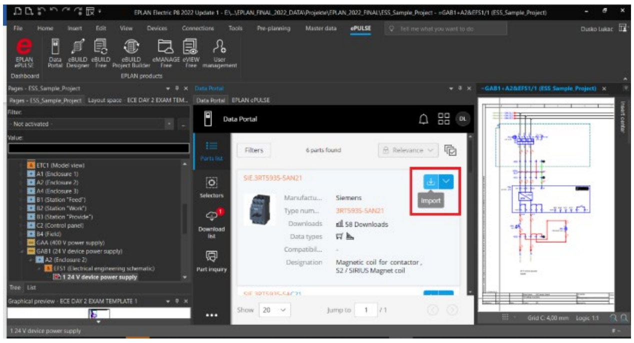

Data Portal

Filters | 6 parts found | Relevance

SIE.3RT5935-5AN21

Manufactu... Siemens

Type num... 3RT5935-5AN21

Downloads 58 Downloads

Data types

Compatibil... -

Designation Magnetic coil for contactor , S2 / SIRIUS Magnet coil

Import

Show 20 | Jump to 1 / 1

Fig. 5. Importing parts from Data Portal into schematics

After importing this data from the EPLAN Data Portal into the EPLAN Platform, this data looks as follows in the parts database.

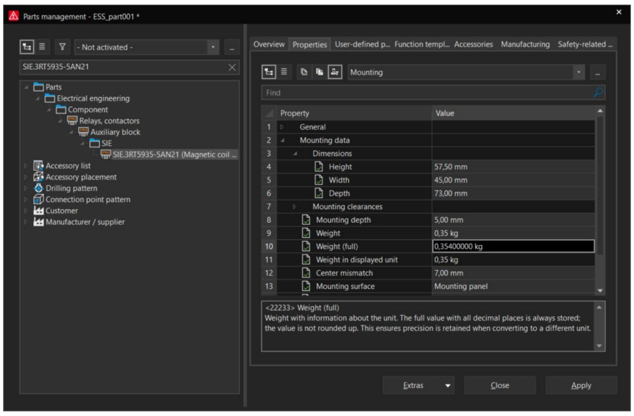

Parts management - ESS_part001 *

- Not activated -

SIE.3RT5935-5AN21

- Parts
  - Electrical engineering
    - Component
      - Relays, contactors
        - Auxiliary block
          - SIE
            - SIE.3RT5935-5AN21 (Magnetic coil ...
- Accessory list
- Accessory placement
- Drilling pattern
- Connection point pattern
- Customer
- Manufacturer / supplier

Overview | Properties | User-defined p... | Function templ... | Accessories | Manufacturing | Safety-related ...

Mounting

	Property	Value
1	General	
2	Mounting data	
3	Dimensions	
4	Height	57,50 mm
5	Width	45,00 mm
6	Depth	73,00 mm
7	Mounting clearances	
8	Mounting depth	5,00 mm
9	Weight	0,35 kg
10	Weight (full)	0,35400000 kg
11	Weight in displayed unit	0,35 kg
12	Center mismatch	7,00 mm
13	Mounting surface	Mounting panel

<22233> Weight (full)
Weight with information about the unit. The full value with all decimal places is always stored; the value is not rounded up. This ensures precision is retained when converting to a different unit.

Fig. 6. EPLAN Parts Database

B. Electrical circuit diagram

The part contains all data that are necessary for the manufacturing process. These are, among other things, the pure dimensions, height, width, depth, weight, but also detailed data such as mounting depth and so on. Before the mechanical manufacturing process, however, the next step is designing an error-free electro-mechanical circuit diagram.

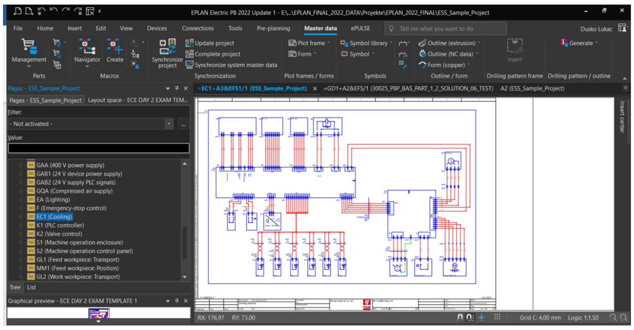

Fig. 6. EPLAN Shemactics example

This means that in addition to the mechanical data, the component must also present logical-symbolic electrotechnical data. These are visible when the coil is placed on a schematic page.

This device and many other devices in the circuit diagram, which are to be part of the future control cabinet, must be connected electrotechnical correctly. To check this, the EPLAN Electric P8 software, for example, as part of the EPLAN platform, responsible for the electrical design, provides numerous functions, including the so-called Messages Management function, with which logical and functional verification of the schematic can be carried out. Once the electrotechnical design is completed, the next step is the design of the 3D digital twin of the system, based on the electrotechnical diagram.

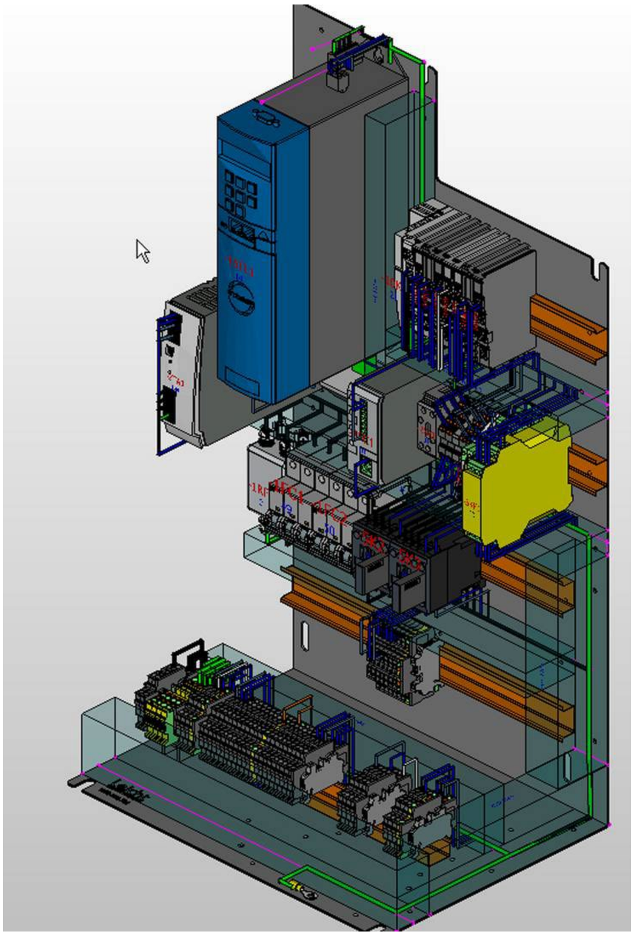

Fig. 6. 3D representation of final device [9]

The following step concerns the construction process of the real, physical system.

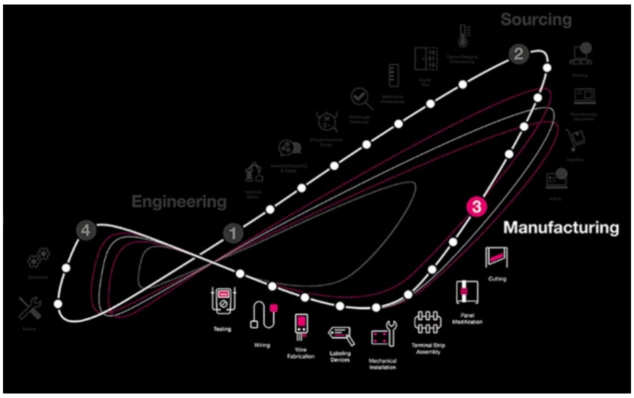

Fig. 7. Integrate Value Chain [11]

The mechanical manufacturing process consists of 8 steps. Besides the data exchange, many individual steps are necessary to produce a real, existing physical system out of the 3D digital representation. These include cutting, panel modification, terminal strip assembly, mechanical installation, labeling devices, wire fabrication, wiring, and testing. All these steps are implemented by special machines such as the following machine, so-called Perforex Milling Terminal MTS. It accelerates the throughput times when machining anything from the smallest enclosures and enclosure panels to large enclosures or control cabinets. Hole-drilling, thread-tapping, and cut-outs in all machinable materials such as steel, stainless steel, aluminum, copper, and plastic. Profitability and process acceleration from a batch size of just 1 [10].

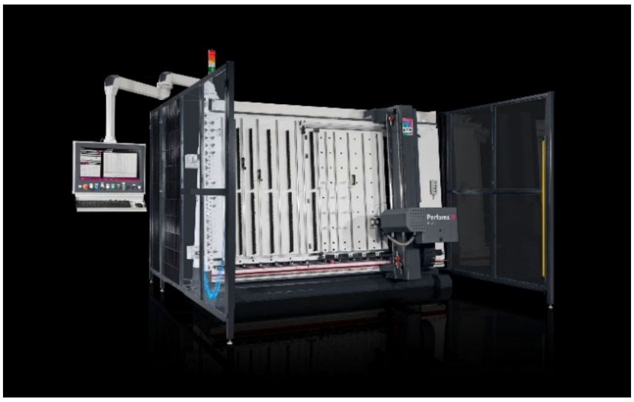

Fig. 8. Perforex Milling Terminal MTS [8]

The Perforex MTS milling terminal speeds up your processing times when machining everything from the smallest cabinets and cabinet walls to large cabinet sizes. With such machines, drilling holes, threads, and cut-outs in machinable materials such as steel, stainless steel, aluminium, copper, and plastic are possible. In this case, cost-effectiveness and process speed-up are already given from a batch size of one. Production automation is the key to fast, reproducible processes with liable high quality. When these steps are done, a real physical plant is created based on a 3D digital twin [12].

Fig. 9. Real representation of final device [9]

Before the development of a finished real plant, the digital twin enables an optimization of the product before its final production in order to avoid possible later (expensive) complaints. In view of these advantages and the high demand for the extended engineering services, one of the goals for the near future is for customers to configure their projects on one platform and receive the (largely automated) design with all parts lists, 3D views and circuit diagrams. The benefits of this new way of dividing the workload are enormous: some companies expect to reduce the time needed for electrical planning by around 75%. At the same time, this new design methodology will also change the cooperation with the mechanical engineers.

IV. CONCLUSION

With the digital twin approach, the companies are developing from control cabinet manufacturers and engineering service providers into system houses. Such approaches are future-oriented and will play a decisive role in international competition.

REFERENCES

[1] Roopinder Tara (2021), "Are We Ready for Digital Twins? Audience survey of perceptions and readiness", Engineering.com, Vol. 1, No. 1, pp. 1-29, Oct. 2021.

[2]Rainhard Geissbauer (2017), "Digital Factories 2022, Shaping the Future of Manufacturing", PWC,Vol. 1, No. 1, pp. 1-48, May 2017. https://www.pwc.de/de/digitale-transformation/digital-factories-2020-shaping-the-future-of-manufacturing.pdf

[3] Daniel Kunz (2021), „No smart factory without digital twins“, Deutsche Telekom Study, March 2021

[4] Christiane Pütter (2019), "The Digital Twin is entering the enterprise", Gartner, 11.03.219

[5] Abdulmotaleb El Saddik; Fedwa Laamarti; Mohammad Alja'Afreh (2021) "The Potential of Digital Twins", Published in: IEEE Instrumentation & Measurement Magazine (Volume: 24, Issue: 3, May 2021),Page(s): 36 - 41,DOI: 10.1109/MIM.2021.9436090, Publisher: IEEE

[6] Roberto Minerva; Gyu Myoung Lee; Noël Crespi (2020) "Digital Twin in the IoT Context: A Survey on Technical Features, Scenarios, and Architectural Models" Proceedings of the IEEE (Volume: 108, Issue: 10, Oct. 2020), Date of Publication: 18 June 2020
DOI: 10.1109/JPROC.2020.2998530, Publisher: IEEE

[7] Andrea Barni; Alessandro Fontana; Silvia Menato; Marzio Sorlini; Luca Canetta (2019) "Exploiting the Digital Twin in the Assessment and Optimization of Sustainability Performances"
Date of Conference: 25-27 Sept. 2018, 09 May 2019,Print on Demand(PoD) ISSN: 1541-1672, DOI: 10.1109/IS.2018.8710554, Publisher: IEEE

[8] EPLAN (2020), “Engineering 4.0 - Studie von E4TC und EPLAN “, Vol. 1, No. 1, pp. 1-29, Oct. 2021.

[9] EPLAN (2021), “Electrical design with the digital twin "Smart Engineering" for Building Services and Industry at Alexander Bürkle”, https://www.eplan.de/branchen/anwenderberichte/alexander-burkle-gmbh-co-kg-elektrokonstruktion-mit-dem-digitalen-zwilling/, accessed 12.12.2021, 16:22h

[10]Rittal Automation (2021), Range of solutions, https://www.rittal.com/com-en/products/PGRP18861RAS1, accessed 12.12.2021, 16:01h

[11]Rittal (2021), Integrated Value Chain, https://webinfo.rittal.com/en/ras-optimize-machining-process, accessed 12.12.2021, 16:33h

[12] Rittal (2021), „Perforex Milling Terminal MT S“ https://www.rittal.com/com-en/products/PGRP18861RAS1/ G21102101RAS1/PGRP38763?hsCtaTracking=3ca3fcbd-5a0f-4b55-acfa-eabf8c881712%7C78abe36d-587b-4bf8-b672-743c9b6460c9,accessed 12.12.2021, 15:21h

Proceedings of the 9th Small Systems Simulation Symposium 2022, Niš, Serbia, 28th February - 2nd March 2022

The Influence of Regression Kernel Function at Predictive Modeling in Electronics

Malinka Ivanova and Zdravka Tchobanova

Abstract - The paper presents an approach for predicting the power dissipation in electronic circuits through utilization of support vector machine, which is an algorithm from controlled machine learning. Three predictive models are created, outlining the power dissipation at different values of power supply and load resistance. The models are evaluated considering four regression kernel functions: dot, polynomial, radial and epachnenikov. The results show that the most suitable kernel function can be found and used for creation of a concrete model with a small error.

Keywords – machine learning, regression analysis, support vector machine, kernel function, electronic circuit

I. INTRODUCTION

Nowadays, machine learning as a part of artificial intelligence is used in electronics with different purposes: for behavioural modelling, parameters prediction, circuits analysis. Also, it is applied in Electronic Design Automation (EDA) software for improving the designers' productivity and facilitating some engineering tasks [1], [2]. Machine learning is a contemporary approach in analog and digital electronics, used for better understanding the circuit processes, for revealing some facts, patterns or anomalies. It utilizes the gathered data from mathematical models, from simulations or from real experiments to process them, giving additional knowledge about circuits' behavior, their properties, parameters and characteristics. Different papers discuss the utilization of some machine learning algorithms, which prove that they are very suitable for performing regression or classification tasks [3], [4]. New methods and methodologies are proposed too in support of decision making when optimization problems have to be solved or controlling functions have to be improved [5], [6]. Our previous research presents the created conceptual framework about machine learning usage in electronics, which summarizes applications of algorithms for supervised, semi-supervised, unsupervised, reinforcement, deep learning, genetic and evolutionary algorithms for adding different level of intelligence in electronic devices and modules, needed for building internet of things infrastructure, for implementation of medical, security, roboticizied systems, for development of precise measurement, fault detection, diagnostic, monitoring devices [7]. It seems that machine learning techniques and methods have great potential for processing big data, collected during operations' conductance of devices or systems and for improving their efficiency.

Regression analyses is applied when an evaluation of a relationship among a dependent and several independent variables has to be performed. Regression algorithms are suitable for determining the dependence between different factors with the aim some predictions to be gathered. Among the most used supervised algorithms for regression tasks is Support Vector Machine (SVM), which is characterized with availability of some parameters for regulating over-fitting and with kernel functions to deal with high dimensional data. The kernel functions possess given properties, which have an impact at developing more precise predictive models.

In this work the focus is placed on examining the importance of kernel functions for finding the best predictive model, which is capable of pointing out the most appropriate values of power dissipation in a given topology of electronic circuits. The correct way for power dissipation guarantees the normal workability of the circuit and of the whole electronic device at various environmental conditions. Several papers propose methods for power estimation taking into account the capabilities of machine learning algorithms and technology specifics [8]. It is known that the process of power estimation is related to the values of power dissipation, as well as to the operating sircuit mode and to other its parameters. The topic about the mutual dependence of power supply, power dissipation and power consumption is substantial for Integrated Circuits (ICs) and Operational Amplifiers (OpAmps) when they are applied for realization of different electronic modules and devices. Further exploration regarding the meaning of machine learning algorithms on the proper recognition of the main factors that influence on power dissipation is required. Also, the evaluation of the predictive ability of created models should be performed.

Thus, the aim of this work is to examine the influence of kernel functions at predictive modelling the behavior of electronic circuits when the regression problems have to be solved. In particular, a study on the power dissipation in an analog circuit is conducted through usage of SVM supervised algorithm. The models are evaluated with the aim the model with the highest accuracy to be outlined at a given kernel function.

II. REGRESSION ANLYSIS AND KERNEL FUNCTIONS

An application of regression algorithms is related to prediction of a dependent output variable taking into account its connection to several other independent input variables. More popular algorithms for conductance regression analysis are linear and polynomial regression, neural network regression, tree-based regression, and support vector regression. The exploration in this work is focused on regression analysis where the SVM algorithm is the learner. The regression process at the SVM concerns solving an optimization task related to finding a straight line and an interval from –ε to +ε where the data dots are allowed to appear. There is a solution of this optimization only when all data dots (x_i, y_i) from the data training set could be approximated with a given accuracy ε. The searched linear function $f(x)$, which is characterized with deviation ε from the observed y_i values, is calculated in the form [9], [10]:

$$f(x) = \langle w, x \rangle + b, \qquad (1)$$

where $\langle w, x \rangle$ is the product and b is bias.

The function flatness could be achieved when w is smaller. Thus, the optimization task when $f(x)$ is defined and approximated all data dots (x_i, y_i) with accuracy ε is formulated in the following way:

$$\begin{aligned} & f(x) - y_i \le \varepsilon \\ & y_i - f(x) \le \varepsilon \qquad (2) \\ & \min \frac{1}{2}\|w\|^2, \end{aligned}$$

where the norm $\|w\|_2$ is:

$$\|w\|_2 = \left(\sum_{i=1}^{n} (w_i . w_i)\right)^{1/2} \qquad (3)$$

In practice this is a very rare case, because some data dots can not be put between the borders (-ε, +ε). For the deviated data dots are used slack variables ζ1 and ζ2 and the optimization problem is defined as follows:

$$\begin{aligned} & f(x) - y_i \le \varepsilon + \xi 1_i \\ & y_i - f(x) \le \varepsilon + \xi 2_i \\ & \xi 1_i . \xi 2_i \ge 0 \qquad (4) \\ & \min\left[\frac{1}{2}\|w\|^2 + C\sum_{i=1}^{l} (\xi 1_i + \xi 2_i)\right], \end{aligned}$$

where C is a positive constant, used to present the balance between the flatness of $f(x)$ and admissible deviation towards ε.

In non-linear case, the optimization task concerns finding a higher dimensional space through an optimal hyperplane. Thus, the data x_i should be mapped into a richer feature space that include non-linear features and in this space a hyperline could be constructed, e.g. the data x_i should be preprocessed $x_i \to \Phi(x)$ and then the obtained map to be learned: $f(x) = w.\Phi(x) + b$. So, here the approximation problem is related to finding the function:

$$f(x) = \sum_{i=1}^{N} (\alpha 1_i - \alpha 2_i) k(x_i, x) + b, \qquad (5)$$

where $\alpha 1_i$ and $\alpha 2_i$ are Lagrange multipliers and $k(x_i, x)$ is the kernel function.

The following kernel functions are explored in this work:

Dot – The dot kernel function is calculated as an inner product of the x_i and x:

$$k(x_i, x) = x_i . x.; \qquad (6)$$

Polynomial – The polynomial kernel function depends on the kernel degree parameter *d* and the following formula is used for calculation:

$$k(x_i, x) = (x_i . x + 1)^d .; \qquad (7)$$

Epachnenikov – The Epachnenikov kernel function has the following form:

$$k(u) = 3/4(1 - u^2), \qquad (8)$$

where *u* is in the range from -1 to 1 and outside this range it has zero value. The changeable parameters are kernel degree and kernel sigma 1.

Radial – The radial kernel is calculated according to the following equation:

$$k(x_i, x) = \exp\left(-\frac{\|x - x_i\|^2}{2\sigma^2}\right), \qquad (9)$$

where σ is adjustable parameter, which reflects on the kernel performance.

The used metrics for models evaluation includes the values of:

Malinka Ivanova, Assoc. Prof. PhD, Technical University of Sofia, Faculty of Applied Mathematics and Informatics, E-mail: m_ivanova@tu-sofia.bg.

Zdravka Tchobanova, Assist. Prof. PhD, Technical University of Sofia, College of Energy and Electronics, E-mail: z.chobanova@tu-sofia.bg.

Root mean square error (RMSE) – it gives the squared value from the difference between the observed value x and predicted $\bar{x}$ as the data set consists of n records:

$$RMSE = \sqrt{\frac{\sum_{i=1}^{n}(x_i - \bar{x}_i)^2}{n}}. \tag{10}$$

Absolute error (AE) – it points out the difference between the observed x and predicted value $\bar{x}$:

$$AE = \left|x - \bar{x}\right|. \tag{11}$$

Relative error (RE) – if x is the observed value and $\bar{x}$ is the predicted one, then the RE is:

$$RE = \frac{x - \bar{x}}{\bar{x}}. \tag{12}$$

Correlation – it gives the relationship among labelled and predicted values. The correlation is positive when these two variables change their values in one direction. In the adverse case, the correlation is negative. At the neutral correlation there is no relationship in the changed variables.

III. USED METHODOLOGY

In this work, the used methodology includes: (1) *Circuit design* in LTspice software, taking into account the recommended parameters in the data sheet of the amplifier AD8038.; (2) *Data collection* – Data sets are gathered through simulations and through mathematical equations, describing the circuit behaviour in frequency and time domain.; (3) *Data pre-processing* – the data sets are prepared in .csv files as different models use different data sets. Part of gathered data is shown via Table I, where V_{out} is the output voltage, PD is power dissipation, R_L is resistance of the load, V_S is the supply voltage.; (4) *Data training*, which is conducted in RapidMiner Studio through applying SVM learner.; (5) *Models evaluation* that is performed at different kernel functions of SVM.

TABLE I. COLLECTED DATA

V_{out}, V	…	PD, mW at R_L=500	PD, mW at R_L=1k	PD, mW at R_L=1.5k	…	V_S, V
4.1300	…	40.3200	20.8500	15.0500	…	9
4.1418	…	40.3251	20.8550	15.0585	…	9
4.1575	…	40.3319	20.8618	15.0704	…	9
…	…	…	…	…	…	…

IV. POWER DISSIPATION

The normal operation of the ICs or OpAmp depends on the proper power dissipation at appropriate environmental conditions. Exceeding the allowable power dissipation could lead to the improper ICs workability or even can damage them irreversible. Therefore, all specifications of the ICs, whether they are micro-power, low-power or high-power, include studies on the values of the released power. The correct settings of the operating mode and operating parameters are responsible for the correct operation of the ICs and the normal power dissipation. The dissipated power from the ICs packages depends on the current and voltage of the power supply I_s and V_s and the output power released on the load V_{out}. Thus, the knowledge about admissible and maximal values of the power dissipation is important to be taken into consideration at the design and analysis of different ICs applications. The Eq. (14) points out how the power dissipation is calculated taking into account the values of power supply, dissipated power in the package and the load power [11], [12]:

$$PD = V_S I_S + \frac{V_{out}}{R_L}\left(\frac{V_S}{2} - V_{out}\right). \tag{13}$$

Knowing power dissipation, the junction temperature T_j could be calculates, considering that its value could not be more that the maximal one, given in the data sheet:

$$T_j = T_A + (PD.R_{jA}), \tag{14}$$

where T_A is the ambient temperature and R_{jA} is the thermal resistance.

V. EXPERIMENTS AND RESULTS

In the conducted experiment a passband fourth order active filter is designed with two MFB stages from second order (Fig 1). The used amplifier is AD8038, which possesses following characteristics: supply range - from 3V to 12V (we used V_s=9V), I_s=1mA (max value is 1.5mA), range of the operating temperature is from -40°C to +85°C, the max safe power dissipation in the package SOIC at 125°C ambient temperature is around 0.2W [11]. More precise information about the power supply voltage and power supply current is taken from the AD8038 data sheet. The low power amplifier AD8038 is chosen, because of its applications in instrumentation, filters, A/D drivers, buffers. The obtained magnitude-frequency and phase-frequency characteristics of the simulated passband filter are presented on Fig. 2.

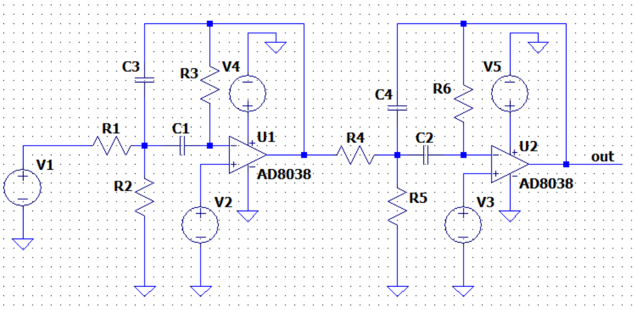

Fig. 1. Passband filter from fourth order

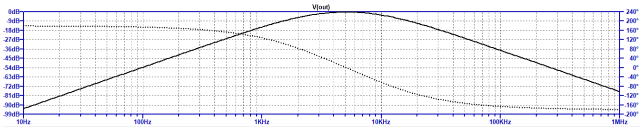

Fig. 2. Magnitude-frequency and phase-frequency characteristics

SVM algorithm is used as a learner of the collected data after conducted filter simulations as well as taking into consideration the equations for power dissipation. The following models are created:

(1) A model for predicting the power dissipation according to the value of the load – the data set is prepared after performed simulations at a constant value of the power supply (I_s and V_s).

(2) A model for predicting the power dissipation at different values of the power supply at one and same load.

(3) A model, predicting the power dissipation in the case when the power supply and the load are with changeable values.

The models are evaluated at different kernel functions of SVM algorithm according to the calculated errors and correlation coefficients.

Table II presents the results after evaluation of the first model, which predicts the power dissipation considering the load value. It seems that the RMSE is the smallest at radial kernel function of the SVM algorithm and it is highest at epachnenikov kernel.

Table III includes the evaluated parameters of the second model, which shows the prognostic power dissipation according to the power supply. The smallest RMSE is obtained at the dot kernel and the highest error is received at the polynomial kernel function.

Table IV shows the evaluated parameters of the third model, which is created to predict power dissipation, considering changeable values of the power supply and load resistance. All kernel functions are characterized with approximately zero errors.

One graphics with simulated and predicted power dissipation regarding the output voltage for the second model is presented on Fig. 3 and it is seen the small error of predictions. It proves that the SVM algorithm can be used for prediction purposes at electronic circuits design and analysis. It is important the parameters of SVM algorithm like kernel function to be chosen correctly for achieving more precise model. The errors received after applying a given kernel function depends on the model construction and the specifics of the data set. Comparison of the regression kernel functions considering the created three models is presented on Fig. 4. It can be said that the highest accuracy of every model is achieved at different kernel function. It means that the correct kernel function has to be found at any specific model.

The obtained correlation coefficients for all models and at all kernel functions are positive, which shows that the changes of the exploraed variables are in one and the same direction. Bigger correlation values reveal close relationships among the explored variables (power dissipation, supply voltage and load resistance) and give possibility to predict one variable from the other. For the first model, the biggest correlation is achieved at the radial kernel. In the second model, the correlation coefficients for three of the kernel functions: dot, radial and epachnenikov are very big. In the third model, the highest correlation is obtained at the radial kernel.

TABLE II. EVALUATION OF THE FIRST MODEL

Kernel/ parameter	dot	radial	polynomial	epachnenikov
RMSE	0.430 +/- 0.000	0.178 +/- 0.000	0.603 +/- 0.000	0.635 +/- 0.000
AE	0.325 +/- 0.282	0.100 +/- 0.147	0.407 +/- 0.445	0.521 +/- 0.363
RE	20.56% +/- 15.25%	8.56% +/- 14.12%	39.19% +/- 45.70%	41.63% +/- 38.94%
correlation	0.707	0.940	0.183	0.436

TABLE III. EVALUATION OF THE SECOND MODEL

Kernel/ parameter	dot	radial	polinomial	epachnenikov
RMSE	0.206 +/- 0.000	0.635 +/- 0.000	5.255 +/- 0.000	0.899 +/- 0.000
AE	0.181 +/- 0.097	0.324 +/- 0.546	4.494 +/- 2.724	0.514 +/- 0.738
RE	1.31% +/- 1.07%	2.82% +/- 5.74%	33.83% +/- 31.34%	4.12% +/- 8.07%
correlation	0.999	0.996	0.000	0.990

TABLE IV. EVALUATION OF THE THIRD MODEL

Kernel/ parameter	dot	radial	polinomial	epachnenikov
RMSE	0.001 +/-	0.000 +/-	0.001 +/- 0.000	0.000 +/- 0.000

	0.000	0.000		
AE	0.001 +/- 0.001	0.000 +/- 0.000	0.001 +/- 0.000	0.000 +/- 0.000
RE	0.72% +/- 0.47%	0.29% +/- 0.18%	0.45% +/- 0.23%	0.25% +/- 0.17%
correlation	0.350	0.936	0.787	0.939

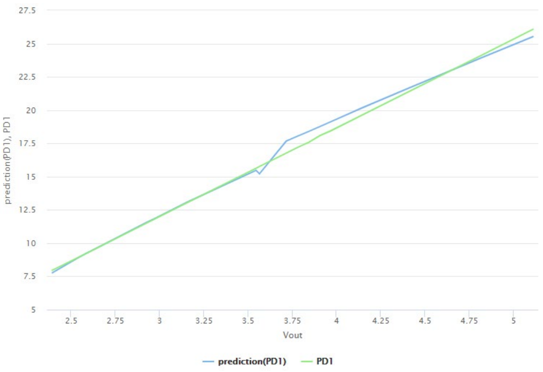

Fig. 3. Simulated and predicted power dissipation for the second model

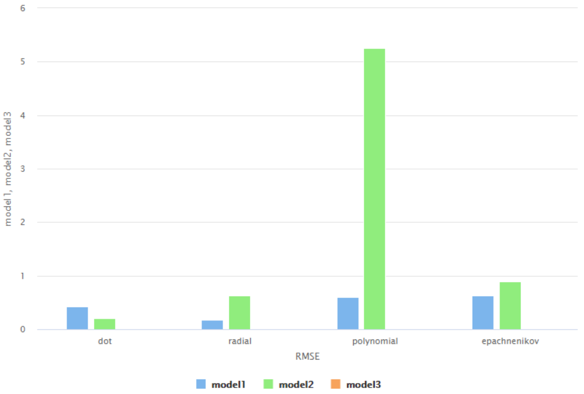

Fig. 4. Comparison of the kernel functions

VI CONCLUSION

In this paper an exploration regarding the influence of the regression kernel functions on the models' accuracy is performed. It is proved that the power dissipation in a low power filter could be predicted taking into account the values of the power supply and the resistance load as the received errors are very small. The calculated correlation coefficients at some kernel functions are very big that gives the possibility the power dissipation to be predicted knowing the power supply and/or resistance load.

ACKNOWLEDGEMENT

This research is supported by Bulgarian National Science Fund in the scope of the project "Exploration the application of statistics and machine learning in electronics" under contract number КП-06-Н42/1.

REFERENCES

[1] Huang, G. et al., "Machine Learning for Electronic Design Automation: A Survey", *ACM Transactions on Design Automation of Electronic Systems*, Vol. 26, Issue 5, pp 1–46, Sept. 2021, https://doi.org/10.1145/3451179.

[2] Fallon, E., "Machine Learning in EDA: Opportunities and Challenges", *2020 ACM/IEEE 2nd Workshop on Machine Learning for CAD (MLCAD)*, 2020, doi: 10.1145/3380446.3430687.

[3] Lin, H. and Li, P., "Circuit Performance Classification with Active Learning Guided Sampling for Support Vector Machines", *IEEE Transactions on Computer-Aided Design of Integrated Circuits and Systems*, Vol. 34, No. 9, pp. 1467-1480, Sept. 2015, doi: 10.1109/TCAD.2015.2413840.

[4] Pandiaraj, K., Sivakumar, P., Jeya Prakash, K., "Machine learning based effective linear regression model for TSV layer assignment in 3DIC", *Microprocessors and Microsystems*, V. 83, June 2021, https://doi.org/10.1016/j.micpro.2021.103953.

[5] Xu, C., L., Yi, Liao, X., Cheng, J, Yang, Y., "Machine Learning Regression-Based Single-Event Transient Modeling Method for Circuit-Level Simulation", *IEEE Transactions on Electron Devices*, Vol. 68, No. 11, pp. 5758-5764, Nov. 2021, doi: 10.1109/TED.2021.3113884.

[6] Dieste-Velasco, M. I., Diez-Mediavilla, M., and Alonso-Tristán, C., "Regression and ANN Models for Electronic Circuit Design", *Complexity*, Vol. 2018, Article ID 7379512, https://doi.org/10.1155/2018/7379512.

[7] Ivanova, M., Petkova, P., Petkov, N., "Machine Learning and Fuzzy Logic in Electronics: Applying Intelligence in Practice", *Electronics*, 10(22), 2021, https://doi.org/10.3390/electronics10222878.

[8] Govindaraj, V. and Arunadevi, B., "Machine Learning Based Power Estimation for CMOS VLSI Circuits", *Applied Artificial Intelligence*, Vol. 35, Issue 13, pp. 1043-1055, doi: 10.1080/08839514.2021.1966885.

[9] Basak, D., Pal, S., Ch, D., and Patranabis, R., "Support Vector Regression", *Neural Information Processing – Letters and Reviews*, Vol. 11, No. 10, Oct. 2007, pp. 203-224.

[10] Muthukrishnan, R. and Maryam Jamila, S., "Predictive Modeling Using Support Vector Regression", *International Journal of Scientific & Technology*, Vol. 9, Issue 2, Feb. 2020, ISSN 2277-8616, pp. 4863-4865.

[11] Analog Devices, "Low Power, 350 MHz Voltage Feedback Amplifiers AD8038/AD8039", https://www.analog.com/media/en/technical-documentation/data-sheets/AD8038_8039.pdf.

[12] Analog Devices, "Ultraprecision Operational Amplifier OP177", https://www.analog.com/media/en/technical-documentation/data-sheets/OP177.pdf.

Proceedings of the 9th Small Systems Simulation Symposium 2022, Niš, Serbia, 28th February - 2nd March 2022

Edge Detection and Image Alignment in Thermal Image Processing Used for PCB Diagnostics

Miljana Milić and Milica Kitić

Abstract— **The paper presents an image processing part of a custom-made system for automatic image registration for thermal imagery of small electronic systems that uses infrared temperature sensor circuitry and a Matlab application. Using this system high quality and more informative thermograms of the discrete electronic circuit can be obtained. The proposed system offers an efficient solution for detecting the faulty components or areas on an electronic printed circuit board, with good accuracy and flexibility.**

Keywords— Matlab; thermal-imaging; electronic circuits; temperature measurement; edge detection; image detection;

I. INTRODUCTION

Thermal imaging or infrared thermography, as a part of engineering and scientific discipline, represents the procedure of detecting energy from infrared radiation with wavelengths between 9µm and 14µm. It requires devices/sensors that can capture infrared radiation emitted from an object, convert it to temperature, and display the image of the temperature distribution in the form of a thermogram. All objects with a temperature above absolute zero emit infrared radiation; thermography makes it possible to see the objects even without their visible illumination. If the object's temperature rises, the IR radiation also increases, which makes temperature changes observable in space and time. Warm objects are then much easier to distinguish against the colder environment.

Thermographic analysis during each development step enables important conclusions for the optimization of heat management and the design of complex electronic assemblies. In electronics production, thermographic temperature measurement is used as a compulsory procedure for quality assurance [1]. High-performance thermography has become obligatory in critical technological parameters set up and their permanent monitoring, as well as for inline testing of products in the production process and their final functional test.

Applications of thermal imaging are numerous, and they can be found in all aspects of engineering, science, and life. The thermographic inspection of electronic components and systems is a well-established test procedure for failure detection and quality management, from the development of first prototypes to the serial production. For example, this enables the detection of hotspots and atypical temperature distributions on the surface of printed circuit boards. Increased contact resistances or increased resistance due to the uneven width of wires can be detected easily and safely. Hidden cracks in contacts of the circuit elements that cannot be detected by a human eye appear clearly on thermal images. Some of the other instances where it is very helpful to use thermal detection are power losses due to RF mismatch, incorrect thermal connections of heat sinks, short circuits, soldering defects such as cold solder joints, etc.

On the other hand, cold spots are one of the most common faults in electronic devices. Tin as a basic bonding material-metal, becomes in the molten state, at a temperature of about 270° C, and is applied to the printed circuit board to achieve an electrically conductive connection between the components and the printed circuit board.

Cold spots are mostly caused due to an insufficiently melted and heated tin that crystallizes. Because the contact between the metals is not realized in the full sense, a bond with transient resistance is created. Over time, the joint oxidizes and the transient resistance increases until permanent or intermittent interruptions occur. At the same time, this interruption is mostly invisible to the naked eye. [2]. Thermal images can also be used in these situations, in order to quickly resolve errors, avoid possible issues and further circuit faults.

This paper presents the development of a computer program that will be able to align thermal and regular images of electronic circuits PCB. The idea behind this procedure is to overlap these two images in order to obtain a thermal image of the PCB with much more useful information than from those images obtained with the regular image of the printed circuit. The proposed non-contact system receives a temperature image obtained from the specific IR sensor MLX90614 and a regular image from a simple web camera. A data processing application for their alignment was developed using the Matlab program. The main purpose of this diagnostics' application is to allow users to notice irregularities in the temperature of the exact problematic electrical circuit element or area, quickly and easily, immediately after uploading images, and react.

It is very important to detect the exact faulty

Miljana Milić, and Milica Kitić are with the Faculty of Electronic Engineering, University of Niš, Aleksandra Medvedeva 14.
E-mail: miljana.milic@elfak.ni.ac.rs, mix.milica@gmail.com

electronic circuit component before it gets to a state that produces irreversible damage to the whole circuit, and this is the key motivation for diving into the described project. Thermal image cameras provide a circuit overview that shows hot and cold areas but do not detect their exact cause. We can obtain the lacking information by aligning a thermal image with a regular one, showing to the user exactly which area of the circuit has potential defects or the exact component that is faulty.

The paper is organized in the following manner. We will analyze the basic concepts and requirements of the suggested system in the next section. It was necessary to develop a specific code for image processing and enhancing and to improve the edge detecting procedure, and this was given in the third section. The fourth section describes the process for achieving the successful image alignment and overlay that allows users to easily detect irregularities. In the fifth section, we will go over the user interface, and provide a detailed explanation of the layout and functions. Final remarks and conclusions, as well as the ideas for further improvement of the system, are given in the conclusion.

II. PROPOSED SYSTEM SET-UP AND FUNCTIONING

The aim of this thermo-vision system is to detect the overheated or cold spots in discrete electronic circuits in a non-destructive, contactless manner, to improve the system's thermal stability and reliability, and enable defect diagnostics [3]. The entire imaging equipment needed to capture the infrared thermal images consists of two parts: hardware and software.

Software part is the problem that we will deal with in this research and it relies on the application of the Matlab program. Matlab (an abbreviation of "MATrix LABoratory") is a proprietary multi-paradigm programming language and numeric computing environment developed by MathWorks [4]. Matlab allows matrix manipulations, plotting of functions and data, implementation of algorithms, creation of user interfaces, and interfacing with programs written in other languages.

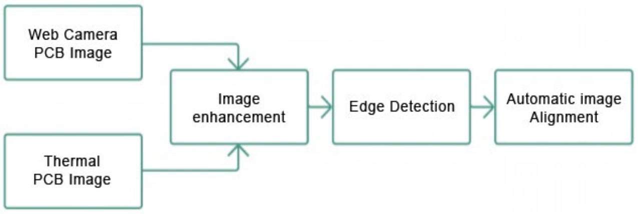

Fig. 1. Steps in image processing

Although Matlab is intended primarily for numeric computing, Image Processing Toolbox provides a comprehensive set of reference-standard algorithms and workflow applications for image processing, analysis, visualization, and algorithm development. One can perform image segmentation, image enhancement, noise reduction, geometric transformations, and image detection/recognition using deep learning and traditional image processing techniques. The toolbox supports processing of 2D, 3D, and arbitrarily large images. This can be very helpful when dealing with low-resolution images from small web cameras, where components would be hard to detect.

The application we are using for images processing and aligning is developed in Matlab. Finalized application could be exported to be executable on other processor units. First, web camera images of electronic circuits are uploaded to Matlab. These images require a certain enhancement in order to be useful for further processing. This allows easy detection of all PCB parts on a combined image. After that, both thermal and web-camera images of a PCB undergo through the edge-detecting process. Finally, thermal images of the circuit are aligned with the corresponding web-camera circuit images. The result of this manipulation is an overlaid and semitransparent PCB image, which provides easy visual detection of heated and cooled circuits components and areas. These steps are illustrated in Fig.1.

III. IMAGE PROCESSING AND EDGE DETECTION

Electrical Circuit images taken with a web camera can have very low quality. To assure the correct web camera image alignment with the thermal image version, Image processing or digital image processing is required. It involves performing certain operations on an image in order to get an enhanced image or to extract some useful information from it before performing further analysis. Procedures that are usually conducted to improve the image quality are noise reduction or removal, deblurring, filtering (brightness, contrast)...

Examples of an image before and after image processing, with the purpose of clearer view is shown in Fig 2. Figure also illustrates the same image after its edge-detection.

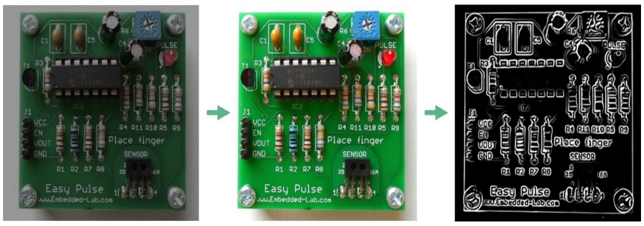

Fig. 2. Example of a Web Camera image after image processing and edge-detecting steps

Edge detection is an image processing technique for finding the boundaries of objects within images. It detects changes in brightness within an image. Besides, edge detection can be a useful pre-processing step for image segmentation. Additional filtering and setting ensure precise edge detection and basis for accurate image alignment.

IV. AUTOMATIC IMAGE ALIGNMENT

Image alignment is a positioning process for images from different data sets or sources, for either visual comparison or computational analysis. There are two major categories of automatic image alignments in Matlab:

- Intensity-based – aligning two images based on intensities, for example aligning a similar extreme change of color or brightness somewhere across the image. One real-life example for using this image registration category would be detecting parts of maps and aligning streets or other standing out components.
- Feature-based – extracting different features like corners, edges, particular unique features within the image.

The first step includes loading images into Matlab and setting 'imregconfig' function parameter to 'multimodal'. This means that images will come from different sources i.e., cameras. After loading images, the function we are calling is with a registration type. Finally, we're selecting the transformation type necessary to overlay images correctly. These functions are shown in Fig. 3.

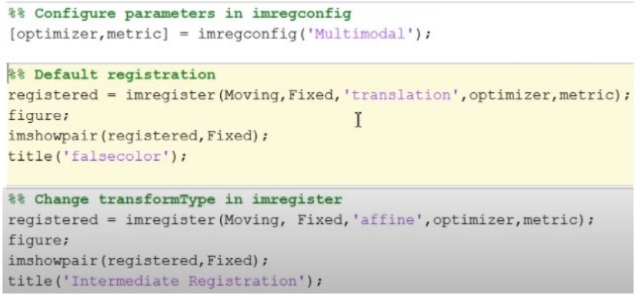

```
%% Configure parameters in imregconfig
[optimizer,metric] = imregconfig('Multimodal');

%% Default registration
registered = imregister(Moving,Fixed,'translation',optimizer,metric);
figure;
imshowpair(registered,Fixed);
title('falsecolor');

%% Change transformType in imregister
registered = imregister(Moving, Fixed,'affine',optimizer,metric);
figure;
imshowpair(registered,Fixed);
title('Intermediate Registration');
```

Fig. 3. MATLAB functions for executing image alignment process

There are four transformation types for correct image alignment that depend on thermal and web-camera image differences in rotation, scale, shear, or position. Those types are shown in Fig. 4.

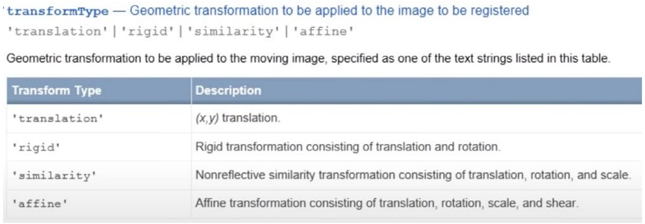

'transformType — Geometric transformation to be applied to the image to be registered

'translation' | 'rigid' | 'similarity' | 'affine'

Geometric transformation to be applied to the moving image, specified as one of the text strings listed in this table.

Transform Type	Description
'translation'	*(x,y)* translation.
'rigid'	Rigid transformation consisting of translation and rotation.
'similarity'	Nonreflective similarity transformation consisting of translation, rotation, and scale.
'affine'	Affine transformation consisting of translation, rotation, scale, and shear.

Fig. 4. MATLAB functions for executing image alignment process

When the images are first imported, besides being different types, their dimensions, rotation, and perspective can vary and be different from one another. Figure 5 shows the two pairs of web camera and thermal images, of which the first pair represents web camera/thermal images of Raspberry Pi model 3A+, and the second one Raspberry Pi model 4. The original images that we are importing for alignment will be converted from RGB to grayscale format, to enable image registration functionality.

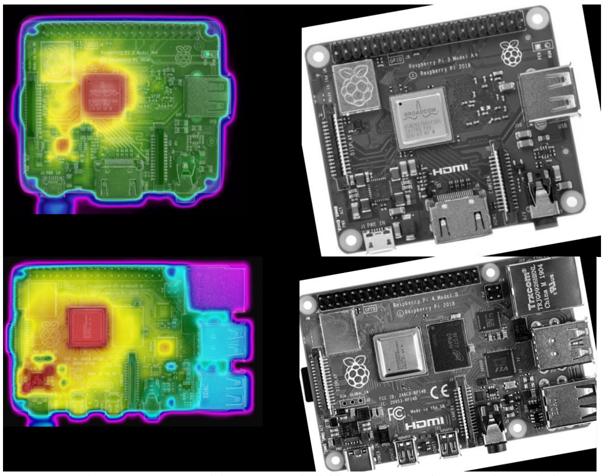

Fig. 5. Imported images of different Raspberry Pi models

When overlaid and blended with a low opacity set for the top image, it's clear that the images are not aligned at all. This can clearly be seen in figure 6.

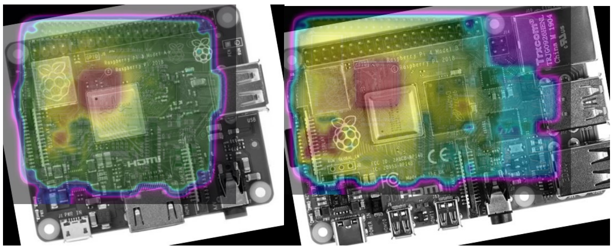

Fig. 6. Overlaid images when originally imported

We fixate the thermal image and do image manipulation to the web camera image. Using image registration, the application scales, rotates, and aligns the web camera image to the fixed thermal image. The result of completed image registration procedure can be seen in figure 7.

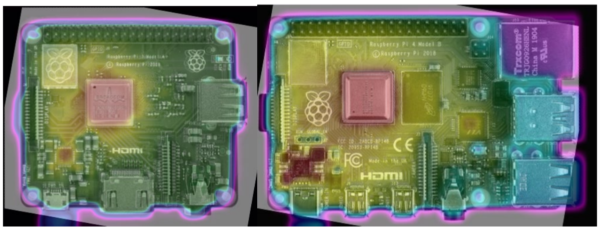

Fig. 7. Combined thermal/web image of the PCB with visible details of different areas

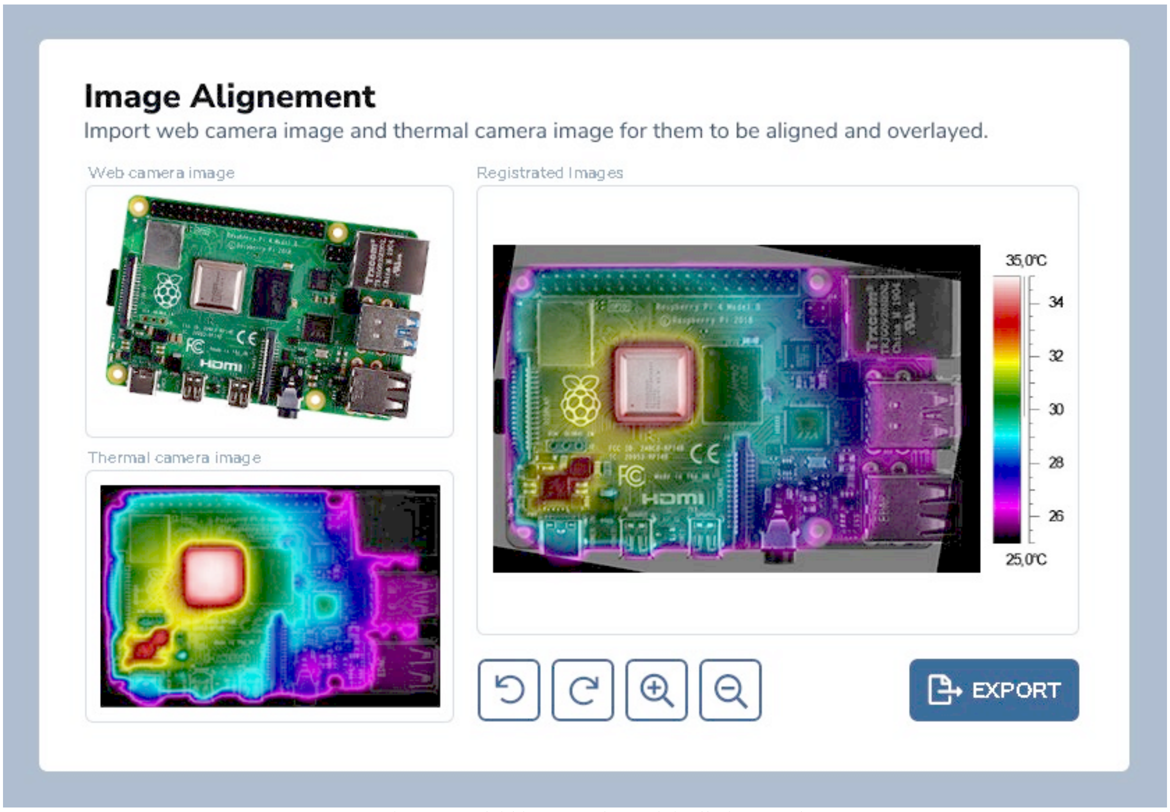

Image Alignement

Import web camera image and thermal camera image for them to be aligned and overlayed.

Fig. 8. Overlaid images when originally imported

V. USER INTERFACE

The application is easy to use and completely user friendly even for non-expert users. It is a one window application, consisting of three blocks. The left two blocks are for import, one for importing web image, and the second one for a thermal image. When those two images are imported, the left block will automatically load when all processes are finished. Correctly positioned and overlaid images will show, with the color scale next to it.

Before exporting the resulting image, the user will be able to rotate and scale the image as needed. The full application screen can be seen in Figure 8.

VI. CONCLUSION

First experiments with the Matlab-based image processing procedures show excellent results. The required functionalities are met. Further research and improvement of the system would be oriented toward development of some AI based diagnostic system that will be able to recognize the exact electrical or electronic component of the PCB that causes the problem.

ACKNOWLEDGMENT

This work has been supported by the Ministry of Education, Science and Technological Development of the Republic of Serbia.

REFERENCES

[1] Lloyd, J. Michael (1975). Thermal Imaging Systems. Springer. p. 70. ISBN 0-306-30848-7.

[2] Anastasios Polydoros 1ID, Constantinos Cartalis 1and Mat Santamouris: Climate Article Recognition of Thermal Hot and Cold Spots in UrbanAreas in Support of Mitigation Plans to CounteractOverheating: Application for AthensThaleia.

[4] "Protect Your Source Code". MathWorks. Retrieved November 1, 2019.

[5] Sazdić-Jotić, B., Pokrajac, I., Bajčetić, J., Bondžulić, B., Joksimović, V., Šević, T., Obradović, D., “VTI_DroneSET_FFT.Mendeley Data”, 2020. Available: https://doi.org/10.17632/s6tgnnp5n2.1

[6] Casabianca, P., Zhang, Y., “Acoustic-Based UAV Detection Using Late Fusion of Deep Neural Networks”, *Drones*, 5, 54. 2021.

[7] Boyd, Jonathan (2007-05-01). "Using Hands-Free Thermal Imaging Cameras". Fire Engineering. 160 (5)

TDoA Positioning in Wi-Fi based Systems

Navaneetha C. Manjappa[1,2], Vladica Sark[1], Jesús Gutiérrez[1] and Eckhard Grass[1,2]

Abstract—In recent years, Wi-Fi-based positioning has become more attractive, as Wi-Fi-capable devices are readily available. Additionally, some positioning methods can be easily integrated using the currently available Wi-Fi devices. In this paper, we investigate a time difference of arrival (TDoA) approach for Wi-Fi positioning. The proposed approach works by receiving the Wi-Fi frames from Wi-Fi user equipment (UE) using a few, localization only, access points (AP), which are precisely synchronized. The TDoAs of the Wi-Fi frame at the different localization APs is used to estimate the position of the UE. Since the Wi-Fi can support bandwidths of up to 160 MHz, high precision positioning is expected. This paper presents the system architecture and signal processing approach for the proposed Wi-Fi positioning scenario.

Index Terms—TDoA, positioning, Wi-Fi, Software Defined Radio.

I. INTRODUCTION

The recent advancements in location-based services have increased the demand for more precise indoor positioning technologies. As the use of the global positioning system (GPS) is limited to outdoor environments, recent research focuses on alternative solutions for indoor positioning. One of the most attractive are Wi-Fi-based positioning solutions [1], due to high availability of Wi-Fi devices. Received signal strength indicator (RSSI) of the Wi-Fi access points (APs) or user equipment (UE) can be used to estimate the position of the UEs. However, high noise and multipath propagation adversely affects this approach, resulting in low precision [2]. The accuracy can be further improved by using Wi-Fi fingerprinting methods. Nevertheless, these methods are time-consuming and not robust in terms of environmental changes introduced later in a given scenario [3].

Unlike RSSI-based methods, Time of Arrival (ToA) or TDoA methods use the finite traveling velocity of radio waves and estimate the propagation time of the radio waves in order to obtain the distance or position. The traveling time of a frame transmitted from an UE and arriving at multiple APs would be different and proportional to the corresponding distances traveled. This can be used for position estimation of the UE if the time difference is known. This method is called time difference of arrival (TDoA), it is more robust and offers better precision proportional to the bandwidth of the transmitted signal.

Over the years various indoor positioning systems have been investigated. Radio frequency Identification (RFID) technology uses active or passive tags attached to an object. When an object with an RFID tag approaches to a RFID reader it is recognizes and its location can be estimated [4], [5]. Due to their simplicity and cost effectiveness, RFID technology is widely used in indoor navigation systems [5], [6]. However RFID based positioning systems have a limited precision and require a dense deployment of RFID readers in order to be able to offer a satisfactory precision.

Bluetooth technology based positioning is another prominent indoor positioning solution with better accuracy compared to that of RFID based positioning. In these systems, user position is estimated with the help of Bluetooth beacon frames. By estimating the RSSI value of the received beacon frames, proximity (i.e. range) can be estimated. Use of different fingerprinting methods can additionally improve the positioning precision [5] [7]. Although Bluetooth technology based positioning systems are limited by short range, they provide high security and consume less power. Additionally, Bluetooth low energy (BLE) technology is optimized for power consumption and enables long operation on battery operated devices.

Infrared (IR) based positioning technology is also attractive, especially for industrial environments. In this systems, the user is equipped with an infrared tag and positions are estimated by a network of interconnected receivers for detecting the active tag. Due to the short range and disruption in presence of sunlight this technology is not widely spread [4].

Visible Light Communication (VLC) [8] technology is lately attracting a lot of attention since it offers a secure way for wireless data communication and, at the same time, it can offer positioning services. This positioning technology works by estimating the received light intensity from a luminary used for data communication. The main disadvantage of this approach is the limited precision, as in all RSSI based positioning systems.

Ultra wide band (UWB) technology is one of the most attractive radio frequency (RF) based indoor positioning technology and is based on time of flight (ToF) methods for position estimation. It offers many benefits over the other technologies such as centimeter level accuracy, little interference with other systems, low throughput data communication capability as well as low power consumption [5]. However, these systems require dedicated infrastructure which increases the costs [4].

Wi-Fi fingerprinting approach has become more attractive in the recent past. Using this method, the location of the user is estimated by characterization of the radio

[1] IHP – Leibniz-Institut für innovative Mikroelektronik, Im Technologiepark 25, D-15236,
Frankfurt (Oder), Germany
[2] Humboldt University of Berlin, Rudower Chaussee 25, D-12489 Berlin, Germany
Emails: {manjappa, sark, teran, grass @ihp-microelectronics.com

signal environment using a dataset obtained in extensive measurement campaign. The UE compares the RSSI values collected from different APs with this dataset. This approach is attractive because the necessary architecture, Wi-Fi APs and UEs, are already widely available. The main disadvantage, which extensively limits this approach, is the need for creating a large fingerprinting dataset. This is a painstaking process which needs to be repeated when the indoor environment changes.

Additionally, a few readily available proprietary solutions for indoor positioning, operating in the 2.4/5 GHz ISM bands [9] already exist [2]. These systems have limited accuracy due to small channel bandwidths available.

In this work, we propose a ToF based approach for Wi-Fi UE localization. The proposed approach uses TDoA to perform position estimates for Wi-Fi-enabled UEs. The proposed approach for localization is being intended for implementation on software defined radios (SDR) since the commercially available Wi-Fi APs are not offering the possibility of introducing changes in their hardware. Nevertheless, it is also possible to implement the proposed approach on hardware in future Wi-Fi implementations.

This paper is organized into five sections. At first, the TDoA positioning approach is described. Further system architecture is presented. In Section IV the implementation details are given. Section V discusses the obtained results and the conclusion and future work are given in section VI.

II. TDOA POSITIONING APPROACH

The fundamental TDoA based positioning approach is shown in Figure 1. The system is consisted of multiple APs (AP1, AP2, ...) with a fixed and known position and a UE (or more UEs), which position should be estimated. The UEs are transmitting known RF signal (e.g. Wi-Fi frame) which is received by the anchor nodes. The anchor nodes are synchronized and estimate the time of arrival of the RF signal.

In order to perform position estimation of the UE, the UE transmits an RF signal at time t_0. The transmitted signal would travel a distance of r_i to each of the APs, AP_i, where $i = 1, 2, 3, 4$. The time of arrival at each AP would therefore be:

$$t_{oai} = \frac{r_i}{c} + t_0 \tag{1}$$

where t_{oai} is the time of arrival at AP_i and c is the speedof light. The distances r_i can be calculated as

$$r_i = \sqrt{(x - x_i)^2 + (y - y_i)^2} \tag{2}$$

By substituting Eq. (1) in (2) and multiplying by c the following system of equations would be obtained

$$\{ \rho_i = \sqrt{(x - x_i)^2 + (y - y_i)^2} + b_i^2 \Big| i = 1,2, \dots \tag{3}$$

Where $\rho_i = t_{oai} * c$, are pseudo distances, x and y coordinates of the UE and x_i and y_i coordinates of the APs.

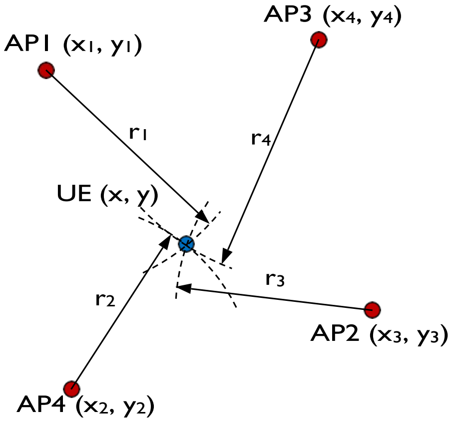

Fig. 1: TDoA based positioning approach

This system of equations can be solved since each of the equation in the system of equations describes a circle and these circles intersect in a single point, i.e. the UE position. In 2-dimensional case, intersection of a total of 3 circles around 3 APs would unambiguously intersect in a single point. Nevertheless, since the time of transmission t_0 is not known at the APs, the parameter b_i would also not be known and, therefore, one more equation would be needed in the system of equations. This means that there would be a total of 4 equations, i.e. 4 APs needed in 2-dimensional case. In 3-dimensional case, additional coordinate would be present, i.e. z, meaning that one more equation in the system of equations would be needed. This means that the system of equations would need a minimum of 5 equations, corresponding to 5 APs.

In a real scenario, the time of arrival of the RF signal would be estimated with an error included in the estimation. This means that the circles around each of the APs would not intersect into a single point. Therefore, the system of equations would not have a solution. The common approach in this case is to use a least squares (LS) method to obtain an approximate solution. Since the system of equations in this case is nonlinear, a non-linear least squares (NLLS) method should be used. A few different methods, like Gauss-Newton or Levenberg–Marquardt algorithm can be used for finding the NLLS solution of this system of equations.

III. SYSTEM ARCHITECTURE

The main components of the proposed localization system are at least four SDRs for 2-dimensional localization, performing the role of localization APs and a Wi-Fi capable UE as shown in Fig. 2. The APs are tightly synchronized.In the best case the the clock and the time of the APs should be synchronized, but, usually, having a good timing synchronization is essential. The affordable timing synchronization error depends on the required positioning precision. The higher the positioning precision required, the lower the synchronization error should be.

In order to perform UE localization, Wi-Fi frames are sent from the UE and are received by the different APs and are saved for further processing.

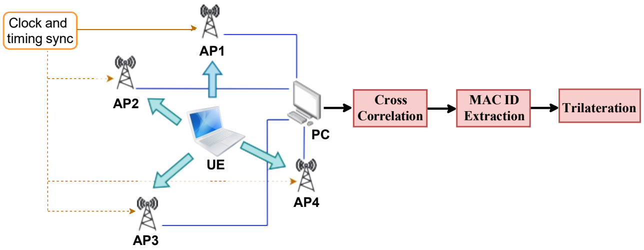

Fig. 2: System model for TDoA estimation.

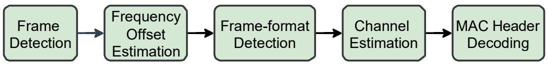

Fig. 3: Wi-Fi frame decoding and MAC ID extraction.

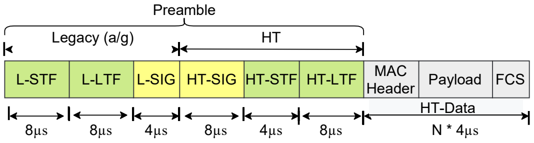

Fig. 4: IEEE 802.11n HT-Mixed frame format.

These Wi-Fi frames are also timestamped using the SDR time, which is synchronized across all the APs. Later, the signals from the different localization APs, containing the received Wi-Fi frame are cross-correlated to find the time differences between the frame received at different APs.

The received Wi-Fi frames are also partially decoded in order to find the MAC ID of the UE, to uniquely identify the UEs. This process is complex and involves several processing steps.

A. MAC ID extraction from Wi-Fi frames

The MAC ID extraction process is performed using the following steps: packet detection, automatic gain control, frequency-offset correction, detection of modulation scheme, and channel estimation, as shown in Fig. 2. These pieces of information are extracted from IEEE 802.11 n/ac standard frame preamble, in this case. The format of 802.11n high throughput (HT) standard mixed-mode frames is shown in Fig. 4. The 802.11n standard is enhanced in high throughput (HT) mode to support data rates up to 600 Mbps and operate at radio frequency (RF) bands of 2.4 and 5 GHz [10], [11]. Once the channel is estimated, the MAC address from the decoded header of the frame is obtained.

B. TDoA estimation

In the process of MAC address extraction, a coarse estimation of the start of the Wi-Fi frame is estimated. This coarse estimate is not sufficient for precise position estimation and, therefore, additional processing must be performed to obtain precise TDoA.

At first, the frames arrived at different APs are extracted and further correlated. The correlation between the frames would produce a signal as the one shown in Fig. 6. The peak, marked with red line in Fig. 6, is the cross-correlation peak, and its position actually corresponds to the TDoA of the same Wi-Fi frame in two different APs. The cross-correlation is performed between the frames received at the different APs.

The TDoA estimation is performed by finding the largest sample in the obtained cross-correlation function. Nevertheless, since the signals are sampled with a finite sampling rate, only a discrete values for the TDoA can be obtained. This would introduce a time quantization error in the TDoA estimate, which would further be translated into a positioning error. In order to mitigate this problem, a common approach is to utilize an interpolation in the cross-correlation function for obtaining a sub-sample TDoA estimate. A few different approaches can be used in order to perform interpolation. In this case, a quadratic interpolation around the correlation peak is chosen, since it is quite simple and compared to other interpolation methods, it offers a similar performance.

IV. IMPLEMENTATION

For the initial experiments, Ettus research USRP N321 SDR platforms were used as APs and a personal computer (PC) with built-in Wi-Fi support as UE. The ISM band of 2.4 GHz offers channels with a limited channel bandwidth of maximum 40 MHz. Hence, for this experiment, we used the 5 GHz ISM band. In the setup, as shown in Fig. 5, four APs and one mobile node as UE are considered. The synchronization of the APs was performed using two different approaches. In the first approach, an OctoClock device was used [13]. This device supplies 10 MHz clock to each of the SDRs for frequency synchronization and additional 1 pulse per second (PPS) signal for timing synchronization. The setup, including the OctoClock is shown in Fig. 5. The main disadvantage of this solution is that the both signals are supplied using coaxial cables which introduces additional jitter to these signals, leading to increased TDoA and positioning errors. The second approach which was also tested is to use WhiteRabbit [14] synchronization which is supported by the USRP N321 SDRs. The WhiteRabbit synchronization implements both SyncE [15] and the PTP [16] protocols and enables sub-nanosecond timing synchronization. Additionally, this synchronization solution requires only a single simplex monomode fiber which additionally simplifies its installation. The supported lengths of the used fibers are in the order of tens of kilometers.

In order to test the system, Wi-Fi frames are transmitted by the UE's Wi-Fi and are received by the SDR APs. The received frames are then processed using the method described in Section III. The acquisition of the samples is performed in a custom C/C++ application developed for this purpose. The acquired data is saved into files and further processed in MATLAB.

These are only the initial experiments, and the TDoA between two APs are only estimated. In a real positioning scenario, a minimum of four APs will be needed for a 2D positioning scenario. Additionally, calibration of the system should be performed before performing any localization experiments.

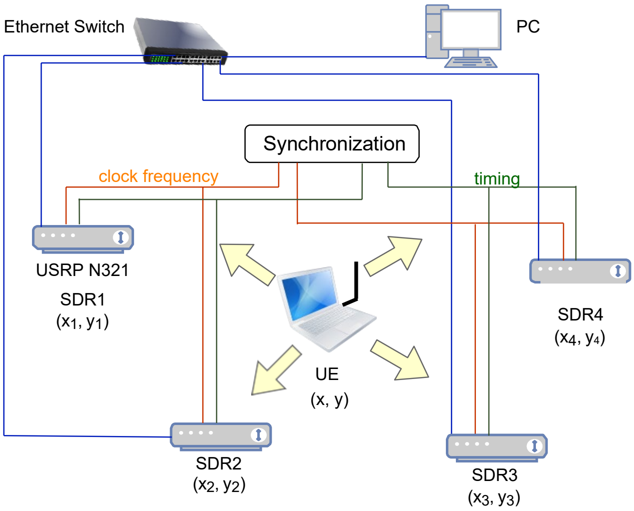

Fig. 5: Setup used for TDoA measurements.

V. RESULTS

In this paper a concept for Wi-Fi localization system was proposed. The proposed concept was partially implemented and initial tests were performed. The main functions that were implemented include synchronization of the APs, data acquisition using the SDRs, decoding of the received Wi-Fi frames and estimation of the TDoA before performing localization of the UEs. Our preliminary results show that we are able to estimate the TDoA using lags between the signals obtained using SDRs by performing cross- correlation.

VI. CONCLUSION AND FUTURE WORKS

In this work, we describe a method for Wi-Fi UE positioning. The proposed approach uses the existing Wi-Fi dataframes, transmitted by the UEs for data exchange with the Wi-Fi APs. No additional frames are needed which means no additional use of the wireless medium for localization purposes. This enables the use of the system with a large number of UEs, since it does not introduce additional overhead in the wireless medium.

In order to test the proposed concept, it was implemented using SDRs. The used SDRs support the largest channel bandwidths that Wi-Fi supports, i.e. 160 MHz. This wouldenable high positioning precision.

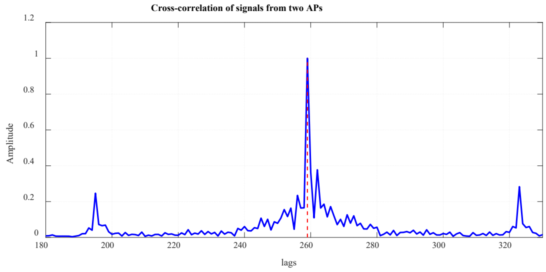

Fig. 6: Cross-correlation output indicating lag between signals.

The proposed approach can be easily implemented in the future Wi-Fi systems with minimal effort.

The future work would be focused on position estimation of UE by using the estimated TDoAs and trilateration.

ACKNOWLEDGMENT

This work has received support from the European Commission's Horizon 2020 research and innovation program, 5G-CLARITY project, under grant agreement No: 871428.

REFERENCES

[1] Liu, F., Liu, J., Yin, Y., Wang, W., Hu, D., Chen, P., and Niu, Q. (2020, June 2). Survey on Wi-Fi-based indoor positioning techniques. IET Communications. Institution of Engineering and Technology. https://doi.org/10.1049/iet-com.2019.1059.

[2] A. Purwita, D. C. Mur, H. Khalili, V. Sark, J. Gutiérrez, I. Hemadeh, J. Kainulainen, C. Turyagyenda, H. Frank, R. Bian, M. Ghoraishi, "State-of-the-Art Review and Initial Design of the Integrated 5GNR/Wi-Fi/LiFi Network Frameworks on Coexistence, Multi-Connectivity, Resource Management and Positioning" , Aug. 2020, pp. 78-79, https://www.5gclarity.com/wp-content/uploads/2020/ 09/5GCLARITY D3.1.pdf, Accessed: Oct. 14, 2021.

[3] Schauer, L., Dorfmeister, F., and Maier, M. (2013). Potentials and lim- itations of WIFI-positioning using time-of-flight. In 2013 International Conference on Indoor Positioning and Indoor Navigation, IPIN 2013. IEEE Computer Society. https://doi.org/10.1109/IPIN.2013.6817861.

[4] Basri, C., and El Khadimi, A. (2017). Survey on indoor localiza-tion system and recent advances of WIFI fingerprinting technique. In International Conference on Multimedia Computing and Sys- tems -Proceedings (Vol. 0, pp. 253–259). IEEE Computer Society. https://doi.org/10.1109/ICMCS.2016.7905633.

[5] Kunhoth, J., Karkar, A., Al-Maadeed, S. et al. Indoor positioning and wayfinding systems: a survey. Hum. Cent. Comput. Inf. Sci. 10, 18 (2020). https://doi.org/10.1186/s13673-020-00222-0.

[6] M. Bouet and A. L. dos Santos, "RFID tags: Positioning principles and localization techniques," 2008 1st IFIP Wireless Days, 2008, pp. 1-5, doi: 10.1109/WD.2008.4812905.

[7] S. He and S. G. Chan, "Wi-Fi Fingerprint-Based Indoor Positioning: Recent Advances and Comparisons," in IEEE Communications Surveys and Tutorials, vol. 18, no. 1, pp. 466-490, Firstquarter 2016, doi:10.1109/COMST.2015.2464084.

[8] Y. Zhuang et al., "A Survey of Positioning Systems Using Visible LED Lights," in IEEE Communications Surveys and Tutorials, vol. 20, no. 3, pp. 1963-1988, third quarter 2018.

[10] K. Keunecke and G. Scholl, "IEEE 802.11 n-based TDOA performance evaluation in an indoor multipath environment," The 8th European Conference on Antennas and Propagation (EuCAP 2014), 2014, pp. 2131-2135, doi: 10.1109/EuCAP.2014.6902230.

[11] Tektronix, "Wi-Fi: Overview of the 802.11 Physical Layer and Transmitter Measurements",2016. https://download.tek.com/ document/37W-29447-2 LR.pdf, Accessed: Oct. 12, 2021.

[12] Brian O' Keefe, "Finding Location with Time of Arrival and Time Difference of Arrival Techniques", May, 2017. https://sites.tufts.edu/eeseniordesignhandbook/files/2017/05/FireBrick OKeefe F1.pdf. Accessed: Sept. 29, 2021.

[13] https://www.ettus.com/all-products/octoclock/

[14] M. Lipi´nski, T. Włostowski, J. Serrano and P. Alvarez, "White rabbit: a PTP application for robust sub-nanosecond synchronization," 2011 IEEE International Symposium on Precision Clock Synchronization for Measurement, Control and Communication, 2011, pp. 25-30

[15] Timing characteristics of a synchronous Ethernet equipment slave clock (EEC), ITU-T Std. G.8262, 2007

[16] IEEE Standard for a Precision Clock Synchronization Protocol for Networked Measurement and Control Systems, IEEE Std. 1588-2008.

Developing a convolutional recurrent neural network for drone classification

Mohammed Mokhtari, Jovan Bajčetić, Boban Sazdić-Jotić, and Boban Pavlović

Abstract - In this paper, we present a convolutional recurrent neural network (CRNN) for drones detection and classification based on their RF signature. The proposed CRNN uses sequences of low-resolution spectrograms to achieve significant classification performances. It is also demonstrated that increasing the sequence of spectrograms by incorporating past observations can lead to better performances compared to only using the calculated spectrogram at a given instant. The proposed network was trained and tested using data from a publically available database. The CRNN has achieved nearly 100% classification accuracy, and can successfully distinguish between 4 classes: background activities, drone 1, drone 2 and drone 3.

Keywords - Classification, CRNN, Detection, UAV.

I. INTRODUCTION

The usage of Unmanned Aerial Vehicle (UAV), commonly known as drones, dates back to the early 1900s; serving as flying targets for pilots and antiaircraft gunners training [1]. Since then, UAV technology has undergone a considerable evolution under the influence of advancements in microelectronics, aeronautics, sensors, and control system technologies. Drones are today involved in many areas ranging from packages delivery to military operations, which is justified by the fact that they can access hazardous areas with ease and without exposing the human operators to danger. Most of the commercially available drones come with many advanced features depending on the task assigned to them, and they can be equipped with a wide variety of sensors including: GPS sensors, obstacle avoidance sensors and high-resolution cameras, among many others.

During the last few years, drones have become accessible to the public, and they are widely in circulation. The US Federal Aviation Administration reported the registration of almost 1.14 million recreational drones by the end of November 2020 in the USA [2]. This growing tendency raises many issues regarding security and public privacy. Consequently, drones have been involved in several illegal activities such as smuggling, illegal surveillance, espionage [3], and cyber-attacks [4]. Besides, many incidents involving drones have been reported especially near areas with high air traffic like airports [5].

In order to effectively deal with misusage of drones, researchers have designed several systems based on different techniques to detect and classify these threats. Radar systems, which are mainly used to detect large aircraft, can be used to detect small drones. Keeping in mind that drones have a low radar cross-section (RCS), detecting them with conventional radars was proved quite challenging. To overcome this limitation, radars operating in the millimeter-wave range have been employed [6]. Another widely used technique is acoustic sensing. The latter leverages the acoustic wave emitted by the drone's rotating propellers to obtain a unique signature and to detect its presence [7]. Moreover, Computer vision techniques can be utilized to identify a flying object using different kinds of electro-optical sensors, along with the employment of several approaches such as motion-based and appearance-based detection [8]. In addition, many commercial drones are controlled by a remote controller, besides; those drones usually stream images or videos to the receiver via a Wi-Fi link. Leveraging the existing Radio Frequency (RF) link between the drone and its controller can be an attractive option regarding the detection and classification of unauthorized drones. Several RF-based algorithms have been proposed in the literature to classify drones according to their RF signature [9], [10], [11]. In particular, deep learning algorithms have drawn a lot of attention given their significant classification performances [12].

In this work, we present a Convolutional Recurrent Neural Network (CRNN) for drones classification based on their RF-signature. The CRNN was trained and tested using data from a publically available database [13]. The latter contains raw RF signals captured from 3 drones: DJI Phantom IV, DJI Mavic 2 Zoom, and DJI Mavic 2 Enterprise. Background activities, when the communication link between the drone and its controller is inactive, were also captured and stored in the database.

In order to prepare the data for CRNN training and validation, data preprocessing was performed. The data preprocessing consists of a segmentation phase, followed by calculating the time-frequency representation (spectrogram) of each segment. The obtained spectrograms were stored in form of PNG images which have a relatively low resolution. Although it is possible to use the currently calculated spectrogram for class prediction, we will investigate the effect of integrating the history of the observations on the classification performances. This will be achieved by integrating the previously calculated

Mohammed Mokhtari, Jovan Bajčetić, Boban Sazdić-Jotić, and Boban Pavlović, Vojna Akademija, Univerzitet odbrane u Beogradu, Veljka Lukića Kurjaka 33, 11042 Beograd, Srbija, E-mail: mokhtari.med91@gmail.com, bajce05@gmail.com, boban.sazdic.jotic@vs.rs, bobanpav@yahoo.com.

spectrograms as a part of an observation sequence, which will subsequently serve as input for the CRNN. By using different sequence lengths, a total of 4 CRNN's configurations will be presented to demonstrate that it is possible to enhance the detection probability of drones. Instead of relying only on the currently calculated spectrogram, the proposed approach incorporates past observations (spectrograms obtained prior to instant *T*).

II. DATA PREPROCESSING

A segmentation of the raw RF signals was performed to prepare the data for CRNN training, and a total number of 11520 segments were obtained. Each segment contains 87378 samples, which corresponds to a signal duration of 0.58 ms. The spectrogram of each segment was calculated using the Short-Time Fourier Transform (STFT) with the following parameters: a Hanning window type, 2048 points for FFT, 128 overlapping points, and the amplitude was represented in dB. Each spectrogram was then stored as a PNG image (101 x 101 pixels) to be integrated within an image sequence, which will be used as input for the CRNN. Table I shows the number of images for each class, and Fig. 1 is an example of the obtained spectrogram images.

The obtained data were split in the following way: 70% of the spectrogram images were used for CRNN training, and 30% for the validation process. Table II summarizes the number of images per class for each dataset.

For each class, the spectrogram sequences were prepared in the following way: Each sequence is a tensor whose dimensions are (*N* x 101 x 101 x 3); where *N* is the sequence length. The sequence is constituted of *N* successive spectrogram images (S_T, S_{T-1},…, S_{T-N+1}). The sequences are then labeled according to their respective classes.

TABLE I
NUMBER OF SPECTROGRAM IMAGES PER CLASS

Class	Number of images
Background activities	2304
Drone 1	3072
Drone 2	3072
Drone 3	3072

TABLE II
NUMBER OF IMAGES FOR THE TRAINING AND VALIDATION DATASETS

Dataset	Class	Number of images
Training	Background activities	1608
	Drone 1	2144
	Drone 2	2144
	Drone 3	2144
Validation	Background activities	696
	Drone 1	928
	Drone 2	928
	Drone 3	928

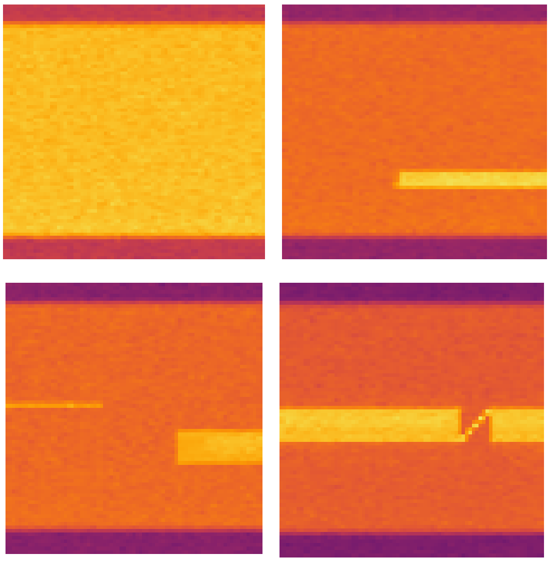

Fig. 1. Spectrogram images: background activities (up-left), drone 1(up-right), drone 2 (down-left), drone 3 (down-right)

III. CRNN FOR DRONE CLASSIFICATION

A CRNN is a combination of Convolutional Neural Network (CNN) and Recurrent Neural Network (RNN). The CNN architecture is very useful in the context of computer vision and image analysis. The convolutional layers can successfully capture the spatial and temporal dependencies presented in an image through the application of a set of different filters.

In the CNN architecture, The Convolutional layer is usually followed by a pooling layer with an aim to reduce the data dimensionality and keep only the dominant features.

RNN architecture can be very efficient in processing sequential data. Given its ability to integrate the previous output as a part of the current input, this architecture can efficiently capture the temporal dependencies between the sequence elements, and it leverages the existing correlation between those elements to provide accurate predictions. This justifies the intensive employment of this architecture in many fields including natural language translation, voice recognition, and text modeling.

The CRNN architecture comes as a natural choice regarding the classification of image sequences. In the case of drone detection and classification, CRNNs have been used to detect drones based on acoustic sensing methods [14], [15]. It is worthwhile to mention that the CRNN proposed in [15] outperformed the RNN, and had slightly lower classification performances compared to the CNN.

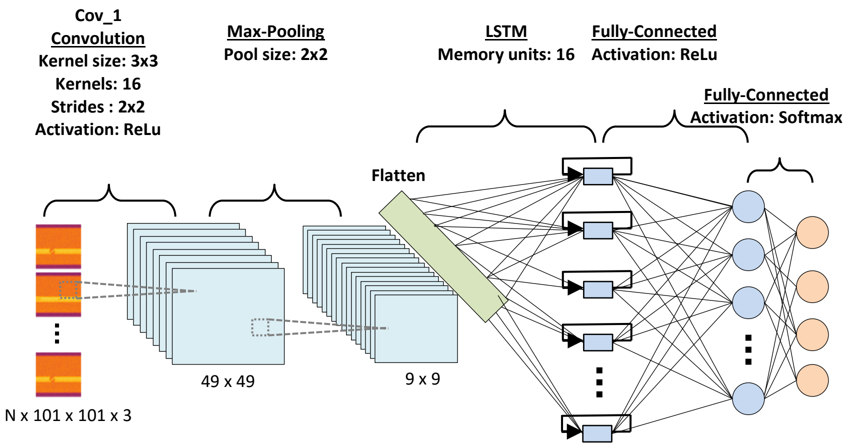

Fig. 2. CRNN structure for drone classification

In this work, we propose a CRNN which is constituted of 4 layers: the first layer is a convolutional layer that performs feature extraction from the spectrogram images, and reduces the length of the input data for the recurrent layer. The second layer is a Long Short-Term Memory (LSTM) layer, with 16 memory units for sequence prediction. The next two layers are fully connected layers to support class prediction. Fig. 2 represents the structure of the CRNN used for drone classification.

Total of 4 configurations of the CRNN were studied; each configuration uses a different sequence length. Let S_T be the spectrogram obtained at instant T. The network uses a sequence of N spectrograms (S_T, S_{T-1},…, S_{T-N+1}) for class prediction (Fig. 3). To predict the signal class, the neural network integrates past observations as part of the current input, which will eventually account for the observations inter-correlation. To evaluate the CRNN performances, 4 different sequence lengths were considered, and they are respectively: *N=1*, *N=2*, *N=4*, and *N=8*.

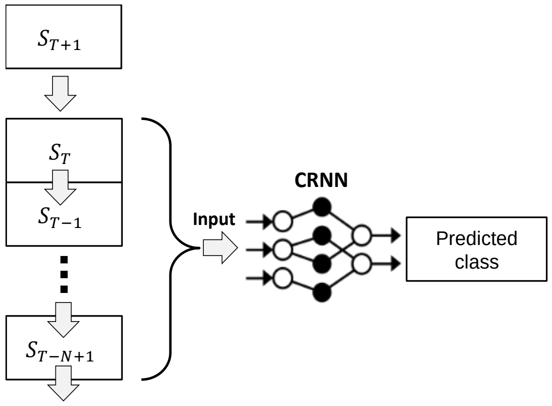

Fig. 3. Sequence prediction using CRNN

For each configuration, the CRNN was trained for 20 epochs. The CRNN performances were evaluated on basis of accuracy and loss during training (Fig. 4 and 5), and accuracy and loss during validation.

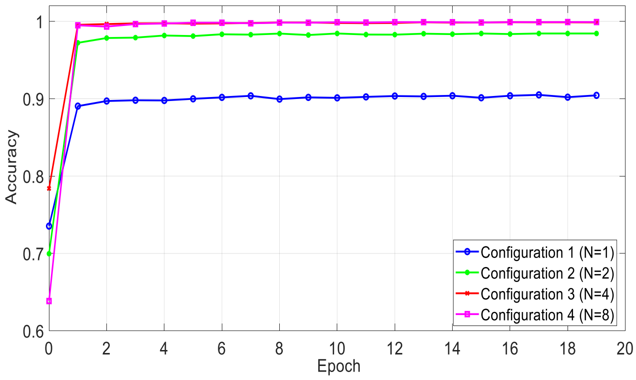

Fig. 4. CRNN accuracy variations during training

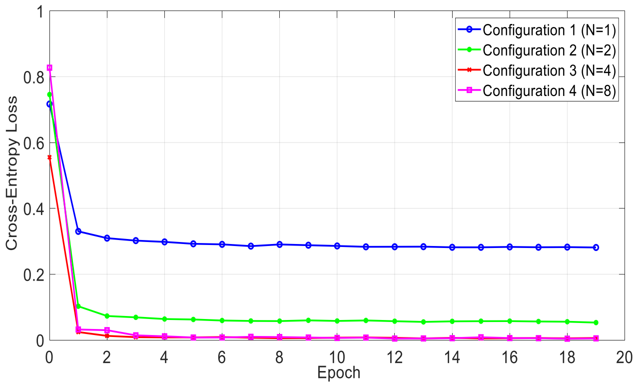

Fig. 5. CRNN loss variations during training

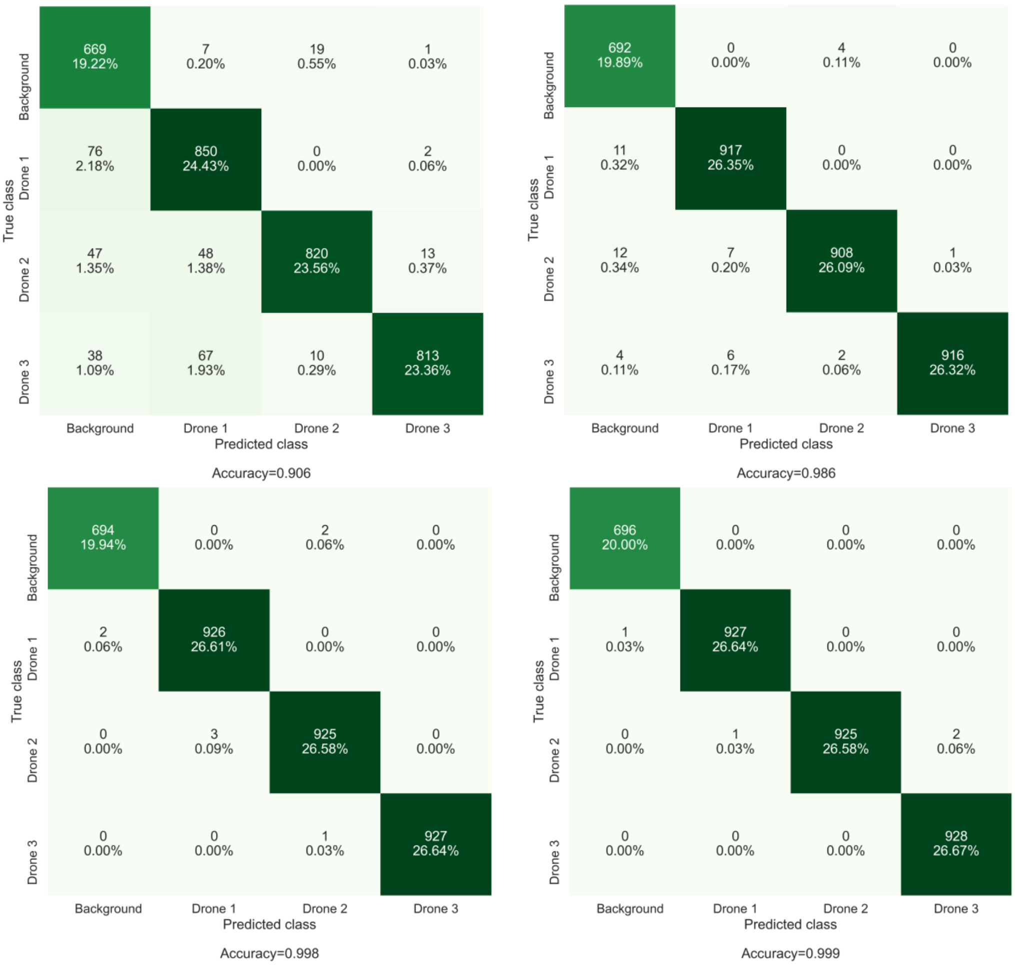

Fig. 6. Confusion matrices with validation data for the 4 configurations: configuration 1 (up-left), configuration 2 (up-right), configuration 3 (down-left), configuration 4 (down-right)

The confusion matrix for each configuration, obtained from the validation data, is represented in Fig. 6. Table III represents the accuracy and loss values obtained after CRNN training, as well as the accuracy and loss after validation. In light of these results, the following points can be highlighted:

- Configuration 1, which utilizes individual spectrogram images for class prediction, has the lowest performance compared to other configurations.
- Configuration 2, which utilizes image sequences of length 2, has reached a higher accuracy with a much lower loss value.
- Although configurations 3 and 4, which use sequences of length 4 and 8 respectively, present higher accuracy values, configuration 2 might be considered as the best compromise between the total training time and the provided performances.

From the confusion matrices, it is noticed that increasing the input sequence length decreases significantly the misclassification rate. Moreover, configuration 4 presents the lowest misclassification rate with 4 misclassified sequences. This can be justified by the usage of a relatively long sequence as input, and this might provide enough details for the neural network to better recognize the captured signal. Relying on the existing correlation between the sequence elements, The CRNN can better capture the interdependencies between successive elements when provided with sequences that have an appropriate length for the considered problem. This approach can be really useful, especially when the neural network is implemented in an application running on a machine with low computational resources.

TABLE III
ACCURACY AND LOSS VALUES FOR THE 4 CONFIGURATIONS

Number of images per sequence	Training accuracy	Training loss	Validation accuracy	Validation loss
1	0.91	0.27	0.91	0.27
2	0.98	$5.10 \cdot 10^{-2}$	0.99	$5.60 \cdot 10^{-2}$
4	0.99	$0.25 \cdot 10^{-2}$	0.99	$0.81 \cdot 10^{-2}$
8	0.99	$0.13 \cdot 10^{-2}$	0.99	$0.63 \cdot 10^{-2}$

IV. CONCLUSION

In this work, we demonstrated the possibility of using sequences of low-resolution spectrogram images to improve the performances of a CRNN. The recurrent structure of the CRNN allows memorizing the dependencies between the sequence images, and leverages the existing correlation to successfully predict the signal class. This concept can be really useful in the context of real-time drone detection. Using low-resolution spectrograms obtained from relatively short-duration RF signals can be very beneficial especially when utilizing a machine with low computational resources. The next step for this work would be implementing the trained CRNN within a complete system for drone detection.

REFERENCES

[1] Jordan, S., Moore, J., Hovet, S., Box, J., Perry, J., Kirsche, K., et al., “State-of-the-art technologies for UAV inspections”, IET Radar Sonar Navigation, vol. 12, pp. 151-164, Feb. 2018.

[2] Federal Aviation Administration, “FAA Aerospace Forecasts. Unmanned Aircraft Systems”, 2021. Available online: https://www.faa.gov/data_research/aviation/aerospace_forecasts/media/Unmanned_Aircraft_Systems.pdf

[3] Sathyamoorthy, D., “A review of security threats of unmanned aerial vehicles and mitigation steps”, The Journal of Defence and Security(In press), vol. 6, no. 2, Oct 2015.

[4] Yaacoub, J. P., Noura, H., Salman, O., Chehab, A., “Security Analysis of Drones Systems: Attacks Limitations and Recommendations”, *Internet of Things*, vol. 11, pp. 100218, 2020.

[5] Lykou, G., Moustakas, D., Gritzalis, D. “Defending airports from UAS: A survey on cyber-attacks and counter-drone sensing technologies”, Sensors, vol. 20, no. 12, pp. 3537, Jun. 2020.

[6] Semkin, V., Haarla, J., Pairon, T., Slezak, C., Rangan, S., Viikari, V., et al., “Analyzing radar cross section signatures of diverse drone models at mmWave frequencies”, *IEEE Access*, vol. 8, pp. 48958-48969, 2020.

[7] Bernardini, A., Mangiatordi, F., Pallotti, E., Capodiferro, L., “Drone detection by acoustic signature identification”, *Electronic Imaging*, vol. 2017, no. 10, pp. 60-64, 2017.

[8] Srigrarom, S., Chew, K. H., “Hybrid motion-based object detection for detecting and tracking of small and fast moving drones”, *International Conference on Unmanned Aircraft Systems 2020*, 2020.

[9] Nguyen, P., Truong, H., Ravindranathan, M., Nguyen, A., Han, R., Vu, T., “Matthan: Drone presence detection by identifying physical signatures in the drone’s RF communication”, Proc. ACM Int. Conf. Mobile Syst. Appl. Services (ACM MobiSys), pp. 211-224, Jun. 2017.

[10] Shi, Z., Huang, M., Zhao, C., Huang, L., Du, X., Zhao, Y., "Detection of LSSUAV using hash fingerprint based svdd", *Proc. IEEE Int. Conf. Commun. (ICC)*, pp. 1-5, May 2017.

[11] Soltani, N., Reus-Muns, G., Salehihikouei, B., Dy, J., Ioannidis, S., Chowdhury, K., "RF fingerprinting unmanned aerial vehicles with non-standard transmitter waveforms", in IEEE Trans. Veh. Technol., vol. 69, no. 12, pp. 15518-15531, Dec. 2020.

[12] Sazdić-Jotić, B., Pokrajac, I., Bajčetić, J., Bondžulić, B., Obradović, D., "Single and multiple drones detection and identification using RF based deep learning algorithm", Expert Syst. Appl., vol. 187, p. 115928, Jan. 2022.

[13] Sazdić-Jotić, B., Pokrajac, I., Bajčetić, J., Bondžulić, B., Joksimović, V., Šević, T., Obradović, D., “VTI_DroneSET_FFT.Mendeley Data”, 2020. Available: https://doi.org/10.17632/s6tgnnp5n2.1

[14] Al-Emadi, S., Al-Ali, A., Mohammad, A., Al-Ali, A., "Audio based drone detection and identification using deep learning", *Proc. 15th Int. Wireless Commun. Mobile Comput. Conf. (IWCMC)*, pp. 459-464, Jun. 2019.

[15] Casabianca, P., Zhang, Y., “Acoustic-Based UAV Detection Using Late Fusion of Deep Neural Networks”, Drones , 5, 54. 2021.

Sequential Control of Water Level in Tanks and Pumps From Remote Location Using PROFINET Network

Igor Kocić, Saša S. Nikolić, Aleksandra Milovanović,
Petar Đekić, and Nikola Danković

Abstract - In this paper, we describes sequential water level control and the remote control of water supply pumps for the production process of a domestic brewery. In order to increase the reliability of the system, communication is performed in two ways, using GSM or PROFINET communication. Hardware and software for both types of communication was created, as well as software for the panel which manages and supervises the operation of the entire plant.

Keywords - Sequential Control, Remote control, PROFINET, PLC controllers, HMI panel.

I. INTRODUCTION

In remote control systems simple wire connection traditionally has been used. The main disadvantage of such systems occurs in the event of a cable break in the control circuit. In this case, the information about the remote management system is completely lost. In recent times, the wired connection is being replaced by a radio connection, which has significantly increased the reliability of such a system. With the development of mobile telephony and the Internet, the possibility of remote control with great reliability has been achieved.

Due to the need to maximize the reliability of the system, control software and hardware have been developed for water level control in tanks using SMS messages and messages sent via a profinet network. With a suitable control algorithm, sequential control of the water level in the tanks is achieved. If the mobile network fails, the software enables automatic transition to the profinet network and vice versa. For the reasons of complete reliability, the existing wired connection has been retained, which the operator can turn on manually at any time.

II. HARDWARE AND SOFTWARE DESCRIPTION

Figure1 shows representation of the location of plants, devices and equipment. The plant is located in two remote locations. The main location is located at the location of the brewery, the location of the water intake is located about 5km from the main location. The location in the brewery is simply called: "Location of the tanks", and the location of the water intake is called: "Location of water intake". These names will be used further in the paper.

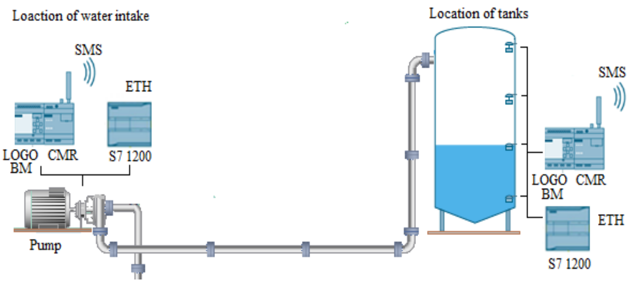

Fig. 1. Schematic representation the process of remote control of pumps

The system consists of a main control center where there are also tanks with a system for measuring water levels and a remote pumping plant in which there is a frequency regulator which performs pump start and pressure regulation in the pipeline and a system for protection against excessive pressure on the pipeline. The delay of the control signals is not of great importance because the water tanks are of large capacity. At both locations there is one Programmable Logic Controller (PLC) of the LOGO series with the communication module CMR2020 [1], [2] and the S7 1200 PLC controller.

Figure 2 shows the topology of the GSM network through which communication is performed by SMS messages.

The CMR module for GSM/GPRS communication has a wide range of applications. Some possible uses are as follows:

- Mobile wireless communication without LOGO PLC controller,
- Mobile wireless communication with LOGO PLC controller,
- 3. Positioning (GPS).

Igor Kocić is with University of Niš, Faculty of Electronic Engineering, Department of Control Systems, Aleksandra Medvedeva 14, Niš, Serbia, and TF KABLE Cable Factory Zaječar, Negotinski drum, Zaječar, Serbia, E-mail: igor.kocic@tfkable.com

Saša S. Nikolić, Aleksandra Milovanović, Nikola Danković are with University of Niš, Faculty of Electronic Engineering, Department of Control Systems, Aleksandra Medvedeva 14, Niš, Serbia, E-mails: sasa.s.nikolic@elfak.ni.ac.rs, aleksandra.milovanovic@elfak.rs, nikola.dankovic@elfak.ni.ac.rs

Petar Đekić is with The Academy of Applied Technical and Preschool Studies-Niš, Aleksandra Medvedeva 20, Niš, Serbia, E-mail: petar.djekic@akademijanis.edu.rs

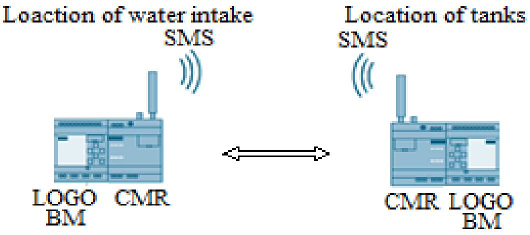

Fig. 2. Topology of the mobile network, communication by SMS messages

SIM cards are placed in each CMR module and the necessary parameters obtained by the network operator "Telekom Srbija " are set. Each CMR module with antenna is connected to LOGO PLC [1]. LOGO plc is connected to the CMR module using a local ethernet network. The antenna for the CMR module is omnidirectional for GSM (2G), UMTS (3G) and LTE (4G) networks. This allows sending and receiving of SMS messages related to events programmed in the LOGO PLC controller, which enables the initiation of actions and the sending of status information via SMS messages.

The CMR module was set up using an internet browser by entering the default address http://192.168.0.1. After setting that address are changed for security reasons. Setting up a CMR module consists of the following steps:

- Setting the parameters of the mobile and local Ethernet network,
- Setting parameters for SMS messages,
- Setting up users and user groups,
- Setting messages, actions, defining inputs, outputs, alarm events and error messages,
- Defining messages and actions for sending and receiving messages.

In Fig. 3 the appearance of the initial configuration screen of the CMR module is shown. Each of the modules is assigned names and local Ethernet addresses. The mobile network was set up by entering the PIN code of the SIM card, the card number and activating the interface for communication via the mobile network. It is also possible to communicate with devices that are in another country by activating the Roaming option.

An example of the syntax of SMS messages is given below in the form:

<Password>;LOGO=VM<Address>,<Value>,<Data type>.

Password represents the password for the write commands, LOGO=VM<Address> represents the local address in memory of LOGO plc, <Value> represents the value being sent or received, <Data type> is the type of data that is sent or received.

An SMS message for the command to write to LOGO plc to the address of the memory location VM0 is given like:

SMSupis; LOGO=VM0, 50, WORD.

General	
Module name	
Module type	LOGO! CMR2020
Plant description	
System runtime (dd:hh:mm:ss)	00:00:02:08
Ethernet interface	
IP address	192.168.0.3
Link status	Up
Connected since (dd:hh:mm:ss)	00:00:02:08
Mobile wireless interface	
Connection established	Yes
Connected since (dd:hh:mm:ss)	00:00:02:08
Data connection established	Yes, GPRS.
Data connection since (dd:hh:mm:ss)	00:00:02:08
APN used	
Signal strength (CSQ / dBm)	25 / -63
GPS	
Status	Not active
Visible satellites	

Fig. 3. Initial configuration screen of the CMR module

The setting of users and user groups was done by entering the user name, password, user phone number and permission to read and send SMS messages. A group of users was created that only receives alarm messages and a group that can perform switching on or off the pumps based on them. The setting of messages and actions to events is done by assigning the message ID number, the message name, the action by which a certain message is sent.

If the level in the tank is low, a message is sent whose syntax is:

SMSwrite;LOGO=VM0,10,WORD.

In case of a communication error, a message is sent to all user groups:

Text:! 'Error: Water intake station unavailable.'.

If a level error is detected, a message is sent:

Text:! 'Error: Level signal is incorrect. Sensor or cable is defective.'

Figure 4 shows the topology of the entire Ethernet network for the connection of both locations. Due to security in communication, a completely independent network was made from the existing Ethernet network in the brewery. The WAN connection was made using the network of the company "Telekom Srbija." Two network routers were procured from the company Telekom Srbija and two static IP addresses were obtained. Both routers are set to "Access point" mode.

DLink type N300 Dir 605L routers were used for network routers. They set up network routes and ports for communication between plc controllers in both networks. Figure 5 shows one of the screens for setting up communication on one of the routers where the setting of the type of connection between remote locations is shown. The paper does not specify the complete procedure for setting up the connection and router because it goes beyond the topic of the paper. Routes and ports for communication have been set up.

Routes (1) to (4) that are used for communication with S7 PLC controllers are listed, but the paper does not list complete static addresses for security reasons (parts of the address are shown with crosses).

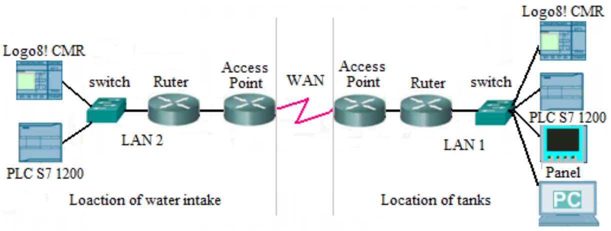

Fig. 4. Block diagram of the Internet connection

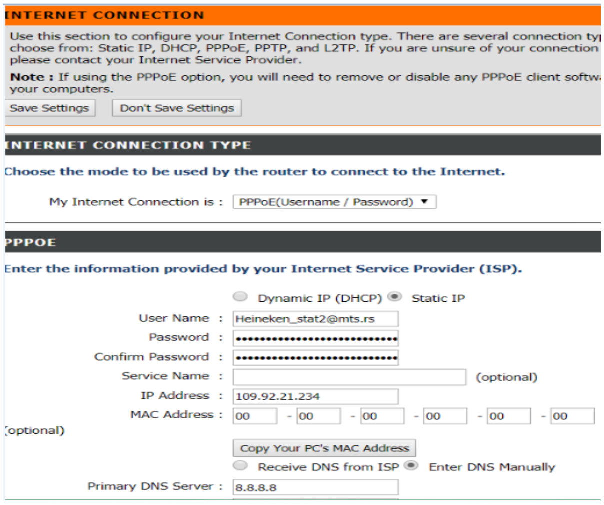

INTERNET CONNECTION

Use this section to configure your Internet Connection type. There are several connection ty
choose from: Static IP, DHCP, PPPoE, PPTP, and L2TP. If you are unsure of your connection
please contact your Internet Service Provider.

Note : If using the PPPoE option, you will need to remove or disable any PPPoE client softw
your computers.

Save Settings | Don't Save Settings

INTERNET CONNECTION TYPE

Choose the mode to be used by the router to connect to the Internet.

My Internet Connection is : PPPoE(Username / Password) ▼

PPPOE

Enter the information provided by your Internet Service Provider (ISP).

○ Dynamic IP (DHCP) ● Static IP

User Name : Heineken_stat2@mts.rs
Password : ••••••••••••••••••••••••••••
Confirm Password : ••••••••••••••••••••••••••••
Service Name : (optional)
IP Address : 109.92.21.234
MAC Address : 00 - 00 - 00 - 00 - 00 - 00
(optional)

Copy Your PC's MAC Address

○ Receive DNS from ISP ● Enter DNS Manually

Primary DNS Server : 8.8.8.8

Fig. 5. Connection type setting

port forwarding 192.168.0.2 80,102,2000,2001,2002 ruter Location of brewery reservoir (1)

port forwarding 192.168.0.202 80,102,2000,2001,2002 ruter Location of water intake (2)

routing dest: 109.92.xx.xxx 255.255.255.255 109.92.xx.xxx ruter Location of rewery reservoir (3)

routing dest: 109.92.xx.xxx 255.255.255.255 109.92.xx.xxx ruter Location of water intake (4)

The device's local Ethernet addresses are assigned in order:

- PLC LOGO 8.2 Brewery reservoir 192.168.0.103,
- CMR module 192.168.0.21,
- PLC LOGO 8.2 Water intake 192.168.0.104,
- CMR module 192.168.0.11,
- PLC S7 1200 Brewery reservoir 192.168.0.3,
- PLC S7 1200 Water intake 192.168.0.4,
- Touch HMI Panel KTP400 192.168.0.232,
- ADSL link (Access Point) Brewery reservoir 192.168.0.1,
- Router Brewery reservoir 192.168.0.2,
- ADSL link Water intake (Access Point) 192.168.0.201,
- Router Water intake 192.168.0.202.

In this way, access to the network from any of the two locations is enabled. Adding convenient routes enables access to the system via the Internet from any location. Communication using SMS messages was done with PLC Siemens LOGO controllers type LOGO! 8.FS4 with CMR communication module type CMR2020. Communication using the profinet network was done with Siemens PLC controllers type S7 1211C AC/DC/Rly, routers type DLink N 300 Dir 605L [5] and ADSL routers installed by local internet provider. At the location of thanks, level detection probes are used to detect levels at several points. The minimum and maximum level is of interest. When the water level in the tanks falls below the minimum value, the water supply pumps are switched on. The pumps are switched off in two cases:

1. operating condition of shutdown, when the desired water level in the tanks has been reached,
2. emergency shutdown, which is performed if the pressure in the pipeline increases above a certain level.

In addition to automatic operation, the plant can also operate in manual mode, when the switch-off is performed using the HMI panel or SMS messages sent by operators who have defined privileges. In case of extreme emergency, trouting can also work using an "old" wired connection, provided that SMS and profinet communication is switched off.

Some of the inputs, outputs used on LOGO PLC at the location of thanks are in order:

- I1 minimum level,
- I2 level 2,
- I3 level 3,
- I4 maximum level,
- I5 operation selection manually or automatically,
- I6 choice SMS or profinet,
- I7 internet communication error,
- Q1 communication error signal,
- Q2 fault indication signal due to excessive pressure on the pipeline.

Some of the inputs and outputs used on the LOGO PLC at the water intake location are in order:

- I2 work permit,
- I4 pressure switch,
- Q1 start pump off.

Figure 6 shows a part of the control algorithm for the operation of the plant when the level is lower than the minimum. In the event of an error or interruption in the communication protocol currently in use, the transition from the current to another type of communication is performed automatically. If SMS is currently active, the switch is made to profinet communication and vice versa. The software for SMS communication was written using Siemens' LOGO! Soft Comfort V8.2 programming tool for the LOGO PLC controller.

In Fig. 7 the part of the software related to sending messages for switching on and off of pumps in a remote pumping plant (location of water intake) is given.

When the water level falls below the minimum level, the first SMS message is sent from the location of thanks. If there is a level fluctuation due to water ripples that can affect the probe for the minimum level signal, the message

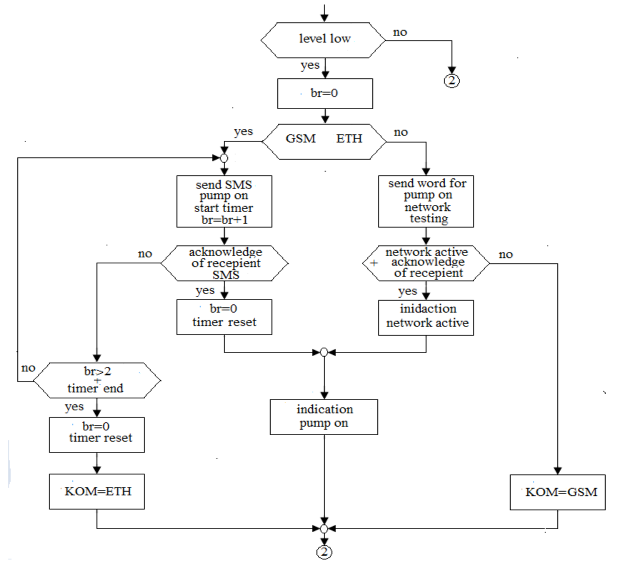

Fig. 6. Part of the plant operation algorithm when indicating the minimum level

activation signal is filtered using a timer with a delay of 10s of the instruction for detecting the rising edge. It is ensured that each sending request is executed once. After sending the message, a timer is activated which defines the maximum time required for the remote pumping station to which the message was sent to respond (60s). This time is experimentally defined so that it does not affect the level regulation. If the reply time expires, the same message is sent a second time. If the reply from the remote water intake location in that case also does not arrive, a message is automatically sent to the location Brdo is inactive. The error message is printed on the HMI panel and sends an SMS to the numbers configured in the CMR module. Communication is automatically switched to the profinet network.

Part of the software for sending the message on and off the pumping station is given in Fig. 7. The registers used in the application are:

- VW0, the register in which the messages to be sent are entered,
- VW1, a register used to indicate the current level value.

The text messages used are:

- VW0 = '10 'pump start,
- VW0 = '20 'pump shutdown,
- VW0 = '11 'pump on,
- VW0 = '12 'pump off.

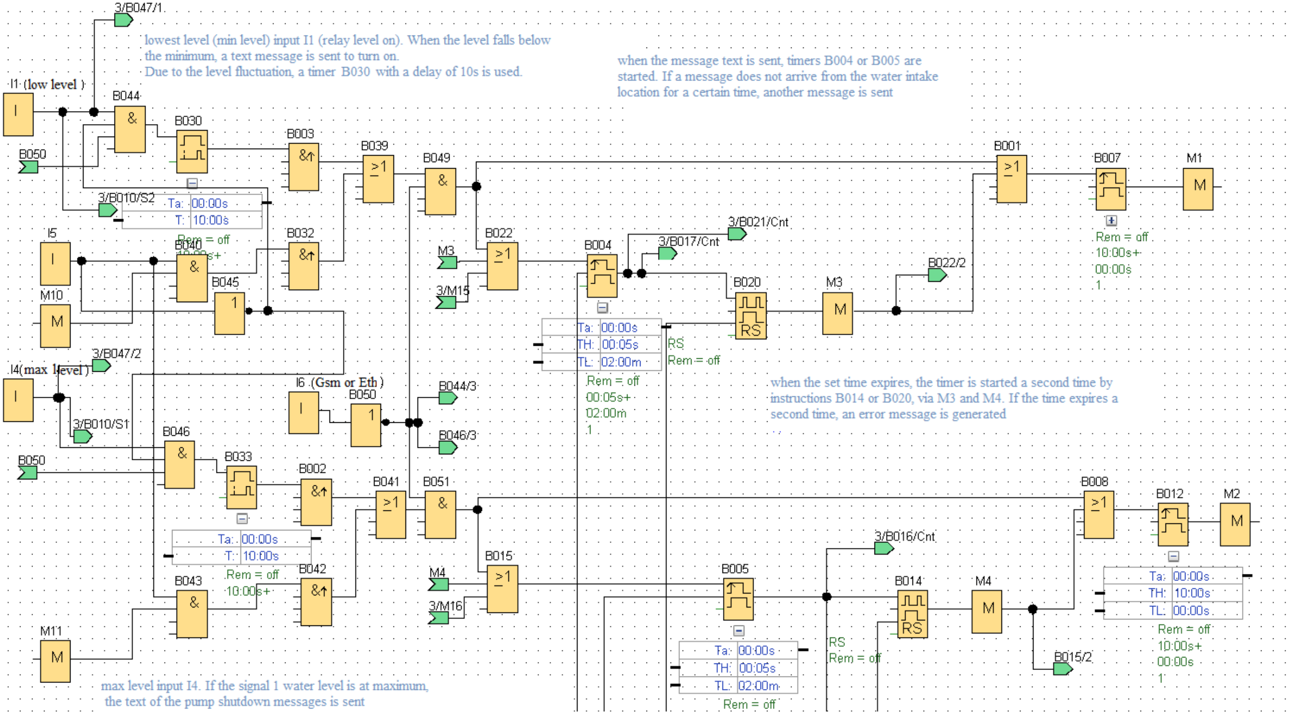
lowest level (min level) input I1 (relay level on). When the level falls below the minimum, a text message is sent to turn on. Due to the level fluctuation, a timer B030 with a delay of 10s is used.

when the message text is sent, timers B004 or B005 are started. If a message does not arrive from the water intake location for a certain time, another message is sent

when the set time expires, the timer is started a second time by instructions B014 or B020, via M3 and M4. If the time expires a second time, an error message is generated

max level input I4. If the signal 1 water level is at maximum, the text of the pump shutdown messages is sent

Fig. 7. Part of the software for sending SMS messages, SMS messages for switching on and SMS messages for switching off the pumping station pump

The part of the software used to turn on and off the pumps at the remote Brdo location is given in Fig. 8. The received message is compared with comparators B006 and B002. If the message located in the register VM0 = 10 is received on the Logo PLC controller, the output Q1 is activated, which activates the frequency controller for controlling the operation of the pumps. Immediately upon receipt, an SMS message with the value '11' is sent to the location of the Brewery, which carries the information that the pumps have started.

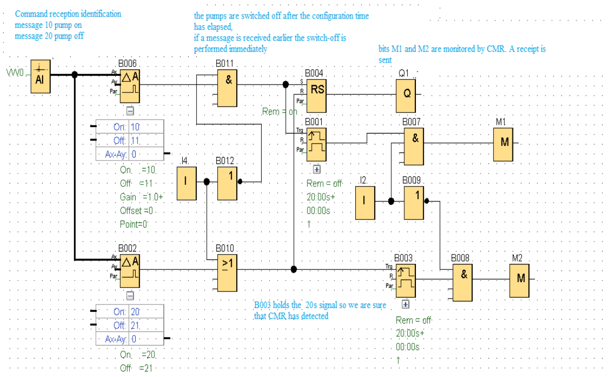

Fig. 8. Part of the software to turn on, off the pumps at remote location

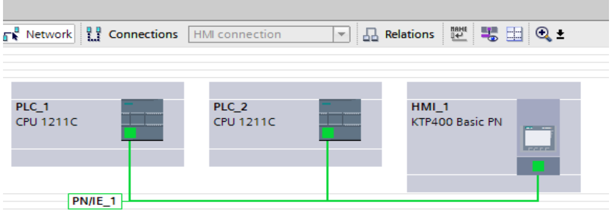

Fig. 9. Profinet network of two plc at remote locations, PLC_1 and HMI_1 location Pivara, PLC_2 location Brdo

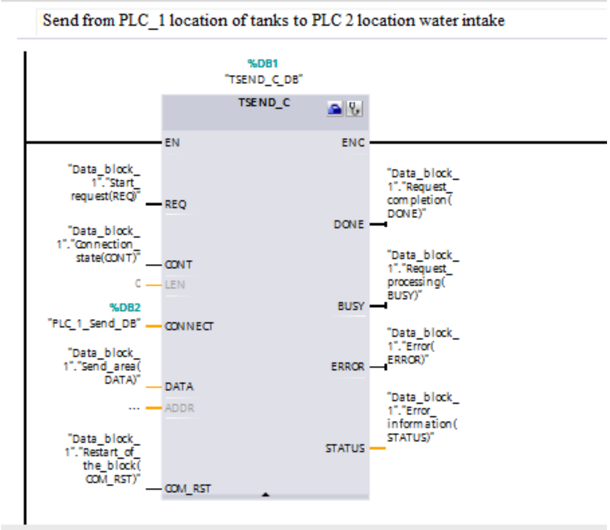
Send from PLC_1 location of tanks to PLC 2 location water intake

Fig. 10. . TSEND_C instructions for the plc software part at the Brewery site to send a pump on or off message at the location of water intake

If the message VM0 = 20 is received, output Q1 is switched off, which stops the operation of the frequency regulator and thus the pump. Upon receipt of this message according to the location of the Brewery, a message is sent with the value '22' pump off. If for some reason the pressure on the pipeline increases, the pressure switch is activated, an emergency shutdown of the pump frequency regulator is performed. According to the location of the Brewery, a message with the value '13' is sent, an alarm is activated with the information that an emergency shutdown of the pump has been performed, the pressure has increased and the pump has been switched off. A SMS message is also sent to the operator who further takes the necessary measures.

In this paper, software for control of plant was developed using S7 1200 PLC controllers [3] that communicate with each other via a profinet network.

Some of the inputs, outputs used on the S7 1200 PLC at the Pivara location are in order:

- I0.0 start of charging,
- I0.1 charging stop,
- I0.4 auto operation selection manually,
- I0.5 GSM ETH operation selection,
- Q0.0 network indication inactive,
- Q0.3 indication of pump started,
- IW50 registry to transfer message manager

Some of the inputs, outputs used on the S7 1200 plc at the Brdo location are in order:

- I0.2 regulator started (pump running),
- I0.3 pressure switch input,
- IW 64 analog current current regulator,
- IW50 message register.

Software for communication between S7 1200 PLC controllers is written in TIA Potal V13 SP1 [4].

Using an internet connection, a profinet network was created between remote locations. Figure 9 shows a block diagram of the profinet connection between remote locations.

Communication of two remote S7 PLC via PROFINET network was achieved by using a router at both locations. Two PLC controllers were added to the same project in the TIA portal, which are connected to the profinet line (see Fig. 9). Communication is done using instruction pairs TSEND_C and TRCV_C. A few instructions of the software package TIA portal TSEND_C and TRCV_C represent communication partners. The TSEND_C instruction is executed asynchronously. To send messages to the first part of the project, the T_SENDC command was added, for which a special DB block was defined (Fig. 10).

As part of the TSEND_C instruction, a communication link is set up and established when a rising edge is detected at the REQ input, provided that the other communication link is not active. When the connection is established the plc controller automatically monitors and maintains it. The CONNECT parameter provides a connection description, and is used to set the connection type. In this case we used a TCP/IP connection. When the controller enters STOP mode, the existing connection is terminated and the connection that was established is removed. Reconnecting TSEND_C is required to reconnect. The data to be transmitted is entered on the DATA input. If the sending job completes successfully, the DONE bit is set, which also does not represent a confirmation that the data has been received, it only says that the data has been sent. The communication reset is performed by bringing "1" to the COM_RST input.

As part of the TRCV_C instruction, a 'TRUE' signal is applied to the EN_R input, which means that read is enabled, and the CONT input is used to check whether the connection has been established. If the connection is established, the data from the communication line is read. The execution status of both commands is checked via the output values BUSY, DONE, ERROR and STATUS. The BUSY output provides information on whether a send or receive operation is in the execution process. The DONE output indicates whether the send or receive task was completed successfully. The ERROR output is set if errors have occurred, while the error type information is in the STATUS variable. By reading the STATUS variable, the sending or receiving diagnostics is performed.

In the first part of the project, in the configuration part of the TIA Portal, a plc with the address 192.168.0.3 was installed. in the second part of the project a plc with the address 192.168.0.4 was placed. Figure 10 shows the method of setting the pair next to sending and receiving: The pair of commands is assumed to be TSEND_C at the brewery location and TRCV_C at the water intake location. Both plc controllers communicate using the TSEND_C and TRCV_C instructions over a WAN using a router so that they are both paired over the appropriate IP address and the appropriate port, in this case port 2000.

Based on the information on the current level, the controller at the Brewery location sends a text message to turn the pump on or off at the Brdo location. A text message to switch the pump off is entered in register IW50.

- IW50 = '12345' to switch on the pump,
- IW50 = '22345' to switch off the pump.

When the need to turn on arises, turning off the pump part of the program written in the leader performs formatting of the text message, transfers it to the data block associated with the send command. At the Fig. 12, we check the connection status and sets a request to send a message. If the communication line is free, a message is sent.

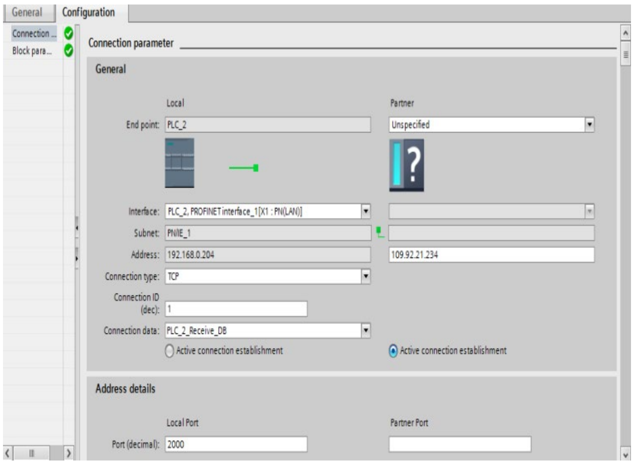

Connection parameter

General

	Local	Partner
End point:	PLC_2	Unspecified
Interface:	PLC_2, PROFINET interface_1[X1 : PN(LAN)]	
Subnet:	PN/IE_1	
Address:	192.168.0.204	109.92.21.234
Connection type:	TCP	
Connection ID (dec):	1	
Connection data:	PLC_2_Receive_DB	
	○ Active connection establishment	● Active connection establishment

Address details

	Local Port	Partner Port
Port (decimal):	2000	

Fig. 11. Setting the connection between the TSEND_C and TRCV_C command pairs to remote locations

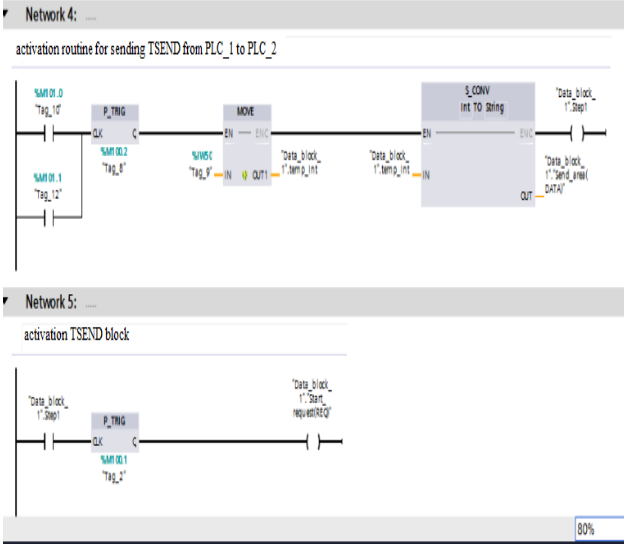

Fig. 12. Part of the program for initializing and sending a message with the command TSEND_C

After that, an examination is performed to see if the message has been sent. If the message is received plc from to the location Brdo sends a response which plc from the location Pivara receives and processes with the command TRCV_C. The applied message is located in the data block associated with the TRCV_C command. The program examines whether the character is in the appropriate position in the IW50 register with a value of '1' or '2' (Fig. 13). If the value of '1' the pumps are on, if the value of '2' the pumps are off.

In case the value is '3', an emergency shutdown was performed due to an increase in pressure.

After the response receive, which is almost instantaneous in the case of an internet connection, the operating status of the pump is displayed on the HMI panel.

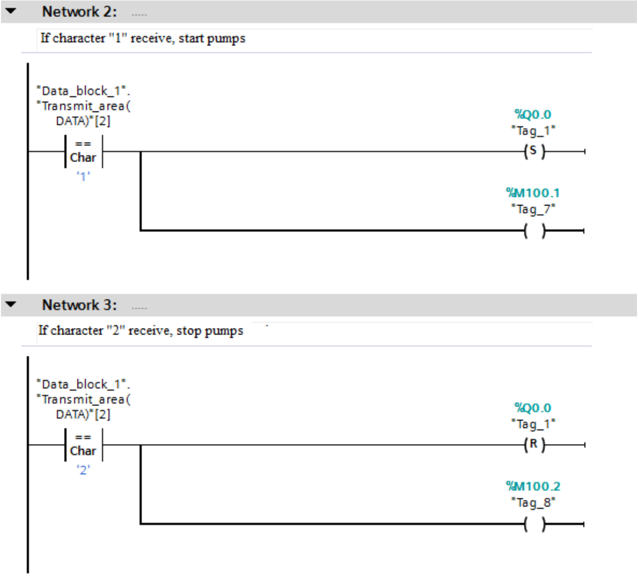

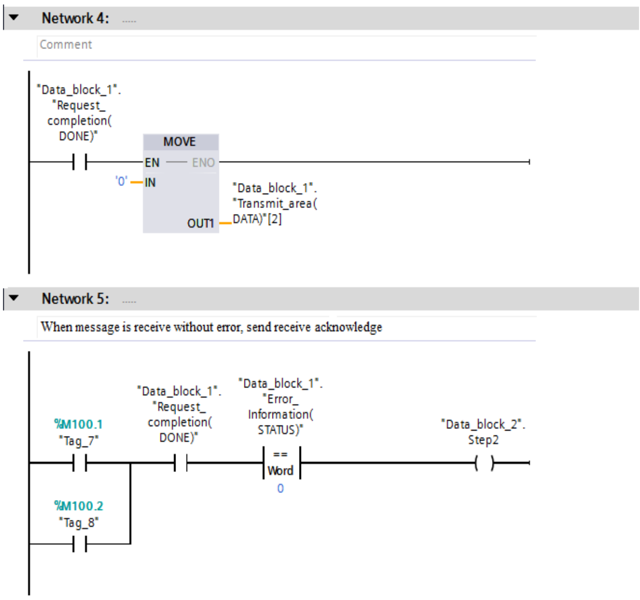

When message is receive without error, send receive acknowledge

Fig. 13. Part of the program for switching on, off and confirmation of sending a message

III. REALIZATION OF PROPOSED APPLICATION

Sequential control of the water level in the tanks at the location of the Brewery was performed by making two control cabinets for transmitting messages using SMS messages and a profinet network, as well as a cabinet with a frequency regulator that controls the operation of the pumps. Figure 14 shows the external appearance of the control cabinets at the location of the water tanks.

Fig. 14. Part of the program for switching on, off and confirmation of sending a message

Figure 15a shows the control cabinet at the location of the Brewery, and Fig. 15b a part of the control cabinet at the water intake location is shown.

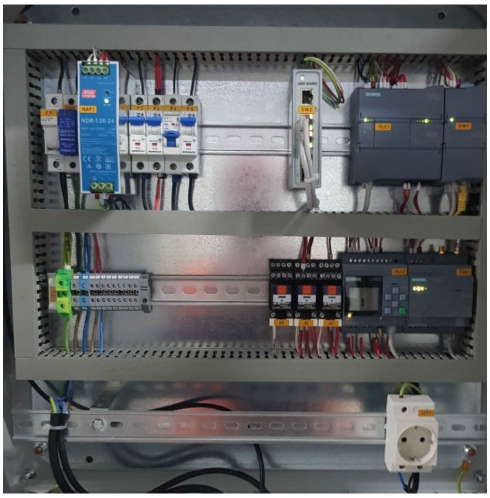

Fig. 15a. The control unit location of the water tanks

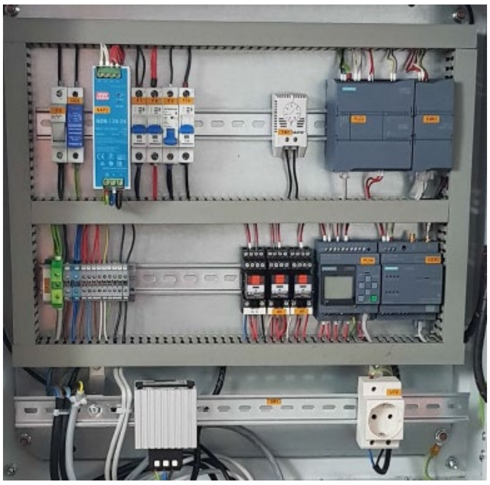

Fig. 15b. Part of the control unit at the location of water intake

One LOGO PLC with a communication CMR module and an S7 1200 PLC controller is installed in each of them.

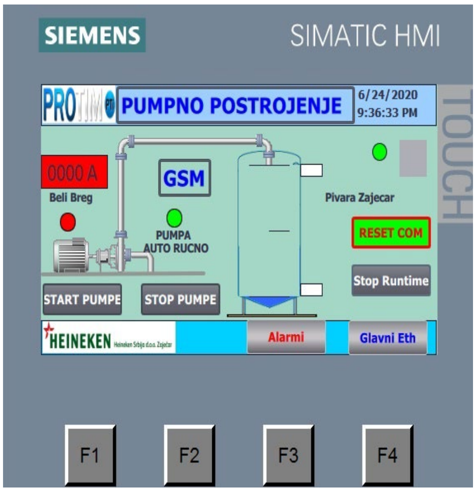

Fig. 16a. SMS communication

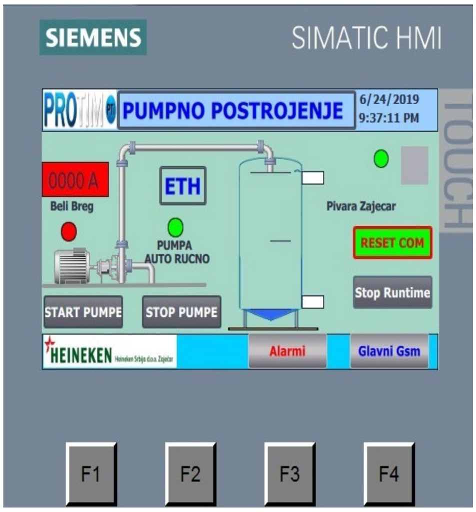

Fig. 16b. PROFINET communication

IV. CONCLUSION

For the realization of this type of management tasks, a wire connection has been used for years. The cost of making a connection for long distances is significant and is usually realized at the time of making the pipeline, when communication and power cables are laid parallel to the pipes to the distance of the location. In case of failure, damage to communication links, it is necessary to re-excavate part of the route in order to detect a break in communication, which requires significant resources. In recent times, communication via SMS using the mobile telephony network is increasingly used. In addition to software and hardware developed for communication via SMS, software and hardware for communication via the profinet network using communication via the Internet were also developed. In this way, the possibility of system system failure is reduced to a minimum. This application was developed for the needs of supplying the brewery with water in Heineken brewery in Zajecar.

REFERENCES

[1]https://cache.industry.siemens.com/dl/files/461/16527461/att_82564/v1/Logo_e.pdf

[2]https://cache.industry.siemens.com/dl/files/268/103657268/att_850514/v1/BA_LOGOCMR2020CMR2040_76_en-US.pdf

[3]https://cache.industry.siemens.com/dl/files/465/36932465/att_106119/v1/s71200_system_manual_en-US_en-US.pdf

[4] Berger, H., Automating with SIMATIC S7-1200, Publicis, 2nd edition.

[5]https://eu.dlink.com/-/media/consumer_products/dir/dir-605l/manual/dir_605l_a1_manual_v1_en_uk.pdf

[6] DiMarzio, J. F., *Sams teach yourself Routing in 24 hours*, Kompjuter biblioteka, 2002.

[7] Brenton, K., Abuhof, B., *Cisco Ruteri*, Kompjuter biblioteka, 2003.

Temperature Characteristics of Submandibular Region Tumors Recorded by Thermal Camera

Andrija Ćosić[1], Igor Jovanović[2], Miona Andrejević Stošović[2],
Dragan Krasić[1], Dragan Mančić[2]

Abstract - In this paper, we present the results of thermal examination of patients with different tumors of the submundibular region, as well as the temperature characteristics of the observed tumors. 13 patients treated at maxillofacial surgery of the Clinic for dental medicine Niš were examined and the results were compared with a control group of 15 healthy subjects. Thermal camera measurements were performed in controlled conditions using the Varioscan 3021ST thermal camera, while the IRBIS Professional 2.2 package was used for software processing and thermogram analysis.

Keywords – Submandibular region, Infrared radiation, Thermal imaging.

I. INTRODUCTION

Measurement of body temperature as an indicator of the existence of the disease has been used since ancient times. Hippocrates used the palm of his hand or a clean linen cloth which he leaned on the patient's skin and thus ascertained the change in temperature. With the invention of the thermometer, measuring body temperature is slowly entering everyday medical practice. The thermal camera, which was developed for military purposes in the last century, in the mid-1960s [1], has found its application in medicine in the diagnosis of breast tumors, malignant melanomas, peripheral vasculopathies, etc. In the middle of the seventies, the first works related to thermographic examinations of the maxillofacial region appeared [2].

Maxillofacial region is an area that can be affected by many pathological conditions, very different from each other.

According to literature [3], 56.3% of all pathological conditions are inflammatory processes (82.5% are acute and 17.5% are chronic), while neodontogenic inflammatory processes account for 16% and 13% are tumors and tumors of similar formation.

Salivary gland tumors account for 4-6% of all head tumors and represent a morphologically and histopathologically diverse group of tumors that most commonly involve the parotid gland (70%), then submandibular (15%), sublingual (1%) and small salivary glands (5-15%) [4].

In the submandibular gland 50-57 % of the tumors are benign while 43-50% are malignant. Among benign tumors pleomorphic adenoma is the most common. Same is with adenoid cistic and mucoepidermid carcinoma regarding malignant tumors [5]. Tumors of the submandibular glands are most often presented as painless masses in the submandibular region and it is often difficult to distinguish benign from malignant tumors on clinical examination.

Therefore, establishing a timely diagnosis in clinical practice is imperative for successful treatment, and there is a constant need to develop new, more modern, and more affordable diagnostic tools. The following diagnostic tools are standardly used for diagnostic purposes in maxillofacial surgery: ultrasound examination, ultrasound-guided needle spiral biopsy (FNAC), computed tomography (CT), positron emission computed tomography (PET CT), and nuclear magnetic resonance (NMR). These tools have their disadvantages and advantages. The ideal diagnostic tool must meet the following conditions: to be non-invasive, harmless to the patient, sensitive and precise in the presentation of structures, with fast processing and obtaining findings with low procurement and maintenance costs, and relatively easy handling. Ultrasound and NMR are non-invasive examination techniques that do not involve exposure of the patient to radiation. Ultrasound finding depends on its accuracy and the experience of the attending physician, while in NMR the economic aspects are what, despite all the advantages, limit the wide application. The thermal imaging camera, whose application is based on detecting infrared rays emitted by all bodies with a temperature above absolute zero, represents a new diagnostic possibility for detecting diseases of the maxillofacial region.

In this paper we will analyse results obtained by measuring temperature characteristics of the observed tumors in submundibular region, trying to capture some kind of dependence between certain kind of tumor and its temperature characteristics.

II. MEASUREMENTS AND METHODS

The measurements were performed at the Clinic for dental medicine in Niš, at the department of maxillofacial surgery, in strictly controlled conditions in terms of

Andrija Ćosić and Dragan Krasić are with University of Niš, Faculty of Medicine, Clinic for Dental Medicine, Bulevar Zorana Đinđića 52, 18000 Niš, Serbia, E-mail: cosa72@yahoo.com, drkrasic@yahoo.com.

Igor Jovanović, Miona Andrejević Stošović and Dragan Mančić are with University of Niš, Faculty of Electronic Engineering, A. Medvedeva 14, 18000 Niš, Serbia, E-mail: {igor.jovanovic,miona.andrejevic,dragan.mancic}@elfak.ni.ac.rs

environmental conditions and adaptation of the patients to these conditions. The study included 13 patients with submandibular gland tumors, 6 women and 7 men, aged 21 to 87 years (mean age 57.6 years). Eight patients with a mean age of 55.5 years (7 men and 2 women) had benign changes: three with adenoma, three with sialoadenitis, one with cystis and one with lipoma. Four patients with an average age of 62 years (all of them are women) had pathohistologically verified malignant tumors: two with metastasis of squamocellular carcinoma, and two with lymphoma, of which one Non-Hodgkin lymphoma and one with diffuse B large cell lymphoma. All patients, after thermographic imaging, underwent standard surgical treatment. In the control group of healthy subjects, thermal characteristics of the submandibular region were observed in 7 women and 8 men aged 40 to 65 years.

The infrared thermographic camera Varioscan high-resolution model 3021 (Jenoptik, Germany) was used. The infrared thermographic camera detects infrared radiation from the skin of the face region directed by the lens system toward the photosensor, where its energy is transformed into electrical impulses that provide visualization of skin temperature values on the display as a range of colours. The camera has a thermal resolution of ±0.03°C, temperature range from –40 to 1200°C, and spectral range 8–12 μm. Absolute accuracy of the temperature measurements (factory calibrated) up to 100°C, at an ambient temperature of 22 ± 2°C, is less than ±2K; otherwise, the accuracy is less than ±1% of full-scale value. Digital images of the skin temperature variations were analyzed by IRBIS Professional 2.2. graphics-oriented software package (InfraTec GmbH, Dresden, Germany).

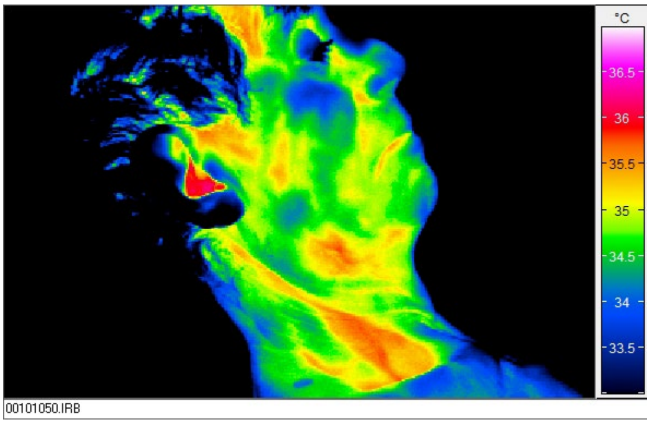

Fig. 1. Thermal image - benign tumor in submundibular region

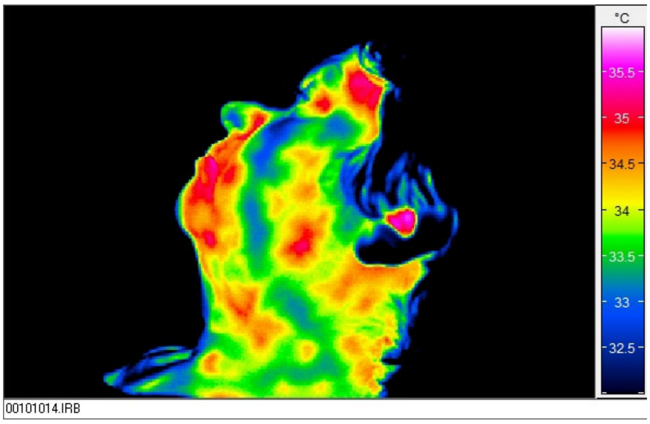

Fig. 2. Thermal image- malignant tumor in submundibular region

TABLE I
MEASUREMENT RESULTS OF THE PATIENTS WITH SUBMANDIBULAR TUMOR

AGE	GENDER	PATHOHISTOLOGICAL DIAGNOSIS	Right side, MAX value	Right side, averag evalue	Left side, MAX value	Left side, average value	Difference of MAX values	Difference of average values
63	F	Adenoma pleomorphum	33.71	32.81	34.20	33.46	**0.49**	**0.65**
59	F	Adenoma pleomorphum	34.01	32.81	33.56	32.16	**0.45**	**0.65**
53	M	Adenoma pleomorphum	35.69	35.15	35.98	35.51	**-0.29**	**-0.36**
72	F	Non-Hodgkin B large cell lymphoma	35.82	35.18	35.58	35.28	**-0.24**	**0.10**
58	F	B large cell lymphoma	35.19	34.32	35.22	34.15	**0.03**	**-0.17**
67	F	B large cell lymphoma	32.85	32.15	33.61	31.56	**0.76**	**-0.59**
51	F	Metastasis carcinomatosa ca sqamocellulare	34.72	33.79	33.95	33.41	**0.77**	**0.38**
76	M	Abscessus subacutus gl. salivariae sialoadenitis chronica fibrosa et obstructiva. lipomatosis gl. salivariae	34.99	33.94	35.48	34.19	**0.49**	**0.25**
87	M	Lipoma gl. salivariae	35.73	35.00	35.11	34.65	**-0.62**	**-0.35**
21	M	Cystis branchialis	33.75	33.25	34.52	33.89	**0.77**	**0.64**
26	M	Sialoadenitis chronica	35.36	34.61	34.66	34.13	**-0.70**	**-0.48**
48	M	Sialoadenitis acuta	33.64	32.88	33.88	33.32	**0.24**	**0.44**
67	M	Warthin tumor	34.86	34.26	34.88	34.17	**0.02**	**-0.09**

TABLE II
MEASUREMENT RESULTS OF THE HEALTHY MALE PEOPLE

	RIGHT SIDE T(°C)	LEFT SIDE T(°C)	DIFFERENCE T(°C)
1	33.43	33.09	0.34
2	33.41	33.01	0.40
3	34.02	34.06	0.04
4	34.64	34.85	0.21
5	34.88	34.43	0.45
6	34.91	35.27	0.36
7	34.66	34.60	0.05
8	33.94	34.23	0.29
Average difference			**0.27**

TABLE III
MEASUREMENT RESULTS OF THE HEALTHY FEMALE PEOPLE

	RIGHT SIDE T(°C)	LEFT SIDE T(°C)	DIFFERENCE T(°C)
1	32.95	33.16	-0.22
2	34.16	33.93	0.23
3	33.61	33.88	-0.27
4	33.79	33.12	0.67
5	30.87	30.81	0.06
6	33.15	32.94	0.21
7	33.81	33.66	0.15
Average difference			**0.26**

III. RESULTS AND DISCUSSION

Some of the most common diseases of the salivary glands are represented by inflammatory disorders of glands, sialolithiasis, mucoceles. Their causes can be bacterial and viral infections, autoimmune disease, and they can occur after cancer therapy [6]. While primary Sjoegren's syndrome and Sarcoidosis predominantly affect the parotid gland, IgG4- associtated disease (Kuttner € 's tumour) often becomes clinically apparent as submandibular gland pseudo-tumor [7]. Salivary gland tumors make up about 6% of all head and neck tumors. The most common benign tumor is pleomorphic adenoma. There are about 20 histological subtypes of malignant tumors [8] and unlike head and neck tumors where squamous cell carcinomas are dominant, in salivary glands adenoid cystic and mucoepidermoid carcinomas are the most common [9]. In addition to salivary gland diseases in the submandibular region, extraglandular tumors may occur. Since there are no lymph nodes in the gland itself, there are no local or distant metastases to the gland, but tumors of the lips and oral cavity often give local metastases submandibularly [10]. Beside this metastasis unspecific lymph nodes, autoimmune lymph node disease, and nodal lymphomas represent the most important extraglandular diseases affecting the submandibular triangle [9].

There is no observable gender bias [8] in distribution of tumors of submandibular region and our results (6 woman and 7 men) are complementary with that. Data from the literature show that the mean age in which these changes occur is between 50 and 70 years, and this is confirmed by our results where the mean age is 57.6 years, 55.5 for benign and 62 years for malignant tumors [8].

The assumption on which the hypothesis of infra red thermal camera is based as a possible diagnostic tool implies that the presence of a pathological process changes the metabolic activity of tissues through changes in tone and blood flow through blood vessels, due to increased flow in inflammatory processes or due to angiogenesis and pathological vascularization in tumors. These changes are registered by a thermal camera, and by analyzing a thermogram it is possible to establish the temperature imbalance of the region with the pathological change and the symmetrical region in which there is no pathological change. Weinstein et al. [11] claimed after review of medical literature on cephalic thermography that skin surface thermal asymmetry between opposing sides of the head of magnitude of 0.5°C was regarded as a positive diagnostic finding, indicative for disease in this region of the body.

Our results show that in two patients with benign pleomorphic adenomas the average temperature of the tumor side was higher by 0.65°C, in one with the same diagnosis it was lower by 0.36°C, in a patient with Warthin tumor the temperature was practically the same (-0.09°C), in two patients with acute sialoadenitis it was higher by 0.25°C and 0.44°C, while in a patient with chronic sialoadenitis it was lower by 0.48°C and in lipoma of the submandibular region by 0.36°C. The patient with cystic change had a higher affected side temperature by 0.64°C. In the group of malignant tumors, patients with pathohistological diagnosis of lymphoma had lower affected side temperatures by 0.17°C and 0.59°C in B large cell lymphoma and respectively 0.10°C and 0.38°C positive differences in Non Hodgkin's lymphoma and in squamous cell carcinoma metastasis.

The average difference in the temperature of the affected and healthy side is 0.399°C. If we compare this with the average differences in the temperature of the left and right side of the region of interest in the control group of 0.263°C, it is noticed that it is significantly smaller, with the temperature difference in only one subject from the control group greater than 0.4°C. A difference of 0.4°C and greater is present in 6 subjects with tumor changes of the submandibular region.

IV. CONCLUSION

Although the thermal camera has been used in medicine for diagnostic purposes for more than 70 years, its use for diagnosing head and neck diseases is still in the testing phase. Given the advantages of this diagnostic method due to its non-invasiveness and availability, if the hypotheses were confirmed about the possibility of thermal cameras to record temperature asymmetries of symmetrical regions of the head and neck thus indicating the existence of particularly tumor changes, it would be a big step in diagnosis and thus treatment of patients with tumor changes in this region. The published results in a small number of papers dealing with this issue, as well as in the paper presented here, provide a good basis and justify the continuation of research on the possibilities of thermal cameras in the diagnosis of head and neck diseases.

ACKNOWLEDGEMENT

This work has been supported by the Ministry of Education, Science and Technological Development of the Republic of Serbia.

Measurements for the purposes of this paper were performed with the help of the staff of the Department for maxillofacial surgery, Clinic for dental medicine in Niš.

REFERENCES

[1] Tattersall G. J., “Infrared thermography: A Non-invasive Window into Thermal Physiology”, *Comparative Biochemistry and Physiology*, Vol. 202, pp.78-98, 2016.

[2] Champy M., Bourjat P., Schnebelen J. M., “Thermograpic exploration of the parotid region”, *Journal of Oral and Maxillofacial Surgery*, Vol. 4, No. 3, pp. 163-171, 1976.

[3] Durnovo E. A., Potekhina Y. P., Marochkina M. S., Yanova N. A., Sahakyan M. Y., Ryzhevsky D. V., “Diagnostic Capabilities of Infrared Thermography in the Examination of Patients With Diseases of Maxilla-facial Area“, *Sovremennye Tehnologii v Medicine*, Vol. 6, No. 2, pp. 61-65, 2014.

[4] Suhela R.,Vijaya G., ”Study of morphological subtypes of major salivary gland tumors”, *Perspectives in Medical Research*, Vol. 5, No.3, pp.24-28, 2017.

[5] Ziglinas P. et al., ”Primary tumors of submandibular glands: A retrospective study based on 41 cases”, *Oral Oncology*, Vol. 46, No. 4, pp. 287-291, 2010.

[6] Delli K., Spijkervet F. K., Vissink A., “Salivary gland diseases: infections, sialolithiasis and mucoceles“, *Monographs in Oral Science*, Vol. 24, pp. 135-144, 2014.

[7] Andreas K., Nikolaus C., Murat B., Naglaa M., Benedikt H., “Multimodal ultrasonographic algorithm in the differentiation of submandibular masses“, *Acta Oto-Laryngologica*, Vol. 137, No. 6, pp. 640-645, 2017.

[8] Barnes L. B., Eveson J. W., Reichart P., Sidransky D., “Pathology and genetics of head and necktumors“, *IARC Press*, Lyon, 2005.

[9] Franzen A. M., Funzel T., Lieder A., “Parotid gland metastasis of distant primary tumours: a diagnostic challenge“, *Auris Nasus Larynx*, Vol. 43, No. 2, pp. 187-191, 2016.

[10] Shiboski C. H., Schmidt B. L., Jordan R. C., “Tongue and tonsil carcinoma: increasing trends in the U.S. population ages 20–44 years“, *Cancer,* Vol. 103, pp. 1843-1849, 2005.

[11]Weinstein S. A., Weinstein G., Weinstein E.L., Gelb M., “Facial thermography, Basis, Protocol, and Clinical Value“, *CRANIO*, Vol. 9, No. 3, pp. 201-211, 1991.

Redundancy in Pseudorandom Position Encoder Operation

Goran Miljković, Dragan Denić, Milan Simić and Aleksandar Jocić

Abstract - Optical absolute position encoders are very important components in many industrial systems that require measurement and control of angular position and speed. The paper discusses a pseudorandom absolute optical encoder that has a synchronization track and two phase-shifted pseudorandom code tracks. It is analyzed how the arrangement of tracks on the disk, the way the code is read and operation algorithm contribute to the increase of redundancy and reliability in the operation of the encoder.

Keywords – Pseudorandom binary sequence, Angular position measurement, Optical position encoder.

I. INTRODUCTION

Optical absolute position encoders play an important role in modern automation systems, robotics, computer peripherals, etc [1, 2]. When measuring the position and speed of the motor using an encoder, depending on the specific application, it usually has to meet some requirements in terms of its parameters: resolution, accuracy, speed, price, power consumption, reliability, etc. The demand for higher resolution encoders is constantly increasing, but other encoder parameters are also becoming important for some applications. The auto industry, the aviation industry, space research, military equipment, in addition to the resolution and accuracy of the position encoder, also require its good reliability.

Absolute encoders based on the application of pseudorandom binary sequences are more and more present on the market. They determine the absolute position using a single code track on which the code words are serially arranged [1, 2, 3]. If any adjacent *n* bits are read from the pseudorandom code track, they represent a unique code word that allows the absolute position to be determined. The code reading can be realized as serial, with one or two reading heads, since the code words are arranged in series. So, unlike classic absolute encoders, pseudorandom absolute encoders have one code track regardless of resolution and can use only one code reading head.

The most important components of a pseudo-random absolute encoder are: code reading [4, 5], synchronization of code reading [6, 7], pseudorandom/natural code conversion [8, 9] and code reading error detection [11]. Each of these components contributes to the accuracy and reliability of the encoder. Pseudorandom code reading can be realized with one code reading head, but also using a linear array of photodetectors, where each approach has its advantages and disadvantages [4, 5]. Synchronization of code reading is usually implemented using external synchronization track, but there are also more complex methods that introduce additional bit encoding instead of additional track [6, 7]. In order to obtain position information in the form of a decimal number, it is necessary to convert the read pseudorandom code word into natural code. Conversion can be implemented in parallel, a fast method using a lookup table, or a serial, simple and slower method [8, 9, 10]. A compromise solution can be applied, in terms of speed, price and complexity of hardware, serial - parallel conversion. Pseudorandom absolute encoders have enabled the application of methods for detecting code reading errors [11]. There are many sources of pseudorandom encoder reading errors: mechanical errors (eccentricity, centering of the disk and code reading system), errors in disk production (incorrectly printed code, ellipticity), external influences (dust, temperature, humidity, vibration), etc.

The paper presents an absolute encoder solution, based on the application of pseudorandom binary sequences, which, in addition to good resolution, has a lower price and better redundancy and reliability in operation compared to classical absolute encoders [12]. In order to achieve better reliability of the proposed encoder, it has a synchronization track and two phase-shifted pseudorandom code tracks on the disk. The code is read in series using avaliable optical sensor used on the market for incremental encoders. The goal is to make the encoder more resistant to various influences that can lead to failures or misread bits of code.

Different variants of the serial code reading method are presented in the first part of the paper, as well as the proposal of an improved solution with two code reading heads for reading code with two phase-shifted code tracks. The proposed method of reading code has enabled an increase in redundancy and reliability in the operation of the encoder. After that, the realization of the encoder was presented using avaliable optical sensors, which made the realization of the encoder cheaper. The algorithm of encoder operation is briefly described, as well as the application of code reading error detection methods. Different modes of operation of the encoder have been defined so that it can efficiently respond to possible failures or errors in reading the code.

Goran Miljković, Dragan Denić, Milan Simić and Aleksandar Jocić are with University of Niš, Faculty of Electronic Engineering, Aleksandra Medvedeva 14, 18000 Niš, E-mail: goran.miljkovic@elfak.ni.ac.rs, dragan.denic@elfak.ni.ac.rs, milan.simic@elfak.ni.ac.rs, aleksandar.jocic@elfak.ni.ac.rs.

II. SERIAL READING OF PSEUDORANDOM CODE

Adjacent n-bit code words from the pseudorandom code track are longitudinally arranged and differ by one bit, allowing serial reading. This is an advantage over classic absolute encoders that do not have this possibility. Serial reading of the pseudorandom code can be realized with one or two reading heads. The disadvantage of serial code reading is the need for initial movement until the formation of the first valid code word. With serial readings with one head, position information is lost when changing the direction of rotation and does not allow the application of a reliable method of checking code reading errors, Fig. 1.

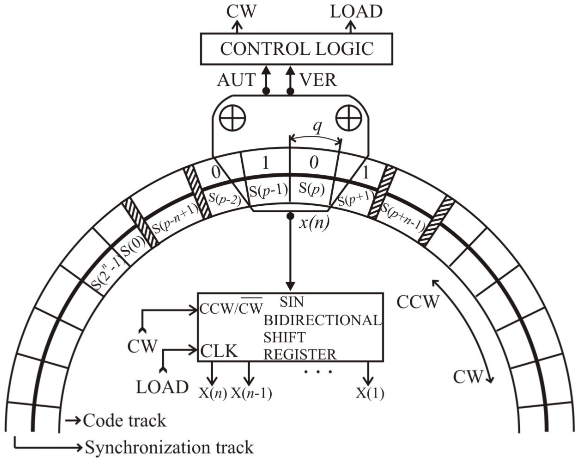

Fig. 1. Serial reading with one code reading head.

The formation of the code word is performed in the bidirectional shift register, where the way of adding the read bits depends on the direction of rotation. An additional two heads, AUT and VER, are needed to obtain a signals from the synchronization track, and they are used to synchronize the readings of the pseudorandom code track and to determine the direction of rotation.

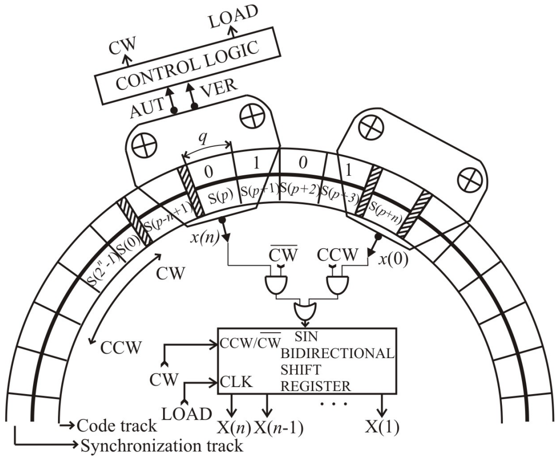

Fig. 2. Serial reading with two code reading heads.

Better solution for serial reading of a pseudorandom code uses two reading heads that are at a distance of *nq*, Fig. 2. When the code reading head *x(n)* reads bit *S(p)*, the code reading head *x(0)* reads bit *S(p+n)*. This solution offers continuity of code word formation even when changing direction of rotation without using any additional control logic. Also, this solution enables the application of a reliable method of detecting code reading errors [11]. However, the small distance between the reading heads is subject to changes due to temperature, vibration, and causes code reading errors.

Therefore, the paper proposes a solution that uses two reading heads to read the code that are now in line, one below the other, as well as two phase-shifted pseudorandom code tracks, Fig. 3. There are synchronization and two phase-shifted code tracks on the disk. One reading head reads bits *S(p)* from the first pseudorandom code track, and the other reading head reads bits *S'(p+n)* from the phase-shifted code track. The reading heads arranged in this way are easier to realize in practice and their position in relation to the disk is not so sensitive to the influence of temperature, vibration, etc. Redundant and more reliable operation of the encoder is obtained, and the price is the introduction of an additional code track. The proposed solution, as well as the previous solution, offers continuity in the formation of code words, but also the application of reliable methods for checking code reading errors.

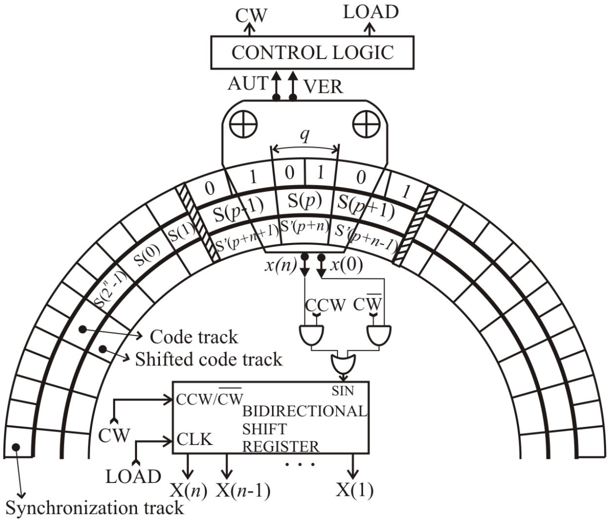

Fig. 3. Serial reading of two phase-shifted code tracks.

III. EXPERIMENTAL SOLUTION

The experimental solution was used to analyze the operation and verify the redundancy and reliability in the operation of the proposed optical encoder, Fig. 4. The two 10-bit pseudorandom code tracks are next to each other and are phase shifted by 9 bits. The encoder disc with diameter 50 mm is mounted on the DC motor shaft and is read by the MO-PMD09 optical sensor (www.micropto.com). Between the disk and the optical sensor is a specially made stationary mask that directs light to the corresponding photodiodes of the sensor. The signals from the optical sensor are converted into rectangular signals by means of a signal conditioning circuit. Four photodiodes are used to read the synchronization track to obtain two phase-shifted signals that define the reading moment of the pseudorandom code and are used to determine the direction of rotation. At the output of the electronic block of the encoder, there are two signals from the synchronization and two from two pseudo-random code tracks. The signals are fed to the digital inputs of the USB acquisition card NI USB-6341, and then the encoder operation algorithm is implemented in the LabVIEW environment.

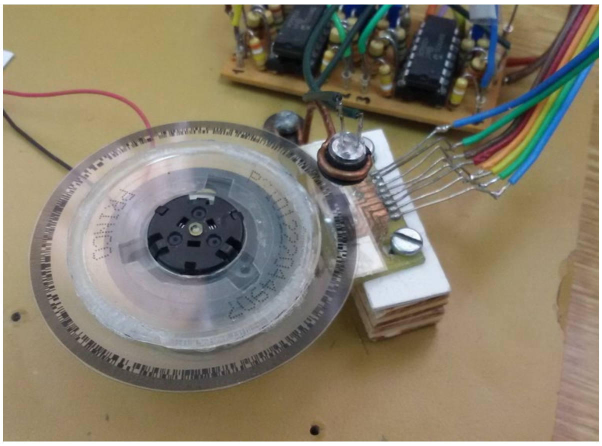

Fig. 4. Experimental solution.

IV. OPERATION ALGORITHM AND ERROR DETECTION

An encoder designed in this way can have several operating modes, which, with the application of appropriate methods for checking code reading errors, enables a more reliable and flexible operation. Depending on the direction of rotation, the main code word used to determine the absolute position is formed from one of two pseudorandom code tracks, PRBS1 or PRBS2, Fig. 5. In order not to overload the figure, the error check for the CW direction is presented on it, and a similar scheme is for the opposite direction of rotation. The bits from the second code track are used to form an control code word, which together with the main code word can be used to apply a reliable error checking method, Fig. 5. When a new bit is read, the content of the control register are shifted according to the direct law of generation and then, after 9 shifts, its content is compared with the content of the main register, whereby we get reliable information whether an error has occurred. In parallel with this method of error checking, we have a check in each track whether the new read bit is valid, by comparing it with the generated bit. A Fibonacci generator with a direct feedback configuration would be used for the opposite direction of rotation (CCW). This way, if an error occurs, it will be known in which track it occurred.

Figure 6 shows a simplified encoder operation algorithm. Because serial code reading is applied, the encoder needs an initial movement when it starts to form the first valid code word. When reading a new bit, the read error is checked and the direction of rotation of the encoder disk is monitored. If no errors were detected in the code reading, the encoder operates in normal mode, and based on the read code word and after the conversion of the pseudorandom to natural code is completed, position information is obtained. If a read error occurs in one of the two code tracks, the encoder may continue to operate in reduced reliability mode where one code track is used. In case we have read errors in both code tracks, the encoder can work in incremental mode using only the synchronization track. The goal is that if the encoder, due to various external influences, has an error in reading the code, it does not give incorrect position information, but is able to change the mode of operation and continue to provide accurate position information. The read error can only occur instantaneously due to some shock or vibration, so the encoder can return to the previous mode if the error does not occur in the same place in the next pass.

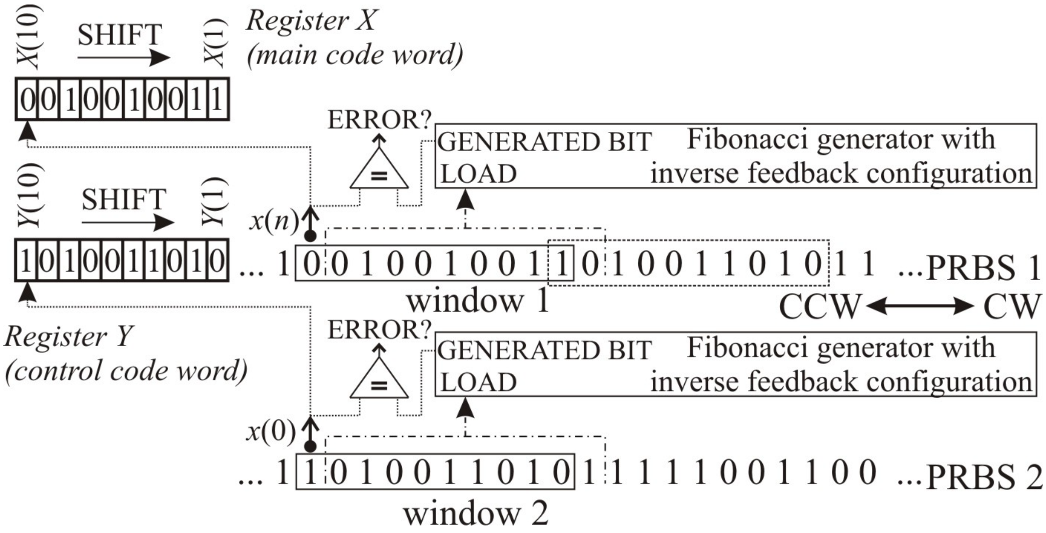

Fig. 5. Code reading error detection.

The redundancy in the work of the encoder is reflected in the fact that we have two separate pseudorandom code tracks and two reading heads, where if one head fails or one track gets dirty, the encoder can continue to work. Also, compared to the classic absolute encoder, the presented encoder has a smaller number of code tracks for the same resolution, so it can be realized on a disk of smaller diameter.

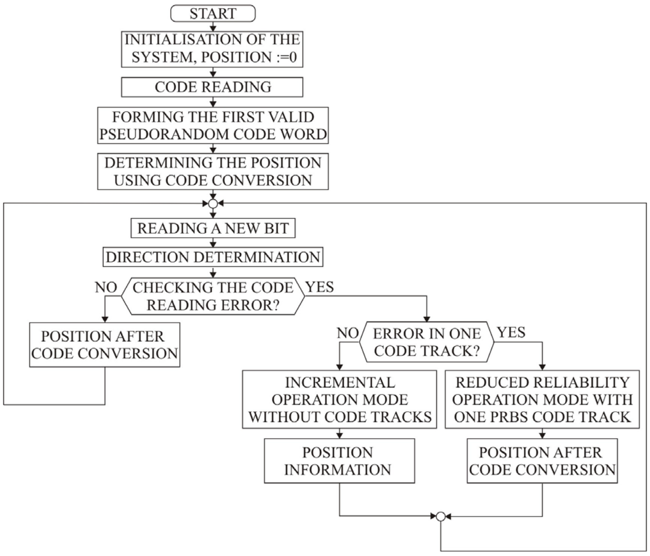

Fig. 6. Operation algorithm.

V. CONCLUSION

The paper presents a redundant and reliable solution of an absolute encoder that is less sensitive to external influences that would cause erroneous bit readings and thus erroneous position information. The advanced encoder design allows the encoder to operate through multiple modes of operation, with the encoder adapting to the currently detected errors. Modern fast processors enable the implementation of more complex encoder operation algorithms, without compromising the speed of encoder operation. Some of the disadvantages of the encoder would be the need for initial movement to the formation of the first valid code word, then a more complex operation algorithm, the time-consuming conversion of pseudo-random to natural code.

ACKNOWLEDGEMENT

This work has been supported by the Ministry of Education, Science and Technological Development of the Republic of Serbia.

REFERENCES

[1] Matsuzoe, Y., Tsuji, N., Nakayama, T., Fujita, K., Yoshizawa, T., “High-performance absolute rotary encoder using multitrack and M-code”, Optical Engineering, vol. 42, no. 1, pp. 124-131, 2003.

[2] Petriu, E.M., “Absolute position measurement using pseudorandom binary encoding”, IEEE Instrum. Meas. Mag., vol. 1, no. 3, pp. 19–23, 1998.

[3] MacWilliams, F.J., Sloane, N.J.A., “Pseudo-random sequences and arrays,” Proc. of the IEEE, vol. 64, pp. 1715-1729, 1976.

[4] Arsić, M., Denić, D., “New pseudorandom code reading method applied to position encoders,” Electronic Letters, vol. 29, no. 10, pp. 893–894, 1993.

[5] Denić, D., Ranđelović, I., Rančić, M., “High – resolution pseudorandom encoder with parallel code reading,” Electronics and Electrical Engineering, vol. 56, no.7, pp. 14-18, 2004.

[6] Petriu, E.M., “Scanning method for absolute pseudorandom position encoders”, Electronic Letters, vol. 24, no. 19, pp. 1236–1237, 1988.

[7] Denić, D., Miljković, G., “Code reading synchronization method for pseudorandom position encoders,” Sens. Actuators A, vol. 150, pp. 188–191, 2009.

[8] Denić, D., Stojković, I., “Pseudorandom/natural code converter with parallel feedback logic configuration,” Electronic Letters, vol. 46, no. 13, pp. 921–922, 2010.

[9] Denić, D., Dinčić, M., Miljković, G., Perić, Z., “A contribution to the design of fast code converters for position encoders”, International Journal of Electronics, vol. 103, no. 10, pp. 1654-1664, 2016.

[10] Petriu, E.M., Basran, J.S., “On the position measurement of automated guided vehicles using pseudorandom encoding,” IEEE Trans. Instrum. Meas., vol. 38, no. 3, pp. 799-803, 1989.

[11] Denić, D., Arsić, M., “Checking of pseudorandom code reading correctness“, Electron. Lett., vol. 29, no. 21, pp. 1843–1844, 1993.

[12] Miljković, G., Denić, D., "Redundant and flexible pseudorandom optical rotary encoder", Elektronika IR Elektrotechnika, Kaunas University of Technology, No. 26(6), pp. 10-16, 2020.

Active power monitoring system for load up to 2kW

Dejan Stevanović, Miona Andrejević Stošović, Milan Savić

Abstract—This paper presents a system for AC current monitoring in home appliances up to 20A. It is implemented on a custom made PCB. System also measures voltage, line frequency, power factor, active power and total imported active energy. Measurement results can be obtained by a remote computer or some other device via serial RS-485 interface. Consumer is enabled to have bigger control over real-time current consumption by installing several monitoring devices and connecting them into a network.

Index Terms—Energy efficiency, Modbus RTU, monitoring system.

I. INTRODUCTION

Energy efficiency has a fundamental role to play in the transition towards a more competitive, secure and sustainable energy system. Although energy powers our societies and economies, future growth must be driven with less energy and lower costs. According to the Energy Efficiency Communication of July 2014 [1], the EU is expected to achieve energy savings of 18%-19% by 2020. Reduced power consumption leads to reduced emissions and, consequently, reduced carbon footprint. This is a straightforward benefit. However, this could happen only if EU countries implement all of the existing legislation on energy efficiency. Unfortunately, efficiency of electrical distribution is currently not much managed or planned by utilities. The unfavourable result is that most utilities waste considerable amounts of electricity. For example, the annual value of transmission and distribution losses runs up to 6% of total generated energy [2]. These losses mainly occur in the low and medium voltage lines, and also in primary and secondary substations. One way for reducing losses and increasing efficiency on low level power distribution system is improving the system for registration of electric energy consumption [3-4]. Another way is to implement home energy monitoring system. A lot of similar systems have been already developed [5]. Some of realized systems are described in [6-8].

Economic return is one of the major reasons why households should consider and adopt smart energy management products. A home energy monitoring system allows consumers to have significant role in energy management activities. It can be implemented by using smart sockets. Probably, the simplest and most straightforward way to monitor and control energy usage is by replacing traditional sockets and plugs with the smart ones. Namely, placing multiple measurement devices in the household enables that consumer has nearly instant information about current consumption of each appliance. Some smart sockets contain relay, so that turning load on and off is supported. In this paper we proposed a system that can be implemented at electric panel. Moreover, our system can be used as smart fuses.

This paper is organized as follows. In the next section, the basic definitions that correlate power parameters with measured current and voltage data will be given. The third chapter will be dedicated to description of realised system, while in the fourth chapter measurement results will be given. The conclusion is in the fifth section.

II. DEFINITIONS OF ELECTRIC POWER QUANTITY

The core of our system is a MCP39F521 [9] which calculates all power quantities that are of interest for utility to control consumption. Usually, these values are defined by appropriate standards. All these circuits relay on digital signal processing of voltage and current samples. The instantaneous value of voltage and current are attenuated through voltage divider, while current transformers can be used for current, Rogowski coil sensors or shunt resistors. The first set of signal conditioning that occurs inside MCP39F521 is shown in Fig.1.

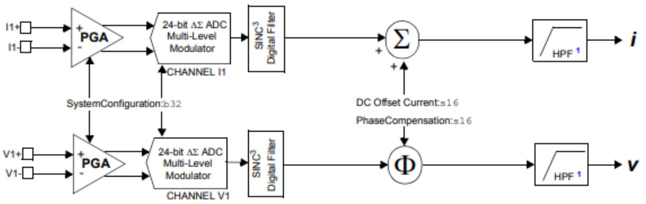

Fig. 1. Channel I1 and V1 signal flow

The obtained signal at output of attenuator is sent to ADC where it is sampled at discrete time points (at least two per period, according to the Nyquist-Shannon theorem) and digitalized. DSP processes digital voltage and current samples and calculates all necessary power quantities. Instantaneous value of signal (current or voltage) in time domain can be expressed as:

$$x(t) = \sqrt{2} X_{RMS} \cdot \cos(2\pi ft + \varphi) \tag{1}$$

Dejan Stevanović and Miona Andrejević Stošović are with University of Niš, Faculty of Electronic Engineering, Aleksandra Medvedeva 14, Niš, Serbia,{dejan.stevanovic, miona.andrejevic}@elfak.ni.ac.rs.

Milan Savić is with the College of Applied Technical Sciences Niš, Aleksandra Medvedeva 20, 18000 Niš, Republic of Serbia (e-mail: milan.savic@ vtsnis.edu.rs).

After the discretization in equidistant time intervals, it is transformed to:

$$x(nT)=\sqrt{2}X_{RMS}\cdot\cos(2\pi\frac{f}{f_{sempl}}n+\varphi)\quad , \tag{2}$$

where f and f_{sempl}, are frequency of the signal and the sampling frequency, respectively. The RMS value is calculated using the following equation:

$$X_{RMS}=\sqrt{\frac{\sum_{n=1}^{N}x(nT)^2}{N}}\quad . \tag{3}$$

The signal flow of calculation of RMS current and voltage values is presented in Fig. 2.

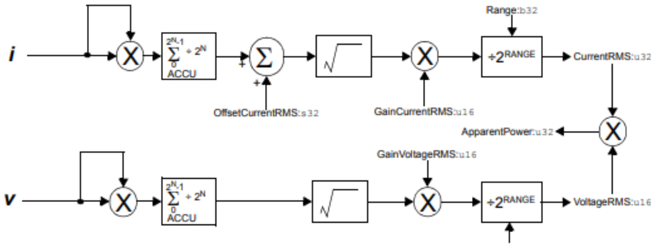

Fig. 2. RMS current and voltage calculation signal flow

The active power is obtained as average value of the multiplied instantaneous values of current and voltage, by using Eq. (4). Signal flow of active power calculation is shown in Fig. 3. The MCP39F521 has two simultaneous sampling A/D converters. For active power calculation, the instantaneous currents and voltages are multiplied in order to create instantaneous power. The instantaneous power is then converted to active power by averaging or calculating DC component.

$$P=\frac{\sum_{n=1}^{N}v(nT)i(nT)}{N}=\frac{\sum_{n=1}^{N}p(nT)}{N}\ . \tag{4}$$

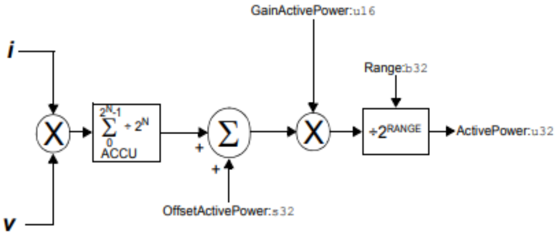

Fig. 3. Active power calculation signal flow

III. REALIZED SYSTEM

The block diagram and photography of our system are shown in Fig. 4. As can be seen from Fig. 4a our system consist relay circuit, RS485 circuit, current/voltage sensor circuit, power measuring circuit and MCU. We used a well-known microcontroller Atmega328P [10] as MCU, which characteristics meet all our demands. MCU communicates with power measuring circuit (MCP39F521) by using I2C protocol and passes the obtained data through RS485 to central monitoring system by using Modbus RTU protocol.

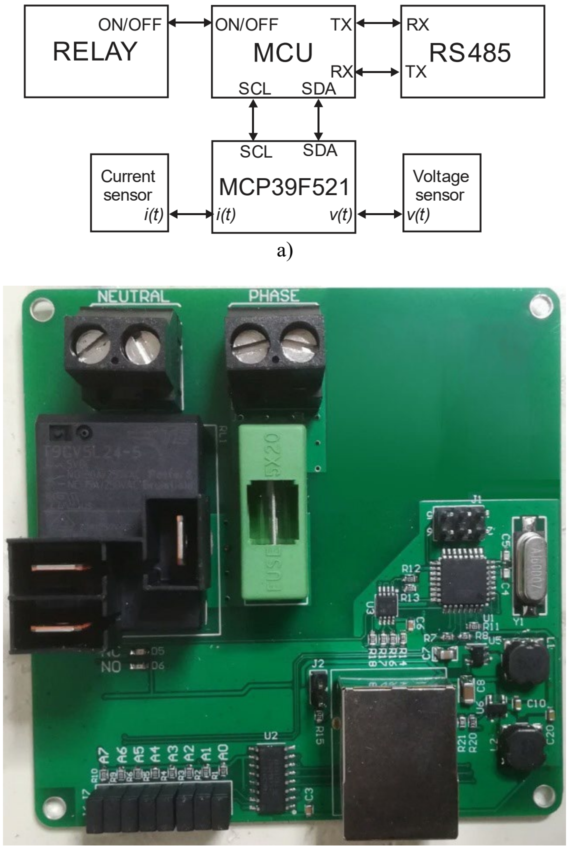

a)

b)

Fig. 4. a) Block diagram of realized system,
b) photo of realized system

RS485 interface supports multiple devices on the same bus. This interface is currently widely used in data acquisition and control applications where multiple nodes communicate with each other. Consequently, each board needs to have unique address (unique on the network level). Because of that remote monitoring computer can send request only to specific node in a network. This address can be set by using jumpers in our system. The maximum number of nodes on the same RS-485 network in our case is 213 [11]. The number of supported devices on same networks depends on IC that is used for RS485 interface, bound rate and distance between nodes.

The load is powered via the T9A series relay, which has normal open (NO) and normal closed terminals (NC) [12]. The relay can be set to normal closed state, which is useful in applications where electrical appliance has to be always on, but on demand it can be turned off. Typical example of this usage is refrigerator in hotel rooms which needs to be always powered on. When customer exits the room, all electrical outlets and devices are disabled, except refrigerator which is connected via the relay board.

As we said before, communication between computer and our device is done by using Modbus RTU protocol and QModMaster application. We use only four functions from Modbus RTU: *write single coil, write multiple coil, read input registers and read holding registers.*

The state of relay can be controlled by using *write single coil* or *write multiple coil* function, while reading measurement results is done by using *read input registers* or *read holding registers* functions. These registers contain value of RMS voltage/current, line frequency, power factor, active power and total accumulated energy, as shown in Fig.5.

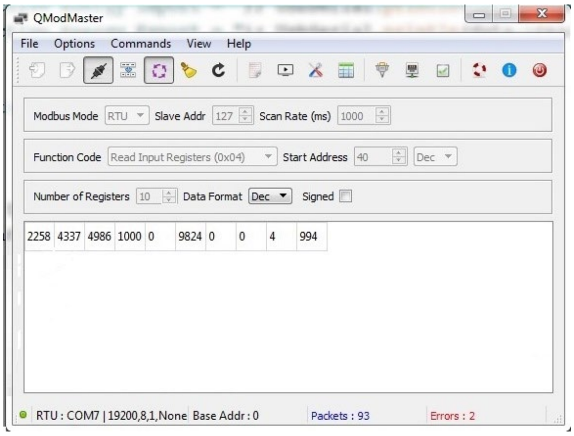

Modbus Mode RTU Slave Addr 127 Scan Rate (ms) 1000

Function Code Read Input Registers (0x04) Start Address 40 Dec

Number of Registers 10 Data Format Dec Signed ☐

```
2258 4337 4986 1000 0    9824 0    0    4    994
```

RTU : COM7 | 19200,8,1,None Base Addr : 0 Packets : 93 Errors : 2

Fig. 5. Modbus application

QModMaster application runs on central computer which is used for reading data from each relay board. For connecting PC to RS-485 network USB-RS485 bridge is used. Before connecting relay board on the network, it is necessary to set slave address of the board, by setting appropriate jumper configuration. In Fig. 5, we showed obtained data when using *read input registers* function. By using this function and setting number of register to 10 we obtain: RMS voltage/current (registers 1 and 2), line frequency (register 3), power factor (register 4), active power (registers 5 and 6) and active energy (registers 7 to 10), respectively. In order to get good accuracy of read values, we introduce correction factors. This factor for voltage is 10, for line frequency and active power is 100, while for current, power factor and active consumed energy is 1000. The negative values of power factor are presented with digit 1 on the 5th position at register 4.

IV. MEASUREMENT RESULTS

The accuracy of the realized system is verified by using a set of different linear and nonlinear loads. As nonlinear loads we chose LED and CFL bulbs. These nonlinear loads are chosen as benchmarks because they characterize small nominal power. Namely, the intention is to show that our system measures current in range from 0.1A to 20A with accuracy less than 2%, having different load conditions. For linear load measuring we have used, heater, water kettle and different types of incandescent light bulbs (ILB). As reference measuring instrument, we have used electronic power meter produced by EWG electronics [13]. It fulfils the IEC 62052-22 standard [14], IEC 62052-23standard [15]. The previously mentioned standards, fulfilled by power meter, guaranty to us that power meter has good accuracy.

TABLE I
MEASUREMENT RESULTS

		Power Meter			**Our System**					
NO.	TYPE OF LOAD	U_{RMS}	I_{RMS}	P (W)	U_{RMS}	I_{RMS}	P (W)	V_{RMS} Error(%)	I_{RMS} Error(%)	P Error(%)
1	LED10W	229.3	0.056	11.8	228.8	0.051	11.4	9.80	3.51	3.51
2	CFL20W	229.3	0.138	19.08	229	0.138	19	0.00	0.42	0.42
3	LED10W+CFL20W	229.26	0.172	30.23	228.7	0.175	30.6	1.71	1.21	1.21
4	ILB100W	229	0.436	99.72	228.70	0.427	98.10	2.11	1.65	1.65
5	ILB250W	228.5	1.175	268.2	227.80	1.150	263.40	2.17	1.82	1.82
6	ILB450W	227.5	2.043	465	227.00	2.000	457.30	2.15	1.68	1.68
7	ILB650W	226.7	2.912	660	226.20	2.860	649.00	1.82	1.69	1.69
8	HR (HEATER)	226.3	3.545	802.4	225.7	3.481	787	1.84	1.96	1.96
9	HR+ILB100W	226.13	3.972	897	225.3	3.905	883	1.72	1.59	1.59
10	HR +ILB250W	225.6	4.704	1061	224.7	4.622	1041	1.77	1.92	1.92
11	HR+ILB450W	225.2	5.55	1250	224.2	5.456	1226	1.72	1.96	1.96
12	HR +ILB650W	224.3	6.404	1437	223.4	6.295	1408	1.73	2.06	2.06
13	WATER KETTLE (WK)	222.6	8.067	1793	221.4	7.918	1760	1.88	1.88	1.88
14	WK+LED10W+CFL20W	222.5	8.231	1825	221.4	8.074	1793	1.94	1.78	1.78
15	HR+WK	220.2	11.385	2499	218.7	11.186	2450	1.78	2.00	2.00
16	HR+WK+ILB100W	220	11.759	2585	218.3	11.573	2535	1.61	1.97	1.97
17	HR+WK +ILB250W	219.4	12.461	2734	217.8	12.260	2676	1.64	2.17	2.17
18	HR+WK +ILB450W	218.6	13.255	2900	217	13.065	2845	1.45	1.93	1.93
19	HR+WK +ILB650W	218.3	14.077	3074	216.6	13.856	3098	1.59	0.77	0.77

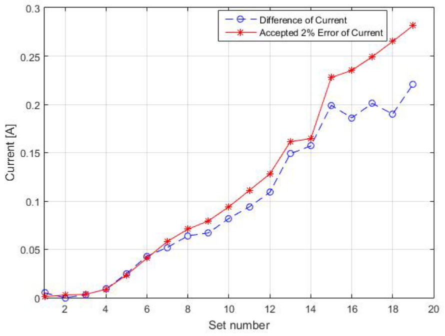

a)

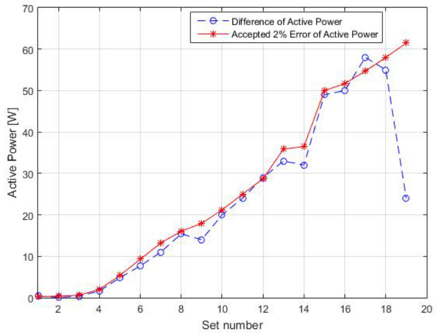

b)

As it is shown in Table I and Fig 6., after measurements with all the loads, we obtained accuracy less than 2%.

V. CALIBRATION PROCEDURE

When performing calibration, one compensates ADC gain error, component tolerances and overall noise in the system. The device provides an on-chip calibration algorithm that allows simple system calibration to be performed quickly. The excellent analog performance of the A/D converters on the MCP39F521 allows for a single point calibration and a single calibration command to achieve accurate measurements.

Calibration can be done either by using the predefined auto-calibration commands, or by writing directly to the calibration registers [9]. In our case we decided to directly write gain value into calibration register. In order to achieve that, we have to use some reference measuring unit. We will include reading from this unit into calculation. The new value of gain will be sent to relay board by using QmodeMaster application. Currently we can change only current and active power gain register at relay board. To achieve that, in QmodeMaster application we set function code to WriteMultipleRegisters (0x10) and set new value for current and active power gain.

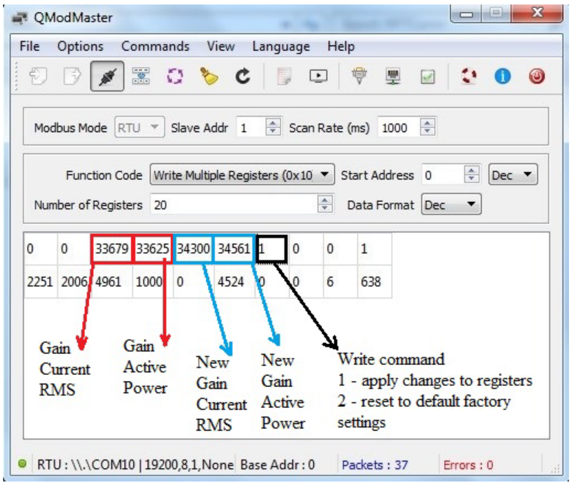

Modbus Mode RTU Slave Addr 1 Scan Rate (ms) 1000

Function Code Write Multiple Registers (0x10 Start Address 0 Dec

Number of Registers 20 Data Format Dec

0	0	33679	33625	34300	34561	1	0	0	1
2251	2006	4961	1000	0	4524	0	0	6	638

Gain Current RMS

Gain Active Power

New Gain Current RMS

New Gain Active Power

Write command
1 - apply changes to registers
2 - reset to default factory settings

RTU : \\.\COM10 | 19200,8,1,None Base Addr : 0 Packets : 37 Errors : 0

Fig. 7 - Modbus calibration

TABLE II
MEASUREMENT RESULTS AFTER CALIBRATION

		Power Meter			**Our System**					
NO.	TYPE OF LOAD	U_{RMS}	I_{RMS}	P (W)	U_{RMS}	I_{RMS}	P (W)	V_{RMS} Error(%)	I_{RMS} Error(%)	P Error(%)
1	LED10W	228.16	0.056	11.95	228	0.053	12	0.07	5.66	0.42
2	CFL20W	228	0.136	19	227.5	0.135	19.1	0.22	0.74	0.52
3	LED10W+CFL20W	228	0.184	31.6	227.8	0.184	31.9	0.09	0.00	0.94
4	ILB100W	227.8	0.442	100.7	227.50	0.441	101.70	0.13	0.23	0.98
5	ILB250W	227.19	1.176	267.6	226.80	1.176	270.20	0.17	0.00	0.96
6	ILB450W	226.26	2.049	463.8	225.60	2.048	468.20	0.29	0.05	0.94
7	ILB650W	225.57	2.911	656.66	225.00	2.911	663.00	0.25	0.00	0.96
8	HR (HEATER)	224.86	3.57	797.4	224.3	3.600	804	0.25	0.83	0.82
9	HR+ILB100W	224.7	3.964	889	224.1	3.967	897	0.27	0.08	0.89
10	HR +ILB250W	224.01	4.667	1050	223.5	4.683	1060	0.23	0.34	0.94
11	HR+ILB450W	223.6	5.54	1250	222.8	5.529	1262	0.36	0.20	0.95
12	HR +ILB650W	222.6	6.364	1415	221.8	6.363	1428	0.36	0.02	0.91
13	WATER KETTLE (WK)	221.2	8.043	1772	220.3	8.000	1783	0.41	0.54	0.62
14	WK+LED10W+CFL20W	221.19	8.16	1805	220.1	8.165	1823	0.50	0.06	0.99

15	HR+WK	218.7	11.279	2466	217.5	11.300	2468	0.55	0.19	0.08
16	HR+WK+ILB100W	218.3	11.764	2552	217	11.723	2576	0.60	0.35	0.93
17	HR+WK +ILB250W	218	12.369	2695	216.6	12.384	2709	0.65	0.12	0.52
18	HR+WK +ILB450W	217.2	13.163	2860	215.8	13.194	2881	0.65	0.23	0.73
19	HR+WK +ILB650W	216.7	13.96	3023	215.4	13.990	3045	0.60	0.21	0.72

New gain value is obtained by using equation:

$$Gain_{NEW} = Gain_{OLD} * \frac{Expected}{Measured}, \qquad (5)$$

Value that is calculated by this equation needs to be between 25000 and 65535.

For example, if our referent measuring device is showing current of 2043 mA (expected value) and relay board is showing 2006 mA (register 11 at Fig. 7), we need to adjust current gain register. In Fig. 7. we see that current gain is 33679 (factory calibrated value). Including all this into above equation we get that new gain is 34300. The results presented in the Table II demonstrated that we successfully implemented calibration procedure and we obtained system which can measure RMS value of current and active power in wide range with accuracy less than 1%.

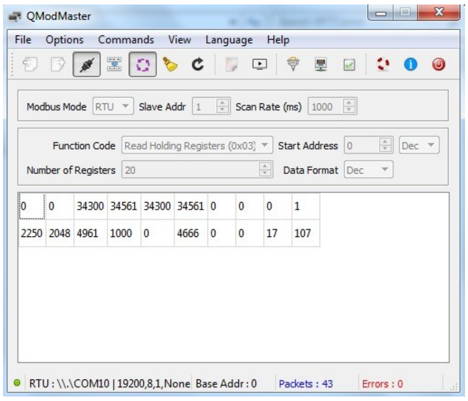

Modbus Mode RTU Slave Addr 1 Scan Rate (ms) 1000

Function Code Read Holding Registers (0x03) Start Address 0 Dec

Number of Registers 20 Data Format Dec

0	0	34300	34561	34300	34561	0	0	0	1
2250	2048	4961	1000	0	4666	0	0	17	107

RTU : \\.\COM10 | 19200,8,1,None Base Addr : 0 Packets : 43 Errors : 0

Fig. 8 – Measurements parameters after calibration

VI. CONCLUSION

This paper presented a current and power monitoring system with accuracy less than 2%. In order to obtain accuracy less than 1%, we additionaly performed calibration of the system. Measuring of the system performance after calibration confirmed that calibration process was properly done. Measuring of voltage, current, line frequency and active power for household appliances gives us sufficient information on which we can perform some action. Built-in relay with NO and NC contacts drastically increases practical usability of our system, so that remote controlling of appliance is also supported. This is very important in terms of creating a power scheme, so that some device can be powered only during night hours, or in case of some unpredicted behaviour we can switch off corresponding device, etc. In the future our goal will be to expand monitoring capabilities so that reactive and apparent power can be measured. Also, beside RS-485 interface, adding WiFi and/or Bluetooth capability will affect places where physically adding cables for RS-485 interface is not an option.

ACKNOWLEDGMENT

This work has been supported by the Ministry of Education, Science and Technological Development of the Republic of Serbia.

REFERENCES

[1] "Energy Efficiency and its contribution to energy security and the 2030 Framework for climate and energy policy", https://ec.europa.eu/energy/sites/ener/files/documents/2014_eec_communication_adopted_0.pdf

[2] M.Clemence, R.Coccioni, A.Glatigny, "How utility electrical distribution networks can save energy in the smart grid era", Schneider Electric, April 2013

[3] M.AndrejevićStošović, D.Stevanović, P.Petković, "*Application of a Standard Power Meter for Detection Source of Harmonic Pollution and Reducing Economic Losses at Power Grid*, Electric Power Components and Systems, Vol. 48, Issue 1-2, Taylor & Francis, UK, 07.04., 2020, pp. 42-55, ISSN 1532-5008, doi:10.1080/15325008.2020.1731879

[4] D.Stevanović, M. AndrejevićStošović, M. Dimitrijević "*Improving the system for registration of electric energy consumption*, 2020 International Symposium on Industrial Electronics and Applications " INDEL 2020, Banja Luka, Bosnia and Hercegovina, 04.11.-06.11., 2020, pp. 1-5, ISBN 978-1-7281-9863-7, doi:10.1109/INDEL50386.2020.9266207

[5] https://nerdtechy.com/best-smart-home-energy-monitor

[6] J. G. Josué, J. M. Pina, M. V. Neves "Home Electric Energy Monitoring System: Design and Prototyping",Proceedings of Technological Innovation for Sustainability – Second IFIP WG 5.5/SOCOLNET Doctoral Conference on Computing 2011, Costa de Caparica, Portugal, 21 – 23. February, 2011, pp. 437 - 444.

[7] E. Barakat, N. Sinno, C. Keyrouz,"*A Remote Monitoring System for Voltage,, Current, Power and Temperature Measurements*", vol 55, no.1, pp. 421 – 428, 2014.

[8] M. J. Manti,A. V Bossche, R. F. Chisab "A Smart Voltage and Current Monitoring System for Three Phase Inverters Using an Android Smartphone Application", Sensors 2017, DOI:10.3390/s17040872

[9] https://ww1.microchip.com/downloads/en/DeviceDoc/20005442A.pdf

[10] https://ww1.microchip.com/downloads/en/DeviceDoc/ATmega48A-PA-88A-PA-168A-PA-328-P-DS-DS40002061B.pdf

[11] https://www.ti.com/lit/ds/symlink/sn65hvd72.pdf?HQS=dis-dk-null-digikeymode-dsf-pf-null-wwe&ts=1621931109406

[12] https://www.te.com/commerce/DocumentDelivery/DDEController?Action=srchrtrv&DocNm=1308242_T9A&DocType=DS&DocLang=English

[13] EWG - multi metering solutions, www.ewg.rs

[14] IEC 62053-22 Electricity metering equipment (AC) - Particular requirements - Static meters for active energy (classes 0.2S and 0.5S).

[15] IEC62053-23 (2003) Electricity metering equipment (a.c.) – Particular requirements – Part 23: Static meters for reactive energy (classes 2 and 3)

Data-Driven Design and Simulation of Two Stage CMOS Operational Amplifier

Dejan Mirkovic and Milena Stanojlovic Mirkovic

Abstract – This paper presents data-driven methodology for the design of analog integrated circuits. Methodology is exemplified with the two stage, Miller compensated, CMOS operational amplifier targeting the 180nm CMOS process node. Detail analysis of the circuit is given with the emphasis on the relation between system level and circuit level parameters. Applied design methodology is confirmed with the simulations at the transistor level.

Keywords –Analog integrated circuits, Design methodology, CMOS, Operational amplifier.

I. INTRODUCTION

Designing the analog circuitry as the integrated circuits (IC) is known to be a challenging task. This fact is even more obvious when the realization in the sub-micron process nodes is sought. Some of the key reasons can be summarised as follows. Since the device sizes shirks with each process node, the parasitics becomes more and more pronounced. Available power supply voltages are getting lower while transistor threshold voltage do not follow that trend (less headroom). The high-speed and low-power designs are in demand, although those two requirements inevitably conflicts with each other (especially in analog world). Also, high-gain, low offset/noise and good linearity/stability of the anaog blocks are expected, as well. All these properties should hold over the process voltage and temperature (PVT) variations. This means that, without proper foundry support and the industry-standard CAD/EDA tools, the design of the ICs is practically impossible.

The well-known fact, among the analog design community, is that the classic square-low model of the MOS-FET transistors are no longer applicable. Arising effects like velocity saturation, length/drain-induced barrier lowering (L/DIBL), electron-migration etc. are overwhelming and impossible to capture with the simple design formulas. On the other hand, these effects are readily captured with the industry-grade device models in order to describe the device operation as true as possible.

Accordingly, new methodologies for analog IC design are developed over the years. Some authors suggest symbolic analysis approach [1], [2]. This approach is usually used for generating a new analog functions or for the system level design. However, for transistor level design i.e. sizing of the devices, data-driven i.e. simulation based approach proves to be more suitable. At the ground level, data-driven approaches are usually based on the g_m/I_D methodology [3], [4]. Therefore, the main goal of this work is to provide one concise tutorial on how to apply the g_m/I_D methodology on the design of the most commonly used amplifier topology. As a case study two stage, Miller compensated, CMOS operational amplifier (opamp) is considered.

The paper is organized in six sections. The second section gives the brief overview of the g_m/I_D methodology and the procedure for building the design lookup tables. The third section covers the key design formulas that relate system and circuit level parameters of the two stage opamp. In fourth section, concrete design example is covered. Adopted trade-offs are discussed as well. Obtained simulation results are given and commented in fifth section. Key findings are summarized in the conclusion.

II. DESIGN LOOKUP TABLES

The g_m/I_D methodology can be implemented in a number of ways. Some closed source, GUI, solutions are Procedural Analog Design (PAD) Tool or ADT (Analog Designer's Toolbox) [5], [6]. Others, open source solutions, such as Gm/ID Starter Kit, are available as a set of MATLAB functions [7]. In a nut shell, these tools provide the automated way of searching the pre-simulated lookup tables. The same can be done with the help of the simple spreadsheet software (e.g. ubiquitous MS Excel).

The g_m/I_D ratio is chosen as the prime design parameter simply because it provides the link between the system level (small-signal gain) and physical domain (current) parameters. Basically, g_m/I_D tells how much current one needs in order to produce desired voltage-to-current conversion i.e. transconductance. In other words, g_m/I_D is the power efficiency of the transistor. It should be noted that for a long-channel (i.e. square-low) devices g_m/I_D equals $2/V_{ov}$, where, $V_{ov} = V_{GS} - V_{TH}$, is the overdrive voltage and V_{TH} the threshold voltage. Therefore, when transistor biasing is chosen designers' intuition, which is usually related to the choice of the overdrive voltage, still holds. However, for low-voltage, short-channel devices only proportionality between g_m/I_D and $2/V_{ov}$ can be assumed.

Practically, once the system level requirements are translated to the small-signal transconductance and the biasing currents are determined, g_m/I_D ratio is fixed. Since, small signal resistance, implicitly small signal gain, of the

Dejan Mirkovic and Milena Stanojlovic Mirkovic are with the University of Nis, Faculty of Electronic Engineering, Aleksandra Medvedeva 14, Nis, Serbia, E-mail: dejan.mirkovic @elfak.ni.ac.rs, milena.stanojlovic.mirkovic@elfak.ni.ac.rs.

transistor is a strong function of the channel length, this parameter is usually chosen based on the designers' intuition and/or experience, matching, noise etc.. Finally, the channel width can be calculated from the current density per transistor width, I_D/W. Fig. 1 exemplifies this procedure for NMOS transistor in 180nm CMOS process node.

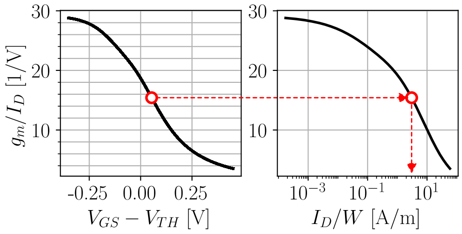

Fig. 1. The g_m/I_D and I_D/W curves for the NMOS 180nm device and channel length of 500nm

For a given g_m/I_D ratio there is a matched I_D/W ratio. The width of the channel is then simply found as the ratio of the current and the current density, I_D/W.

The g_m/I_D and I_D/W curves can be easily obtained from the simple DC, gate-source voltage sweep, analysis of the single transistor with the fixed channel width and chosen length. Drain-source voltage should be such to ensure the transistor active mode of operation for a swept gate-source voltages. Usually, it is good enough to choose $V_{DS} \geq V_{DD}/2$ and $50\text{mV} \leq V_{GS} \leq V_{DD}/2 + V_{TH}$, where V_{DD} is the supply voltage. This way all regions of interest are covered. When looking at the g_m/I_D curve, following regions can be identified: subthreshold (max. g_m/I_D), week inversion (around the first inflection point), moderate inversion (around the max slope of the g_m/I_D curve) and strong inversion (tail of the g_m/I_D curve).

The curves given in Fig. 1 for a various channel lengths can be formatted as a set of lookup tables as well. Once this data set is formed, sizing of the transistors comes down to the search of the appropriate (g_m/I_D, I_D/W) pairs for each transistor. The key point here is that this data set is created only once per target process node. Then, the design can be done independently of the circuit simulation i.e. trail-and-error process is eliminated. Also, all transistor nonidealities are confined within the data if the industry-grade models are used. Therefore, calculated device sizes should be simulation accurate at least for the nominal process corner. Of course, some adjustments can be done later in the design to compensate for the mismatch and PVT variations.

III. TWO STAGE OPERATIONAL AMPLIFIER

Schematic of the two stage, Miller compensated, CMOS opamp is shown in Fig. 2. It is a class A amplifier. This topology is known as the most commonly used for a general purpose opamp design. It also quite often serves as the testbench circuit for exploring the performances of the new process node. Practically, three key components available in ICs are present, namely: transistor, resistor and capacitor.

The design of the circuit starts with the system level specifications. These are usually given as: small-signal gain (A_o), unity-gain frequency i.e. gain-bandwidth product (f_u), maximum slope of the output voltage in transient i.e. slew-rate (SLR), phase margin (Φ_M), input/output common mode range ($I/OCMR$), power dissipation (P_d), input referred noise ($\overline{v}_{in}$) and offset (V_{os}). Depending of the application, some of the specifications are hard requirements while the others are chosen according to the acceptable trade-offs in order to meet the hard ones. E.g. for general purpose opamps usually A_o, f_u and SLR are considered as a performance metrics i.e. hard requirements. $I/OCMR$ are limited with the available power supply, but it should be maximized within reason. In general, P_d, $\overline{v}_{in}$ and V_{os} should be minimized.

A. Small-signal analysis

After performing the small-signal analysis of the circuit given in Fig. 2, following transfer function is obtained,

$$A(s) = A_o \frac{1 - s/\omega_z}{(1+s/\omega_{p1})(1+s/\omega_{p2})(1+s/\omega_{p3})} \tag{1}$$

where,

$$A_o = g_{m3}(r_{o3} \parallel r_{o5}) g_{m7}(r_{o7} \parallel r_{o8}) = A_{o1}A_{o2} \tag{1a}$$

$$\omega_z = \frac{1}{C_m(1/g_{m7} - R_m)} \tag{1b}$$

$$\omega_{p1} \approx \frac{1}{C_m g_{m7}(r_{o3} \parallel r_{o5})(r_{o7} \parallel r_{o8})} \tag{1c}$$

$$\omega_{p2} \approx \frac{g_{m7}}{C_2} \tag{1d}$$

$$\omega_{p3} \approx \frac{1}{C_1 R_m} \tag{1e}$$

$$\omega_u = A_o \omega_{p1} \approx \frac{g_{m7}}{C_m} \tag{1f}$$

are the small-signal gain at low frequencies, right-half plane (RHP) zero, first (dominant) pole, second (nondominant) pole, third (nondominant) pole and unity-gain frequency, respectively. Parasitic capacitances are,

$$\begin{aligned} C_1 &\approx C_{DB3} + C_{DB5} + C_{GS7} + (1 + A_{o2})C_{GD7} \\ &\approx C_{GS7} + A_{o2}C_{GD7} \end{aligned} \tag{2}$$

$$C_2 \approx C_{DB7} + C_{DB8} + C_{GD7} + C_L \approx C_L \tag{3}$$

Based on the qualitative reasoning relation between parasitic capacitances are $C_1 < C_m < C_2$. Taking into account this relation, and the fact that the small-signal gains are rather high at low frequencies, approximate results given in (1c-f) emerges. Since Miller compensation is introduced, dominant pole approximation can be safely applied to (1)

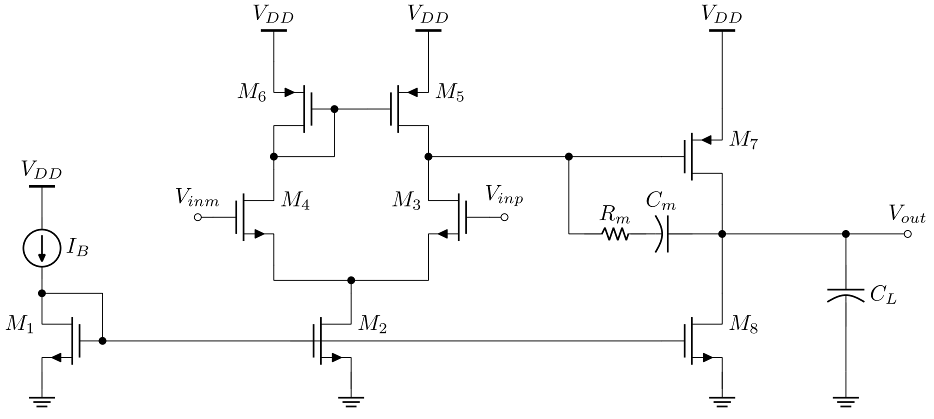

resulting with the $\omega_{p1} < \omega_{p2} < \omega_{p3}$ relation. Since R_m and C_1 are the lowest resistance and capacitance in the circuit, it is expected that the ω_{p3} is at the high frequency.

It should be noted that there is a pole-zero doublet in the transfer that is not shown in (1). This pole-zero doublet is result of the two signal paths in the input stage. One path goes through the M_3, and the other through M_4 and over the current-mirror (transistors M_5 and M_6). This doublet lies roughly at $g_{m5,6}/C_{GS5,6}$ which should be very high frequency (order of the transient frequency, $\omega_T = g_m/C_{GS}$). Therefore, sizing of the current-mirror transistors should be taken with care. Using too large dimensions for the transistors M_5 and M_6 can move this doublet to lower frequencies, hence jeopardizing the stability.

B. Stability

When looking in (1b) two scenarios are possible. The first one is to push RHP zero, ω_z, away from the unity gain frequency, ω_u, as much as possible. This way, influence of RHP zero to the frequency characteristics is minimized. The RHP zero pushout is done by choosing the compensation resistor, $R_m = 1/g_{m7}$. The second scenario is to choose, $R_m > 1/g_{m7}$, i.e. to move ω_z from RHP to LHP (left-half-plane) and to position it above the second, nondominant, pole ω_p (zero-pole cancelation) [8]. Since zero-pole cancelation assumes fixed load it is not suitable for general purpose design. Of course, if more than 80° phase margin is sought, zero-pole cancelation is a valid option. In this work RHP zero pushout is adopted, assuming the general purpose design. Combining the argument of (1) and phase-margin definition leads to the formula for compensation capacitance,

$$C_m \approx C_L \frac{1/n}{\tan(180^\circ - \Phi_M - \arctan(A_o) - \arctan(1/n))}, \quad (4)$$

where $n = g_{m7}/g_{m3}$.

C. Biasing

Biasing currents are determined based on the slew-rate and/or power consumption constraints. If the dynamics of the circuit are the hard requirement, there is inevitable speed-power trade-off. Power consumption is simply matter of current distribution through the circuit's branches. For the circuit in Fig. 2, $P_d = V_{DD}(I_B + I_2 + I_8)$, where I_B is the available biasing current drawn from the nearest, stabile, biasing source, and I_2 and I_8 are the drain currents of the transistors M_2 and M_8.

For slew-rate estimate, worst-case large-signal analysis should be applied. Usually this is done for the unity gain buffer configuration (shorted inverting input and output of the opamp). Since the large-signal, i.e. nonlinear, analysis is preformed, influence of the compensation resistor R_m can be neglected. For positive slew-rate (rising edge at the input/output) input voltage rises and M_3 becomes more conductive than M_4. In a limit M_3 caries complete current of the tail current source M_2. Simultaneously, gate potential of M_7 drops down ensuring the conduction of M_7. Since M_7 stays active second stage still provides decent amount of gain. This means that the change of the M_7 gate potential is approximately $1/A_{o2}$ times less than the change of the output potential. Therefore, change of the output voltage is nearly the same as the change of the voltage drop across compensation capacitor C_m, i.e. $\Delta V_{out} \approx \Delta V_{Cm}$. Accordingly, positive slew-rate is,

$$SLR_p \approx I_2 / C_m \quad (5)$$

For negative slew-rate (falling edge at the input/output) input voltage decreases and M_4 becomes more conductive than M_3. In a limit M_4 caries I_2 which is mirrored over M_5 and M_6 and pumped into the C_m. The potential of the M_7 rises pushing the M_7 into the cut-off. Now two current sources are active, I_2 and I_8. The C_m is discharged with the I_2, and C_L with the $I_2 - I_8$. Since the potential of the M_7 is near V_{DD} i.e. relatively constant, relation $\Delta V_{out} \approx \Delta V_{Cm}/\Delta t = -I_2/C_m$ still holds. As the output voltage physically drops across C_L, $\Delta V_{out}/\Delta t = (I_2 - I_8)/C_L = -I_8/(C_L + C_m)$ is valid as well. Therefore, negative slew-rate is,

$$SLR_m \approx -\min\{I_2 / C_m, I_8 / (C_m + C_L)\} \quad (6)$$

TABLE I
TRANSISTOR BIASING AND DIMENSIONS

Transistor	Type	L [nm]	V_{ov}[mV]	I_D [μA]	g_m/I_D [V^{-1}]	I_D/W [A/m]	$\lvert V_{GS}\rvert$ [mV]	W [μm]	$\lfloor W/m \rceil$ [μm]	m
$M_{3,4}$	N	500	127	4	15.75	2.84	500	1.41	1.4	1
$M_{5,6}$	P	500	167	4	11.98	1.17	540	3.43	1.72	2
M_2	N	750	200	8	10	6.70	580	1.19	1.2	1
M_7	P	500	167	52	11.98	1.17	540	44.63	1.4	32 (34)
M_8	N	750	200	52	10	6.70	580	7.76	1.3	6
M_1	N	750	200	2	10	6.70	580	0.3	1.2 (1.3)	0.25

Results given in (4) and (5) can be used further as the design equations for meeting the *SLR* requirement.

IV. DESIGN EXAMPLE

The data-driven methodology is applied to the two stage CMOS opamp with the following set of hard requirements: A_o=60dB, f_u=10MHz, SRL=8V/μs, Φ_M= 50° and P_d=150μW. Target process node is 180nm where nominal power supply voltage is V_{DD}=1.8V. Therefore, 50% of V_{DD}, *ICMR*=*OCRM*=0.9V is adopted. Also it is assumed that there is a I_B=2μA, stable reference current source, readily available. Resulting biasing conditions and dimensions of the transistors are given in Table I. In order to discuss the results given in Table I, the design process is explained next.

First, the compensation capacitance should be determined. According to (4), C_m=890fF assuming the phase margin of 55° and transconductance ratio, n=10. Next, transconductance of the first stage is calculated using (1f). Taking the 10% margin, $g_{m3} = g_{m4}$ = 62.2μS. Based on the chosen ratio n, $g_{m7} = ng_{m3}$ = 622μS. Since adopted compensation strategy is RHP zero-pushout, compensation resistance is $R_m=1/g_{m7}$ =1.62kΩ. Biasing current of the tail current source can be calculated with the help of (5), I_2≈8μA. Therefore, $I_3=I_4=I_5=I_6=I_2/2$=4μA. Similarly, using the (6), biasing current of the second stage should be $I_8=I_7$=52μA. When calculating biasing currents, 10% margin is accounted in *SLR* requirement.

It is important to note that the transistors M_5, M_6 and M_7 should have the same current densities and gate biasing. Practically, any difference in the source-gate voltages of these transistors will be translated in the difference of the M_3 and M_4 currents leading to the systematic offset at the input of the opamp. Accordingly, $g_{m5}/I_5 = g_{m6}/I_6 = g_{m7}/I_7$ is chosen.

To define the $g_m/I_D=2/V_{ov}$, for biasing and current source transistors i.e. M_1, M_2 and M_8, one needs to decide the appropriate V_{ov}. If no hard constraint is put on these transistors, V_{ov} can be chosen such that maximizes *ICMR* (*OCMR* is within $V_{DD} - V_{ov7} - V_{ov8}$ i.e. maximized by design). Therefore, $V_{ov2} \leq V_{DD} - V_{SG6} - V_{ov4} - ICMR$ = 0.233V. In this work $V_{ov1,2,8}$ =0.2V i.e. $g_{m1,2,8}/I_{D1,2,8}$=10V^{-1} is adopted, targeting the $ICMR \approx$ 1V.

When the biasing currents and g_m/I_D i.e. V_{ov} parameters are known for each transistor, dimensions can be determined (channel lengths, L, and widths W). As g_m/I_D methodology suggests, first lengths should be chosen. In 180nm CMOS process node, minimal L is 180nm. This, minimal channel length, even good for digital standard-cells, is not the best choice for analog circuitry simply because of the matching. Also, small-signal low-frequency gain is directly proportional to the channel-length justifying the choice of larger L. However, choosing to large value for L may increase parasitics and slow down the circuit. Besides, there is a direct economical trade-off between circuit dimensions and occupation of the chip area i.e. cost of the final product. Therefore, nearly three times the minimal, channel length of 500nm is chosen for amplifying devices M_3, M_4 and M_7. Since, M_5 and M_6 should match with the M_7, same channel length is adopted for these transistors as well. For higher output resistance and better matching, 750nm is chosen for the tail current source M_2 and the dynamic load M_8.

Finally, channel widths are calculated based on the current densities, I_D/W. To make final schematic layout-ready, each transistor is divided into the m unit devices (last two columns of Table I).

After initial operating point (OP) analysis, in unity-gain buffer configuration, dimensions of the M_8 and M_1 are slightly corrected (changes are given in the parenthesis in Table I). M_8 width is increased to better match M_5, M_6 and M_8 source-gate voltages when mid-*ICMR* input common-mode, $V_{in,cm} = (V_{TH4} - V_{SG6} + V_{DD} + V_{GS4} + V_{ov2})/2 \approx 1.2$V, is applied. This way the systematic offset is minimized.

It should be noted that the W/L ratio of the bias transistor M_1 is smaller than one. Therefore, M_1 is realized as a series combination of four unit instances (m=1/4). This means that all instances, except the one closest to the ground rail, experience the body effect. Accordingly, widths of the M_1 unit devices are increased to compensate for the body effect, ensuring the necessary gate-source voltage for the M_2 and M_8.

The final dimensions of the compensation componetns are given in Table II. The deviation from the initially designed, C_m=890fF and R_m=1.6kΩ, is evident. Initially designed values were good enough for the nominal corner. However, f_u parameter could not be met over the PVT corner variations with the initial values. Accordingly, C_m is reduced to 630fF to meet the $f_u \geq$ 10MHz and R_m is increased to 3.6kΩ to preserve the $\Phi_M \geq 50°$.

TABLE III
PROPERTIES OF THE OPAMP FOR NOMINAL CORNER (T=27C, V_{DD}=1.8V)

A_o	Φ_M [°]	f_u [MHz]	SLRp	SLR_m [V/μS]	P_d [μW]	$V_{os,sys}$ [μV]	$\overline{v_{in}}^*$[μV]	f_o [kHz]
1890 (65.53dB)	53.7	12.38	13.55	−9.81	128.6	21.65	131.8	7.94

* Integration range 10Hz to 8kHz.

TABLE II
COMPENSATION COMPONENTS

Property/Component	R_m	C_m
Type	N+ diff.	MiM
L [μm]	5	4.5
W [μm]	1.5	4.5
m	14	16
Value	3.6kΩ	630fF

V. SIMULATION RESULTS

The parameters of the designed opamp in the unity gain buffer configuration for the nominal corner (T=27°C, V_{DD}=1.8V) are given in Table III. One can see that all hard design requirements are met. Loop gain and the root-mean-square (RMS) of the input referred noise power spectral density (PSD) for nominal corner are shown in Fig. 3.

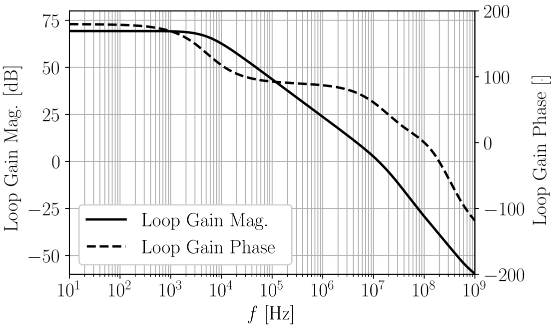

(a) Loop gain

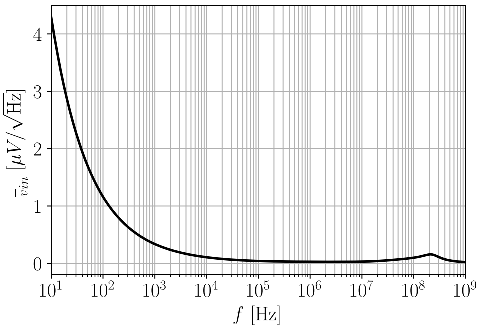

(b) RMS input referred noise PSD

Fig. 3. Opamp frequency characteristics

According to Fig. 3a, more than three orders of magnitude pole-splitting is achieved, while RHP zero lies in the 100MHz range. Time response to the sinusoidal excitation is shown in Fig. 4. Good linearity is preserved over the 1V$_{pp}$ range.

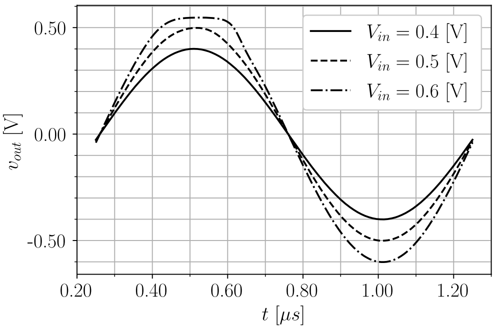

Fig. 4. Time response to the sine input

It should be noted that the V_{os} given in Table III is the systematic offset. To check the V_{os} level when input devices in differential pair, M$_3$ and M$_4$, are mismatched a set of 200 Monte Carlo analysis is performed. The offset voltage distributions are shown in Fig. 5 and the statistics parameters for nominal corner are given in Table IV.

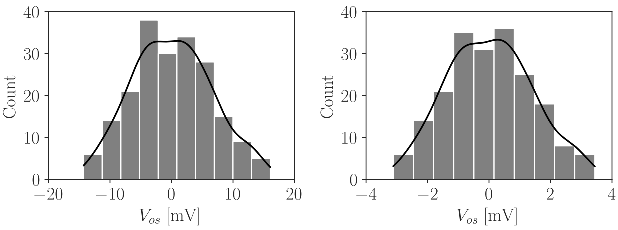

(a) Area factor 1 (b) Area factor 25

Fig. 5. Offset voltage distribution

TABLE IV
OFFSET VOLTAGE STATISTICS

Param.	Min.	Max.	Mean	Median	Std. dev.	Area factor
V_{os} [mV]	−14.32	16.07	0.158	0.177	6.39	1
	−3.12	3.44	0.032	0.072	1.38	25

For the initially designed sizes of M$_3$ and M$_4$, given in Table I, standard deviation of V_{os} is about $\sigma_{V_{os}}$=6.4mV, which may be too high for some applications. Typical measure to reduce the V_{os}, is to increase the area of the input devices. Since these devices are currently the smallest one in the design, there is a room for applying this technique. To illustrate the technique, let's assume that the chip area constraint allows for the 25 times increase in area factor of the input devices. Practically, length and width should be scaled with the same, 5 times, factor in order to preserve W/L

ratio. According to the Pelgrom's rule, standard deviation should scale with the square-root of the area factor i.e. $\sigma_{V\mathrm{os}}=6.4\mathrm{mV}/5\approx1.28\mathrm{mV}$ [9]. As Monte Carlo analysis shows, this improvement is approximately achieved i.e. $\sigma_{V\mathrm{os}}$ drops to 1.38mV, if the area of the input devices is increased 25 times.

The robustness of the design is checked with the set of the PVT corners analysis. The 66 corner analysis are done combining the appropriate models for the devices which capture the process corners, two boundary temperatures from commercial temperature range, T={0°C, 70°C} and ±10% power supply voltage variations. Summary results of the corner analysis are given in Table V.

TABLE V
CORNER ANALYSIS SUMMARY

Param./Stat.	Min	Max	Mean	Median	Std Dev.
A_o [V/V]	2594	3477	3018	3103	336.2
A_o [dB]	68.28	70.82	69.54	69.83	0.9709
Φ_M [°]	50.74	60.07	55.27	55.06	2.92
f_u [MHz]	10.32	15.25	12.59	12.51	1.288
SLR_p [V/μs]	11.83	15.35	13.52	13.63	1.131
SLR_m [V/μs]	−10.09	−8.998	−9.576	−9.582	0.2844
P_d [μW]	114.7	143.8	129	128.7	12.86
$V_\mathrm{os,\,sys}$ [μV]	−58.04	61.3	1.946	2.19	31.75
$\overline{v}_\mathrm{in}{}^{*}$[μV]	25.81	33.93	29.75	29.48	2.627
f_o [kHz]	3.583	7.127	5.118	5.025	0.8387

* Integration range 10Hz to 8kHz.

All hard design requirements are met over the PVT corner variations. In order to achieve these results, compensation components had to be designed according to Table II.

VI. CONCLUSION

This paper presents the data-driven design approach to the anolog IC circuits design. Generally accepted, $g_\mathrm{m}/I_\mathrm{D}$ methodology is discussed and process of creating the design lookup tables is described. The $g_\mathrm{m}/I_\mathrm{D}$ methodology is applied to the design of a two-stage, Miller compensated, CMOS op amp. Chosen topology is analysed and appropriate design formulas relating the system and circuit level parameters are discussed. The complete design process is outlined together with the accepted trade-offs appreciating the physical realization (layout) and the PVT variations.

Effectiveness of the applied, data-driven approach, is verified with the set of a transistor-level simulations targeting 180nm CMOS process node. With the help of the Monte Carlo analysis, effect of mismatch is shown. The one possible offset-voltage minimization technique is suggested and confirmed. Finally, the robustness of the design is checked with the PVT corner analysis.

Based on the obtained results, one can conclude that the data-driven methodology provides systematic and simulation-accurate, technology-independent, approach to the anlog IC circuits design which was the prime goal of this work. Therefore, authors hope that this work will serve well as the comprehensive tutorial covering the whole design process i.e. creation of the design look-up tables, analysis, design and simulation of the analog IC block.

ACKNOWLEDGEMENT

This work has been supported by the Ministry of Education, Science and Technological Development of the Republic of Serbia.

REFERENCES

[1] M. B. Elamien, B. J. Maundy, L. Belostotski, and A. S. Elwakil, "Analog Circuit Design Using Symbolic Math Toolboxes: Demonstrative Examples," *IEEE Transactions on Very Large Scale Integration (VLSI) Systems*, vol. 29, no. 11, pp. 1850–1860, 2021.

[2] S. Djordjević and P. Petković, "Topology oriented symbolic circuit analysis based on limit variables," in *Proceedings of Papers 5th European Conference on Circuits and Systems for Communications (ECCSC'10)*, 2010, pp. 63–66.

[3] P. Jespers, *The gm/ID Methodology, a sizing tool for low-voltage analog CMOS Circuits: The semi-empirical and compact model approaches*. Springer Science & Business Media, 2009.

[4] P. G. A. Jespers and B. Murmann, *Systematic Design of Analog CMOS Circuits*. Cambridge University Press, 2017.

[5] D. Stefanovic, M. Kayal, M. Pastre, and V. B. Litovski, "Procedural analog design (PAD) tool," in *Fourth International Symposium on Quality Electronic Design, 2003. Proceedings.*, 2003, pp. 313–318.

[6] H. Omran, "ADT Analog Designer's Toolbox." 2022. [Online]. Available: https://adt.master-micro.com/

[7] B. Murmann, "Gm/ID Starter Kit." 2022. [Online]. Available: https://web.stanford.edu/~murmann/gmid

[8] P. E. Allen and D. R. Holberg, *CMOS analog circuit design*. Elsevier, 2011.

[9] A. Sheikholeslami, "Process Variation and Pelgrom's Law [Circuit Intuitions]," *IEEE Solid-State Circuits Magazine*, vol. 7, no. 1, pp. 8–9, 2015.

Electric Field Distribution in the Vicinity of Dental Implant Exposed to the Electromagnetic Radiation from the Mobile Phone

Dejan Jovanovic, Vladimir Stankovic, Nenad Cvetkovic,
Dragana Zivaljevic, Dragan Vuckovic and Zeljko Hederic

Abstract – Determining the electric field distribution in the vicinity of dental implant exposed to the mobile phone electromagnetic radiation is aim of this paper. For this purpose, the numerical models of human head, dental implant and actual smartphone are created. Human head modelling includes using the values of electromagnetic properties of biological tissues (conductivity, electric permittivity and magnetic permeability). In order to obtain the electric field distribution within human head, the numerical calculation based on the Finite Integration Technique (FIT) is performed. The simulation is performed for the frequency of 1800 MHz. Computational results suggest a conclusion that the electric field strength inside the biological tissues is higher in the vicinity of dental implants.

Keywords – Dental implants, Electric field distribution, Finite integration technique, Non-ionizing radiation.

I. INTRODUCTION

A number of used mobile phones and broadband wireless communication devices has rapidly grown over the last few decades. These devices have become an integral part of modern everyday life. Consequently, there is a significant increasing of users' exposure to radio frequency (RF) radiation originating from these devices.

One way to determine the impact of RF radiation of mobile phones is based on the realization of numerical models for calculation of the penetrated electromagnetic field inside the user's head tissue. The accuracy of, in that way obtained results, is increasing due to the constant development of numerical methods and improvement of computer performances.

Some of the initial studies have used simple models of the human head to determine the spatial distribution of the EM field. The head was usually modelled with one or two homogeneous layers, with main goal to properly simulate the human brain characteristics [1-3]. The accuracy of the results obtained by application of these models is limited, since they do not take into account the boundary conditions on the separation surface of different biological tissues. However, within the studies [4] and [5] authors designed models of the human head which approximate real head's structure more realistic. These results can be considered as more accurate related to those ones presented in the framework of previously realized studies.

Since the effects of exposure to electromagnetic radiation depend on the composition, morphology and dimensions of observed biological structure, it is justified to expect that dental implant presence has significant influence on the distribution of mobile phones electromagnetic radiation.

The results of available research suggest that the presence of metal objects can significantly increase the amount of absorbed energy [6- 7]. Also, electrochemical effects are often present, which leads to increase in levels of certain elements which can cause allergic and other adverse reactions [8-9].

The previously mentioned presence of the mobile phones in everyday life and the fact that phone users often have dental implants, justify the interest to characterize the impact of metal dental implant on the electric field distribution in its vicinity. Such analysis requires designing of the adequate numerical models of adult person's head with dental implants that sufficiently approximate the morphology, dimensions, biochemical and electromagnetic characteristics of biological tissues and used materials. Also it is necessary to create appropriate model of actual smart phones.

II. NUMERICAL MODELS

Within the research that is the topic of this paper, it was necessary to create the following numerical models: human head model, titanium dental implants model, actual smartphone model and the corresponding antenna model for frequency of 1.8GHz.

A. Numerical model of the human head

In order to determine the influence of dental implants on the spatial distribution of electromagnetic field inside

Dejan Jovanovic, Nenad Cvetkovic, Dragana Zivaljevic and Dragan Vuckovic are with the University of Nis, Faculty of Electronic Engineering, Nis, Serbia. E-mails: [dejan.jovanovic, nenad.cvetkovic, dragana.zivaljevic, dragan.vuckovic]@elfak.ni.ac.rs.

Vladimir Stankovic is with the University of Nis, Faculty of Occupational Safety, Nis, Serbia. E-mail: vladimir.stankovic@znrfak.ni.ac.rs.

Zeljko Hederic is with the J.J. Strossmayer University of Osijek, Faculty of Electrical Engineering, Computer Science and Information Technology, Osijek, Croatia. E-mail: zeljko.hederic@ferit.hr.

the user's head, which originates from mobile phone, it is necessary to create a 3D realistic head model. It is designed so that its anatomical and morphological characteristics correspond to the real structure of the average adult person's head, as closely as possible (Fig. 1).

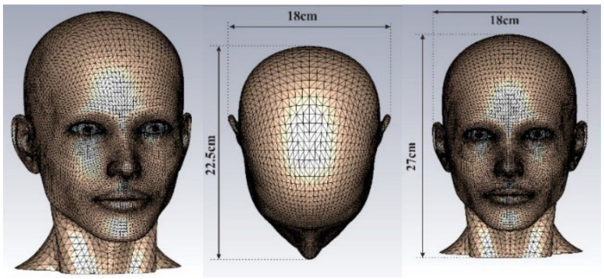

Fig. 1. External look of human head model and its dimensions.

The realistic 3D model of the user's includes the following biological tissues and organs: skin, fat tissue, muscle tissue, skull, mandible, tongue, teeth, vertebrae, cartilage, thyroid gland, eyes, cerebrospinal fluid, brain and pituitary gland. The construction of the head model is shown in Figure 2, where individual biological tissues and organs can be observed in the corresponding cross-sections.

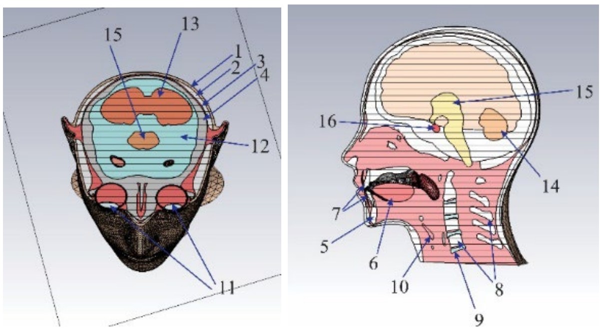

Fig. 2. Construction of the user's head model: 1 - skin; 2 - fat tissue; 3 - muscle tissue; 4 - skull; 5 - mandible; 6 - tongue; 7 - teeth; 8 - vertebrae; 9 - cartilage; 10 - thyroid gland; 11 - eyes; 12 - cerebrospinal fluid; 13 - cerebrum; 14 - cerebellum; 15 – brain tree and 16 - pituitary gland

After the forming of the 3D model head's structure it is necessary to assign appropriate electromagnetic characteristics values and join them with biological tissues and organs. The characteristics of tissues and organs at the frequency of 1.8 GHz, used in the simulation, are overtaken from [10].

B. Numerical model of dental implants

It should be noticed that realization of a dental implant numerical model was performed based on 3D images of real implants used in certain surgical interventions. The dimensions of the implant and the values of the electrical parameters of the material used for implant production applied in the numerical analysis, correspond to the real parameters of the medical implants. Dental implants, as well as the corresponding 3D models used in the simulation, are shown in Figure 3, including their position within the 3D model of the user's head related to other biological tissues and organs.

C. Numerical model of actual smart phone

The appearance and position of the smartphone used as electromagnetic radiation source related to the user head model is shown in Fig. 4. The corresponding 3D numerical model of the smartphone consists of the following parts: housing, camera, battery, display, PCB board, and antenna for the 3G mobile network.

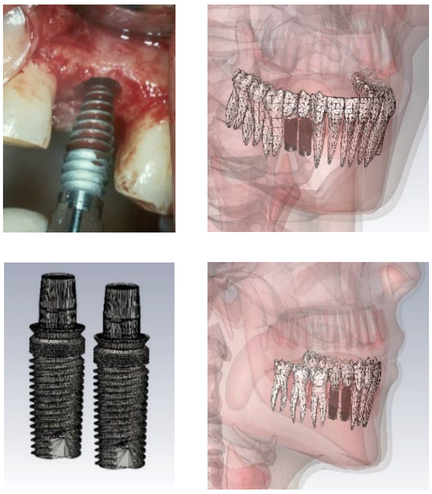

a) b)

Fig. 3. a) external appearance of dental implants b) position of the implant within the 3D model of the user's head

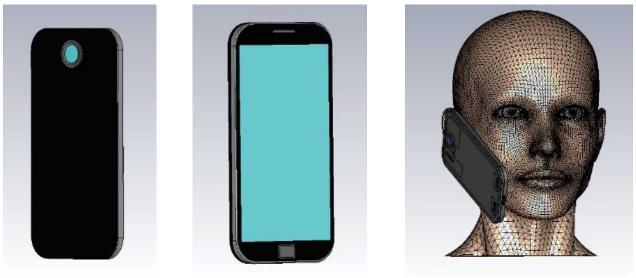

Fig. 4. Appearance of a 3D numeric model of a mobile phone.

III. RESULTS

Described simulation procedure is applied on the structure which cross-section is shown in Fig. 5. Since the analysis of the influence of dental implants on the distributions of electric field intensity is realized for the tissues placed in the vicinity of dental implant, the cross sections chosen for simulation are positioned at the implant level. The case when implants are positioned in the mandible placed in teeth 4 and 5 are considered.

A comparative representation of the spatial electric field distribution within the model, with and without implants, is given in Fig. 6 a-b. The maximum value of the electric field on the colour palette is set to be the same for both models in order to provide more simple comparison of the obtained results.

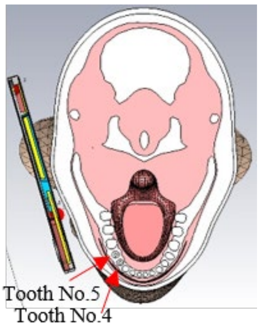

Fig. 5. Cross-sections of the head model for the analysis of the obtained results.

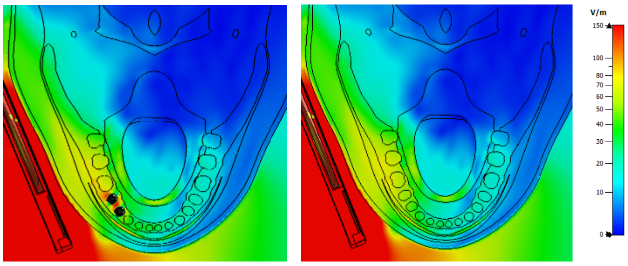

a) b)

Fig. 6. Spatial distribution of electric field *E* [V/m] within the head model: a) with dental implants and b) without dental implants.

From Figs. 5-6, it can be noticed that higher electric field intensity values occur within the model with dental implants. These values of the electric field are mainly detected inside the mandible, in which the implants are placed.

In accordance with the previous, there is an interest to present the spatial distribution of the electric field within the mandible with and without implants (Fig. 7).

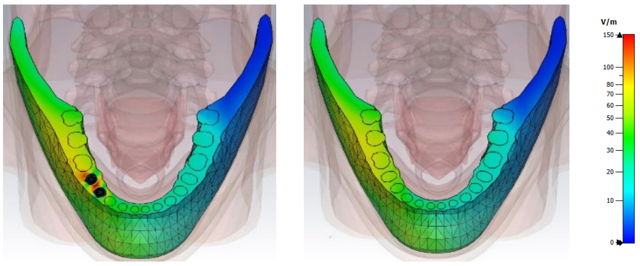

a) b)

Fig. 7. Spatial distribution of electric field *E* [V/m] within the mandible: a) with dental implants and b) without dental implants.

In order to illustrate the increase in electric field intensity, in the case of the model with implant related to the model without implant, the dependence of electric field intensity within both models versus distance from the radiation source is shown in Fig. 8.

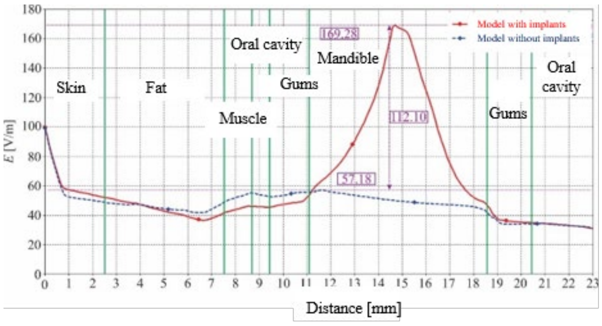

Fig. 8. Electric field intensity *E* [V/m] within both models.

Based on the results shown in Fig. 8, increasing of the electric field value within the mandible can be clearly seen in the case of the model with dental implants. The maximum value of the electric field intensity in the presence of implants is 169.28 V/m, which is 112.10 V/m higher in comparison to the value for the model without implants, having maximum of 57.18 V/m. Also, graphics from Fig. 8 suggests that, the presence of the implant does not significantly affect the distribution of the electric field intensity within other tissues included in model.

IV. CONCLUSION

The aim of this study was to examine the influence of dental implants on the electromagnetic radiation, which originates from the mobile phone, inside the users' biological tissues and organs. To realize this goal, the certain numerical models have been used: human head model, dental implants model, as well as the model of smartphone.

Based on the presented results, one can conclude that there is difference in the values of penetrated electric field strength for the cases with and without dental implants.

The overall analysis of the previously presented results for the electric field intensity, within the tissue in the vicinity of the dental implants, leads to the conclusion that the presence of dental implants cause increasing of the maximum values of penetrated electrical field within the mandible at the working frequency of 1800 MHz.

REFERENCES

[1] Lee, A.K., Choi, H.D., Lee, H.S., Pack, J.K., „Human Head Size and SAR Characteristics for Handset Exposure“, *Etri Journal*, Vol. 24, pp. 176-180, 2002. doi:10.4218/etrij.02.0202.0202.

[2] Kouveliotis, N., Panagiotou, S., Varlamos, P., Capsalis, C.N. „Theoretical Approach of the Interaction Between a Human Head Model and a Mobile Handset Helical Antenna Using Numerical Methods“, *Progress In Electromagnetics Research*, Vol. 65, pp. 309-327, 2006. doi:10.2528/PIER06101901.

[3] El Dein, A.Z., Amr, A., „Specific absorption rate (SAR) induced in human heads of various sizes when using a mobile phone“, *7th International Multi- Conference on*

Systems, Signals and Devices, Amman, Jordan, 27-30 June 2010, pp. 1-6. doi: 10.1109/SSD.2010.5585549.

[4] Whittow, W.G., Panagamuwa, C.J., Edwards, R.M., Vardaxoglou, J.C., „The Energy Absorbed in the Human Head Due to Ring-Type Jewelry and Face-Illuminating Mobile Phones Using a Dipole and a Realistic Source“, *IEEE Transactions on Antennas and Propagation*, Vol. 56, No. 12, pp. 3812-3817, 2008. doi: 10.1109/TAP.2008.2007353.

[5] Khalatbari, S., Sardari, D., Mirzaee, A.A., Sadafi, H.A., „Calculating SAR in Two Models of the Human Head Ex-posed to Mobile Phones Radiations at 900 and 1800 MHz“, *Progress In Electromagnetics Research Symposium*, Cambridge, USA, 26-29 March, 2006. doi:10.2529/PIERS050905190653.

[6] Whittow, W.G., Edwards, R.M., Panagamuwa, C.J., „Effect of tongue jewellery and orthodontist metallic braces on the SAR due to mobile phones in different anatomical human head models including children“, *Loughborough Antennas and Propagation Conference*, Loughborough, UK, 17-18 March, 2008, pp. 293-296. doi: 10.1109/LAPC.2008.4516924.

[7] Jovanovic, B.D., Krasic, Dj.D., Stankovic, B.V., Cvetkovic, N.N., Vuckovic, D.D., „Electric Field and SAR Distribution in the Vicinity of Orthodontic Brace Exposed to the Cell Phone Radiation“, *ACES Journal*, Vol. 34, No. 12, pp. 1904-1914, 2019.

[8] Mortazavi, S.M.J., Paknahad, M., Khaleghi, I., Eghlidospour, M., „Effect of radiofrequency electromagnetic fields (RF-EMFS) from mobile phones on nickel release from orthodontic brackets: An in vitro study“, *International Orthodontics*, Vol. 16, No. 3, pp. 562-570, 2018. doi: 10.1016/j.ortho.2018.06.013.

[9] Fujii, Y., „Gold Alloy Dental Inlay for Preventing Involuntary Body Movements Caused by Electromagnetic Waves Emitted by a Cell Phone“, *Open Journal of Antennas and Propagation*, Vol. 2, No. 4, pp. 37-43, 2014. doi: 10.4236/ojapr.2014.24005

[10] *Dielectric properties of tissues*, ITIS Foundation, Available at: https://goo.gl/76SnEN

Proceedings of the 9th Small Systems Simulation Symposium 2022, Niš, Serbia, 28th February - 2nd March 2022

Prediction of Electricity Consumption in Cold Storage Facility using Gated Recurrent Unit Neural Networks

Novak Radivojević, Miona Andrejević Stošović

Abstract - In this paper a method for predicting electrical energy consumption using a recurrent neural network architecture is presented. A gated recurrent unit (GRU) neural network model is constructed and then trained to predict the consumption values upon the historical consumption data provided by a cold storage company. Different models will be presented and analysed.

Keywords – Gated recurrent unit, Electricity consumption, Prediction, Time series.

I. INTRODUCTION

With the tremendous rise of electrical energy demand worldwide and with numerous new electronic devices being produced each day, many problems related to efficient use of electrical energy are posing difficult challenges to electricity consumers of all levels – from households to facilities of large companies.

Most of these challenges could be overcome by accurate prediction of electricity demand. Knowing how the consumption values will vary in the near future would make a good support for supply management, because this would greatly simplify the task of taking required actions to regulate the supply level to match the device operation demands in a timely manner. At the same time, this would also make electricity costs predictable and it would provide a basis upon which a consumer could make financial plans. This makes consumption prediction a very important task and many companies and facilities nowadays include such a system that employs consumption predicition in order to prevent shortages or reduce costs.

In order to solve prediction problems, a quantity is usually represented as a time series and then the values from a number of consecutive time steps in series are taken as an input to a mathematical model which generates predicted value(s) for the next timestep(s). Traditionally, mathematical models used on forecasting time series employ statistical methods such as Autoregressive Integrated Moving Average (ARIMA) [1], exponential smoothing etc., but using these methods requires that some statistical properties of data being predicted must fulfil some conditions, i.e. the data must be stationary in order to gain reasonable prediction results. Recently, deep learning models have been recognized as a prominent tool for solving prediction problems due to the simplicity of implementation and availability of software which allows to easily create neural network models and implement machine learning algorithms. Another reason is that unlike statistical models, neural networks can perform well even without examining statistical properties of data.

The most popular kind of neural network models used in time series prediction problems is the recurrent neural network (RNN) structure [2]. Unlike traditional feed-forward networks where the weights connecting hidden layers are directed from the input to the output, RNN's introduce temporal feedback connections in such a way that outputs of an RNN depend not only on the current input data, but also on the data presented to the network in previous timesteps. This way, RNNs are capable of capturing temporal dependence and patterns within data which makes them suitable for time series prediction.

As a concept, RNNs originated in the '80s and have undergone numerous improvements in terms of performance and complexity since then. Many new versions of RNN structures have emerged lately, most popular of which are Long Short-Term Memory (LSTM) [3] and Gated Recurrent Unit (GRU) [4]. These models have found their use in many fields of science and technology ranging from internet search engines to speech recognition. In this paper, the structure of the GRU model will be discussed and applied to solving the problem of electricity consumption prediction.

II. ELECTRICITY CONSUMPTION DATASET

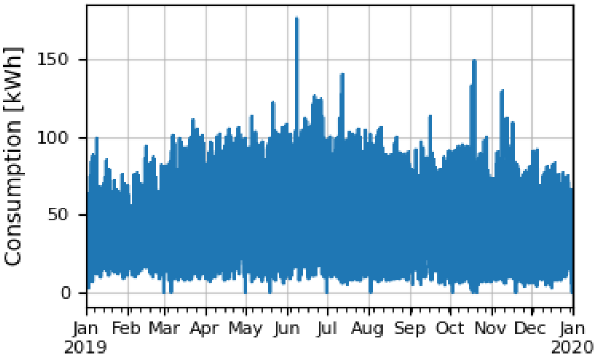

Fig. 1. A part of the electricity consumption dataset

Novak Radivojević and Miona Andrejević Stošović are with the University of Niš, Faculty of Electronic Engineering, A. Medvedeva 14, Niš, Serbia, E-mail: {novak.radivojevic, miona.andrejevic}@elfak.ni.ac.rs

The electricity consumption dataset is obtained from a cold storage facility which uses a consumption measurement system that generates data in hourly intervals. The data obtained is measured in kilowatt-hours, and measurements are taken for the period from January 1st, 2019. to February 28th, 2021, containing a total of 18960 data points. Fig. 1 shows values of consumption recorded during the year of 2019. Measured consumption values are quantized with a quantization step of 0.128 kWh.

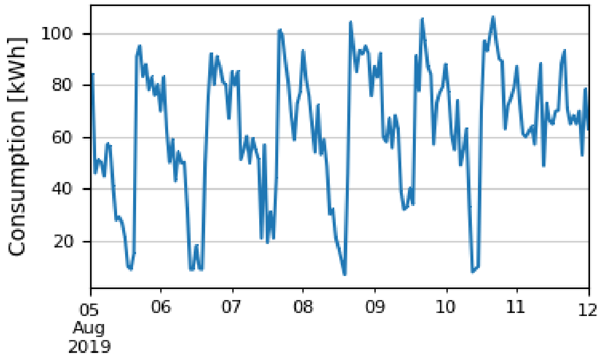

Fig. 2. Single week seasonal pattern

By exploring the dataset in more detail, it can be seen that the consumption values change in a periodical manner, i.e. the consumption time series shows a seasonal pattern. An example of this pattern is shown in Fig. 2. Each day, electricity consumption oscillates around higher values (60-110 kWh) during the period between midnight and early morning hours, drops to the lowest levels at noon, reaches a peak value in the early afternoon and returns to the 60-110 kWh range in the afternoon. This pattern holds for all days of the week, except for Sundays when the usual drop at the noon is absent. Taking this into account sets the conclusion that this time series shows a week level seasonality and it is expected that the neural network model should easily capture this pattern.

III. THE STRUCTURE OF GRU MODEL

The concept of gated recurrent units was first introduced in 2014 by Kyunghyun Cho et al. [5]. The structure of these neural networks is similar in form to the structure of an LSTM unit but has a fewer number of trainable network parameters which is why GRUs are considered to be more efficient than LSTM in terms of training performance and memory usage.

The structure of a single GRU cell is given in Fig. 3. Its main components are the input node which accepts sequential input data, the activation node which represents the memory unit of the structure and contains calculated data which is later used to make sequence predictions, the *reset* gate which decides which data in the activation node will take part in making a prediction in the following timestep, the *update* gate which decides which parts of the memory state should be updated with new information and which should be transmitted to the next timestep without change and the output stage which processes the gated data and directs them to the cell output.

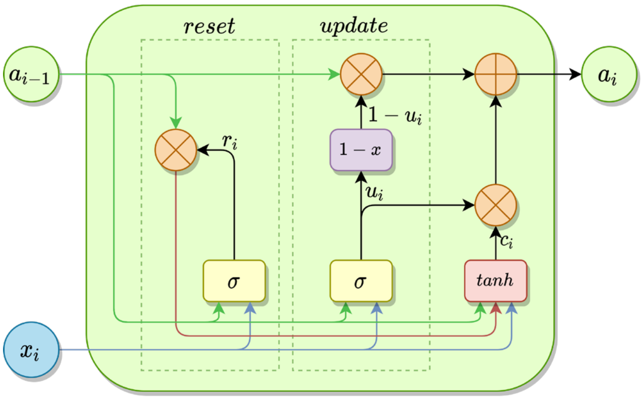

Fig. 3. Architecture of a GRU cell

The operation of a GRU cell can be described with the following equations:

$$r_i = \sigma(W_r \cdot [a_{i-1}, x_i]) \tag{1}$$

$$u_i = \sigma(W_u \cdot [a_{i-1}, x_i]) \tag{2}$$

$$c_i = \tanh(W \cdot [r_i * a_{i-1}, x_i]) \tag{3}$$

$$a_i = u_i * c_i + (1-u_i) * a_{i-1} \tag{4}$$

Where "σ" denotes the sigmoid function, "[,]" is the concatenation of two vectors, "·" is the vector dot product and "*" is the pointwise vector product. Quantities involved in the Eqs (1) to (4) are the following:

- x_i - input data vector at i-th timestep
- a_i - activation data vector at i-th timestep
- W_u, W_r, W - matrices of hidden layer parameter weights for update gate, reset gate and output activation node, respectively
- r_i - state of the reset gate at i-th timestep
- u_i - state of the update gate at i-th timestep
- c_i - new activation vector candidate

In each timestep, new input data as well as the activation vector from the previous timestep are presented to the GRU cell and their values are transmitted to both reset and update gate. Reset gate structure is represented by Eq. (1) – it consists of a sigmoid activation function neuron layer which calculates the reset state. Sigmoid function is defined by:

$$\sigma(x) = \frac{1}{1+e^{-x}} \tag{5}$$

The range of the sigmoid function takes values between 0 and 1 which makes it very suitable for data gating by pointwise multiplication of a vector of data by a gating vector. Gating vector elements with values close to 0 diminishes the corresponding element in the data vector, while values close to 1 leave the data element unchanged and thus allow their propagation. Here, the resulting reset state vector is a gating vector which is multiplied by a previous activation and thus determines which previous activation elements can take effect on the prediction in the current timestep and the neuron layer is trained to learn how to calculate the reset state based on the input and previous activation.

Eq. (2) represents the update state. Update gate functions in the similar way as the reset gate, except that the update state as its gating vector here decides which elements of the activation vector should be given a new value.

Based on the reset and update state, the ouput stage generates the new activation vector. Eq. (3) determines the activation data candidate, and it is calculated by a neuron layer with hyperbolic tangent activation function. Inputs to this layer are the input data, previous activation and the reset state, and the layer generates a vector of new data for updating the activation vector. Eq. (4) explains how the cell chooses which data is updated and which is unchanged – values of update state close to 1 pick the candidate data and values close to 0 transmit the previous data to the output.

Fig. 4 shows how multiple GRU cells are incorporated in order to perform the task of sequence prediction. A number of *N* cells are arranged to form a chain, passing the activation data in sequence from the first cell to the last. When predicting the $k+1^{st}$ member of the, the cells receive *N* previous consecutive members in the corresponding order (S_{k-N+1}, S_{k-N+2}, … S_{k-2}, S_{k-1}, S_k). The predicted value is calculated based on the activation vector of the last cell in the chain. The structure of the output node of this network is the same as the output layer of a feed-forward network – the predicted value is connected through trainable weights with the elements of the last activation vector in the sequence.

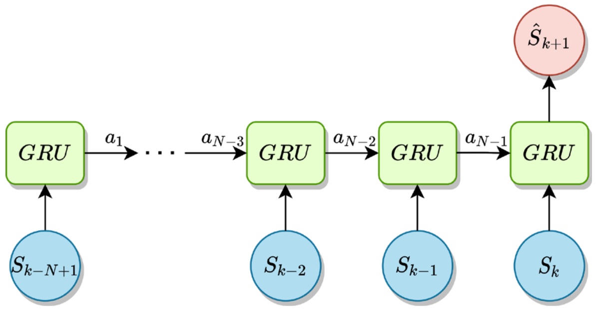

Fig. 4. GRU Chain

IV. GRU Model Development

In time series prediction, length of input sequence is a factor that greatly affects the prediction accuracy. For that reason, several GRU models with different input sequence lengths are constructed based on the GRU chain structure. For each model, the training and testing dataset is generated by creating pairs of input and desired output data vectors from the main dataset. For a model of input length *N*, vector pairs are generated by the sliding window technique: given dataset *S*, *i*-th input-output pair is created from *N*+1 consecutive dataset points where S_i, S_{i+1}, S_{i+2}, S_{i+3}, … S_{i+N-1} are taken as input data and S_{i+N} is the desired output, where *N* is the length of input sequence i.e. the length of the GRU chain. If the length of the dataset is *L*, then the total number of input-output pairs generated is *L*-*N*-1. The generated pairs are split into training and testing subsets so that the test subset contains values measured after June 1st, 2020 which is about 34.5% of total number of pairs for *N*=24.

In order to inspect how daily and weekly seasonality impact the predictions, the amount of data with previous values of consumption (input sequence length) should cover multiple days or weeks. For this reason, 6 GRU models are created with so input lengths of 24, 48, 96, 168, 336 and 720 datapoints, respectively.

During the training process, hyperparameter optimization is done for each model in order to see how different model attributes affect the prediction accuracy and which hyperparameter values should be used to achieve optimal performace. The models are optimized over the following hyperparameters:

- Number of neurons in each hidden layer of all GRU cells
- Number of epochs (training iterations)
- Batch size – the number of input-output training pairs given to the network in each iteration
- Probability distribution function used for randomized weight initialization
- Dropout rate – the percentage of weights discarded from the network to avoid overfitting

Optimization is done using the randomized cross-validation technique. A list of possible values/atrributes for each hyperparameter is given and the model is trained multiple times with different combinations of values of hyperparameters which are picked randomly from the given lists. After each training iteration, the hyperparameter combination is evaluated by model prediction accuracy and training time. Lists of hyperaparmeter values used are given as:

- Number of hidden neurons: 80, 120, 160, 200
- Number of epochs: 100, 200, 300, 400, 500
- Batch size: 1000, 2500, 5000
- Probability functions for initializing weights: normal, uniform, glorot uniform, lecun uniform
- Dropout rate: 0, 0.1, 0.25, 0.5

V. RESULTS

After completing the training process, the models are tested by making predictions based on the data from the test set and comparing them to the actual values. Model accuracy is evaluated by calculating prediction errors over the whole test set using an error function. For the given models, four error measuring criteria are used: mean absoulte error (MAE), mean absolute percentage error (MAPE), mean squared error (MSE) and root-mean-square error (RMSE). Table I shows the resulting accuracy of each of the six models according to the given criteria.

TABLE I
PREDICTION ACCURACY OF DIFFERENT MODELS

Input length	MAE [kWh]	MAPE [%]	MSE [kWh^2]	RMSE [kWh]
24 h	9.18652	30.39272	152.27621	12.31703
48 h	8.90783	28.42099	141.72927	11.8594
96 h	8.62057	28.39520	132.34083	11.45233
168 h	**8.20198**	**26.68128**	**118.12174**	**10.85477**
336 h	8.31308	26.64113	119.42588	10.88098
720 h	8.96186	27.65428	135.72690	11.42495

The results show that the model with the input sequence length of 168 data points has the highest accuracy according to MAE (8.20198 kWh), MSE(118.12174 kWh) and RMSE (10.85477 kWh). The lowest MAPE is achieved by the model with the length of 336 (26.64113%), but given that its value is slightly lower than the one for the 168-length model (26.68128%) and that the 336-length model is more complex to train, it can be considered that the 168-length model is optimal. Table II shows the combination of hyperparameter values for this optimal model.

Figs. 9 to 13 show the prediction results for one week period from different places in the test set. Figs. 9 and 10 show the weeks for which the root-mean-square prediction error is the lowest and highest, respectively. Figs. 11, 12 and 13 show cases randomly selected from the dataset. From the figures, it can be seen that the model captures the trend and the daily and weekly seasonal pattern of consumption values very well. Larger errors occasionally happen when there are unexpected peaks/drops in consumption which happen at few places in the test set.

TABLE II
HYPERPARAMETERS OF OPTIMAL MODEL

No. of hidden units	Epochs	Batch size	Initializer	Dropout rate
200	200	2500	Glorot uniform	0.5

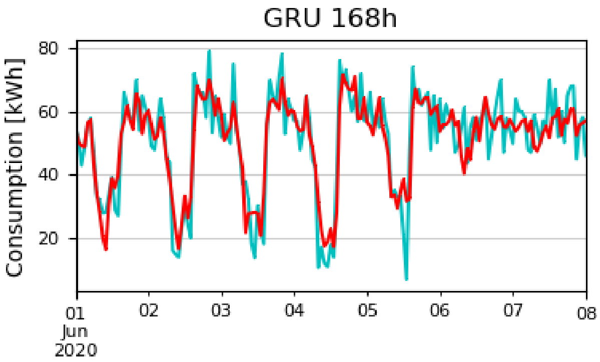

Fig. 9. Lowest prediction error week

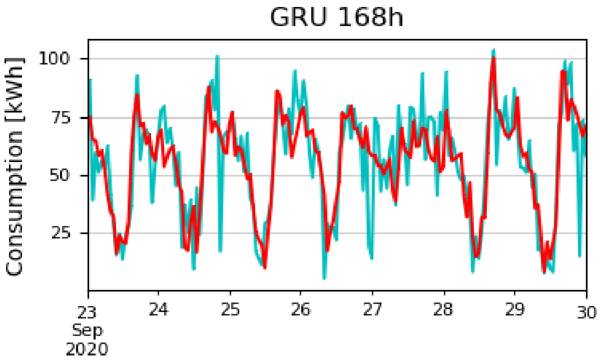

Fig. 10. Highest prediction error week

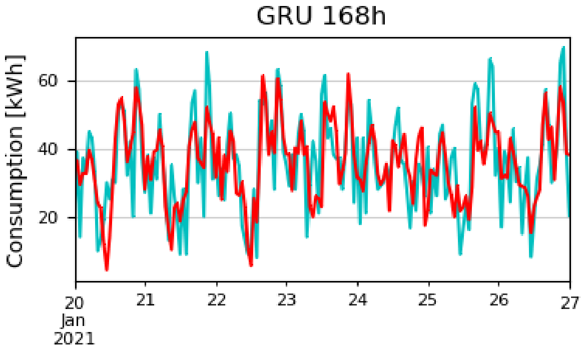

Fig. 11. Predictions for the week of January 20th – 27th, 2021

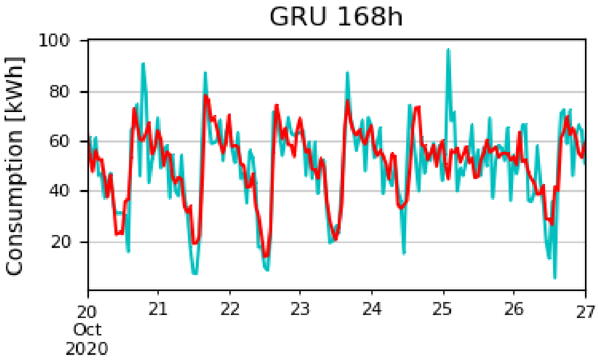

Fig. 12. Predictions for the week of October 20th – 27th, 2020

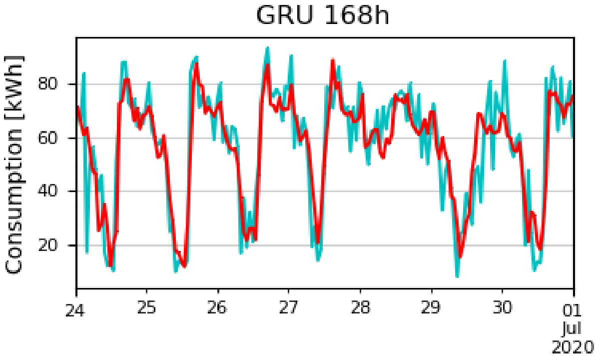

Fig. 13. Predictions for the week of June 24th – July 1st , 2020

VI. CONCLUSION

In this paper a gated recurrent unit neural network model was trained to predict the consumption values upon the historical consumption data provided by a cold storage company.

Different models were discussed regarding length of input vector, i.e. previous data necessary to obtain a good prediction.

Prediction accuracy of different models is given using four error measuring criteria.

Analysing these results, we concluded that a model that includes 168 previous results predicts the best.

ACKNOWLEDGEMENT

This work has been supported by the Ministry of Education, Science and Technological Development of the Republic of Serbia.

REFERENCES

[1] C. Nichiforov, I. Stamatescu, I. Făgărăşan and G. Stamatescu, "Energy consumption forecasting using ARIMA and neural network models," 2017 5th International Symposium on Electrical and Electronics Engineering (ISEEE), 2017, pp. 1-4, doi: 10.1109/ISEEE.2017.8170657.

[2] S. Haykin, Neural Networks and Learning Machines, Pearson, Prentice Hall, 2008.

[3] Sepp Hochreiter, Jürgen Schmidhuber; Long Short-Term Memory. Neural Comput 1997; 9 (8): 1735–1780.

[4] Junxiang Wang, Canyang Guo, Ling Wu, "Gated Recurrent Unit with RSSIs from Heterogeneous Network for Mobile Positioning", Mobile Information Systems, vol. 2021, Article ID 6679398, 7 pages, 2021. https://doi.org/10.1155/2021/6679398

[5] Junyoung Chung, Caglar Gulcehre, Kyunghyun Cho, Yoshua Bengio, “Empirical Evaluation of Gated Recurrent Neural Networks on Sequence Modeling”, arXiv.org, 2014

VHDL Logic Design Exercises Simulating COVID-19 Protection Systems

Nenad Petrović

Abstract – Coronavirus pandemic has brought unexpected challenges not only to medical personnel, but engineers as well. Information technology and digital devices are recognized among key-enablers for realization of systems aiming the reduction of COVID-19 disease spread. In this paper, it is explored how electronics and computer engineering education can be enriched with exercises relevant to the current pandemic. As case study, Logic Design (accreditation 2019.) course exercises in VHDL at the second year of undergraduate Computer Science and Informatics track within Faculty of Electronic Engineering, University of Nis are considered. Two illustrative examples are presented, covering the aspects of modelling and simulation from two different perspectives: combinational logic and finite state machine implementation.

Keywords – coronavirus, logic design, VHDL.

I. INTRODUCTION

Despite that the current pandemic has put enormous pressure on doctors and other medical science-related personeel, the importance of engineering in global battle against coronavirus has been recognized as well [1, 2]. Various digital systems are leveraged in order to enforce the adoption of safety measures which aim to reduce the spread of COVID-19 disease. On the other side, such systems automatize check procedures and eliminate the need of human interventation in many cases. Considering the fact that it is mainly identified as flu-alike respiratory disease, mask wearing and temperature checks are becoming obligatory within most of the public institutions, especially indoors. Moreover, at current stage of the pandemic, validation of vaccination-related documents and so-called "green certificates" is being performed as routine in hospitality and travelling [3].

In this paper, the main focus is on introducing exercises within undergraduate computer science and electronics curriculum that would make students more aware about their possible contribution during the pandemic situation. The considered case study is based on topics of new elective course Logic Design for computer science students, which cover Very High-Speed Integrated Circuits Hardware Description Language (VHDL) design of both combinational and sequential digital systems. As outcome of this paper, two example exercises are presented with full implementation in VHDL.

Previously, the author has been incorporating the implementation of COVID-19 protection systems within other related courses at the Faculty of Electronic Engineering, Universty of Nis, as well. In [4], exercises covering PIC family microcontrollers as part of Microcomputer Systems course at the third year of bachelor degree (accreditation) were descrbied. On the other side, [5] introduces Intel 8086 assembly language examples for the same course and finite state machine model aiming the earlier accreditation of Logic Design course (2013), together with Matlab code for corresponding graph representation and its verification.

II. BACKGROUND

A. Very High-Speed Integrated Circuits Hardware Description Language (VHDL)

The development of VHDL started in 1983, when US Department of Defense (DoD) decided to fund a project whose goal was standardization of methods used for documenting behavior of digital systems. As outcome, a language-alike system behaviour model notation was introdced. However, it was extended with aspects enabling simulation based on textual notation and IEEE released the first standardized version IEEE 1076-1987 in 1987, while there are also two later revisons from 1993 and 2008. The main properties of VHDL language can be summarized as: not case-sensitive; comments start with "--"; assignments and declarations end with ";" . It includes the following types of data [1]: bit {0,1}; Boolean {true, false}; character {256 ASCII characters}, integer, real, bit_vector {*end_index* downto *begin_index*}.

Table I shows an overview of VHDL elements, crucial for modelling, simulation and verification of digital systems [6], relevant to the scope of this paper.

TABLE I
OVERVIEW OF BASIC VHDL ELEMENTS

Element	Usage	Template

Entity	Represents named interface of a digital system, expressed in form of ports with several possible directons (in, out, inout or buffer) and types (such as bit/logic, vector and others).	`entity <e_name> is`
		`port (`
		`port1: <mode><type>;`
		`...`
		`portN: <mode> <type>`
		`);`
		`end entity;`

Architecture	Description of digital system's behavior.	`architecture <a_name> of <e_name> is`
		`--user-defined enums`
		`--signals`
		`--constants`
		`--components`
		`begin`

		--behavior description **End**

Testbench	Simulation and system verification.	<instance_name> :
		<DUT_name> **port map**
		(port1 => signal1,
		...
		portP => signalP);
		
		STIMULUS: **process**
		begin
		-- time point t1
		SIGNAL1_TB <=
		<signal_value_1>;
		...
		SIGNALN_TB <=
		<signal_value_K>;
		wait for <duration1>
		...
		--- time point tN
		...
		end process;

Report	Used within testbench to set the status of the current test (severity level) depending on outcome. Possible levels of severity are: failure, error, warning and note.	**report** "message" **severity** <level_of_severity>
Assert	Performs system verification in synergy with report. Checks if given Boolean condition is false in order to print the corresponding message.	**assert** <boolean_condition> **report** "message" **severity** <level_of_severity>;

Testbench represents a concept in VHDL leveraged for simulation of system behavior and its verification in case of various input values. It is a component without any real inputs and outputs, but it generates input signal patterns (stimulus) and leads them to the input of the system entity whose beahvior is examined (Device Under Test – DUT). However, the inputs and the outputs of the DUT have to be mapped to the appropriate signals contained within the testbench, as shown in template from Table I. Moreover, it also provides the ability to observe the output generated as a response. This way it is possible to perform system automated system verification in synergy with additional VHDL constructs – report and assert [6]. Fig. 1 depicts how testbench is used for system simulation and verification.

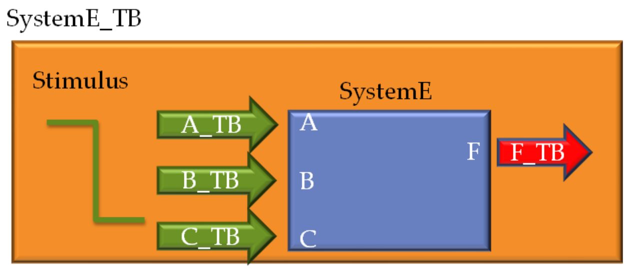

Fig. 1. VHDL entity (DUT) and testbench usage

Additionally, when it comes to architecture, there are various levels of abstraction [6] adopted for system behavior description (covering both combinational and sequential logic), as it is given in Table II.

TABLE II
VARIOUS ABSTRACTIONS FOR SYSTEM BEHAVIOR DESCRIPTION IN VHDL

Method	Template
Concurrent assignments with logic operators	<signal$_1$> **<=** <in$_1$> op <in2> <signal$_2$> **<=** <signal$_k$> op ... <signal$_j$> <output> **<=** <signal$_1$> op ... <signal$_n$> op = {and, or, exor, not}
Selection	**with** *<input_name>* **select** **<signal_name> <=** expression_1 **when** condition_1, ... expressionN **when** **others;**
Conditional assignment	<signal_name> <= expr1 **when** cond1 **else** expr2 **when** cond2 **else** ... exprN;
Component reuse with mapping	*<instance_name> : <component_name>* **portmap(port1=>signal1,...** **portN=>signalN);**

When it comes to digital circuits considered in this paper, two main types are covered: combinational and sequential. While combinational circuits are time-independent and do not rely on previous system states and inputs for output generation, on the other side, sequential circuits are those which are depend on clock cycles, present and past inputs together with system states as well.

Regarding VHDL implementation of sequential circuits, three main processes have to be defined [6], as described in Table III. In general, there are two types of finte state machine used for modelling of sequential circuits: Mealy and Moore. While Mealy machine generates output values determined by both its current state and current inputs, the output of Moore machine depends only on its current state. Therefore, the implementation of output logic for these two finite state machine models is different, Mealy includes the inputs apart from current state within the sensitivity list of the underlying VHDL process.

TABLE III
SEQUENTIAL LOGIC CIRCUIT PROCESSES IN VHDL

Method | Template

State memory

```
STATE_MEM : process (Clock, Reset)
begin
if (Reset = '0') then
<current_state> <= <initial_state>;
elsif (Clock'event and Clock='1') then
<current_state> <= <new_state>;
end if;
end process;
```

Transitions

```
TRANSITIONS : process
(<current_state,<input> )
begin
case (<current_state>) is
when state1 => if (<input> = '1') then
<new_state> <= <state2>;
else
<new_state> <= <state3>;
end if;
...
when others => <new_state> <= <stateN>;
end case;
end process;
```

Output logic

```
OUTPUT_LOGIC : process (<current_state>,
<input1>)
begin
case (<current_state>) is
when <state1> => if (<input1> = '1')
then
<output1> <= '1'; <output2> <= '0';
else
...
when others => <output1> <= '0';
<output2> <='0';
end case;
end process;
```

III. IMPLEMENTATION

A. COVID-19 Indoor Protection - Combinational Logic with Select and Testbench

The goal of the first assignment is to model and implement a COVID-19 indoor safety system using combinational logic in VHDL, inspired by realistic IoT implementation from [7]. The system consists of a control unit, door lock and two 7-segment displays showing message. For implementation, it is required to make use of concurrent assignments and select construction in VHDL. The system itself can be represented as block diagram depicted in Fig. 2. It has three input bits representing the outcomes of condition checks, assumed to be coming from external systems (considered as black boxes): 1) A0 – takes value "1" if person has body temperature greater than normal 2) A1 – becomes "1" in case that person does not wear mask 3) has value "1" when the current number of guests inside the room is greater than the allowed threshold. Otherwise, in the opposite cases, each of these bits becomes "0". On the other side, the system has three outputs: 1) 7-bit vector F1 – the contents shown on the first display 2) 7-bit vector F2 – the letter shown on the second 7-segment display 3) 1-bit control signal C – if its value is "1", the door will be opened, otherwise they stay closed. The two displays show corresponding messages, depending on the outcome of the checks represented as 3-bit input vector A. In case that person has normal temperature, wears mask and people count is below the limit (A="000"), the door will be opened (C="1") and "OK" message will be displayed. Otherwise, the door remains closed, while the message on display is "HE". However, the only exception is the situation when person does not wear mask, but the other checks pass, then, the message "ЧК" will be shown, but the door remains closed, as person has to wait for the mask to be brought by the security guard. When it comes to 7-segment displays, it is assumed that single segment is active on "1", while the segment annotations are shown within the illustration. Additionally, it is required to construct an appropriate test bench for simulation purposes and illustrate the system behavior within the characteristic cases (different messages on display).

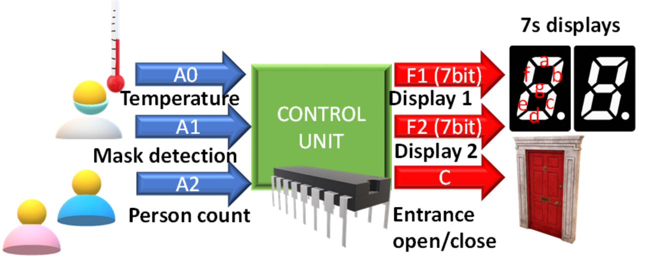

Fig. 2. COVID-19 indoor safety system model

In what follows, Fig. 3 shows the full VHDL code of system implementation, including the test bench for simulation of cases covering various messages shown on 7s displays. First, the interface (inputs and outputs with corresponding data types) of this system is declared in form of entity element, according to the given specification. After that, the behavior of this system is described within the architecture block. The first par of architecture block assigns the value to the entrance open/close signal, denoted as C using select construction, depending on the input A. Moreover, there are two more select consturctions, each of them used for the assignment of the correct value for decoding messages which are shown on 7-displays. On the other side, the rest of VHDL file describes a testbench used for simulation and observation of system's behavior. Fig. 4 shows the screenshot from Intel ModelSim [8] environment depicting the outcome of simulation for within the defined testbench from Fig.3.

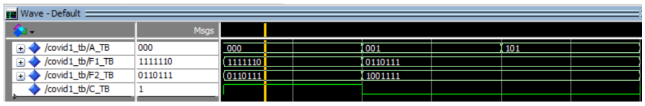

```
/covid1_tb/A_TB    000       000       001       101
/covid1_tb/F1_TB   1111110   1111110   0110111
/covid1_tb/F2_TB   0110111   0110111   1001111
/covid1_tb/C_TB    1
```

Fig.4. Intel ModelSim screenshot – example 1

```
entity covid1 is
     port (A : in  bit_vector (2 downto 0);
          F1 : out bit_vector (6 downto 0);
          F2 : out bit_vector (6 downto 0);
          C : out bit
);
end entity;

architecture covid1_arch of covid1 is
begin

with (A) select
C <= '1' when "000",
     '0' when "001",
     '0' when "010",
     '0' when "011",
     '0' when "100",
     '0' when "101",
     '0' when "110",
     '0' when "111";

with (A) select
F1 <= "1111110" when "000",
      "0110111" when "001",
      "0110011" when "010",
      "0110111" when "011",
      "0110111" when "100",
      "0110111" when "101",
      "0110111" when "110",
      "0110111" when "111";

with (A) select
F2 <= "0110111" when "000",
      "1001111" when "001",
      "0110111" when "010",
      "1001111" when "011",
      "1001111" when "100",
      "1001111" when "101",
      "1001111" when "110",
      "1001111" when "111";

end architecture;

entity covid1_TB is
end entity;

architecture covid1_TB_arch of covid1_TB is
component covid1
     port (A : in  bit_vector (2 downto 0);
           F1 : out bit_vector (6 downto 0);
           F2 : out bit_vector (6 downto 0);
           C : out bit
);
end component;

     signal A_TB : bit_vector (2 downto 0);
     signal F1_TB :  bit_vector (6 downto 0);
     signal F2_TB :  bit_vector (6 downto 0);
     signal C_TB :  bit;
begin
     DUT1: covid1 port map (A => A_TB, F1 => F1_TB, F2 => F2_TB, C=>C_TB);

     STIMULUS : process

     begin
          A_TB <= "000"; wait for 100 ps;
          A_TB <= "001"; wait for 100 ps;
          A_TB <= "101"; wait for 100 ps;
     end process;

end architecture;
```

Fig. 3. COVID-19 indoor safety system VHDL implementation using combinational logic and select

B. Vaccination Record Check - Sequential Logic Example

On the other side, another example represents vaccination record check and hand sanitizer system which could be installed at the entrance of places like galleries, museums, shopping malls or restaurants, which is a simplified version of work presented in [1]. The goal is to perform the following checks for each new visitor. First, the person is prompted to show valid QR code of vaccination record or negative COVID-19 test. If record is not valid, the entrance would remain closed. Otherwise, proximity sensor detects presence of hands and dispenses sanitizer if they are detected. After that, the entrance is opened. However, person should not be able to enter the building without performng hand disinfection.

When it comes to solution, the system is modelled as Mealy automaton, with three possible states: *Start* – new person is detected; *Cert* – checking the COVID-19 vaccination record or certificate; *Hand* – detecting hands. There are three possible inputs encoded with 2 bits: “00” – new person detected; “01” – check passed; “10” – check failed. When it comes to output, there are also three possible outputs: “00” – entrance remains closed; “01” – entrance opened; “10” – hand sanitizer activated. The corresponding graph with state transitions is illustrated in Fig. 5.

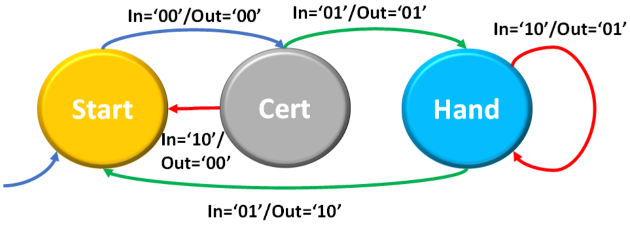

Fig. 5. Mealy automaton representing vaccination record check and hand sanitizing system

In what follows, VHDL implementation of the previously introduced system will be described. First, the following entity is defined, with 2-bit inputs and outputs, together with 1-bit clock and reset input signals, as shown within the code excerpt in Fig. 6.

```
entity covid2 is
     port (Clock, Reset : in std_logic;
           Input      : in std_logic_vector (1 downto 0);
           Output           : out std_logic_vector (1 downto 0));
end entity;

architecture covid2_arch of covid2 is
     type State_Type is (Start, Cert, Hand);
     signal current_state, next_state : State_Type;
begin
```

Fig. 6. Entity definition for vaccination record check and hand sanitization system

As it was told in *Background* section, three main processes have to be defined for sequential logic cicuits. The code of state memory process is presented within Fig. 7. It contains clock and reset input signals within the sensitivity list, which is quite generic for such circuits. In case of reset signal (which is active on “0”), current state is set to the initial - *Start*. On the other hand, when rising clock edge is detected (transition from “0” to “1” on clock input), the current state will be updated.

```
STATE_MEMORY : process (Clock, Reset)
begin
     if (Reset='0') then
          current_state <= Start;
     elsif (Clock'event and Clock='1') then
          current_state <= next_state;
     end if;
end process;
```

Fig. 7. State memory process definition in VHDL for vaccinaton record and hand disifection system

Furthermore, it is also necessary to define the logic which deermines next state as distinct process. It includes both the current state and input within the sensitivity list, as they affect the outcome of state transition. The corresponding VHDL code based on graph edges from Fig. 5 is given in Fig. 8.

```
NEXT_STATE_LOGIC : process (current_state, Input)
begin
     case (current_state) is
          when Start => if (Input = "00") then
               next_state <= Cert;
          else
               next_state <= Start;
          end if;

          when Cert =>  if (Input = "01") then
               next_state <= Hand;
          else
               next_state <= Start;
          end if;

          when Hand =>  if (Input = "01") then
               next_state <= Start;
          else
               next_state <= Start;
          end if;
          when others => next_state <= Start;
     end case;
end process;
```

Fig. 7. State transition process in VHDL for vaccinaton record and hand disifection system

On the other side, the process for system output generation is presented in Fig. 8. Due to fact that implementation is based on Mealy's automaton, both current state and input are also present in the sensitivity list of this process.

```
OUTPUT_LOGIC : process (current_state, Input)
begin
          case (current_state) is

               when Start   => if (Input = "00") then
                    Output <= "00";
               else
                    Output <= "00";
               end if;

               when Cert    => if (Input = "01") then
                    Output <= "01";
               else
                    Output <= "00";
               end if;

               when Hand    => if (Input = "10") then
                    Output <= "01";
               else
                    Output <= "10";
               end if;

               when others => Output <= "00";
          end case;
end process;

end architecture;
```

Fig. 8. Output generation process in VHDL for vaccinaton record and hand disifection system

Finally, the VHDL code of the testbench used for system verification is shown in Fig. 9. The input sequence from the testbench illustrates example when entrance is unlocked. First, the system is restarted to initial state, by setting Reset="0". Once the system goes back to Start state, Reset becomes "1", in order to enable transition from the initial state for the corresponding state (otherwise, the system would keep reseting, as Reset is active on "0"). After that, the following sequence of Input signal is generated "00" – new person arrived, "01" – valid COVID-19 certifficate, "01" – hands detected for disinfection. For each transition, rising clock edge is generated. In the last step, the expected value of final Output is "10" – entrance opens. Therefore, for purpose of verification, assert construct checks the output value and reports error if it does not match with the expected one.

```
Library IEEE;
use IEEE.std_logic_1164.all;
use IEEE.numeric_std.all;

entity covid2_TB is
end entity;

architecture covid2_TB_arch of covid2_TB is
component covid2 is
     port (Clock, Reset : in std_logic;
          Input      : in std_logic_vector (1 downto 0);
          Output          : out std_logic_vector (1 downto 0));
end component;

signal Clock_TB : std_logic;
signal Reset_TB: std_logic;
signal Input_TB : std_logic_vector (1 downto 0);
signal Output_TB : std_logic_vector (1 downto 0);

begin
     DUT1: covid2 port map (Clock => Clock_TB, Reset => Reset_TB,
          Input => Input_TB, Output => Output_TB);

     STIMULUS : process

     begin

          Reset_TB <= '0'; wait for 100 ps;
          Reset_TB <= '1'; wait for 100 ps;
          Input_TB <=  "00"; wait for 100 ps;
          Clock_TB <= '0'; wait for 100 ps;
          Clock_TB <= '1'; wait for 100 ps;
          Input_TB <=  "01"; wait for 100 ps;
          Clock_TB <= '0'; wait for 100 ps;
          Clock_TB <= '1'; wait for 100 ps;
          Input_TB <=  "01"; wait for 100 ps;
          assert Output_TB="10"
          report "Entrace should open" severity error;
          Clock_TB <= '0'; wait for 100 ps;
          Clock_TB <= '1'; wait for 100 ps;

     end process;

end architecture;
```

Fig. 9. VHDL testbench for verification of vaccination record check and hand disifection system

ModelSim screenshot showing the execution of input sequence for entrance unlocking is given in Fig. 10.

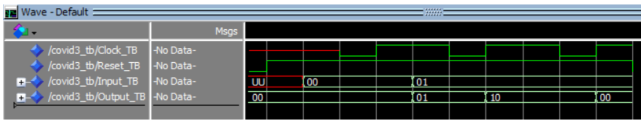

Fig. 10. Intel ModelSim screenshot – example 2

V. CONCLUSION AND FUTURE WORK

This paper introduces a concept of coronavirus protection system-related exercises within the introductory courses of computer science and electronics undergraduate studies. The presented exercises were aligned with Logic Design course curriculum (2019.) at the Faculty of Electronic Engineering. The major course topic were covered: VHDL design, combintional and sequential logic. In next course iterations and upcoming exam sessions, it is planned to include such exercises and compare with previous course outcomes. Moreover, in future, it is also planned to perform electronic survey among the students who selected the course, considering the grades, exam pass rate, motivation and interest. Furthermore, we will analyse the results using data mining methods (such as clustering, classification and regression), which could help to finally determine the effectiveness of such approach in practice.

VI. ADDITIONAL REMARKS

VHDL code of exercise implementation aiming ModelSim - Intel FPGA Starter Edition 10.5b (Quartus Prime 18.1) simulation and execution environment are publicly available on GitHub: https://github.com/penenadpi/covid_VHDL

ACKNOWLEDGEMENT

This work has been supported by the Ministry of Education, Science and Technological Development of the Republic of Serbia.

REFERENCES

[1] Petrović, N., Kocić, Đ., “Smart technologies for COVID-19 indoor monitoring”, *Viruses, Bacteria and Fungi in the Built Environment*, ISBN: 9780323852067, Woodhead Publishing, pp. 251-272, 2021. https://doi.org/10.1016/B978-0-323-85206-7.00012-5

[2] Wang, Q., Su., M., Zhang, M., Li, R., “Integrating Digital Technologies and Public Health to Fight Covid-19 Pandemic: Key Technologies, Applications, Challenges and Outlook of Digital Healthcare”, International Journal of Environmental Research and Public Health. 2021; 18(11):6053, 2021. https://doi.org/10.3390/ijerph18116053

[3] Petrović, N., Roblek, V., Radenković, M., Nejković, V., Papachashvili, N., “Smart Technologies for the Post-COVID-19 Tourism Industry”, 15th International Online Conference on Applied Electromagnetics - ПЕС 2021, pp. 133-136.

[4] Petrović, N., “Prototyping PIC16-based COVID-19 indoor safety solutions within microcomputer systems course”, IEEESTEC – 13th Student Projects Conference, pp. 185–189, 2020.

[5] Petrović, N., “COVID-19 Safety Systems Design Exercises in Computer Science University Courses”, YuInfo 2021, pp. 1-6, 2021.

[6] B. J. LaMeres, “Introduction to Logic Circuits & Logic Design with VHDL”, *Springer*, 2017.

[7] Petrović, N., Kocić Đ., “IoT-based System for COVID-19 Indoor Safety Monitoring”, IcETRAN 2020, pp. 603-608, 2020.

[8] ModelSim*-Intel® FPGA Edition Software [online]. Available on: https://www.intel.com/content/www/us/en/software/programmable/quartus-prime/model-sim.html, last accessed: 18/02/2022.

List of Authors